MinEx CRC Limited
26 Dick Perry Avenue, Kensington, WA, 6151
PO Box 1130, Bentley, WA, 6102, Australia
admin@minexcrc.com.au

MinEx CRC
ABN: 66 625 533 913

MinEx CRC provides financial support to the value of $1K to promote Honours and Masters by Coursework projects that are aligned with the mission of MinEx CRC and to encourage young researchers toward a career in mineral exploration research. Projects are not restricted to MinEx CRC Participants and Affiliates.

Please note that the content of this thesis has not been subjected to peer-review and subsequent corrections.

Australian Government
Department of Industry, Science and Resources
Cooperative Research Centres Program

Investigations into the geology of the Tumut Trough, Lachlan Orogen, NSW

Travis Batch

Bachelor of Science (Honours)

Supervisors: Alistair Hack, Robin Offler
Co-supervisors: Ryan Dwyer, Mark Eastlake

University of Newcastle
28^{th} May 2021

DECLARATION

I declare that, except where otherwise indicated, this thesis is composed of my own work.

Abstract

The tectonic setting and age of sequences in the Tumut Trough are poorly understood. To provide a better understanding of the development of the area, detailed geochemical, isotopic and geochronological studies of the mafic rocks and granites were carried out.

As a result of the geochronological studies and literature review, the stratigraphy of the Tumut Trough was refined, showing three distinct phases: the basement material, the trough infill and the subsequent granitic intrusions. Units were related based on geochemistry and geochronology. By relating different rock units, the timing of the units without age constraints can be inferred.

The Wermatong Metabasalt is a multiply deformed mafic schist with deformation unlike most other rocks found in the Tumut Trough. It is interpreted to have an Early Cambrian - Late Ordovician age similar to the Bullawyarra Schist, which is also multiply deformed; it forms part of the basement to the Tumut Trough. The Kimo Diorite and Benwerrin Diorite are related geochemically and likely to be coeval. The Honeysuckle Beds and North Mooney Complex are also related geochemically and likely to be coeval.

U-Pb analysis of zircons show that the granites in the area were emplaced between 420 and 410 Ma. These ages update the existing K-Ar ages on the Bogong Granite and Gocup Granite, and refine the existing U-Pb ages on the Gocup Granite and Kimo Diorite. Ages are presented for the previously undated Killimicat Granite

(410.0 ± 1.5 Ma) and Warrienbah granite (415.9 ± 2.6; proposed name).

The Snowball Metabasic Igneous Complex has a minimum age of 427.8 ± 13.4 Ma based on secondary titanite. Chondrite normalised and NMORB patterns, and Th/Yb and Nb/Yb ratios indicate it and the Long Tunnel Metabasic Igneous Complex are unrelated, providing oceanic arc (Nb/Yb < 1, flat NMORB diagram) and continental arc signatures (Nb/Yb > 1, light rare earth element enriched) respectively.

The Blowering Formation and Honeysuckle Beds are both part of the basin infill and recorded ages of 426.2 ± 1.3 and 429.1 ± 1.5 Ma respectively.

With the use of Lu-Hf isotopes, the granites, Blowering Formation and Honeysuckle Beds show a similar trend to the rest of the Lachlan Orogen, with backarc closure crustal signatures progressing to more primitive signature during slab rollback. Within the Lachlan Orogen, this happens over a period of 40 million years, but in Tumut it occurred over a period of 20 million years. The trough is compared to the northern Lachlan Orogen and southern Thomson Orogen granites where the same Lu-Hf isotopic trend appears.

The Tumut Trough is also geochemically compared to the Okinawa Trough, south-west of Japan. As a developing backarc basin, the Okinawa Trough shows similar Nb/Yb and Th/Yb ratios to most of the mafic rocks in the Tumut Trough, indicating the tectonic setting for both are also similar.

Potential mineralisation based on this study is thought to be limited to fault bound structures on the eastern edge of the trough and small VAMS deposits. The Gocup granite is the most likely granite to host mineralisation.

Acknowledgements

After a year where everything seemed to go wrong, amongst natural disasters (bushfires, floods and the COVID-19 pandemic), these people made it all possible.

Firstly, I would like to thank and acknowledge Alistair Hack for setting me up with this project and supervising me for the first 12 months. It has been enjoyable to work on. Robin Offler for taking over supervision when the university restructure occurred, making sense of the geochemistry would have been much harder without you. Ryan Dwyer for working so hard, this project could not have been in the state it is without your efforts. Mark Eastlake for also helping to make sense of the area with your knowledge of the NSW geology.

This project was a MinEx CRC supported Honours project and would like to thank them for the resources made available by them and all associated affiliates.

I'd also like to thank and acknowledge those who helped with sampling and the analysis of the samples. Jake Moltzen from the Londonderry Core Library for sampling core when the public health order was in effect. Michael Bell for coming on the field trip to Tumut to sample. Bill Collins for helping me to understand the area more when on the trip to Tumut and for helping to interpret the isotope data. All of the landowners for providing access to the rocks we sampled. Yanyan Sun for making thin sections and teaching me the process so that I could make some myself. Staff at Intertek Adelaide for quickly analysing the geochemistry samples. Roland Maas for analysing the Sm-Nd isotopes. Huiqing Huang (Jeffrey) for analysing the titanite

sample. Chris Clark, Chris Kirkland, Sean Makin and staff at Curtin University for analysing the zircons and doing a first pass on the data reduction.

Those on the periphery, David Boutelier, John Greenfield, Phil Gilmore, Millicent Crowe, Alicia Caruso and Violet Perry, thanks for the help you all provided, whether that be academic or social.

Finally, I'd like to thank Mum, Dad, and my brother Lachlan for your love, support and understanding. I could not be where I am now without you.

Table of Contents

List of Figures

List of Tables

Chapter 1

Introduction

The Lachlan Orogen forms a key element of the Tasmanides of eastern Australia (Glen, 2005), extending from southeastern Queensland, through much of central and southeast New South Wales, into eastern Tasmania, and encompassing most of Victoria (Fig. 1.1). It is an extensional accretionary orogen formed from the extension of crust during slab rollback with sediment infill and subsequent thickening during contraction events (Collins, 2002b). Mineralisation is common in rift settings where metalliferous fluids can become more mobile and form mineral deposits (Gemmell et al., 1998; Zappettini et al., 2017; Downes, 2019).

Ages of the rocks in the Tumut Trough range from Cambrian to Devonian in the Lachlan Orogen (Gray and Foster, 1997; Glen, 2005). Rocks units include deep marine Ordovician turbidites, Ordovician volcanics of the Macquarie Arc, shallow marine sediments, granite bodies and volcanic complexes (Glen, 2005; Hough et al., 2007). The orogen is host to many large mineral deposits such as Woodlawn and Cadia (Downes et al., 2004; Hough et al., 2007; Ford et al., 2019a). It has experienced three deformation cycles: the Benambran cycle, Tabberabberan cycle and Kanimblan cycle (Glen, 2005). One of the major faults is the Gilmore Fault Zone (GFZ), which divides the Eastern Province from the Central and Western Provinces (Glen and Walshe, 1999) (Fig. 1.2). Within the Eastern Province lies the Tumut Trough.

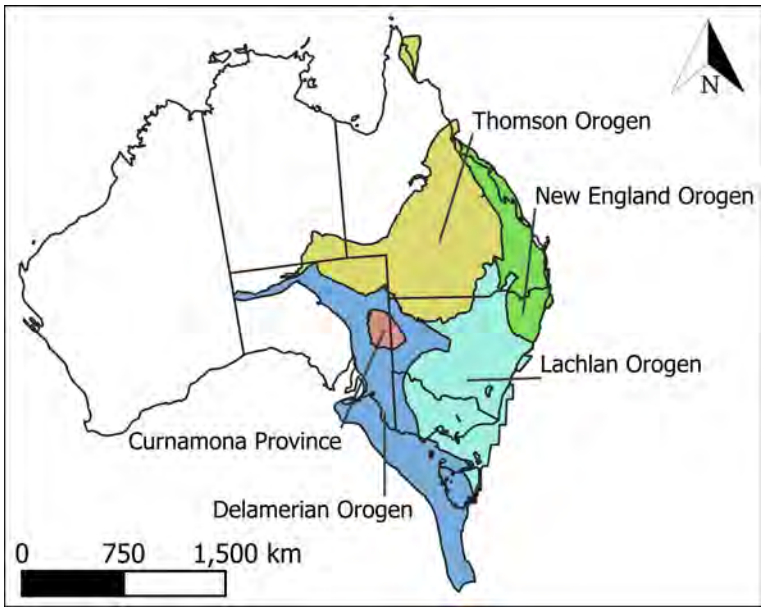

Figure 1.1: Location of the Lachlan Orogen within the Tasmanides (Modified from Raymond et al. 2018).

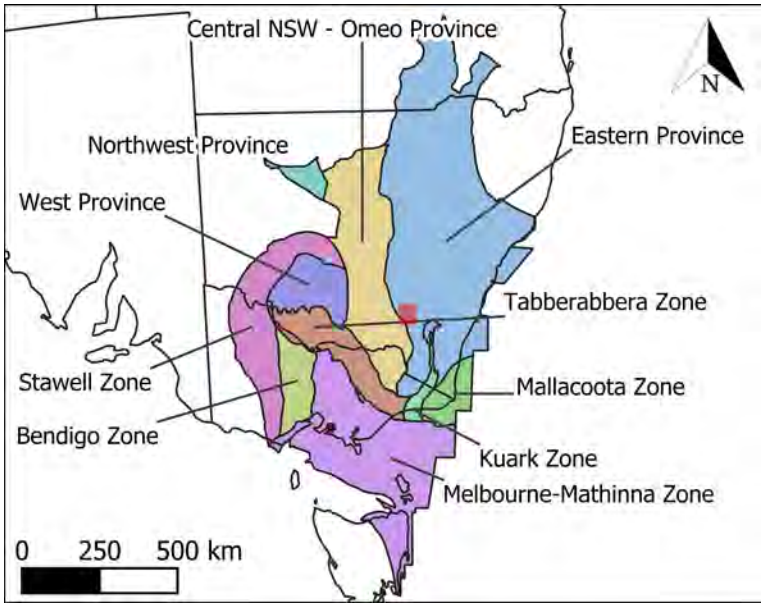

Figure 1.2: Provinces within the Lachlan Orogen and their locations. The Tumut Trough is located in red box (Modified from Raymond et al. 2018).

The Tumut Trough (Fig. 1.3) is an extensional basin located between Wagga Wagga and Canberra. Named after the small town of Tumut, a locality within the trough, it forms a component of the eastern Lachlan Orogen. It is bounded by the GFZ to the west and Coolac Serpentinite to the east (Fig. 1.3). The tectonic setting, stratigraphy and mineral potential of the Tumut Trough are all poorly understood compared to other areas of the Lachlan Orogen (e.g. Cobar), with limited geochemical data and geochronological age constraints available. This study focuses on the southern portion of the Tumut Trough where the trough is best exposed.

1.1 Background

1.1.1 Previous Work in the Tumut Trough

Much of the existing lithostratigraphic framework of the Tumut Trough was assembled during the compilation of the first edition Tumut 1:100 000 geological sheet (Basden, 1990) in the 1980s, incorporating information from earlier mapping projects. Basden described each unit within the area, provided a summary of the geology, including distribution, type section, geochemistry, age, boundary relationships, physical descriptions, metamorphism and structure, and mentioned any previous studies carried out on the unit or formation. Concurrently, Stuart-Smith (1990b) investigated the tectonics of the Tumut Trough, describing the stratigraphy from the north-east of the area, associated with the Brungle Creek Metabasalt and Bullawyarra Schist. Stuart-Smith et al. (1992) presented a revised stratigraphy for most of the trough that included modifications to Basden (1990). There are some discrepancies between these studies (Table 1.1). In his studies, Bell (2019) produced data that conflicted with that reported by Basden (1990, Table 1.1). Apart from these studies, only analyses or interpretations of individual areas or units have been carried out.

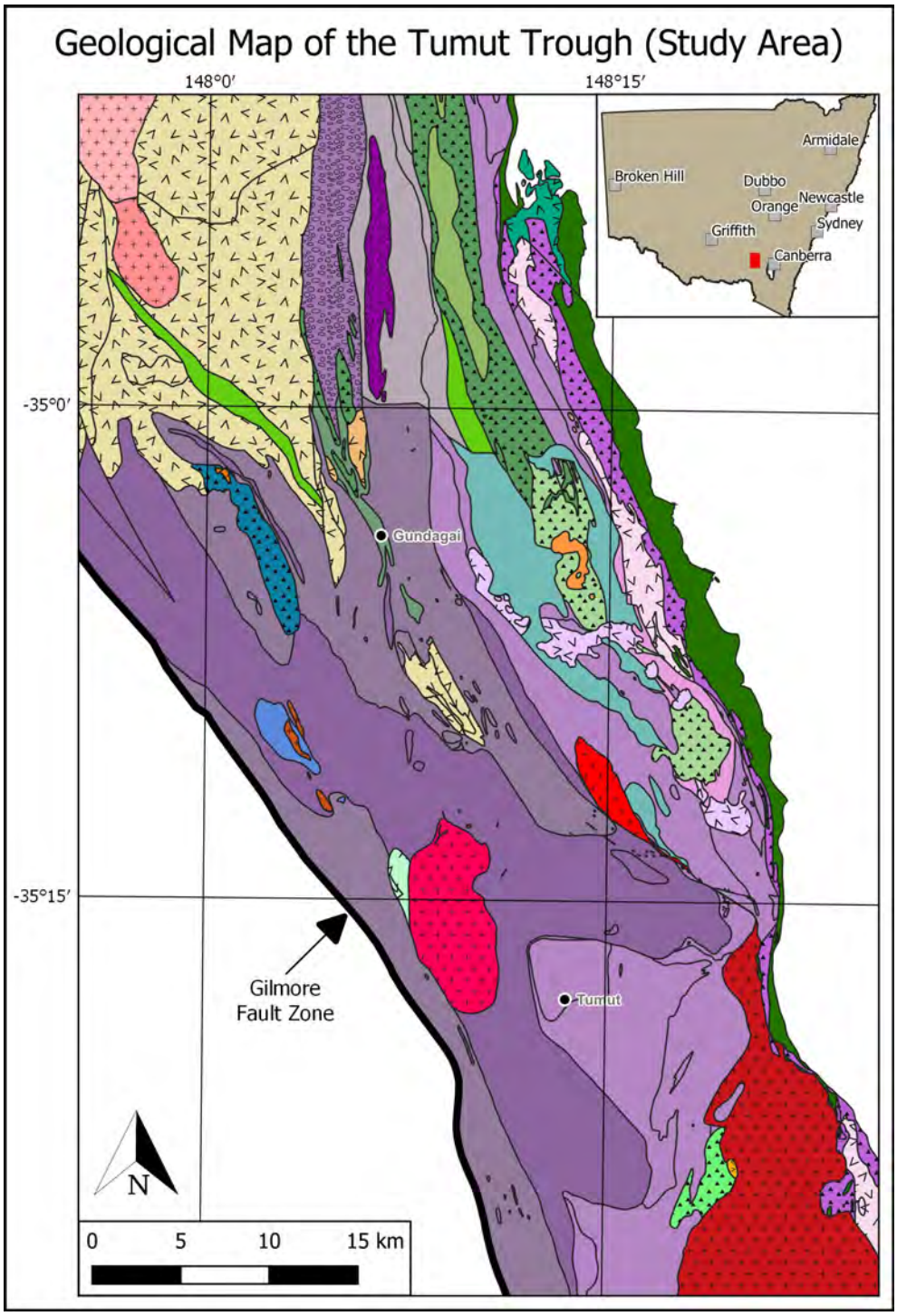

Figure 1.3: Geological map of the study area within the Tumut Trough. (Modified from Colquhoun et al. 2019). Legend appears on the following page.

More recently, U-Pb ages have been obtained from zircons (Geoscience Australia, 2007; Ickert and Williams, 2011; Bodorkos et al., 2013; Fraser et al., 2014), constraining the age of the rock units relevant to those studies. Some units, like the Killimicat Granite and Honeysuckle Beds, are still yet to have any modern ages. Others (Dadd, 1998; Dadd and Plioplis, 2005; Meffre and Glen, 2006; Bruce, 2018) have added to the limited geochemistry that is available, as well as giving their own interpretations on the rock unit relevant to the study, based on the geochemistry and previous work.

1.1.2 Stratigraphy

The Tumut Trough contains syn-extensional sediment fill and magmatic bodies unconformably overlying Cambrian - Early Ordovician basement. Post basin magmatism occurs in the form of granites. Most sediments and associated mafic units have been metamorphosed resulting in assemblages characteristic of greenschist facies (Stuart-Smith, 1990b). Rocks range between Early Devonian to Cambrian in age.

The Tumut Trough has the following currently accepted stratigraphy (Fig. 1.4).

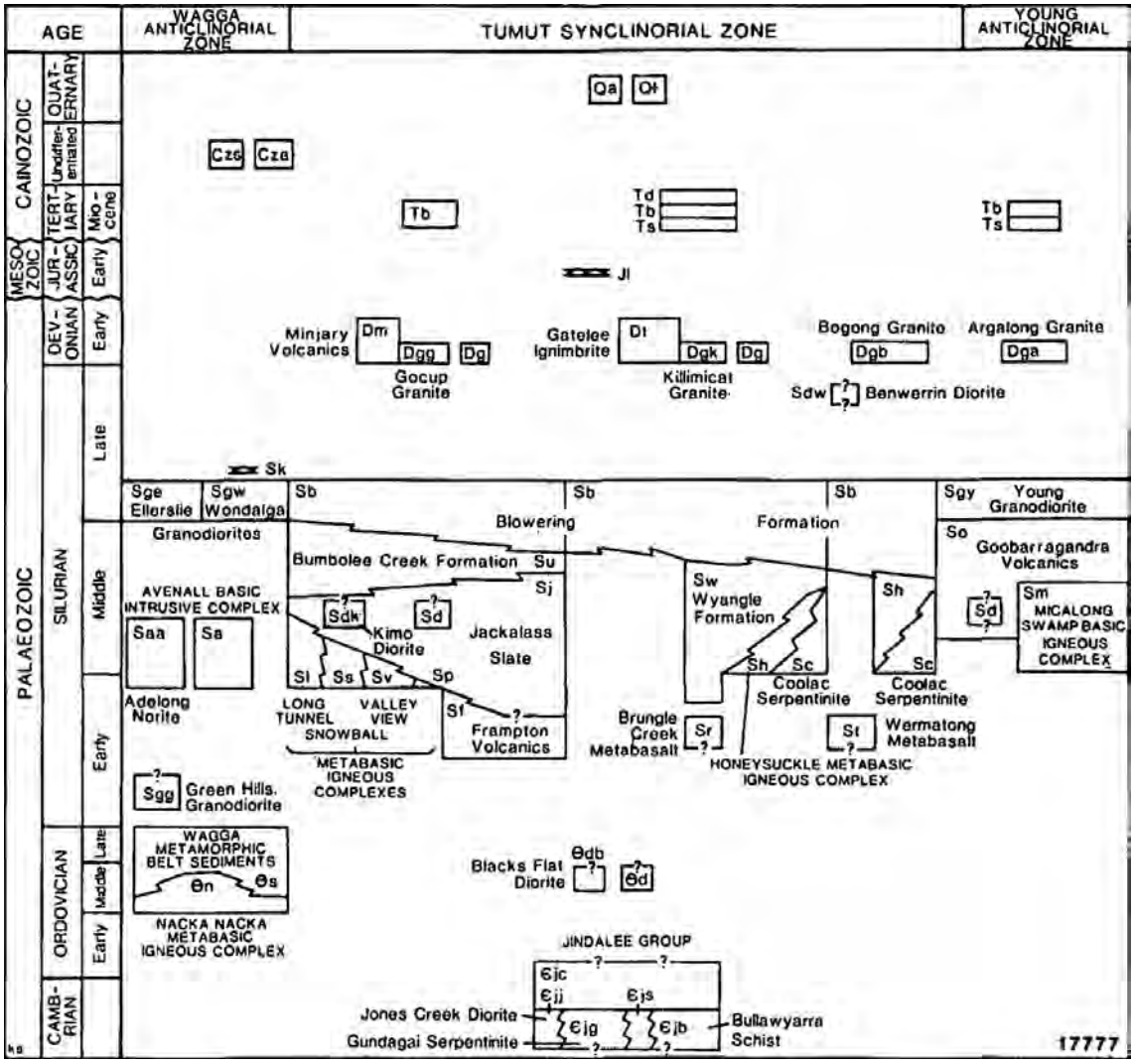

Figure 1.4: Time-Space plot of the Tumut Trough and surrounding zones. From Basden (1990). Synclinorial and anticlinorial zones are old terminology for large scale geological regions.

The oldest rocks in the Tumut Trough are considered to be the Jindalee Group, composed of the Gundagai Serpentinite, Bullawyarra Schist, Jones Creek Diorite and Wambidgee Serpentinite (Basden, 1990; Stuart-Smith et al., 1992). These rocks are of Cambrian and Early Ordovician in age. The Coolac Serpentinite is most likely Ordovician in age (potentially Cambrian) according to Belousova et al. (2015) and

Bruce (2018). Intruding the Jindalee group is the Blacks Flat Diorite. The Snowball Metabasic Igneous Complex, Long Tunnel Metabasic Igneous Complex (intruded by the Kimo Diorite), Brungle Creek Metabasalt and Wermatong Metabasalt are all mafic igneous units ranging in age from Middle Ordovician (Stuart-Smith et al., 1992) to Middle Silurian (Basden, 1990). The Frampton Volcanics of rocks of rhyolitic to dacitic composition are Early Silurian. The Jackalass Slate (Early to Middle Silurian) is the oldest unit of sedimentary origin in the Tumut Trough, which intertongues and underlies the Bumbolee Creek Formation. The Blowering Formation unconformably overlies the Bumbolee Creek Formation and the Wyangle Formation. The volcanic Honeysuckle Beds intertongue with (Basden, 1990) and overlies (Stuart-Smith et al., 1992) the Wyangle Formation and Blowering Formation (Dadd, 1998). Granites intruded during the Early Devonian, namely the Gocup Granite (intruding the Jackalass Slate), Killimicat Granite (intruding the Blowering Formation), Bogong Granite and some unnamed granites (intruding the Snowball Metabasic Igneous Complex and Jackalass Slate). Sometime prior to the emplacement of granites, the Benwerrin Diorite formed. During the Early Devonian, the Gatelee Ignimbrite was also deposited. Tertiary and Quaternary sediments were most recently deposited.

The first indication of the granite bodies near the Snowball Metabasic Igneous Complex (Fig. 1.5) is on a map in Nethery (1975) and was subsequently mentioned by Basden (1990). In this study, it has been informally referred to as the Warrienbah granite, after the name of the property on which it occurs. It has a NW trend, forming elongate bodies that intrude the Snowball Metabasic Igneous Complex and Bumbolee Creek Formation.

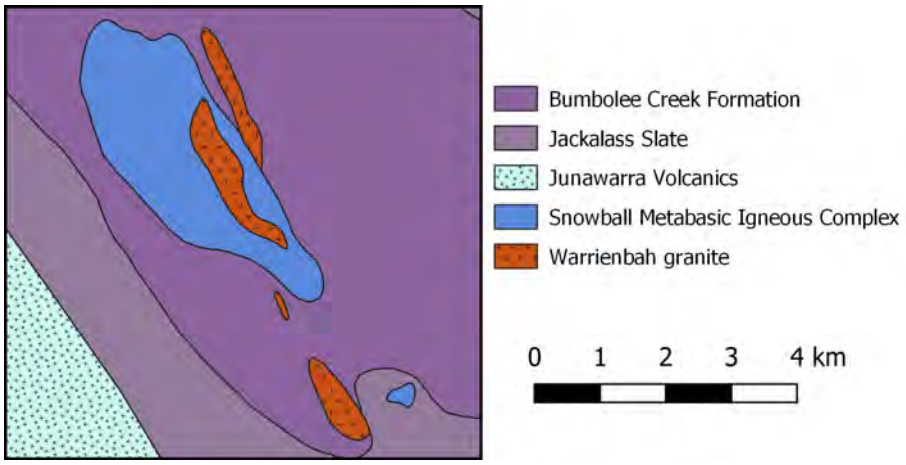

Figure 1.5: A map of the Warrienbah granite in relation to the Snowball Metabasic Igneous Complex and Bumbolee Creek Formation. Modified from Colquhoun et al. (2019).

1.1.3 Age Constraints and Knowledge Gaps

Age constraints of units in the Tumut Trough are mostly based on field relationships, with limited modern radiogenic isotope ages (Table 1.1). Some units were dated using methods prone to resetting like the K-Ar system (Akker et al., 2021) and Rb-Sr whole-rock geochronology (Glodny et al., 2008; Walker et al., 2016) that are not necessarily indicative of the age of the whole rock and may be recording a metamorphic event. While field relationships can be useful, they do not necessarily appear across major structural elements (e.g. the Gilmore Fault Zone), which makes it difficult to establish links to other regions and tectonic events. When used in a wider tectonic model, like Ford et al. (2019a), these relationships may cause issues.

Some interpretations conflict with Basden (1990), Stuart-Smith (1990b) and Stuart-Smith et al. (1992). For example, Graham et al. (1996) dated plagiogranites within the Coolac Serpentinite and returned ages ca. 400 Ma. This is much younger than the 426 ± 6 Ma crystallization age and ca. 417 Ma emplacement age (both

Table 1.1: Absolute and interpreted ages for key rock units in the Tumut Trough from the literature. Overall order is based on the stratigraphy given in Basden (1990) (except for the North Mooney Complex which is not mentioned), and the order of ages for each rock unit is based on the order of appearance in the literature.

Rock Unit	Age	Reference
Gatelee Ignimbrite	Early Devonian 409 ± 7.3 Ma (U-Pb)	Stuart-Smith et al. (1992) Bell (2019)
Unnamed Granites	Early Devonian	Basden (1990)
Killimicat Granite	Early Devonian	Basden (1990) Stuart-Smith et al. (1992)
Minjary Volcanics	Early Devonian	Basden (1990) Stuart-Smith et al. (1992)
Bogong Granite	410 ± 16 Ma (K-Ar)	Basden (1990) Stuart-Smith et al. (1992)
Gocup Granite	402 ± 3 Ma (Rb-Sr) 409 ± 2 Ma (K-Ar) 411 ± 5 Ma (U-Pb)	Richards et al. (1977) Stuart-Smith et al. (1992)
Benwerrin Diorite	Late Silurian Early Devonian	Basden (1990) Stuart-Smith et al. (1992)
Kimo Diorite	Middle Silurian 419.1 ± 2.7 Ma (U-Pb)	Basden (1990) Fraser et al. (2014)
Honeysuckle Beds	425 ± 6 Ma (K-Ar) 426 ± 6 Ma (K-Ar) Early - Late Silurian	Basden (1990) Stuart-Smith et al. (1992)
Goobarragandra Volcanics	429 ± 16 Ma (Rb-Sr)	Owen and Wyborn (1979)

Rock Unit	Age	Reference
North Mooney Complex	425 ± 6 Ma (K-Ar) 426 ± 6 Ma (K-Ar) Late Silurian 426.8 ± 2.2 Ma (U-Pb)	Webb (1980) Stuart-Smith et al. (1992) Bodorkos et al. (2013)
Wyangle Formation	Silurian	Basden (1990) Stuart-Smith et al. (1992)
Blowering Formation	Late Silurian Early - Late Silurian 432.1 ± 1.6 Ma (U-Pb) 432.4 ± 4.3 Ma (U-Pb)	Basden (1990) Stuart-Smith et al. (1992) Geoscience Australia (2007) Ickert and Williams (2011)
Bumbolee Creek Formation	Middle Silurian Ordovician - Early Silurian 417 ± 2.3 Ma (U-Pb)	Basden (1990) Stuart-Smith et al. (1992) Bell (2019)
Jackalass Slate	Silurian Ordovician - Early Silurian 430 ± 8 Ma (U-Pb)	Basden (1990) Stuart-Smith et al. (1992) Bell (2019)
Frampton Volcanics	Silurian 428 ± 6 Ma (U-Pb) 420.1 ± 1.7 Ma (U-Pb)	Basden (1990) Stuart-Smith et al. (1992) Geoscience Australia (2007)
Wermatong Metabasalt	Early Silurian Ordovician - Early Silurian	Basden (1990) Stuart-Smith et al. (1992)

Rock Unit	Age	Reference
Brungle Creek Metabasalt	Early Silurian Ordovician - Early Silurian Middle Ordovician (465-468 Ma, Conodont)	Basden (1990) Stuart-Smith et al. (1992) Bruce et al. (2021)
Snowball Metabasic Igneous Complex	Middle Silurian Ordovician - Early Silurian	Basden (1990) Stuart-Smith et al. (1992)
Long Tunnel Metabasic Igneous Complex	Middle Silurian $>$ 419.1 $\pm$ 2.7 Ma (U-Pb)	Basden (1990) Fraser et al. (2014)
Blacks Flat Diorite	417 $\pm$ 6 Ma (K-Ar) Ordovician - Early Silurian 435.8 $\pm$ 2.1 Ma (U-Pb) 435 $\pm$ 6.4 Ma (U-Pb)	Webb (1980) Stuart-Smith et al. (1992) Bodorkos et al. (2013) Bell (2019)
Coolac Serpentinite	426 Ma (inferred) Cambrian - Ordovician ca. 400 Ma (U-Pb) $\geq$ 439 Ma (U-Pb) $>$ 483.5 $\pm$ 2.3 Ma (U-Pb)	Basden (1990) Stuart-Smith et al. (1992) Graham et al. (1996) Belousova et al. (2015) Bruce (2018)
Jindalee Group	Cambrian - Early Ordovician	Basden (1990)

inferred) reported by Basden (1990) and much younger than the Cambrian-Ordovician suggested by Stuart-Smith et al. (1992). The ca. 400 Ma age is disputed by Belousova et al. (2015), finding zircons in plagiogranites that are the same age and older than the Young Granodiorite. They instead suggest the Coolac Serpentinite is $\geq$ 439 Ma. Bruce (2018) later suggested it cannot be younger than 483.5 $\pm$ 2.3 Ma based on a

U-Pb age of an intrusion into the related Wambidgee Serpentinite.

The ages of the Snowball Metabasic Igneous Complex, Brungle Creek Metabasalt and Wermatong Metabasalt are not well constrained, inferred to be between Ordovician and Middle Silurian in age. Further, the Killimicat Granite and Bogong Granite are thought to be related geochemically and petrologically (Basden, 1990), but the Killimicat Granite has never been dated.

1.1.4 Previous Tectonic Models

The following is the model proposed by Basden (1990). According to Basden (Fig. 1.4), the Jindalee Group is the oceanic basement material to the trough. During the Silurian, the Tumut area was in a period of rifting. Mafic igneous activity was manifest resulting in the Snowball and Long Tunnel Igneous Complexes and metabasaltic units (Brungle Creek and Wermatong Metabasalts). At this time sediments and felsic volcanics belonging to the Jackalass Slate, Bumbolee Creek Formation and Blowering Formation were deposited. Volcanic activity responsible for the Goobarragandra and Frampton volcanics also occurred around this time. Deformation occurred during the Bowning Orogeny (417 Ma). The Bogong, Gocup and Killimicat Granites were then emplaced in the Early Devonian.

Dadd (1998) indicated the timing of the Honeysuckle Beds coincided with the start of backarc formation, based on the geochemical signature of the Honeysuckle Beds.

Recently, Bell (2019) presented a model for the formation of the Tumut Trough. He concluded that it formed after the subduction zone that was responsible for the accretion of the Lachlan Orogen moved eastwards. As a result, the crust thinned

resulting in intrusive units like the Blacks Flat Diorite to be emplaced. The subsequent melting of the crust induced S-type granite magmatism at the time the precursor of the Jackalass Slate was being deposited. The basin then began to briefly contract, during which the E-W compression developed folds throughout the region, with the metabasic complexes and Honeysuckle Beds forming during this event, before the renewed extension allowed the Bumbolee Creek Formation and Blowering Formation to be deposited. Late magmatism occurred with the emplacement of the Bogong and Gocup Granites, with the emplacement of the Gatelee Ignimbrite effectively signalling the end of the geological evolution of the Tumut Trough.

From these accounts, the Tumut Trough is considered to be an extensional basin (in a backarc setting), with cycles of extension and contraction. Sedimentation and igneous activity occurs mostly during extension, while deformation occurs during contraction.

1.1.5 Historical Mineral Exploration

Mineral deposits in the Tumut Trough have historically been worked to produce a variety of commodities, most notably gold and base metals. The last operating mines ceased production in the 1940s (Basden, 1990). Some of the more significant deposits are listed below.

Long Tunnel Mine (and Robinson and Rices Mine)

The Long Tunnel mine was worked between 1898 and 1941, producing 423 kg of gold (Basden, 1990). The Robinson and Rices mine is the northern extension of this mine. Mineralisation was found at the faulted contact between diorite and serpentinite as well as in veins in the mafic rocks.

Snowball Mine

Mineralisation was discovered at the Snowball mine site in 1873 and was worked until 1917. It is a copper deposit in the form of disseminated sulfides along a shear zone in the metabasalt (Basden, 1986), which contains up to 16.82% Cu (Carne, 1908).

Tumut Gold Mine

The Tumut gold mine contained both gold and copper, with minor silver and zinc (Basden, 1986). The ore body occurs in a massive to schistose altered metabasalt within the Honeysuckle Beds.

McAlpine and Bogong Mines

The McAlpine and Bogong mines contain the largest metalliferous deposits associated with the Coolac Serpentinite (Basden, 1990). After being reopened in 1898, by 1908 the McAlpine mine had produced 38 tons of ore at 10% Cu and the Bogong mine produced 30 tons of ore at 25% Cu (Carne, 1908). The ore was hosted at contacts between serpentinite and other rock types.

Goobarragandra Mine

The Goobarragandra mine opened in 1915 and was worked until 1919. It was briefly reopened in 1941, but closed again the next year. In 1917 and 1918, the mine produced 354.6 tons of ore at 10% Cu (Basden, 1986). The orebody occurs in amphibolites close to the faulted boundary between the Honeysuckle Beds and Coolac Serpentinite (Basden, 1990).

Callifat Mines

The Callifat Mines were operating between 1899 and 1932, mainly producing copper, and minor gold, silver and zinc. The mineral deposit occurred in quartz stringers and talcose zones within sheared volcanics (Basden, 1986).

Resurgence of Exploration

Interest in mineral exploration in the area recommenced in the mid 1960s, and peaked in the 1980s (Basden, 1990). Since then, exploration has been sporadic, with companies drilling holes and assaying samples in the search for mineralisation.

1.1.6 Current Mineral Exploration

Exploration for mineralisation is currently limited in the area. However, DevEx Resources commenced with rock chip sampling and drilling in the Basin Creek No.1 prospect (DevEx Resources, 2021a) looking for gold mineralisation and on the eastern margin of the Bogong Granite (DevEx Resources, 2021b) drilling for porphyry copper-gold mineralisation respectively. The Basin Creek No.1 prospect has been described as a Volcanic-Associated Massive Sulfide (VAMS) deposit (Downes, 2019), with lenses of disseminated sulfides derived from a volcanic source (Nethery and Ramsden, 1976).

Recently, Ford et al. (2019a) undertook mineral prospectivity mapping throughout the Lachlan. One of the major outcomes of this study was the Tumut Trough was found to be moderately to highly prospective for VAMS deposits, especially along the western edge of the trough (Fig. 1.6). VAMS deposits form in extensional settings, like mid-ocean ridge and spreading arc environments. They form near the seafloor,

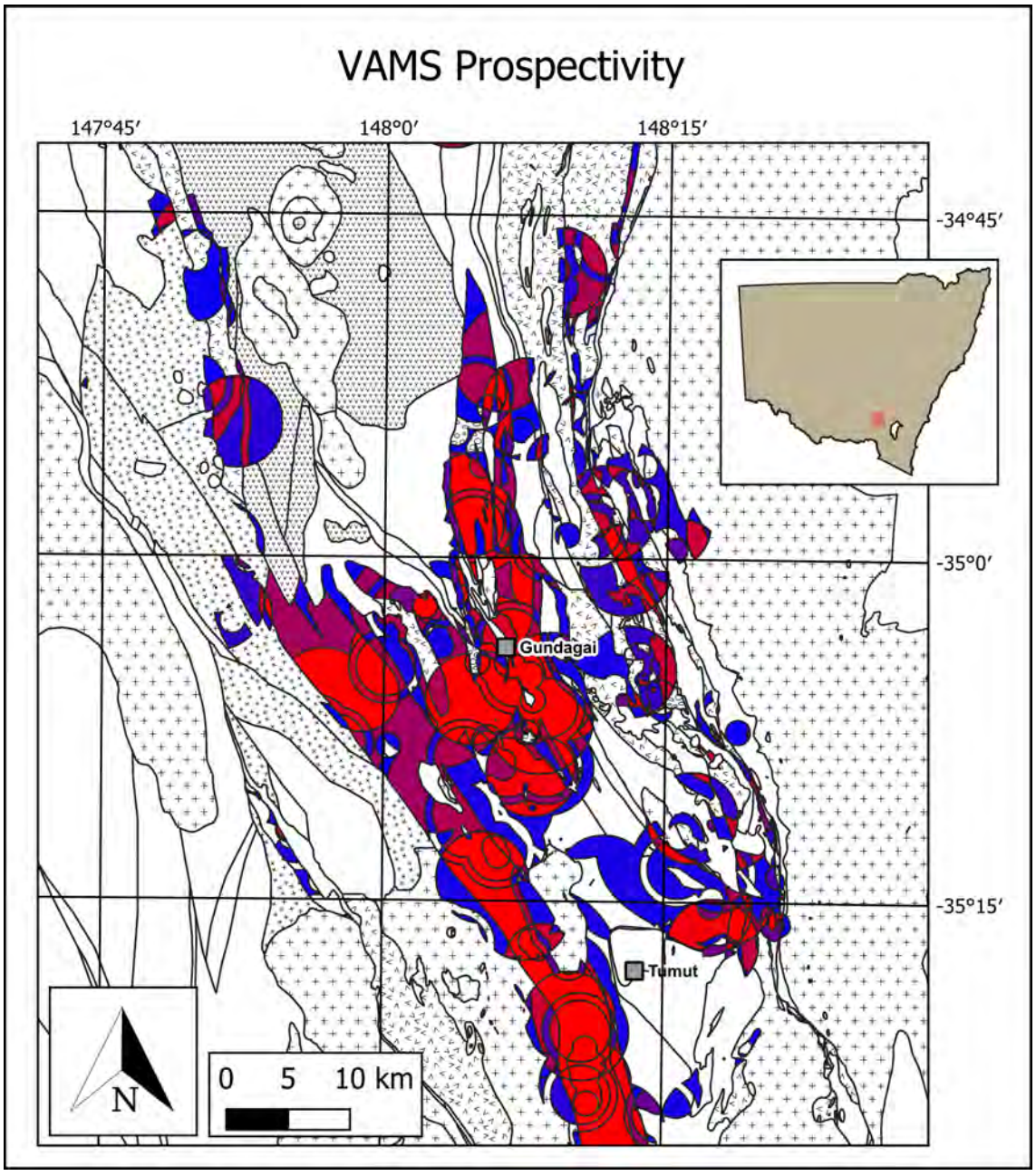

Figure 1.6: Volcanic-Associated Massive Sulfide (VAMS) mineral prospectivity map overlying a map of the Tumut Trough. Areas coloured red are highly prospective. Modified from Colquhoun et al. (2019) and Ford et al. (2019b)

with the discharge of high-temperature, metalliferous fluids that interact with cold seawater, precipitating massive sulfides (Galley et al., 2007; Downes, 2019).

Ford et al. (2019a) used large geoscientific datasets to produce geological models. Pre-existing mines were used as training sites to develop criteria on the mineralisation types of interest. By feeding the criteria back into the geological model, the mineral prospectivity map was produced. Therefore, it is critical that the information that is used to produce the initial geological model is correct, and thus poorly understood areas like the Tumut Trough need to be investigated.

1.2 Aims

The primary objectives of this project were to:

1. Date rock units isotopically (U-Pb) using zircon or titanite to add or confirm the ages provided in the previous literature.

2. Explore the geochemistry of key rock units to determine their tectonic setting and, where appropriate, commenting on units that may host mineralisation (e.g. VAMS) where appropriate. This included the analysis of whole-rock geochemistry (major, trace and rare earth elements) and isotopes (Lu-Hf and Sm-Nd).

3. Sample, date, and geochemically and isotopically define the plutons in the Tumut Trough to determine relationships (if any) between them, along with any mineralisation potential. The ages will also provide minimum constraints for mafic units they intrude.

4. Refine the stratigraphy proposed by Basden (1990) and Bell (2019).

By achieving these aims, modelling, prospectivity mapping and the knowledge of the geology of the Tumut Trough will improve. As a result, undercover resource deposits are more likely to be discovered.

It is expected that at the conclusion of this study detailed geochemistry of key rock units will be available, the timing of key rock units will be constrained, the evolution and stratigraphy of the Tumut Tough will be refined and units that formed in settings that could potentially host mineralisation identified.

Chapter 2

Methods

2.1 Sampling

2.1.1 Drillcore

Select drillcore at the Londonderry Core Library were sampled. The holes were selected as they intersect key mafic rock units held at the core library. Mafic units were initially targeted for geochemical analysis, but were later only used for petrography as field samples became available, while felsic units were sampled to attempt to extract zircons. Holes DDH4 (Snowball Mine), DD90LT2 (Long Tunnel), IDY8 (Idylway) and R1 (Rosehill) (from technical reports Berkman and Nethery (1974), Funnell (1990), Robinson (1995) and Schmidt et al. (1975) respectively). Due to the public health restrictions in the first half of 2020, sampling had to be performed remotely during this time. Sampling was performed by Jake Moltzen from the Londonderry Core Library. Core was selected based on the information from these technical reports, with HyLogger data that was available for IDY8 and R1. HyLogger data from hole DD90LT4 aided core selection from DD90LT2 due to being drilled approximately 80 m apart, with some units being laterally equivalent. The HyLogger data was also used in the identification of stratigraphy and alteration zones/minerals when sampling and doing petrography. The coordinates and intervals of these samples can be found in Appendix A.

2.1.2 Field Sampling

Fieldwork was undertaken in the second half of 2020 when the public health restrictions were relaxed. The aim was to gather surface samples of key mafic rock units with reference to the sampled drillcore, poorly investigated units and granites. This was done by locating previous sampling sites on MINVIEW (Geological Survey of New South Wales, 2019) to indicate where units outcrop and subsequently visiting these sites to acquire samples.

2.1.3 Thin Section Preparation

Thin sections were made by using standard laboratory procedures at UoN. Thin sections were examined under transmitted light.

2.2 Geochronology and Mineral Chemistry

Zircon ($ZrSiO_4$) and titanite ($CaTiSiO_5$) are common accessory minerals that can host U^{4+} (among other trace elements such as Hf, Th, REEs) substituting for Zr^{4+} and Ti^{4+} respectively. The U-Pb isotopic system (Schoene, 2014) can be used for both minerals to determine an age for the host rock (Schaltegger and Davies, 2017; Kohn, 2017).

Rocks that contained zircons and titanites were cleaned in an ultrasonic bath and scrubbed to remove any residual dirt and lichen. They were split in a hydraulic press, crushed to gravel in a Retsch BB200 jaw crusher and crushed to < 1 mm in a Retsch DM200 Disc Mill and sieved to capture any grains less than 250 μm in size. This population was separated based on density using a Wilfley table, with the more dense

material captured as this contained the minerals of interest. A Frantz magnetic separator was then used to separate the magnetic minerals from the titanite and zircon. LST (lithium heteropolytungstates, density of 2.85 g/mL) was used to further refine the separation, leaving only the densest minerals like zircon and titanite. The zircon and titanite grains were hand-picked under an optical microscope and placed onto an adhesive tape. Resin was poured onto the grains to form a resin mount.

2.2.1 Zircon

The zircon mounts were imaged at UoN using transmitted light (TL) and cathodoluminescence (CL). Spot plans were created on the CL images with spots 30 μm in diameter (Fig. 2.1). Spots were placed on areas with magmatic zoning (Corfu et al., 2003). TL images were used to avoid fractures and inclusions where possible. The zircon analysis was split into two sessions. Session 1 included the analysis of U-Pb and trace elements, then Lu-Hf (both split stream) and was done over 3 days (2 for U-Pb/trace elements and 1 day for Lu-Hf). Session 2 was a follow up session and only U-Pb was analysed and took 1 day. Methods for the first zircon analysis session are outlined below (C Clark 2021, pers. comm. 15 April) with session 2 having slight differences. Methods for the Lu-Hf methods are also outlined below (C Kirkland 2021, pers. comm. 15 April).

Elemental and isotopic composition data were collected using the laser ablation split stream (LASS) inductively coupled plasma mass spectrometer (ICP-MS) housed at the GeoHistory Facility in the John de Laeter Centre at Curtin University. Zircon was ablated using a Resonetics RESOlution M–50A–LR system, incorporating a COMPex 102 193 nm excimer UV laser. Following two cleaning pulses and a 40 s period of background analysis, samples were spot ablated for 35 s (30 s for session 2) at a 10 Hz

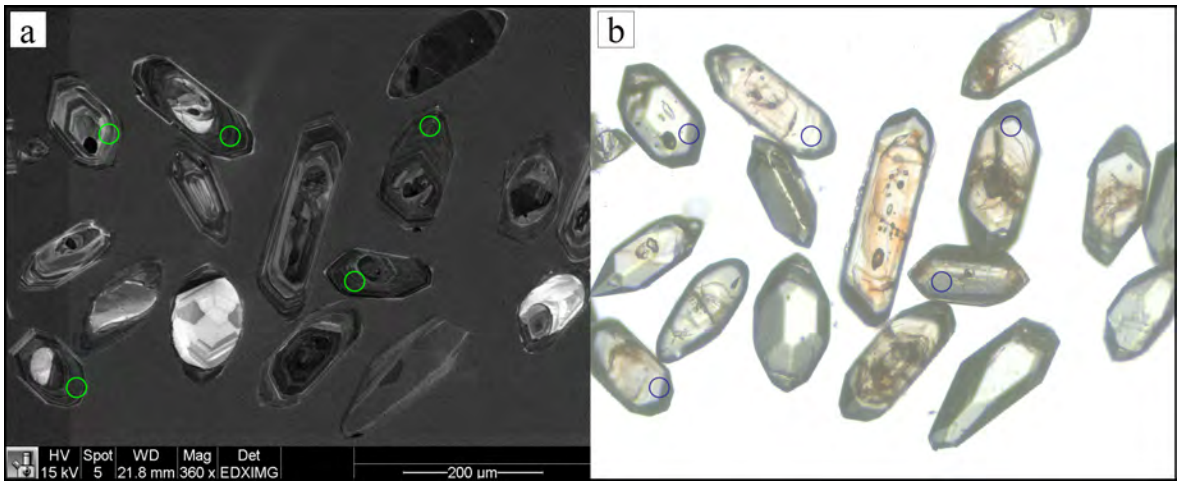

Figure 2.1: Example of a spot plan for a zircon mount using (a) a cathodoluminescence (CL) image and (b) a transmitted light (TL) image. Scale is the same for both images.

repetition rate using a 30 μm beam and laser energy at the sample surface of 2.3 J/cm^2. An additional 40 s of baseline was collected after ablation. The sample cell was flushed with ultrahigh purity He (300 mL/min) and N_2 (1.0 mL/min) and high purity Ar was employed as the plasma carrier gas. U–Pb were measured a Nu-Plasma2 HR multi-collector ICP while trace elements were measured using an Agilent 7700s quadrupole ICPMS, with high-purity Ar as the plasma gas (flow rate 0.98 L/min). Zircon standard 91500 was used as the primary standard to calculate element concentrations (using ^{90}Zr as an internal standard element, assuming a 43.14% Zr content in zircon) and to correct for instrument drift.

Between the sessions, the spot size and ablation time changed. Session 1 used a spot size of 30 μm with an ablation time of 35 s while session 2 used a spot size of 23 μm and an ablation time of 30 s. All other conditions remained the same.

The time-resolved mass spectra were reduced using iolite 4 (Paton et al., 2011) with the Geochronology 3 data reduction scheme, with individual spots inspected with

Table 2.1: Zircon secondary standard ages for each day compared to the reported ages in the literature.

Standard Name	Session/Day #	n	Age (Ma)	Reported Age (Ma)
GJ-1	1-1	18	601.8 ± 0.1	601.7 ± 1.4 (Jackson et al., 2004)
	1-2	20	601.8 ± 0.1	
	2-1	18	601.7 ± 0.6	
Plešovice	1-1	18	340.8 ± 1.6	337.1 ± 0.4 (Sláma et al., 2008)
	1-2	20	340.7 ± 1.6	
	2-1	18	340.0 ± 3.1	

VizualAge (Petrus and Kamber, 2012). The primary reference material used for U–Pb dating in this study was zircon standard 91500 with secondary standards zircon GJ-1 and Plešovice also used. For each secondary standard, the ages for each day and reported ages are in Table 2.1. GJ-1 was consistently indistinguishable with the reported age. Plešovice was consistently older than the reported age, all by approximately 3 million years.

Corrections for common lead (^{204}Pb) and lead loss were performed in iolite 4. All of the data was plotted with IsoplotR (Vermeesch, 2018). Data was filtered to only include concordant data; concordance was defined as between 90 - 110% concordance using the following equation:

$$\text{Concordance} = \frac{^{206}\text{Pb}/^{238}\text{U Age}}{^{207}\text{Pb}/^{206}\text{Pb Age}} \times 100$$

Weighted means were calculated using the ^{206}Pb/^{238}U ages from concordant data.

Lutetium-Hafnium Isotopes (Lu-Hf) in Zircon

The ablated split for Lu–Hf analysis was measured on a Nu Plasma II multi-collector inductively coupled plasma mass spectrometer. All isotopes (^{180}Hf, ^{179}Hf, ^{178}Hf, ^{177}Hf, ^{176}Hf, ^{175}Lu, ^{174}Hf, ^{173}Yb, ^{172}Yb and ^{171}Yb) were counted on the Faraday collector array. Time-resolved data were baseline subtracted and reduced using Iolite (data reduction scheme after Woodhead et al., 2004), where ^{176}Yb and ^{176}Lu were removed from the 176 mass signal using ^{176}Yb/^{173}Yb = 0.7962 and ^{176}Lu/^{175}Lu = 0.02655 with an exponential-law mass bias correction assuming ^{172}Yb/^{173}Yb = 1.35274 (Chu et al., 2002). The interference-corrected ^{176}Hf/^{177}Hf was normalized to ^{179}Hf/^{177}Hf = 0.7325 (Patchett and Tatsumoto, 1981) for mass bias correction. Zircon crystals from the Mud Tank carbonatite locality were analysed together with the samples in each session to monitor the accuracy of the results. 91500, Plešovice and GJ-1 zircons were also run as secondary standards.

The mean ^{176}Hf/^{177}Hf value for the Mud Tank carbonatite zircons was 0.282539 ± 0.000031, which is within the reported value of 0.282522 ± 0.000042 (Griffin et al., 2006). The reported value of 0.282523 ± 0.000010 (Gain et al., 2019) is also within error of the value in found in this session. The 91500 secondary standard returned a ^{176}Hf/^{177}Hf value of 0.282328 ± 0.000040 which is within error of the reported value of 0.282302 ± 0.000042 (Fisher et al., 2014). The Plešovice secondary standard returned a ^{176}Hf/^{177}Hf value of 0.282513 ± 0.000031 which is slightly higher than the reported value of 0.282436 ± 0.000028 (Fisher et al., 2014). The GJ-1 secondary standard returned a ^{176}Hf/^{177}Hf value of 0.282053 ± 0.000037 which is also slightly higher than the reported value of 0.282000 ± 0.000005 (Morel et al., 2008).

Rare Earth Elements in Zircon

The REE in zircon were analysed concurrently with the U-Pb analysis. The standard used was a NIST glass standard reference material 612 (Hollocher and Ruiz, 1995).

2.2.2 Titanite

The titanite mount was imaged at UoN using transmitted light and back scattered electron imaging (BSE). Spot plans were created on the BSE images with spots 50 μm in diameter (Fig. 2.2). Spots were placed on areas that had no variation in the BSE image, avoiding fractures and inclusions with reference to the TL image. The spot size was adjusted at James Cook University before analysis. Methods for the titanite analysis are outlined below (H Huang 2021, pers. comm. 29 January).

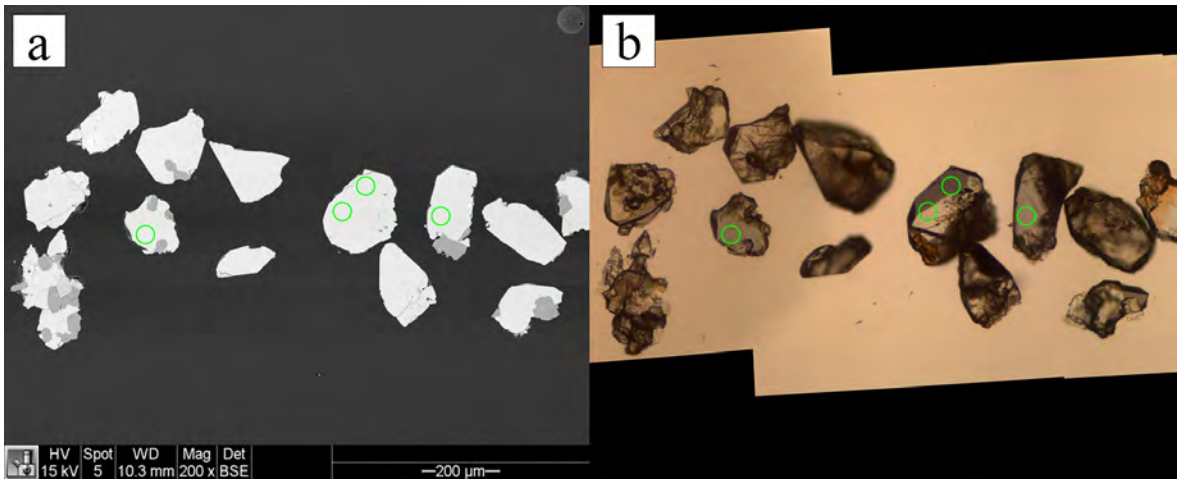

Figure 2.2: Example of a spot plan for a titanite mount using (a) a back-scattered electron (BSE) image and (b) a transmitted light (TL) image. Scale is the same for both images.

Titanite analysis was performed at the Advanced Analytical Centre of James Cook University with a Photon Machines Analyte.G2 193 nm ArF Excimer laser ablation system connected to a Thermo iCAP-RQ ICP-MS. The ablation cell was connected to

the iCAP-RQ via Tygon tubing. Ablation was conducted in a HelEx II Active 2-Volume Cell using high-purity He as the carrier gas, which was subsequently mixed with ~ 0.54 L/min Ar and ~ 5 ml/min N_2 prior to introduction into the ICP-MS. The ICP-MS was optimized using auto tune on a solution basis. It was tuned further for maximum sensitivity in laser ablation mode using standard glass NIST 610 under robust plasma conditions (U/Th = ~ 1) while maintaining oxide production rates (ThO/Th) to $<$ 0.3%. RSD of U and Th signals of NIST 610 are typically better than 3% when laser fluence was set to ~ 3 J/cm^2 at the sample surface with a laser repetition rate and a beam diameter of 5 Hz and 50 μm, respectively. Conventional spot analyses were used for data acquisition using a laser fluence of 2 J/cm^2. 85 μm spots were used for analysis.

2.3 Geochemistry

Preparation of the geochemistry samples was done by using a hydraulic press, crushed to gravel in a Retsch BB200 jaw crusher and made into a powder with a Tungsten Carbide Vibratory Ring Mill. The material was packaged to be sent for whole rock geochemistry (Section 2.3.1), and Sm and Nd isotopic analysis (Section 2.3.2), where required.

2.3.1 Whole Rock

The whole rock analysis of powders was undertaken at Intertek Adelaide, S.A using lithium borate fusion inductively coupled plasma optical emission spectroscopy (ICP-OES), lithium borate fusion inductively coupled plasma mass spectrometry (ICP-MS) and 4 acid digest ICP-OES, each following their standard procedures. Elements analysed and respective detection limits can be found in Appendix C.

2.3.2 Samarium-Neodymium Isotopes (Sm-Nd)

Samarium and neodymium isotopic analyses were carried out at the University of Melbourne, methods for which are outlined below (R Maas 2021, pers. comm. 10 February).

Radiogenic isotope compositions (Sm-Nd) were measured by isotope dilution MC-ICP-MS, using procedures adapted from Donnellan et al. (2018) and Maas et al. (2020). Sample powder (60-70 mg) was weighed into Krogh-type PTFE teflon vessels, spiked with ^{149}Sm-^{150}Nd spike and dissolved in an oven (160^{o}C) using 3:1 HF-HNO_3, conc. HNO_3 and 6M HCl over 4 days. This resulted in clear solutions in all cases. Nd and Sm were extracted and purified using a combination of EICHROM TRU- and LN-resin (Pin et al., 2014). Procedural blanks (< 0.1 ng Nd) produced blank corrections that were negligible in all cases.

Sm-Nd isotopic analyses were carried out on a NU Plasma multi-collector inductively coupled plasma mass spectrometer (MC-ICP-MS), with sample uptake via a CETAC Aridus desolvating system and slow-uptake (0.07 ml) PFA nebulizer. Neodymium fractions were re-dissolved in 2% nitric acid running solution and adjusted (60-80 ppb) to yield total Nd signals in the range 15-25V. Data were collected for 30 cycles (30 $\times$ 10 sec) and corrected for instrumental mass bias by internal normalization to ^{146}Nd/^{145}Nd = 2.0719425 (equivalent to the more familiar ^{146}Nd/^{144}Nd = 0.7219, Vance and Thirlwall, 2002), using the exponential law as part of an on-line iterative spike-stripping/internal normalisation procedure. Final ^{143}Nd/^{144}Nd is reported relative to a value of 0.511860 for the La Jolla Nd isotope standard. Instrumental mass bias in Sm isotope dilution analyses was corrected by internal normalisation to

$^{152}Sm/^{147}Sm$ = 1.78307. Typical in-run precision (2se) for $^{143}Nd/^{144}Nd$ is $\sim \pm$ 0.000012, while the reproducibility of rock and solution standards indicates an external precision of ± 0.000030 (2sd). External precision for $^{147}Sm/^{144}Nd$ is ± 0.2% (2sd).

Nd isotope result for three USGS rock standards (basalt BCR-2, basalt BHVO-2, andesite AGV-2) analysed over several months in 2020, including the present campaign, yield average $^{143}Nd/^{144}Nd$ of 0.512640 ± 0.000031, 0.512998 ± 0.000030 and 0.512795 ± 0.000036 (2sd, n = 30, 23 and 29), respectively, consistent with TIMS and MC-ICP-MS reference numbers (e.g. http://georem.mpch-mainz.gwdg.de/ Jochum et al., 2005). A single isotope dilution analysis of the USGS GSP2 granite standard (a Proterozoic LREE-rich A-type granite) yielded 26.05 ppm Sm, 206.2 ppm Nd, $^{147}Sm/^{144}Nd$ = 0.0764 and $^{143}Nd/^{144}Nd$ = 0.511381 ± 0.000010 (2se), consistent with the TIMS results of Raczek et al. (2001, 2003).

ϵ_{Nd} values, $\epsilon_{Nd}(t)$ and T_{DM} model ages (where applicable) are calculated using $^{147}Sm/^{144}Nd$ = 0.1960 and $^{143}Nd/^{144}Nd$ = 0.512630 for the modern chondritic mantle (CHUR, Bouvier et al., 2008); a composition of $^{147}Sm/^{144}Nd$ = 0.2129 and $^{143}Nd/^{144}Nd$ = 0.513145 for the model depleted mantle (DM) is used in the calculation of T_{DM}. The Sm decay constant is 6.54×10^{-12}/yr.

Chapter 3

Results

A list of samples collected for analysis can be found in Appendix A. Sample descriptions (hand specimen and thin section descriptions) can be found in Appendix B.

3.1 Mafic and Intermediate Rock Geochemistry

Rocks of mafic and intermediate composition are abundant in the Tumut Trough. For the purposes of discriminating between mafic and intermediate rocks and any further diagrams, trace elements (Fig. 3.1) were used as some rocks are mineralogically altered (chlorite bearing) and/or chemically altered (high loss on ignition, up to 4.45%). By plotting the immobile elements (like Nb and Y), the rocks can be compared geochemically without bias from alteration. Since immobile elements were used due to alteration, all of the samples that plotted in the sub-alkaline basalt and andesite/basalt fields were considered mafic, and those in the andesite and rhyodacite/dacite fields were considered intermediate (Fig. 3.1).

Most samples in Figure 3.1 plot as andesites/basalts. The Wermatong Metabasalt (TDBHons008.01), Benwerrin Diorite (TDBHons009.01) and Wyangle Formation (TDBHons014.01) all plot as sub-alkaline basalts. Rocks classified as andesites are the Wyangle Formation (020.01) and Frampton Volcanics (TDBHons023.01) while the volcanics from the Blowering Formation (TDBHons015.01) and Honeysuckle Beds

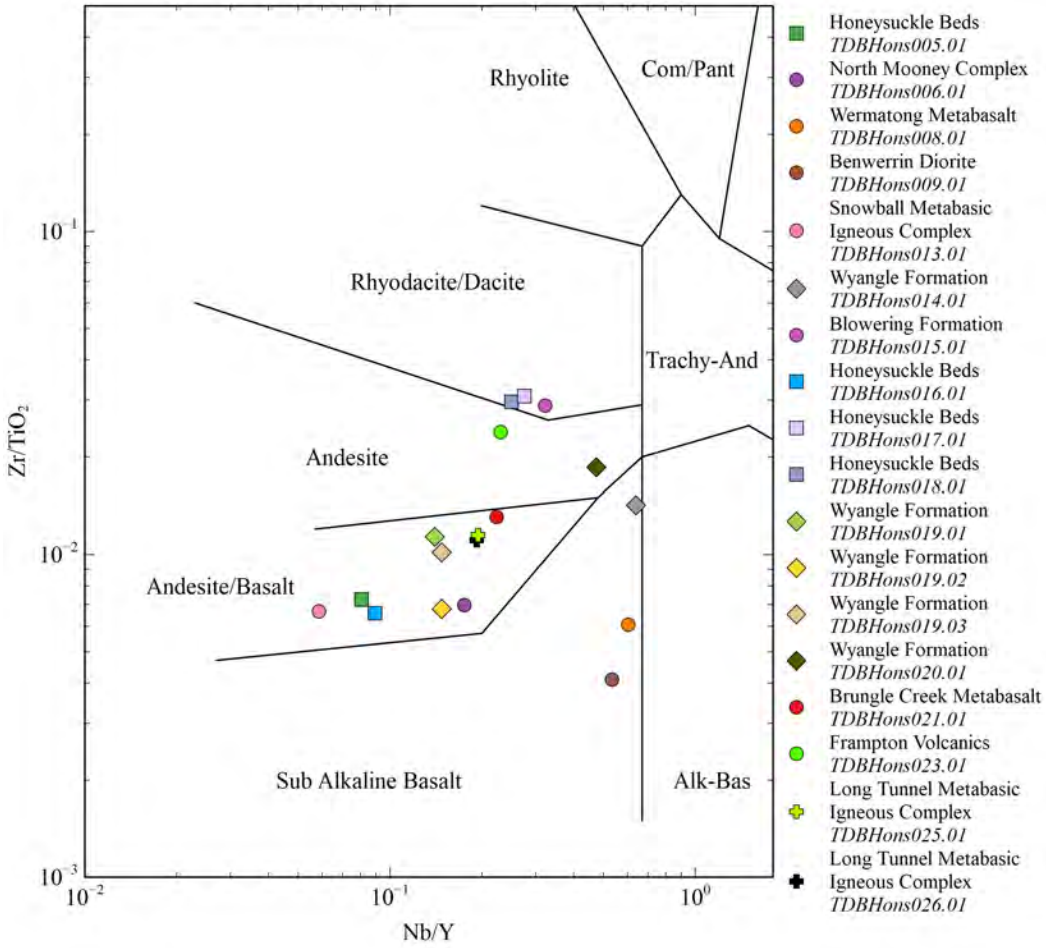

Figure 3.1: Rock type classification of collected mafic and intermediate samples based on immobile elements (after Winchester and Floyd, 1977).

(TDBHons017.01 and TDBHons018.01) are classified as rhyolites/dacites.

3.1.1 Mafic Rock Geochemistry

The chondrite normalized REE patterns (Fig. 3.2) show light REE enrichment in most samples, with variable slope. The Snowball Metabasic Igneous complex (TDBHons013.01) is the only sample with an almost flat spider diagram (La/Yb = 1.08). Also worthy of note is the Brungle Creek Metabasalt (TDBHons021.01), with erratic heavy REE concentrations compared to the other samples. The Brungle Creek

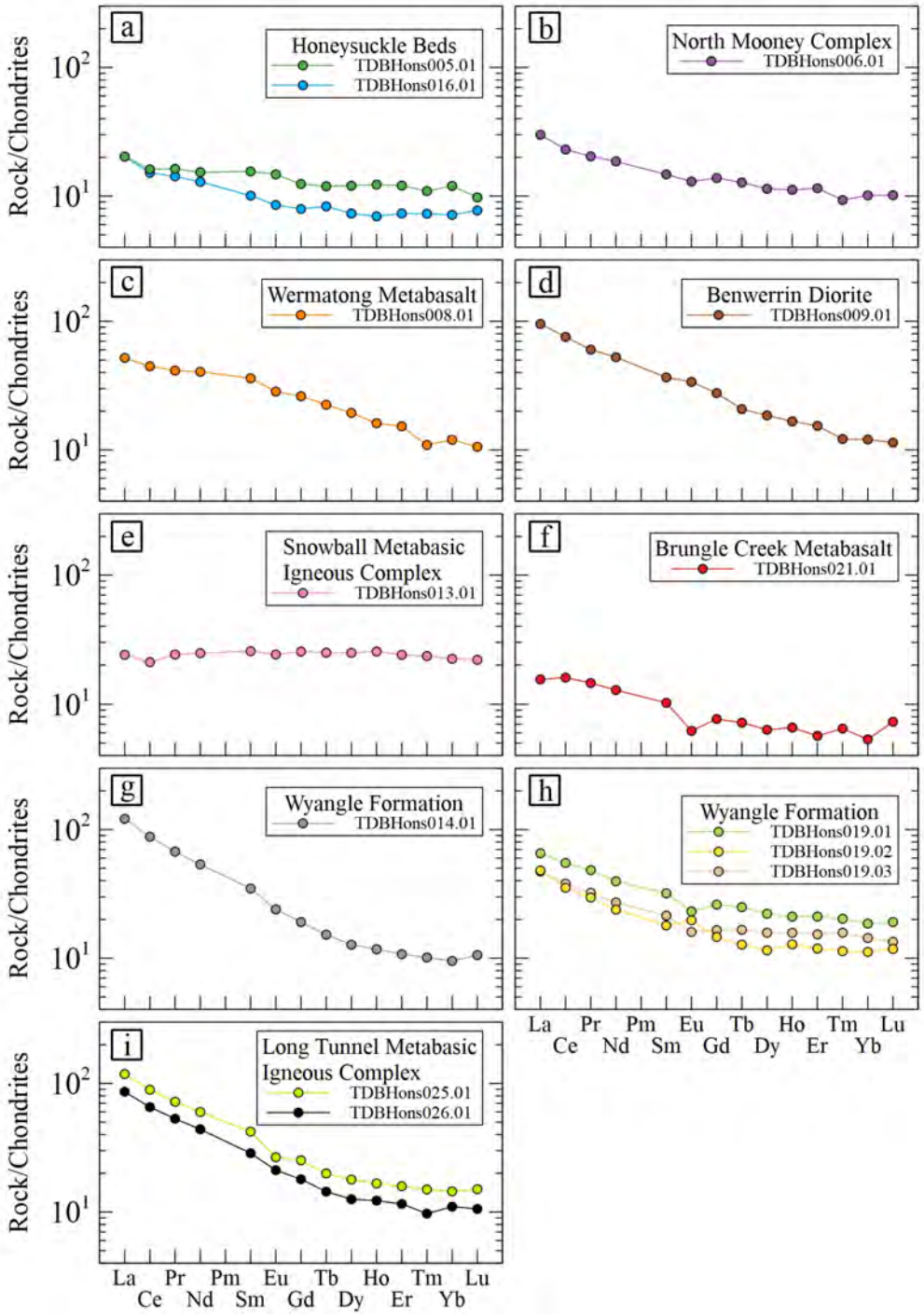

Figure 3.2: Chondrite normalized REE patterns of the mafic rocks (after McDonough and Sun, 1995).

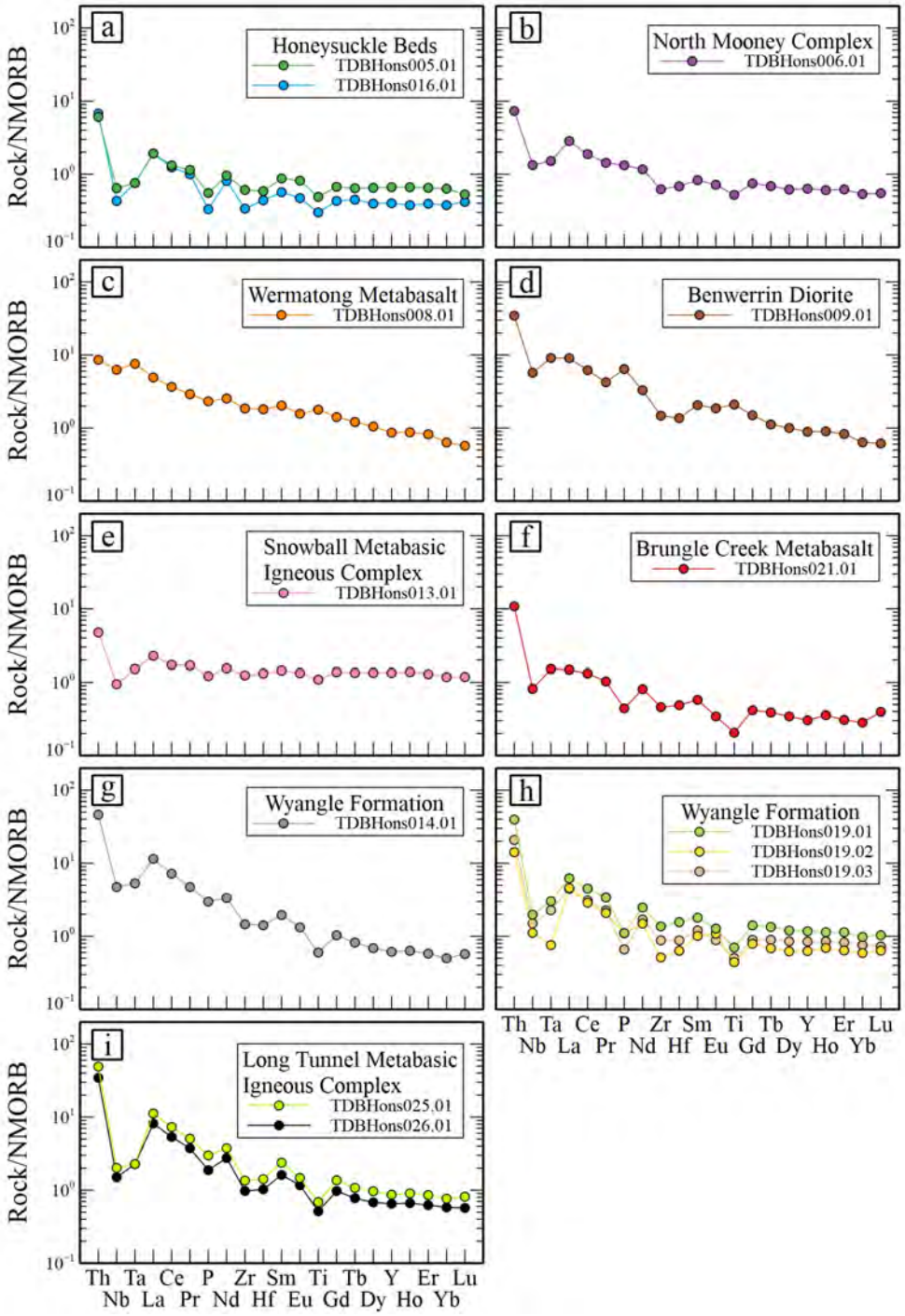

Figure 3.3: Trace element patterns of the mafic rocks normalized to N-MORB (after Sun and McDonough, 1989).

Metabasalt sample and one Wyangle Formation sample (TDBHons019.01) have a negative Eu anomaly.

The trace element patterns of the mafic rocks (Fig. 3.3) indicate most have features of continental rift basalts, with smaller Nb depletion than would be expected in an arc basalt and lower Nb/Yb ratios than continental arc basalts (compared to the continental arc basalts in Xia and Li (2019)). The exceptions to this are the Wermatong Metabasalt (TDBHons008.01, Fig 3.3 c) and Snowball Metabasic Igneous Complex (TDBHons013.01, Fig 3.3 e). The Wermatong Metabasalt has E-MORB like chemistry, as it is enriched in incompatible elements (Th, Nb, etc.). By comparison, the sample from the Snowball Metabasic Igneous Complex shows smaller Nb depletion and has no light REE enrichment. The continental influence as indicated by the Nb/Yb ratio is greatest in the Benwerrin Diorite (TDBHons009.01, Fig 3.3 d) and Wyangle Formation (TDBHons014.01, Fig 3.3 g).

The Wermatong Metabasalt sample plots in the mantle array on Figure 3.4. All of the other samples have a subduction signature, plotting off the mantle array. Most of these samples with a subduction signature plot within the overlap between oceanic and continental arcs, indicating they have compositions transitional between the two. The Snowball Metabasic Igneous Complex sample by contrast plots in the oceanic arc field. The samples that plot in the continental arc region with no overlap are samples from the Wyangle Formation (TDBHons014.01), Benwerrin Diorite (TDBHons009.01) and the Long Tunnel Metabasic Igneous Complex (TDBHons025.01, TDBHons026.01). The Wyangle Formation and Benwerrin Diorite samples both have large Nb/Yb ratios on the N-MORB normalized plot (Fig. 3.3 d,g), indicating they have compositions typical of continental arcs. The Long Tunnel Metabasic Igneous

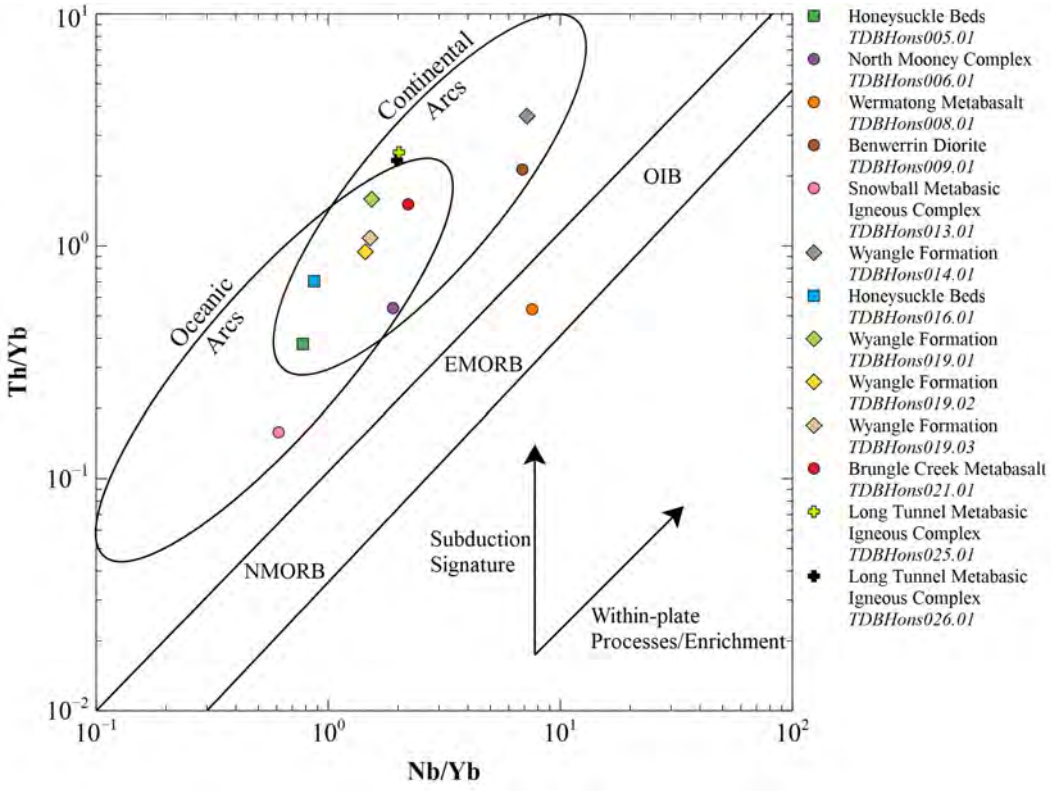

Figure 3.4: Th/Yb versus Nb/Yb (after Pearce, 2008, 2014) for the mafic samples with the mantle array, oceanic arc and continental arc fields shown.

Complex samples do not show the same influence on the N-MORB plot, but do plot close to the overlap.

3.1.2 Intermediate Rock Geochemistry

All of the intermediate rocks plot in the active continental margin field in Figure 3.5 with Th/Ta values between 13 - 15.

3.2 Pluton Geochemistry

Existing geochemistry on the plutonic units in the region are limited, with most of the existing data coming from the 1970s and 1980s (Basden, 1990) and Bruce Chappell's

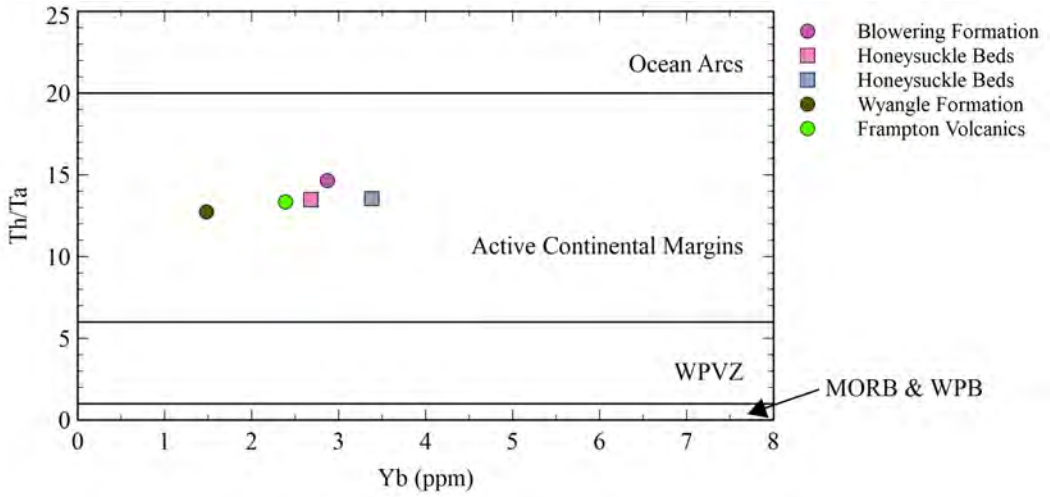

Figure 3.5: Tectonic settings of the intermediate rocks (Th/Ta versus Yb plot after Gorton and Schandl, 2000). WPVZ = Within Plate Volcanic Zone, MORB = Mid-ocean Ridge Basalt, WPB = Within-plate Basalt.

analyses which can be found on MINVIEW (Geological Survey of New South Wales, 2019). These datasets have major element analyses and limited trace elements, with no complete sets of rare earth elements.

The plutons are all either metaluminous or peraluminous (Fig. 3.6). The Kimo Diorite (TDBHons003.01, TDBHons024.01) is the most metaluminous of the plutonic units, with the Bogong, Killimicat and Warrienbah granites on the border between metaluminous and peraluminous. The Gocup Granite (TDBHons010.01, TDBHons011.01) is highly peraluminous.

The Killimicat (TDBHons022.01) and Bogong (TDBHons007.01) Granites discriminate from the others, plotting as A-type granites (Fig. 3.7). The Gocup Granite is an S-type granite as it is depleted in Zr and light rare earth elements (Villaros et al., 2009), has a normative corundum of 2.58 and 2.81 in samples TDBHons010.01 and TDBHons011.01 respectively, and both samples are highly

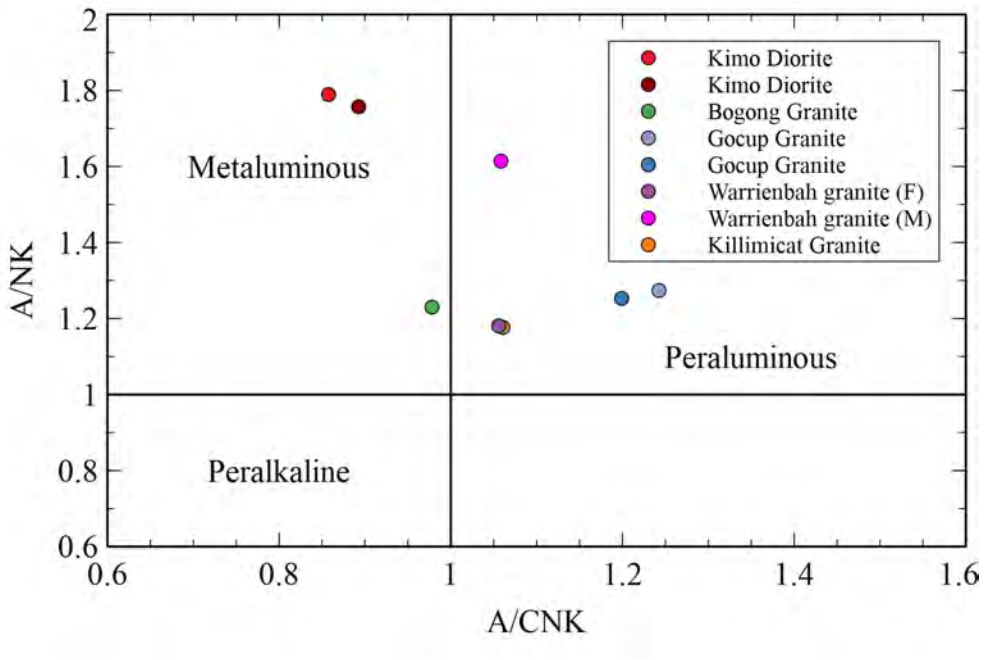

Figure 3.6: A/NK v A/CNK plot after Shand (1943) discriminating between metaluminous, peraluminous and peralkaline units. A/NK = Al/Na+K, A/CNK = Al/Ca+Na+K

peraluminous (A/CNK of 1.242 and 1.199 respectively). The Kimo Diorite plots in the I and S-type field. It is metaluminous which makes it an I-type, which is consistent with Fraser et al. (2014), having previously identified it as an I-type. The Warrienbah granite (TDBHons012.01, TDBHons012.02) plots on the boundary of the discrimination fields, but it contains interstitial biotite which makes it an A-type as mafic minerals crystallise late and thus appear interstitial (Whalen et al., 1987).

Harker diagrams (Fig. 3.8) demonstrate some clear trends among the plutons. With increasing silica (SiO_2), Al_2O_3 and Fe_2O_3 concentrations systematically decrease (Fig. 3.8 a,b), while MgO, CaO, Na_2O, P_2O_5, TiO_2 also decrease with increasing silica content, but do so less systematically (Fig. 3.8 c,d,e,h,i). K_2O and Na_2O + K_2O increase systematically with increasing silica (Fig. 3.8 f,g). Rb also increases with increasing silica (Fig. 3.8 j) while Sr concentrations decrease (Fig. 3.8 l). Ba does not

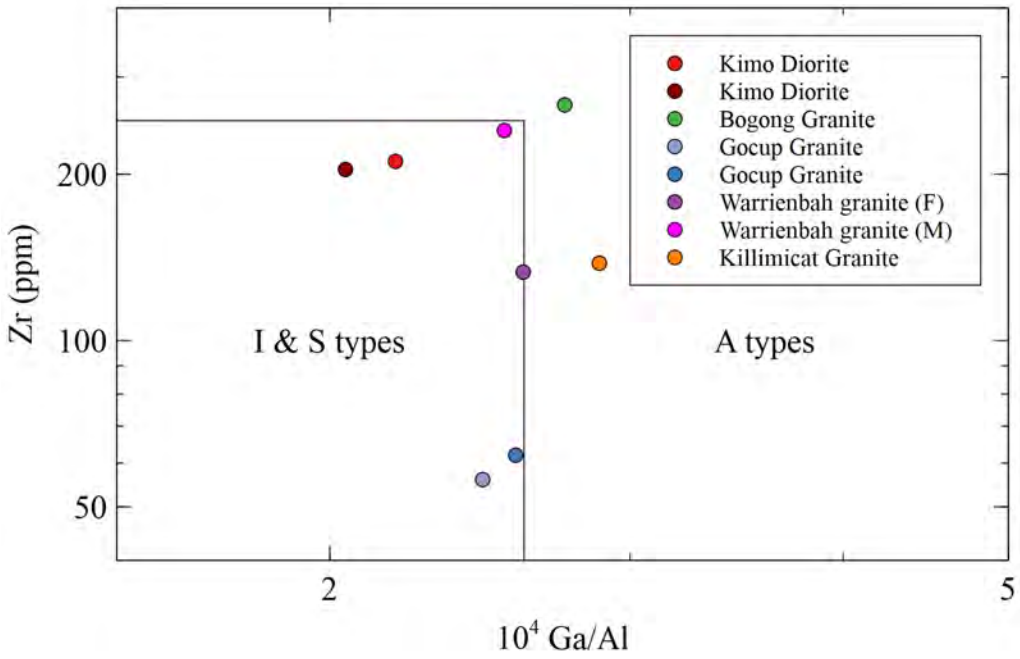

Figure 3.7: Discrimination diagram that separates A-type plutons from I and S-type plutons (after Whalen et al., 1987).

form a straight line with silica content, but rather most units have concentrations of between 600 - 800 ppm, with the exception of the Gocup Granite, with concentrations of approximately 200 ppm (Fig. 3.8 k).

The chondrite-normalized rare earth element (REE) patterns (Fig. 3.9) indicate light REE enrichment with pronounced negative Eu anomalies in most samples. The Kimo Diorite displays the smallest Eu anomaly due to the abundance of plagioclase in the rock, suggesting the Kimo Diorite in not fractionated. Plagioclase is able to incorporate both Eu^{2+} and Eu^{3+} (Eu^{2+} substituting for Ca^{2+}) where other minerals that contain REE can only incorporate Eu^{3+} as other REE (except for Ce^{4+}) only have a 3+ charge (Sinha, 1983). The Gocup Granite has low REE concentrations over all of the lanthanides, with the least light REE enrichment and most pronounced Eu

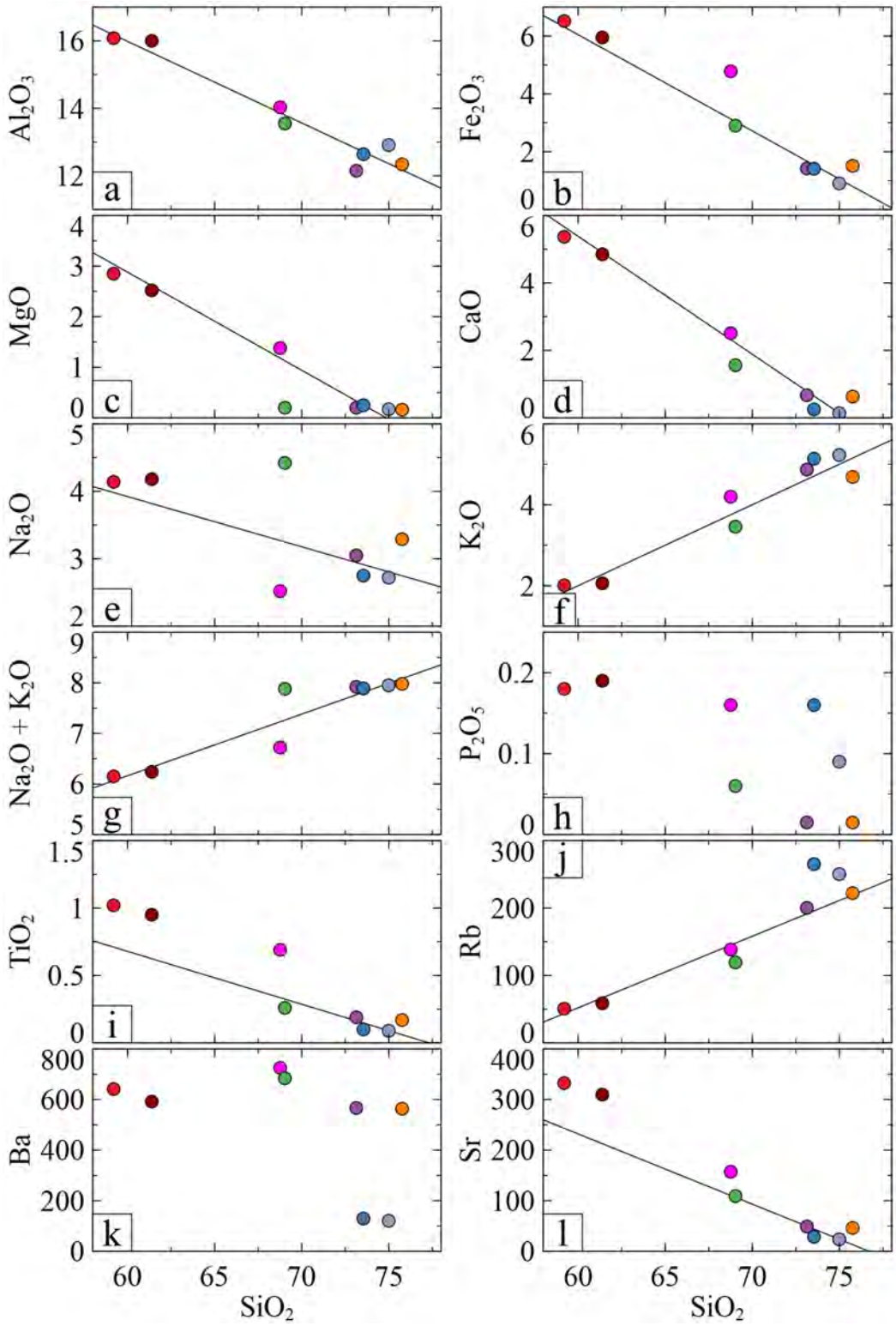

Figure 3.8: Selected Harker diagrams for the plutons within the Tumut Trough. Legends for each plot are the same as Figure 3.6.

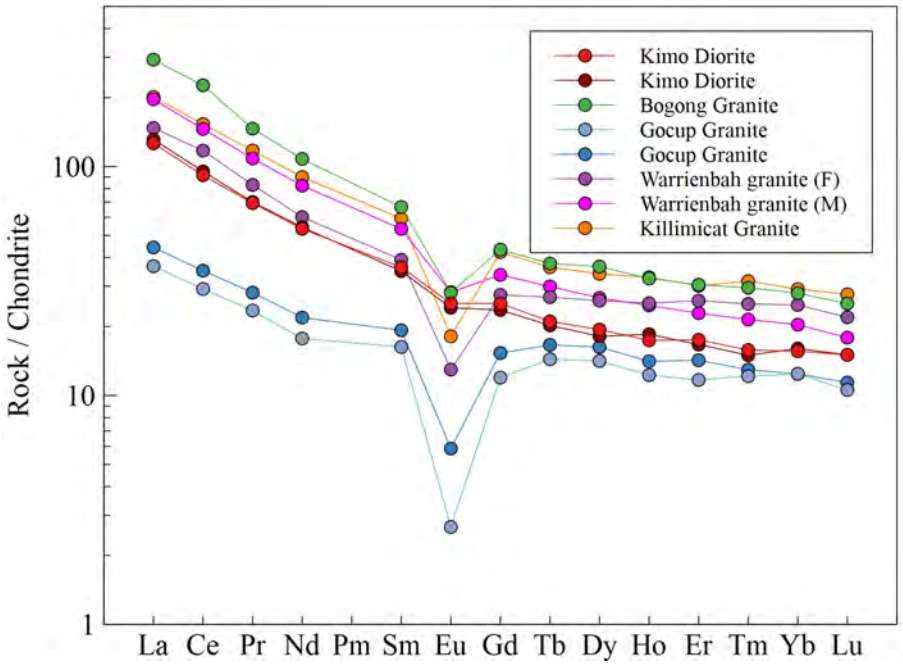

Figure 3.9: Chondrite-normalized (after McDonough and Sun, 1995) REE patterns of the plutonic units.

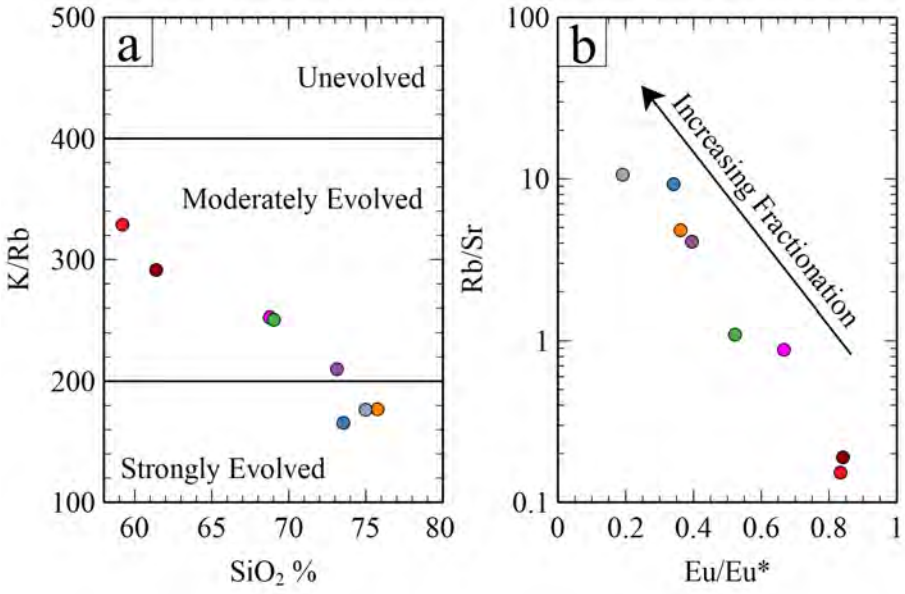

Figure 3.10: a) The K-Rb ratio to indicate how evolved the pluton is (Blevin, 2004). b) Degree of fractionation using Rb-Sr ratio (Plimer and Elliott, 1979) and the europium anomaly (Eu/Eu*). Legends for the samples in both graphs are the same as Figure 3.6.

anomaly. The Eu anomaly is calculated using the following:

$$\mathrm{Eu/Eu^*} = \frac{\mathrm{Eu}}{\sqrt{\mathrm{Sm}^2 \times \mathrm{Gd}^2}}$$

Fractionation and degree of evolution are both important for determining the mineralisation potential of a pluton and type of mineralisation a pluton can host (Blevin, 2004). The K/Rb ratio distinguishes between unevolved and evolved plutons (Fig. 3.10 a) while the europium anomaly (Eu/Eu*) is related to the degree of fractionation experienced by the pluton (Fig. 3.10 b). The Gocup Granite is the most evolved and fractionated of all the plutons (Fig. 3.10), with the Killimicat Granite also being strongly evolved and fractionated.

3.3 Geochronology

Key rock units within the basin units were targeted for zircon and titanite geochronology (Blowering Formation, Honeysuckle Beds and Snowball Metabasic Igneous Complex), with plutons also being targetted to constrain the post-basin magmatism within the trough. Data for this section can be found in Appendix D.

3.3.1 Zircon Features and Ages

Kimo Diorite

Zircon Description

Zircons in the Kimo Diorite (Fig. 3.11) generally have long prisms and short pyramids terminating in obtuse to right angled points, appearing like G1 zircons (Pupin, 1980). They have well-defined magmatic zoning surrounding xenocrystic cores. Grains appear euhedral where they have not been split by fractures.

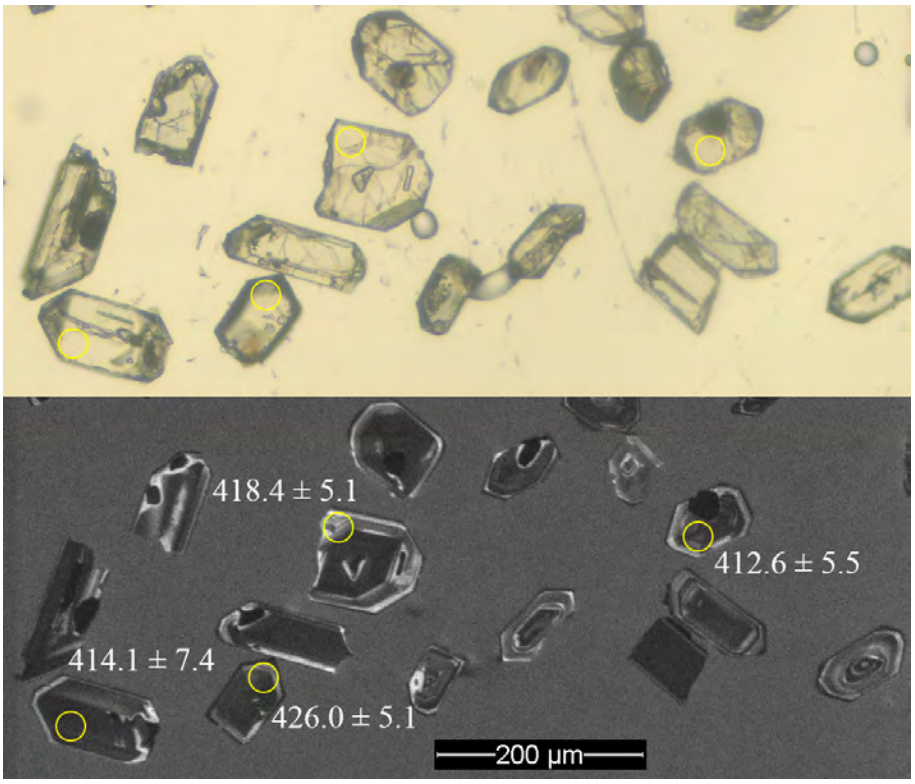

Figure 3.11: Transmitted light (TL; top) and cathodoluminescence (CL; bottom) images of representative zircons from the Kimo Diorite.

U-Pb Isotopic Results

198 zircon grains and fragments were mounted for the Kimo Diorite (TDBHons003.01). 25 zircons were analysed for U-Pb and REE, 12 for Lu-Hf and a further 24 for U-Pb as a follow up session. 29 concordant (90 - 110% concordance; Fig. 3.12 a) U-Pb ages were obtained with 23 discordant ages removed from initial age determination due to suspected Pb loss or gain. The results of the analyses are presented in Tera-Wasserburg and Wetherill concordia plots and weighted mean plots (Fig. 3.12 a-d).

The youngest analysis TDB003.01_1-9 (412.5 ± 6.5 Ma) is 94.7 % concordant. It is within uncertainty of the next 20 youngest concordant ages and returns a weighted mean average of 417.4 ± 1.3 Ma (Fig. 3.12 b). The weighted average of 417.4 ± 1.3

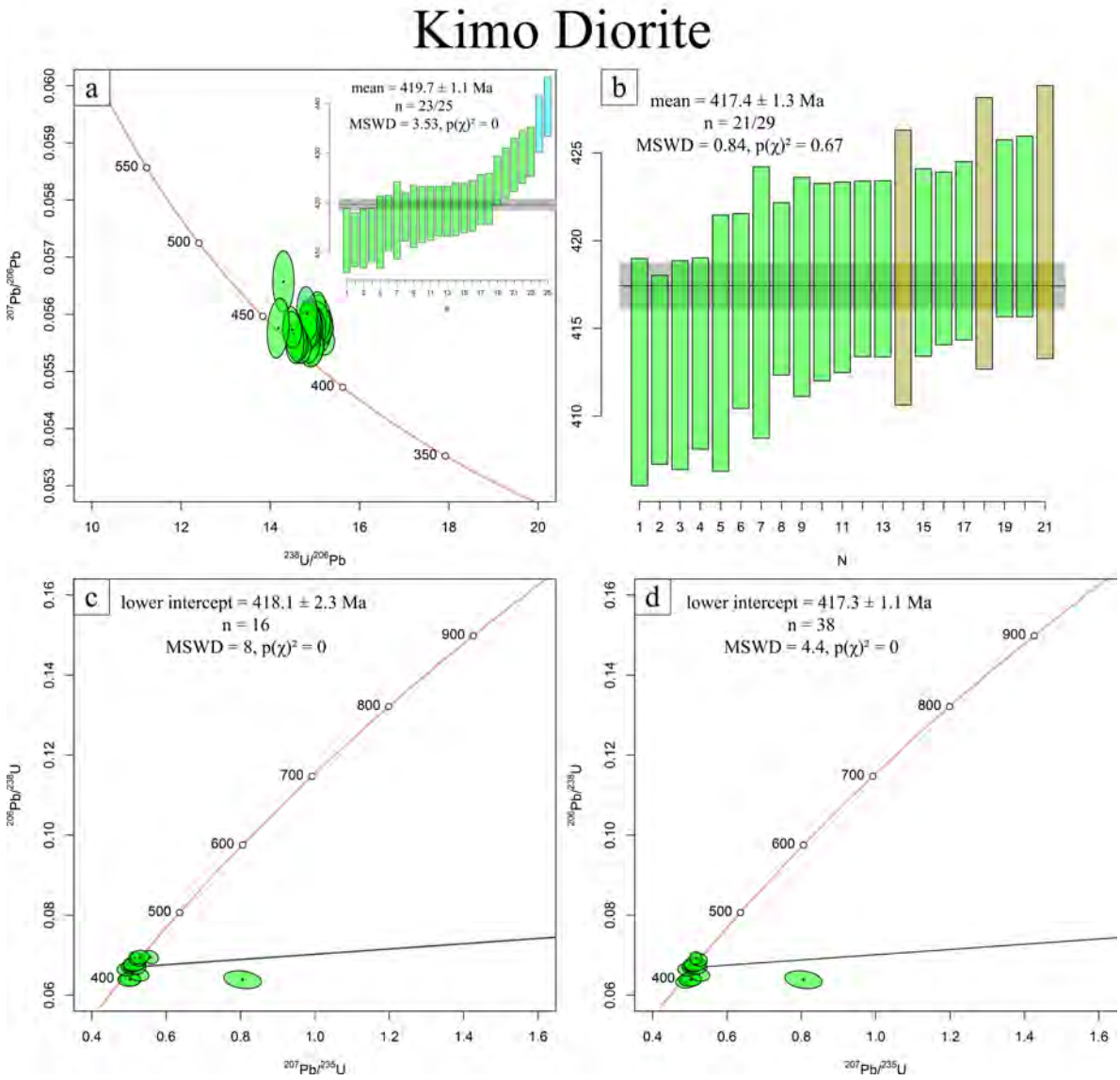

Figure 3.12: a) Tera-Wasserburg concordia diagram for the session 1 analyses of the Kimo Diorite sample with an inset diagram of the weighted mean of these analyses. Note the high MSWD and low $p(\chi)^2$ values. b) Weighted mean of the 21 youngest ages defining the preferred age for the Kimo Diorite of 417.4 ± 1.3 Ma. Green analyses are from the first session and the brown analyses are from session 2. c) Wetherill concordia diagram with a model-1 discordia age formed from the session 2 data. d) Wetherill concordia diagram with a model-1 discordia age formed from both sessions to form an age indistinguishable from weighted mean of the concordant data.

Ma is interpreted to be the emplacement age for the Kimo Diorite.

The Kimo Diorite age of 417.4 ± 1.3 Ma is statistically robust with an MSWD of 0.84 indicating a single statistical population. The $p(\chi^2)$ is 0.67 which is > 0.05, indicating the age is not overdispersed with respect to analytical uncertainty. All data from session 2, and all data from both session are presented on Wetherill concordia plots and Pb anchored model-1 discordia intercept ages of 418.1 ± 2.3 Ma and 417.3 ± 1.1 Ma were calculated (Fig. 3.12 c, d). These results are indistinguishable from the weighted mean age calculated from the youngest concordant ages and supports the interpreted emplacement age.

All 21 grains have the concentric zoning and euhedral grain shape suggestive of magmatic origin. They generally have broad magmatic bands typical of dioritic zircons (Corfu et al., 2003).

The concordant zircon trace element patterns of the Kimo Diorite zircons (see Appendix E) show REE patterns similar to the magmatic zircons from Long et al. (2012). They all have Ce anomalies, pronounced Eu anomalies and a strong La/Lu slope (Hoskin, 2005).

Bogong Granite

Zircon Description

Zircons in the Bogong Granite (Fig. 3.13) generally have long prisms and short pyramids with right angled terminations, appearing like euhedral P5 zircons (Pupin, 1980). Most grains well-defined magmatic zoning with small cores. Other grains have inclusions overprinting the magmatic zoning.

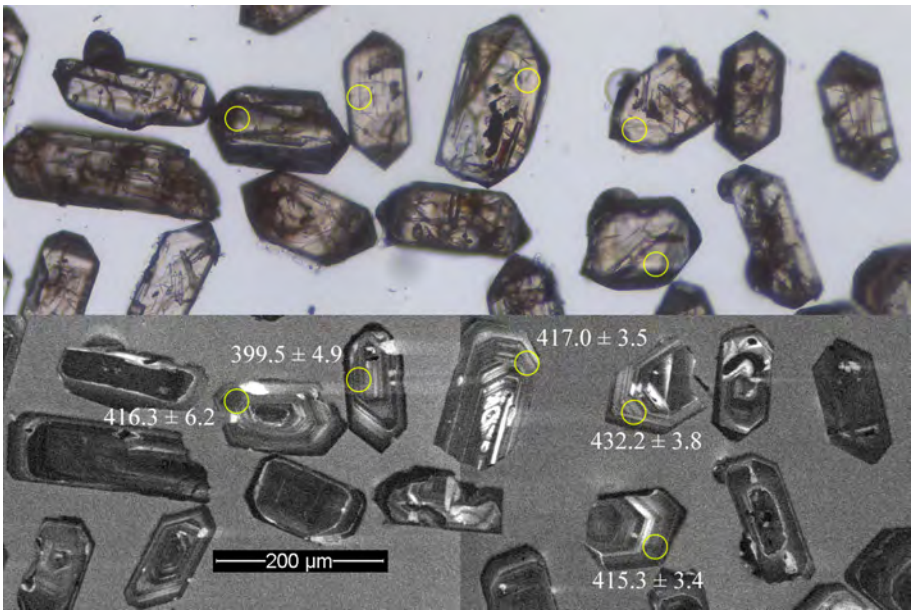

Figure 3.13: Transmitted light (TL; top) and cathodoluminescence (CL; bottom) images of representative zircons from the Bogong Granite. Note the fractures and inclusions in each TL image.

U-Pb Isotopic Results

153 zircon grains and fragments were mounted for the Bogong Granite (TDBHons007.01). 24 zircons were analysed for U-Pb and REE, 12 for Lu-Hf and a further 29 for U-Pb as a follow up session. 24 concordant (90 - 110% concordance; Fig. 3.14 a) U-Pb ages were obtained with 36 discordant ages removed from initial age determination due to suspected Pb loss or gain. The results of the analyses are presented in Tera-Wasserburg and Wetherill concordia plots and weighted mean plots (Fig. 3.14 a-d).

The youngest analysis TDB007.01_2-15 (411.2 ± 7.4 Ma) is 91.4 % concordant. It is within uncertainty of the next 10 youngest concordant ages and returns a weighted mean average of 416.8 ± 1.5 Ma (Fig. 3.14 b). The weighted average of 416.8 ± 1.5 Ma is interpreted to be the emplacement age for the Bogong Granite.

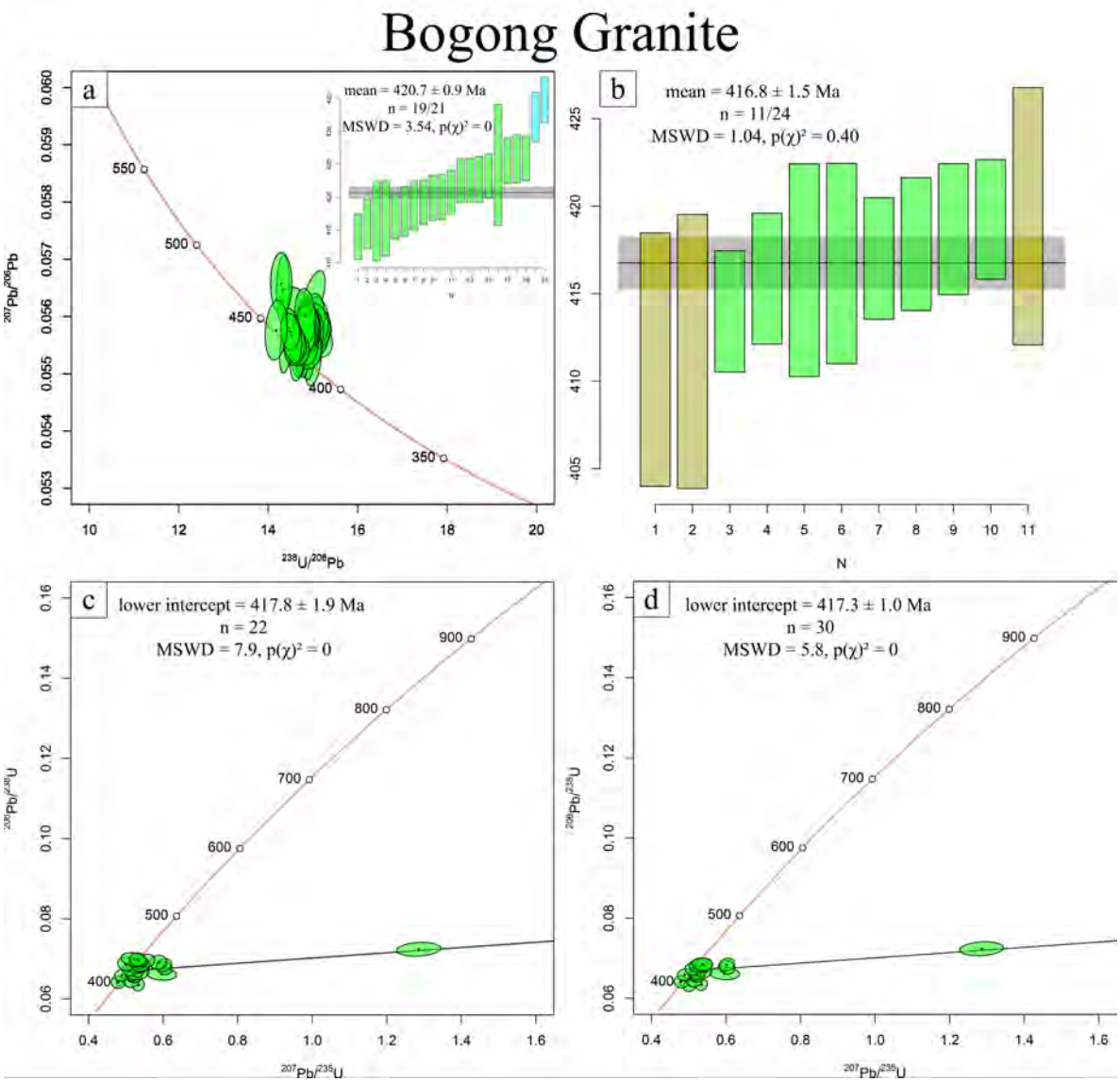

Figure 3.14: a) Tera-Wasserburg concordia diagram for the session 1 analyses of the Bogong Granite sample with an inset diagram of the weighted mean of these analyses. Note the high MSWD and low $p(\chi)^2$ values. b) Weighted mean of the 11 youngest ages defining the preferred age for the Bogong Granite of 416.8 ± 1.5 Ma. c) Wetherill concordia diagram with a model-1 discordia age formed from the session 2 data. d) Wetherill concordia diagram with a model-1 discordia age formed from both sessions to form an age almost indistinguishable from weighted mean of the concordant data.

The Bogong Granite age of 416.8 ± 1.5 Ma is statistically robust with an MSWD of 1.04 indicating a single statistical population. The $p(\chi^2)$ is 0.40 which is > 0.05. All

data from session 2, and all data from both session are presented on Wetherill concordia plots and Pb anchored model-1 discordia intercept ages of 417.8 ± 1.9 Ma and 417.3 ± 1.0 Ma were calculated (Fig. 3.14 c, d). These results are almost indistinguishable from the weighted mean age calculated from the youngest concordant ages and supports the interpreted emplacement age.

All 11 grains have the concentric zoning and euhedral grain shape suggestive of magmatic origin. They generally have narrow magmatic bands typical of granitic zircons (Corfu et al., 2003).

The concordant zircon trace element patterns of the Bogong Granite zircons (see Appendix E) show REE patterns similar to the magmatic zircons from Long et al. (2012). They all have Ce anomalies, pronounced Eu anomalies and a strong La/Lu slope (Hoskin, 2005).

Gocup Granite

Zircon Description

Zircons in the Gocup Granite (Fig. 3.15) generally have short prisms, but can extend up to 4 times the width of the zircon. Pyramids are long with acute terminations, appearing like S1 zircons (Pupin, 1980). Magmatic zoning surrounds small cores. Grains vary in size with some having equant prisms with pointed pyramids while others have elongate prisms with equant pyramids.

U-Pb Isotopic Results

123 zircon grains and fragments were mounted for the Gocup Granite (TDBHons011.01). 26 zircons were analysed for U-Pb and REE, 12 for Lu-Hf and a

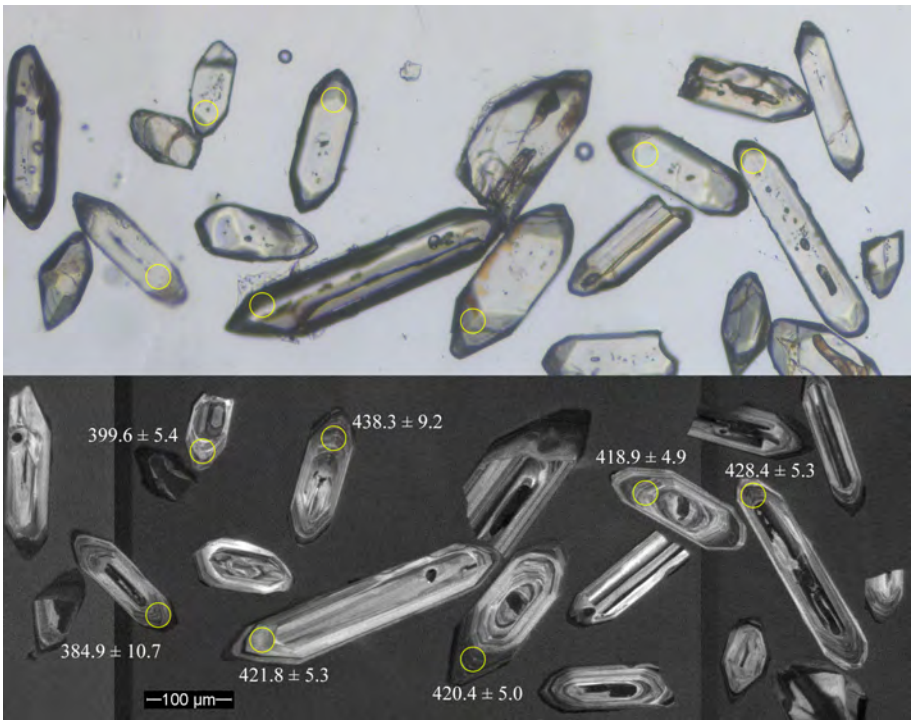

Figure 3.15: Transmitted light (TL; top) and cathodoluminescence (CL; bottom) images of representative zircons from the Gocup Granite.

further 32 for U-Pb as a follow up session. 21 concordant (90 - 110% concordance; Fig. 3.16 a) U-Pb ages were obtained with 37 discordant ages removed from initial age determination due to suspected Pb loss or gain. The results of the analyses are presented in Tera-Wasserburg and Wetherill concordia plots and weighted mean plots (Fig. 3.16 a-d).

The youngest analysis TDB011.01_1-25 (414.9 ± 5.2 Ma) is 92.2 % concordant. It is within uncertainty of the next 14 youngest concordant ages and returns a weighted mean average of 418.7 ± 1.5 Ma (Fig. 3.16 b). The weighted average of 418.7 ± 1.5 Ma is interpreted to be the emplacement age for the Gocup Granite.

The Gocup Granite age of 418.7 ± 1.5 Ma is statistically robust with an MSWD of

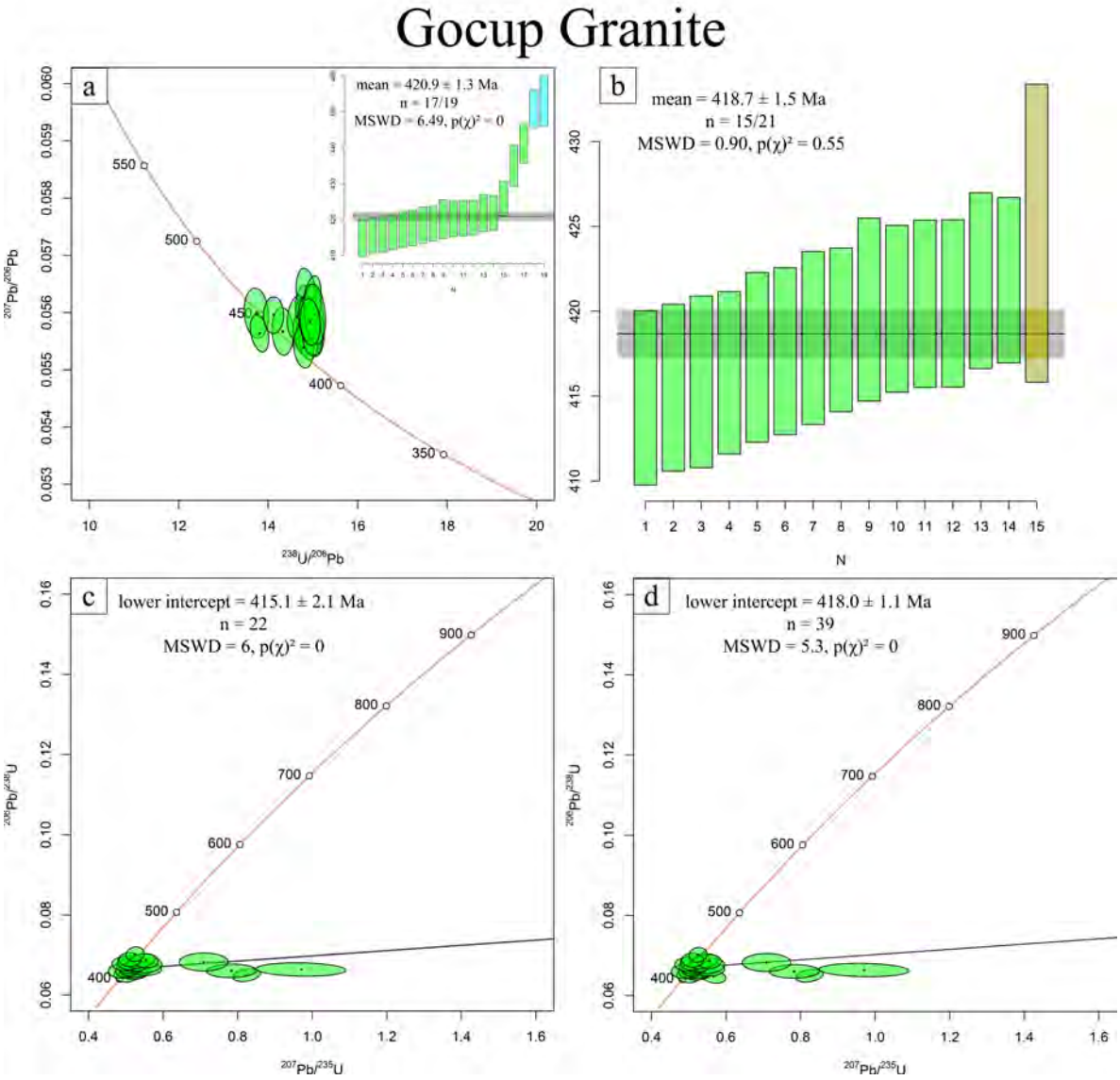

Figure 3.16: a) Tera-Wasserburg concordia diagram for the session 1 analyses of the Gocup Granite sample with an inset diagram of the weighted mean of these analyses. Note the high MSWD and low $p(\chi)^2$ values. b) Weighted mean of the 15 youngest ages defining the preferred age for the Gocup Granite of 418.7 ± 1.5 Ma. Green analyses are from the first session and the brown analysis is from session 2. c) Wetherill concordia diagram with a model-1 discordia age formed from the session 2 data. d) Wetherill concordia diagram with a model-1 discordia age formed from both sessions to form an age within error of the weighted mean of the concordant data.

0.90, being close to a single statistical population. The $p(\chi^2)$ is 0.55 which is > 0.05.

All data from session 2, and all data from both session are presented on Wetherill

concordia plots and Pb anchored model-1 discordia intercept ages of 415.2 ± 2.1 Ma and 418.0 ± 1.5 Ma were calculated (Fig. 3.16 c, d). These results are almost indistinguishable from the weighted mean age calculated from the youngest concordant ages and supports the interpreted emplacement age.

All 15 grains have the concentric zoning and euhedral grain shape suggestive of magmatic origin. They generally have narrow magmatic bands typical of granitic zircons (Corfu et al., 2003).

The concordant zircon trace element patterns of the Gocup Granite zircons (see Appendix E) show REE patterns similar to the magmatic zircons from Long et al. (2012). They all have Ce anomalies, pronounced Eu anomalies and a strong La/Lu slope (Hoskin, 2005).

Warrienbah granite

Zircon Description

Zircons in the Warrienbah granite (Fig 3.17) generally have long prisms and short pyramids with right angled terminations, appearing like euhedral, P5 zircons (Pupin, 1980). Grains generally had a weak response in CL, but magmatic zoning can be seen surrounding the cores.

U-Pb Isotopic Results

183 zircon grains and fragments were mounted for the Warrienbah granite (TDBHons012.01). 26 zircons were analysed for U-Pb and REE, 12 for Lu-Hf and a further 39 for U-Pb as a follow up session. 11 concordant (90 - 110% concordance; Fig. 3.18 a) U-Pb ages were obtained with 55 discordant ages removed from initial

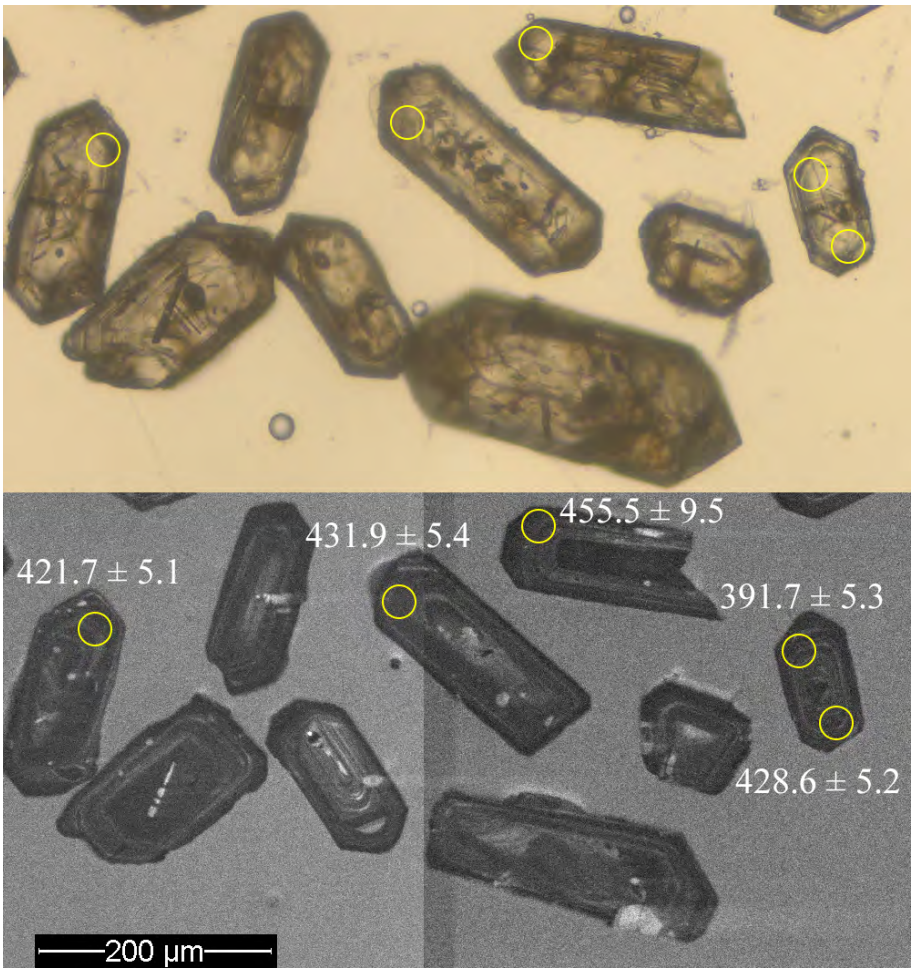

Figure 3.17: Transmitted light (TL; top) and cathodoluminescence (CL; bottom) images of representative zircons from the Warrienbah granite.

age determination due to suspected Pb loss or gain. The results of the analyses are presented in Tera-Wasserburg and Wetherill concordia plots and weighted mean plots (Fig. 3.18 a-d).

The youngest analysis TDB012.01_2-12 (411.9 ± 8.5 Ma) is 90.5 % concordant. It is within uncertainty of the next 6 youngest concordant ages and returns a weighted mean average of 415.9 ± 2.5 Ma (Fig. 3.18 b). The weighted average of 415.9 ± 2.5 Ma is interpreted to be the emplacement age for the Warrienbah granite.

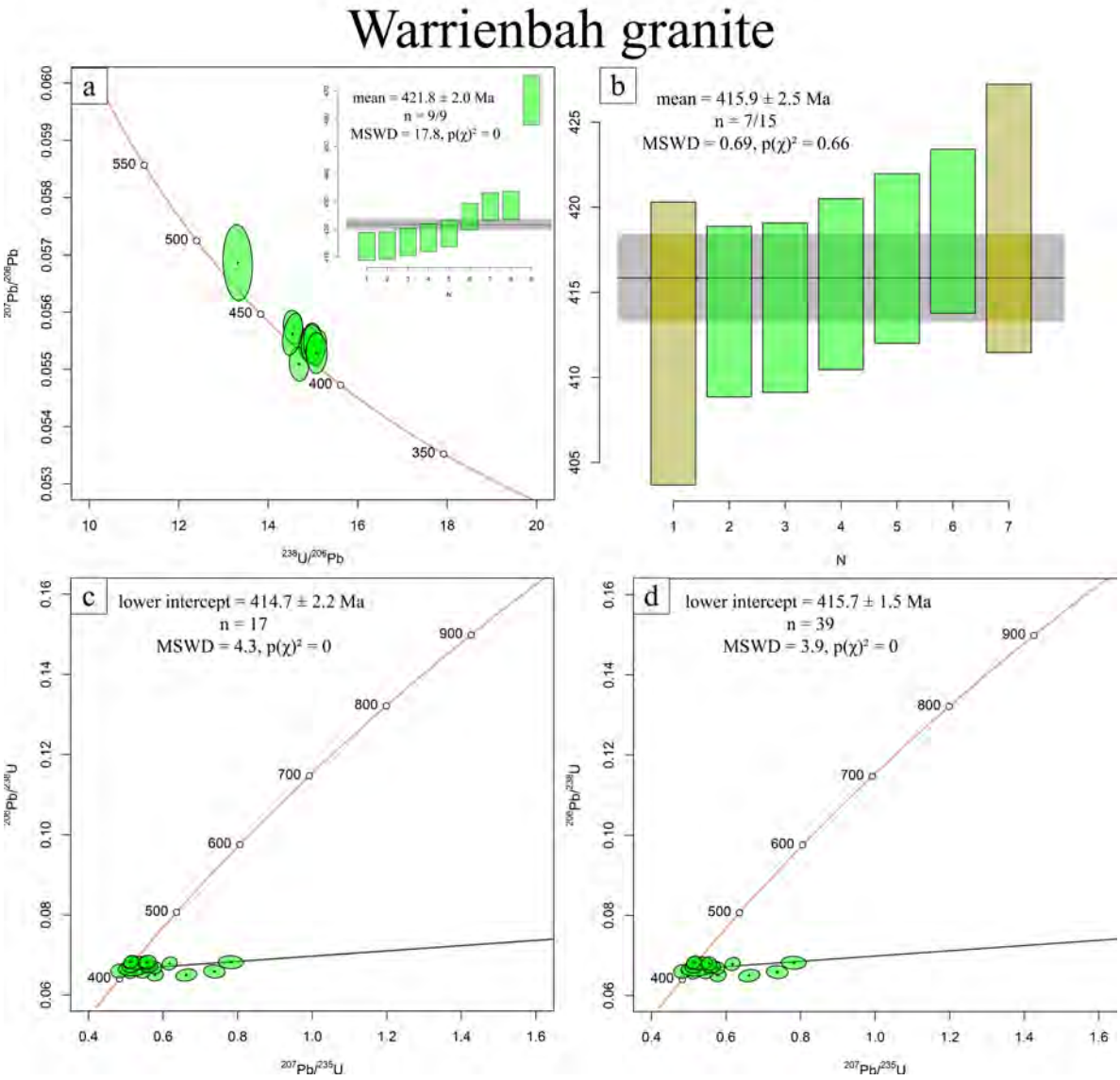

Figure 3.18: a) Tera-Wasserburg concordia diagram for the session 1 analyses of the Warrienbah granite sample with an inset diagram of the weighted mean of these analyses. Note the high MSWD and low $p(\chi)^2$ values. b) Weighted mean of the 7 youngest ages defining the preferred for the Warrienbah granite of 415.9 ± 2.5 Ma. Green analyses are from the first session and the brown analysis is from session 2. c) Wetherill concordia diagram with a model-1 discordia age formed from the session 2 data. d) Wetherill concordia diagram with a model-1 discordia age formed from both sessions to form an age indistinguishable from weighted mean of the concordant data.

The Warrienbah granite age of 415.9 ± 2.5 Ma is statistically robust with an MSWD

of 0.69. The p(χ^2) is 0.66 which is > 0.05. All data from session 2, and all data from both session are presented on Wetherill concordia plots and Pb anchored model-1 discordia intercept ages of 414.7 $\pm$ 2.2 Ma and 415.7 $\pm$ 1.5 Ma were calculated (Fig. 3.18 c, d). These results are indistinguishable from the weighted mean age calculated from the youngest concordant ages and supports the interpreted emplacement age.

All 7 grains have the concentric zoning and euhedral grain shape suggestive of magmatic origin. They generally have narrow magmatic bands typical of granitic zircons (Corfu et al., 2003).

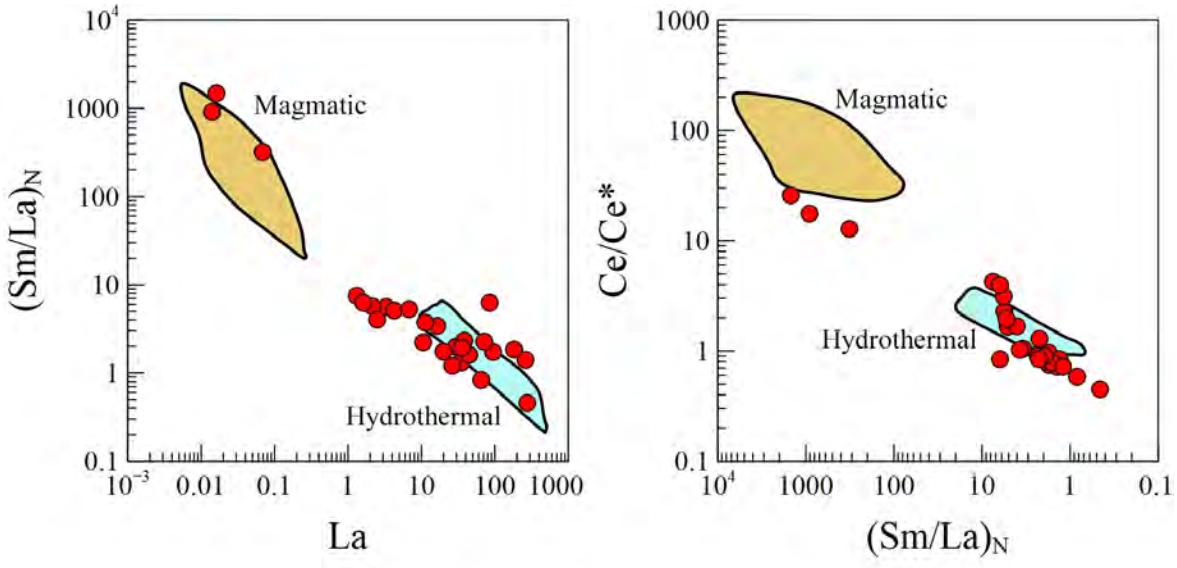

Figure 3.19: Zircon chemistry discriminating between magmatic and hydrothermal influenced zircons in the Warrienbah granite (after Long et al., 2012).

Most zircons discriminate as hydrothermal (Fig. 3.19), but the concordant ones are magmatic. The concordant magmatic ages (TDB012.01_1-9, TDB012.01_1-23, TDB012.01_1-23b, TDB012.01_1-26 and TDB012.01_1-26b) are all used in the weighted mean. This supports that the age determined could represent the emplacement age.

The concordant zircon trace element patterns of the Warrienbah granite zircons (see Appendix E) show REE patterns similar to the magmatic zircons from Long et al. (2012). They all have Ce anomalies, pronounced Eu anomalies and a strong La/Lu slope (Hoskin, 2005).

Blowering Formation

Zircon Description

Zircons in the Blowering Formation (Fig. 3.20) generally have short prisms and pyramids, almost appearing equant. Some zircons do have long prisms. They appear like euhedral, S10 zircons (Pupin, 1980). Grains have magmatic zones around inherited cores. Zircons are generally equant, but some do appear elongate.

U-Pb Isotopic Results

120 zircon grains and fragments were mounted for the Blowering Formation (TDBHons015.01). 27 zircons were analysed for U-Pb and REE, 13 for Lu-Hf and a further 17 for U-Pb as a follow up session. 30 concordant (90 - 110% concordance; Fig. 3.21 a) U-Pb ages were obtained with 22 discordant ages removed from initial age determination due to suspected Pb loss or gain. The results of the analyses are presented in Tera-Wasserburg and Wetherill concordia plots and weighted mean plots (Fig. 3.21 a-d).

The youngest analysis TDB015.01_1-26b (420.2 ± 3.6 Ma) is 94.5 % concordant. This is part of a young population around 420 Ma and was not used in the weighted mean. The youngest analysis of the main population TDB015.01_21b (423.2 ± 3.6 Ma) is 95.0 % concordant. It is within uncertainty of the next 9 youngest concordant ages of

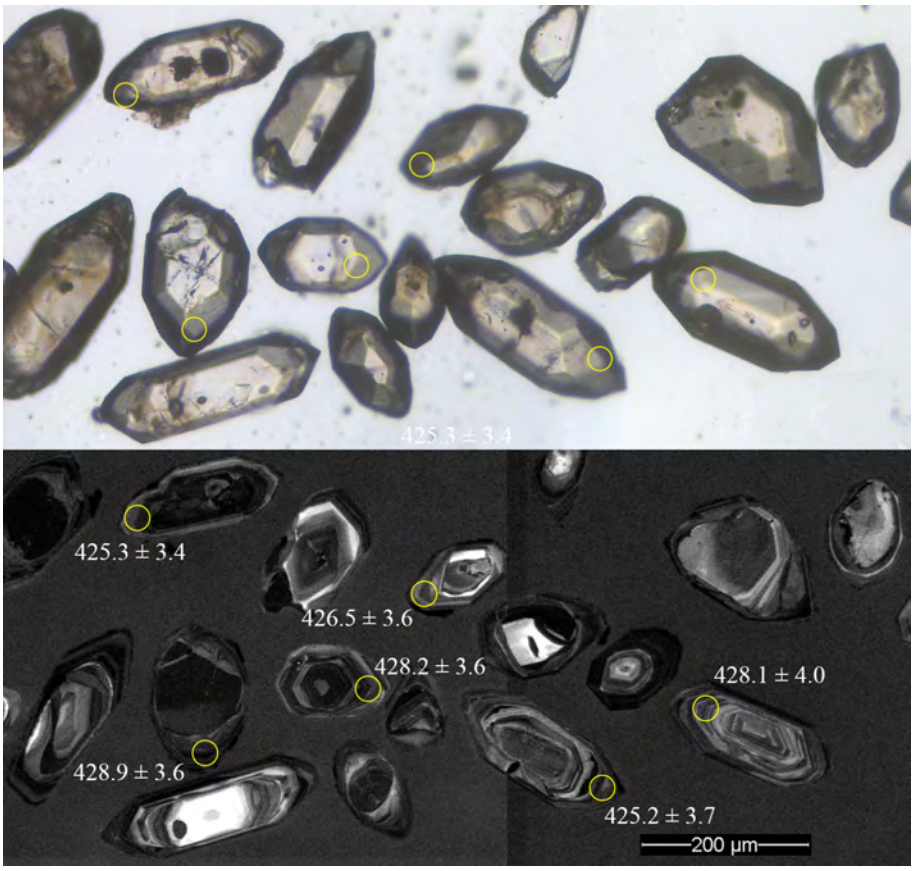

Figure 3.20: Transmitted light (TL; top) and cathodoluminescence (CL; bottom) images of representative zircons from the Blowering Formation.

the main population and returns a weighted mean average of 426.2 ± 1.3 Ma (Fig. 3.21 b). The weighted average of 426.2 ± 1.3 Ma is interpreted to be the age of the Blowering Formation. One inherited grain was found with an age of 499.2 ± 4.1 Ma.

The Blowering Formation age of 426.2 ± 1.3 Ma is statistically robust with an MSWD of 1.07, being close to a single statistical population. The p(χ^2) is 0.38 which is > 0.05. All data from session 2, and all data from both session are presented on Wetherill concordia plots and Pb anchored model-1 discordia intercept ages of 426.2 ± 4.2 Ma and 426.4 ± 0.9 Ma were calculated (Fig. 3.21 c, d). These results are indistinguishable from the weighted mean age calculated from the youngest

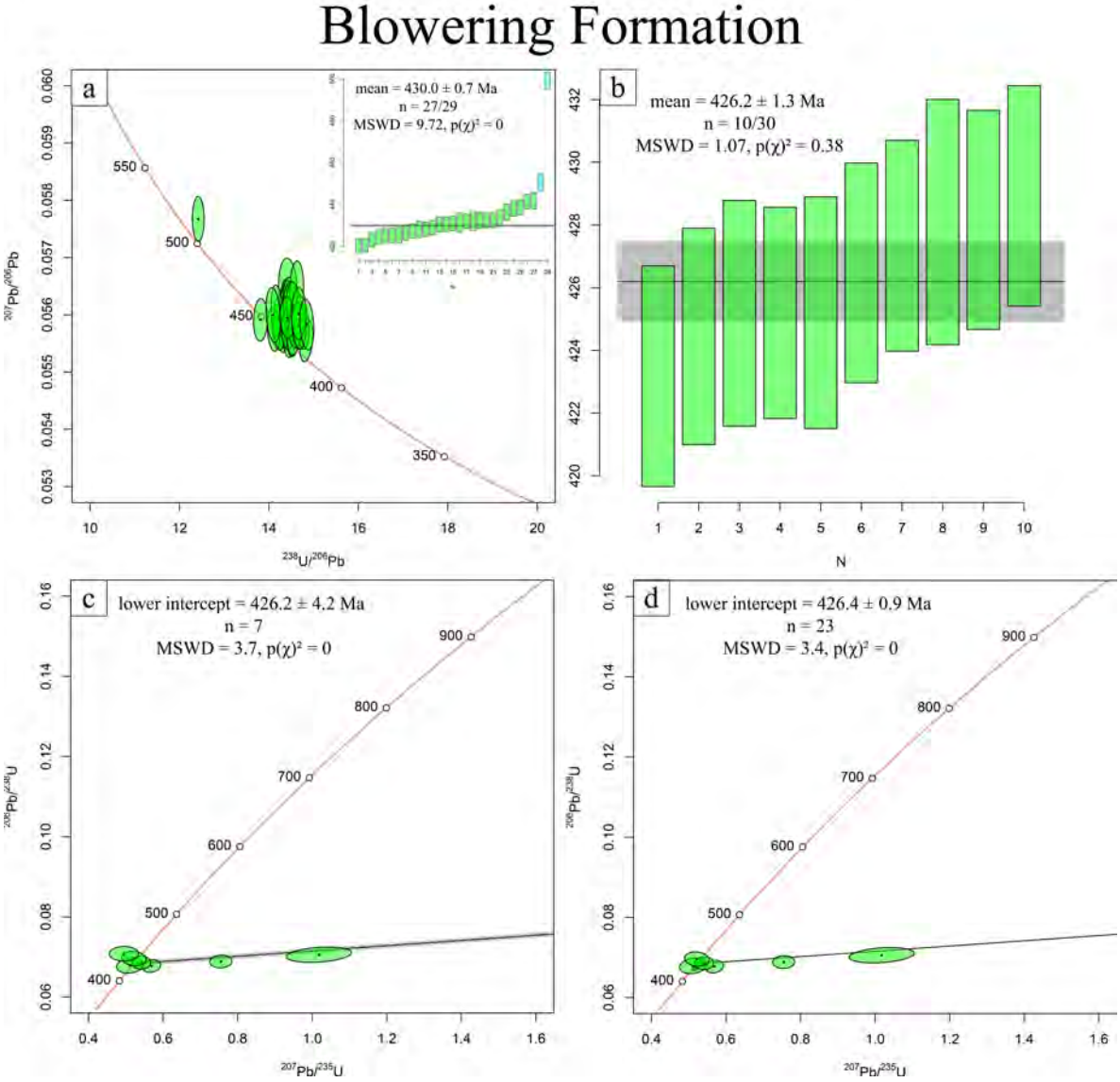

Figure 3.21: a) Tera-Wasserburg concordia diagram for the session 1 analyses of the Blowering Formation sample with an inset diagram of the weighted mean of these analyses. Note the high MSWD and low $p(\chi)^2$ values. b) Weighted mean of the 10 youngest ages defining the preferred age for the Blowering Formation of 426.2 ± 1.3 Ma. c) Wetherill concordia diagram with a model-1 discordia age formed from the session 2 data. d) Wetherill concordia diagram with a model-1 discordia age formed from both sessions to form an age indistinguishable from weighted mean of the concordant data.

concordant ages and supports the interpreted depositional age.

All 10 grains have the concentric zoning and euhedral grain shape suggestive of

magmatic origin.

The zircon trace element patterns of the Blowering Formation zircons (see Appendix E) show REE patterns similar to the magmatic zircons from Long et al. (2012). They all have Ce anomalies, pronounced Eu anomalies and a strong La/Lu slope (Hoskin, 2005).

Honeysuckle Beds

Zircon Description

Zircons from the Honeysuckle Beds (Fig. 3.22) have both short and long prisms, generally having long pyramids with right angled terminations, appearing like S16 and S17 zircons (Pupin, 1980). Cores are inherited, with a distinct boundary between core and magmatic zoning on some grains. All grains have magmatic zoning around the cores.

U-Pb Isotopic Results

181 zircon grains and fragments were mounted for the Honeysuckle Beds (TDBHons01701). 27 zircons were analysed for U-Pb and REE, 13 for Lu-Hf and a further 20 for U-Pb as a follow up session. 32 concordant (90 - 110% concordance; Fig. 3.23 a) U-Pb ages were obtained with 20 discordant ages removed from initial age determination due to suspected Pb loss or gain. The results of the analyses are presented in Tera-Wasserburg and Wetherill concordia plots and weighted mean plots (Fig. 3.23 a-d).

The youngest analysis TDB017.01_1-15 (422.4 $\pm$ 5.0 Ma) is 94.4 % concordant. This is a young grain that was not used in the weighted mean. The youngest analysis of

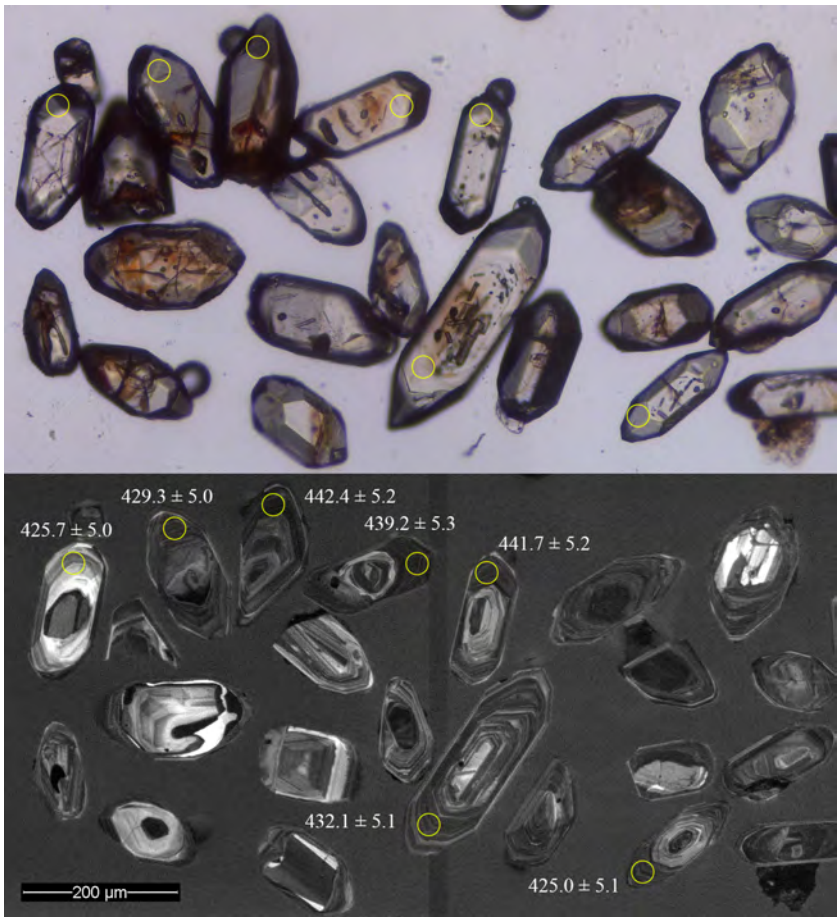

Figure 3.22: Transmitted light (TL; top) and cathodoluminescence (CL; bottom) images of representative zircons from the Honeysuckle Beds.

the main population TDB015.01_12 (425.0 ± 5.1 Ma) is 94.5 % concordant. It is within uncertainty of the next 12 youngest concordant ages and returns a weighted mean average of 429.1 ± 1.7 Ma (Fig. 3.23 b). The weighted average of 429.1 ± 1.7 Ma is interpreted to be the emplacement age for the Honeysuckle Beds. Two inherited grains was found with ages of 544.3 ± 6.5 Ma and 774.0 ± 15.2 Ma.

The Honeysuckle Beds age of 429.1 ± 1.7 Ma is statistically robust with an MSWD of 1.16, being close to a single statistical population. The $p(\chi^2)$ is 0.31 which is > 0.05. All data from session 2, and all data from both session are presented on Wetherill

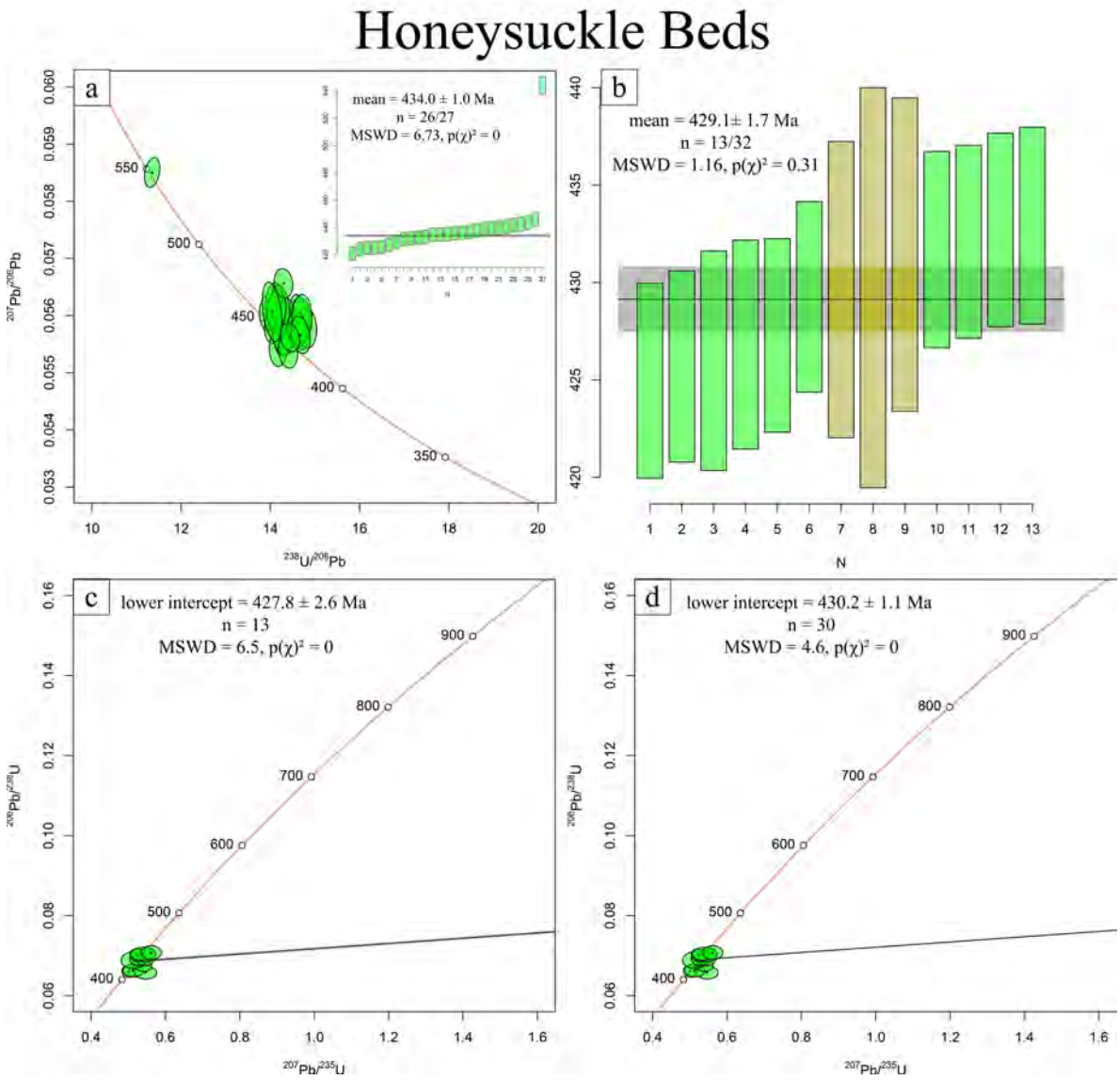

Figure 3.23: a) Tera-Wasserburg concordia diagram for the session 1 analyses of the Honeysuckle Beds sample with an inset diagram of the weighted mean of these analyses. Note the high MSWD and low $p(\chi)^2$ values. b) Weighted mean of the 13 youngest ages defining the preferred for the Honeysuckle Beds of 429.1 ± 1.7 Ma. Green analyses are from the first session and the brown analysis is from session 2. c) Wetherill concordia diagram with a model-1 discordia age formed from the session 2 data. d) Wetherill concordia diagram with a model-1 discordia age formed from both sessions to form an age indistinguishable from the weighted mean of the concordant data.

concordia plots and Pb anchored model-1 discordia intercept ages of 427.8 ± 2.6 Ma and 430.2 ± 1.1 Ma were calculated (Fig. 3.23 c, d). These results are close to the

weighted mean age calculated from the youngest concordant ages and supports the interpreted emplacement age.

All 13 grains have the concentric zoning and euhedral grain shape suggestive of magmatic origin.

The zircon trace element patterns of the Honeysuckle Beds zircons (see Appendix E) show REE patterns similar to the magmatic zircons from Long et al. (2012). They all have Ce anomalies, pronounced Eu anomalies and a strong La/Lu slope (Hoskin, 2005).

Killimicat Granite

Zircon Description

Zircons from the Killimicat Granite (Fig. 3.24) have both short and long prisms with short pyramids and right angled to acute terminations, generally appearing like S10 zircons (Pupin, 1980). Grains vary in morphology, with some being equant and others more elongate. Some grains have obvious inherited cores surrounded by magmatic zoning while others chow continuous magmatic zoning.

U-Pb Isotopic Results

151 zircon grains and fragments were mounted for the Killimicat Granite (TDBHons022.01). 23 zircons were analysed for U-Pb and REE, 11 Lu-Hf and a further 32 for U-Pb as a follow up session. 23 concordant (90 - 110% concordance; Fig. 3.25 a) U-Pb ages were obtained with 38 discordant ages removed from initial age determination due to suspected Pb loss or gain. The results of the analyses are presented in Tera-Wasserburg and Wetherill concordia plots and weighted mean plots

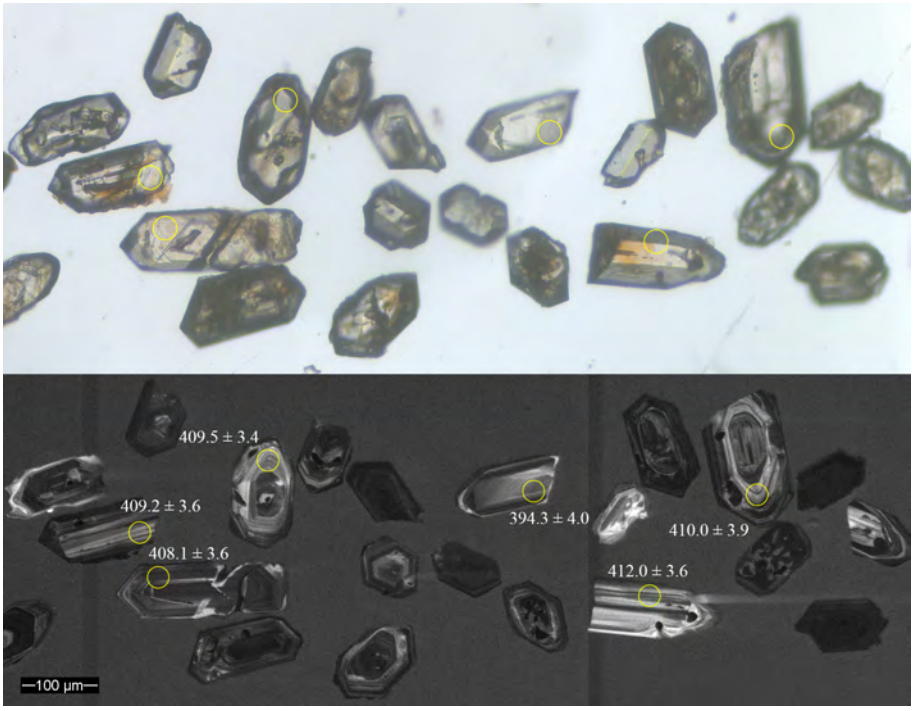

Figure 3.24: Transmitted light (TL; top) and cathodoluminescence (CL; bottom) images of representative zircons from the Killimicat Granite.

(Fig. 3.25 a-d).

Some spots showed evidence of two ages, most likely due to crossing magmatic domains so each of these ages are presented. Out of the 23 spots (28 ages) from the first session, 18 ages were concordant (90 - 110% concordance; Fig. 3.25 a). Out of the 33 spots (33 ages) from the second session only 5 were concordant. From the total of 23 concordant ages, 8 were used to form a statistically robust final age of 410.0 ± 1.5 Ma (Fig. 3.25 b).

The youngest analysis TDB022.01_17 (408.1 ± 3.6 Ma) is 93.2 % concordant. It is within uncertainty of the next 7 youngest concordant ages and returns a weighted mean average of 410.0 ± 1.5 Ma (Fig. 3.25 b). The weighted average of 410.0 ± 1.5 Ma is interpreted to be the emplacement age for the Killimicat Granite.

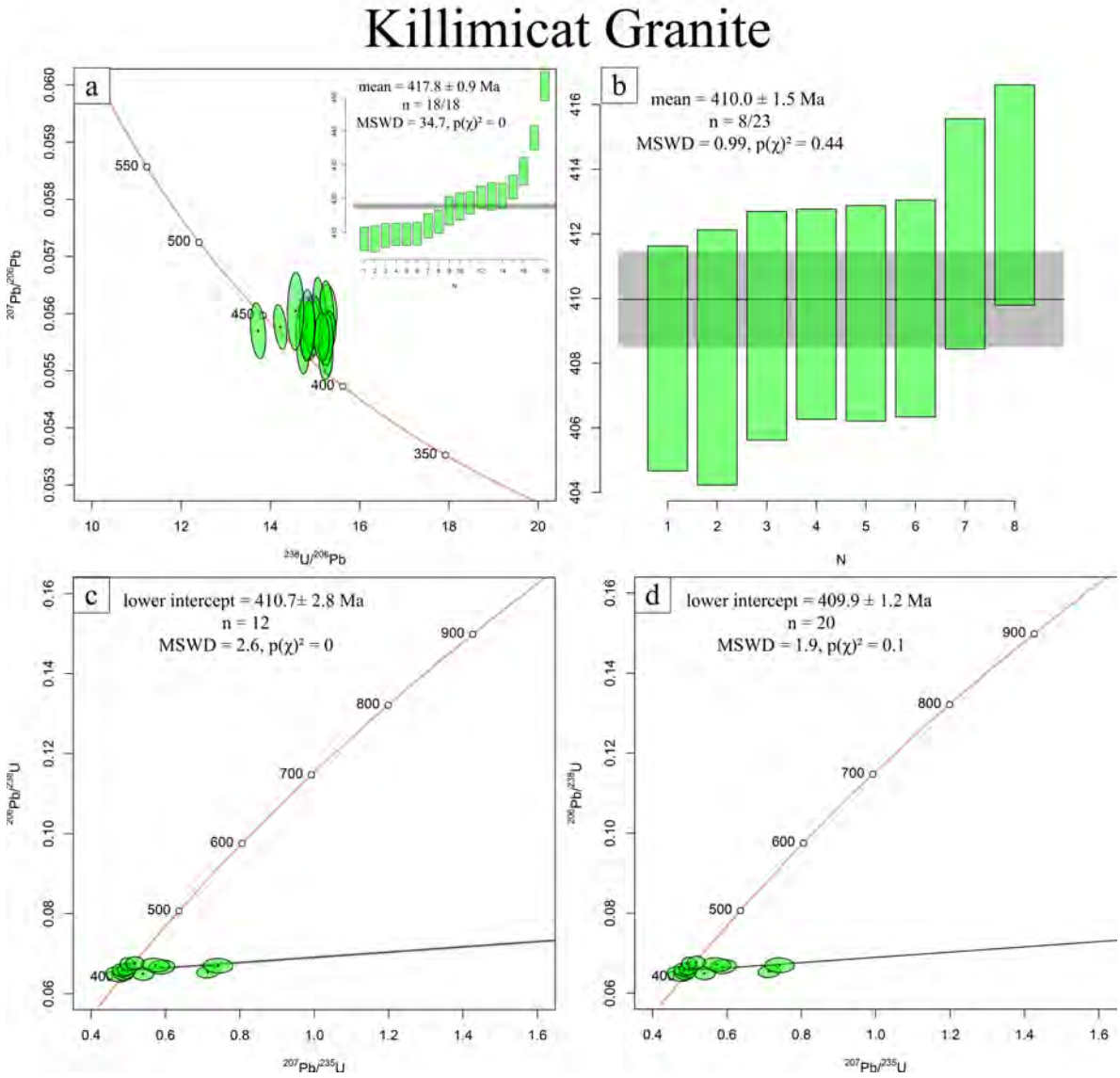

Figure 3.25: a) Tera-Wasserburg concordia diagram for the session 1 analyses of the Killimicat Granite sample with an inset diagram of the weighted mean of these analyses. Note the high MSWD and low $p(\chi)^2$ values. b) Weighted mean of the 8 youngest ages defining the preferred age for the Killimicat Granite of 410.0 ± 1.5 Ma. c) Wetherill concordia diagram with a model-1 discordia age formed from the session 2 data. d) Wetherill concordia diagram with a model-1 discordia age formed from both sessions to form an age indistinguishable from weighted mean of the concordant data.

The Killimicat Granite age of 410.0 ± 1.5 Ma is statistically robust with an MSWD of 0.99, being close to a single statistical population. The $p(\chi^2)$ is 0.44 which is > 0.05.

All data from session 2, and all data from both session are presented on Wetherill concordia plots and Pb anchored model-1 discordia intercept ages of 410.7 ± 2.8 Ma and 409.9 ± 1.2 Ma were calculated (Fig. 3.25 c, d). These results are almost indistinguishable from the weighted mean age calculated from the youngest concordant ages and supports the interpreted emplacement age.

All 8 grains have the concentric zoning and euhedral grain shape suggestive of magmatic origin. They generally have narrow magmatic bands typical of granitic zircons, although some bands are broader (Corfu et al., 2003).

The zircon trace element patterns of the Killimicat Granite zircons (see Appendix E) show REE patterns similar to the magmatic zircons from Long et al. (2012). They all have Ce anomalies, pronounced Eu anomalies and a strong La/Lu slope (Hoskin, 2005).

3.3.2 Titanite Features and Ages

Snowball Metabasic Igneous Complex

Titanite Description

One titanite grainset from the Snowball Metabasic Igneous Complex (TDBHons013.01) was analysed. Titanites have an average size of 200 μm. The largest titanites are 400 μm across. Grains are translucent to almost opaque. They are mostly fractured, with little to no inclusions and minor colouration. Grains are subhedral to anhedral and form metamorphic secondary aggregates in thin section (see Appendix B). BSE images indicate most grains are composite grains, with major fractures within the titanites clearly visible.

U-Pb Isotopic Results

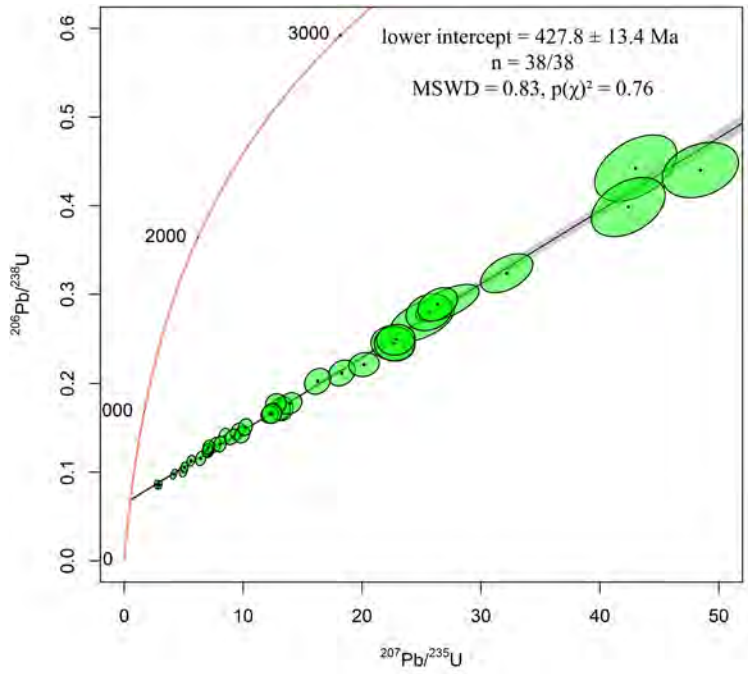

Figure 3.26: Wetherill concordia diagram for TDBHons013.01 from the Snowball Metabasic Igneous Complex. Discordia line also plotted.

The common-lead corrected U-Pb data forms a discordant line on the concordia plot (Fig. 3.26). From the 38 spot analyses, none were rejected since they all fall along the discordia. The age was calculated in IsoplotR using a discordia (model-1) age. The discordia gives a lower intercept age of 427.8 ± 13.4 Ma (95% confidence).

The age on these titanites (427.8 ± 13.4) is statistically robust with an MSWD of 0.83, which is close to a single statistical population. The p(χ^2) is 0.76 which is >> 0.05.

3.4 Sm-Nd and Lu-Hf Isotopes

Whole-rock Sm-Nd isotopes (Section 3.4.1) were analysed to give further insight on some key samples from which zircons could not be extracted. These units include the Honeysuckle Beds, Wyangle Formation, Long Tunnel Metabasic Igneous Complex and Wermatong Metabasalt.

Lu-Hf isotopic analyses of zircons (Section 3.4.2) previously dated by the U-Pb technique (Section 3.3) were carried out to track the isotopic evolution of the Tumut Trough. The Blowering Formation, Honeysuckle Beds, Bogong Granite, Killimicat Granite, Gocup Granite, Warrienbah granite and Kimo Diorite are all represented.

3.4.1 Sm-Nd

Sm-Nd isotopic analyses (data can be found in Appendix F) reveal that the Wermatong Metabasalt, Long Tunnel Metabasic Igneous Complex and one of the Wyangle Formation samples have moderately positive ϵNd values (5.5, 4.1 and 5.3 respectively), the other Wyangle Formation sample has a low positive ϵNd value (2.0) and the Honeysuckle Beds has a moderately negative ϵNd value (-7.3).

3.4.2 Lu-Hf

Lu-Hf isotopes (data can be found in Appendix G) show that the Honeysuckle Beds and Blowering Formation have moderate to low ϵHf values (between 0 and -10), the Gocup Granite has ϵHf values around 0, the Bogong and Killimicat Granites have low positive ϵHf values (mostly between 2 and 6), the Warrienbah granite has moderately positive ϵHf values (mostly between 2 and 10) and the Kimo Diorite has highly positive ϵHf values (between 8 and 14).

Chapter 4

Discussion

4.1 Tectonic Settings and Relationships Between Units

4.1.1 Mafic Unit Relationships

Wyangle Formation

Several samples of the Wyangle Formation were collected for this study as part of the syn-basin infill. However, two metabasaltic samples (TDBHons014.01 and TDBHons020.01) are geochemically quite different to the others (Fig. 4.1). Notably, the Nb and Ta depletion is not as great in TDBHons014.01 and TDBHon020.01 as in the others. The Nb/Yb and Ta/Yb ratios of the samples are also quite different, with TDBHons014.01 and TDBHons020.01 having a Nb/Yb of 7.19 and 5.68 respectively, compared to a Nb/Yb of 1.54 in TDBHons019.01 (the largest values of the three samples). TDBHons014.01 and TDBHons020.01 have comparable Nb/Yb to the Early Carboniferous continental calc-alkaline volcanics of the southern New England Orogen with values up to 6.22, which was found to have a crustal thickness similar to that recorded in the continental calc-alkaline volcanics in the Andes (Jenkins et al., 2002). TDBHons014.01 and TDBHons020.01 are metabasaltic rocks while the other three (TDBHons019.01, TDBHons019.02 and TDBHons019.03) are gabbros. These

geochemical differences suggest they are not the same sequence as they are quite geochemically and petrographically distinct.

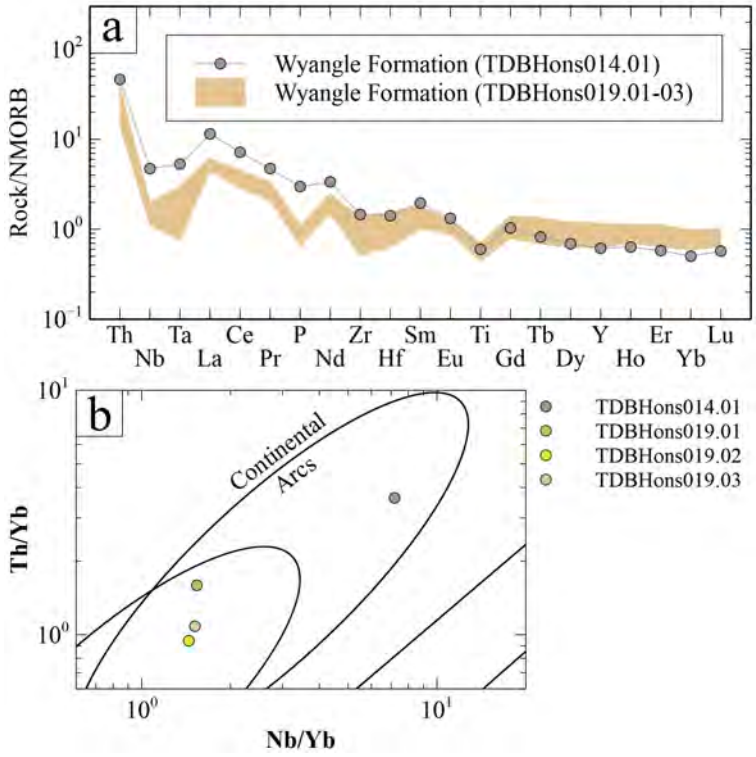

Figure 4.1: Geochemical comparison between samples from the Wyangle Formation on a) an N-MORB normalized spider diagram (after Sun and McDonough, 1989) and b) a Th/Yb v Nb/Yb (after Pearce, 2008, 2014).

North Mooney Complex and Honeysuckle Beds

The North Mooney Complex and Honeysuckle Beds has previously been thought to be related to the Coolac Serpentinite as part of an ophiolite suite (Ashley et al., 1979). This interpretation has been questioned by many authors (Stuart-Smith, 1990a; Dadd, 1998; Meffre and Glen, 2006; Bruce, 2018; Bruce et al., 2021) and has since fallen out of favour. However, the Honeysuckle Beds and North Mooney Complex appear to be related. They are stratigraphically related, with the North Mooney Complex intruding and overlying the Honeysuckle Beds (Basden, 1990; Stuart-Smith et al., 1992). The

426.8 ± 2.2 Ma age for the North Mooney Complex (Bodorkos et al., 2013) and 429.1 ± 1.7 Ma for the Honeysuckle Beds (this study) are close to within error of each other. Their geochemistry is also similar, although the Nb and Ta depletion is not as pronounced in the North Mooney Complex (Fig. 4.2). Therefore, having a similar age and geochemistry, it is possible that the North Mooney Complex and the Honeysuckle Beds are cogenetic.

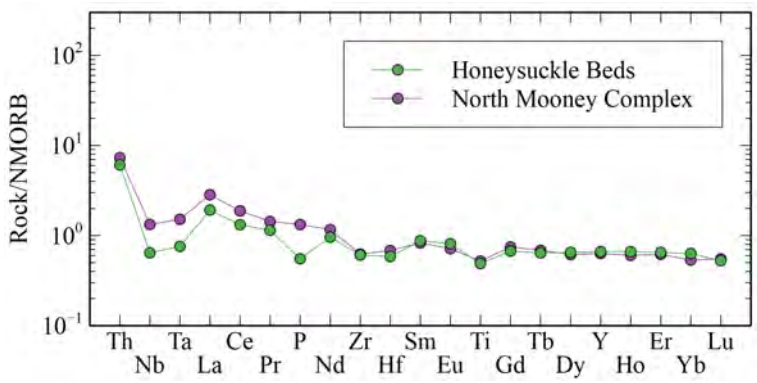

Figure 4.2: Geochemical comparison between the Honeysuckle Beds and the North Mooney Complex on an N-MORB normalized spider diagram (after Sun and McDonough, 1989).

Benwerrin Diorite and Kimo Diorite

The Benwerrin Diorite is similar to the Kimo Diorite in composition and setting according to both the N-MORB and Th/Yb v Nb/Yb plots (Fig. 4.3). The N-MORB plot has similar concentrations for most elements, apart from higher P and Ti concentrations, and Zr and Hf that are depleted in the Benwerrin Diorite. Both samples have Th/Yb and Nb/Yb ratios characteristic of continental arcs. They are both described in the literature as I-type units (Fraser et al., 2014; Stuart-Smith et al., 1992). Basden (1990) and Stuart-Smith et al. (1992) consider the Benwerrin Diorite as Late Silurian - Early Devonian, which is similar to the date obtained from the Kimo Diorite 417.4 ± 1.3 Ma, suggesting they may have intruded in the same

magmatic pulse. The Benwerrin Diorite is considered a satellite pluton associated with the Bogong Granite with a crenulated dyke contact suggesting the granite and diorite are coeval (W Collins 2020, pers. comm. 30 August).

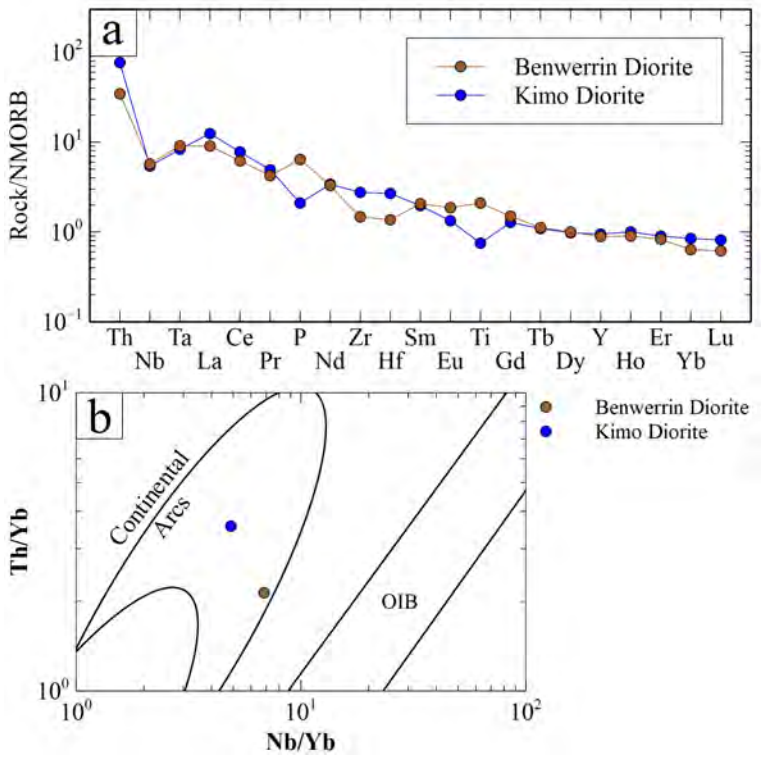

Figure 4.3: Geochemical comparison between the Kimo Diorite and the Benwerrin Diorite on a) an N-MORB normalized spider diagram (after Sun and McDonough, 1989) and b) a Th/Yb v Nb/Yb (after Pearce, 2008, 2014).

4.1.2 Pluton Relationships

The Gocup Granite has previously been identified as both an I-type (Basden, 1990) and S-type (Stuart-Smith et al., 1992), but this study shows it is an S-type based on mineralogy (muscovite replacing cordierite; B Landenberger, pers. comm. 2 March; see Appendix B), geochemistry (highly peraluminous, high normative corundum, low Zr and light REE) and isotopes (crustal influence). The total magnetic intensity map of the area also displays a magnetic low where the Gocup Granite is mapped

(Geological Survey of New South Wales, 2019), which is typical for S-type granites due to their lack of accessory magnetite (Whalen and Chappell, 1988).

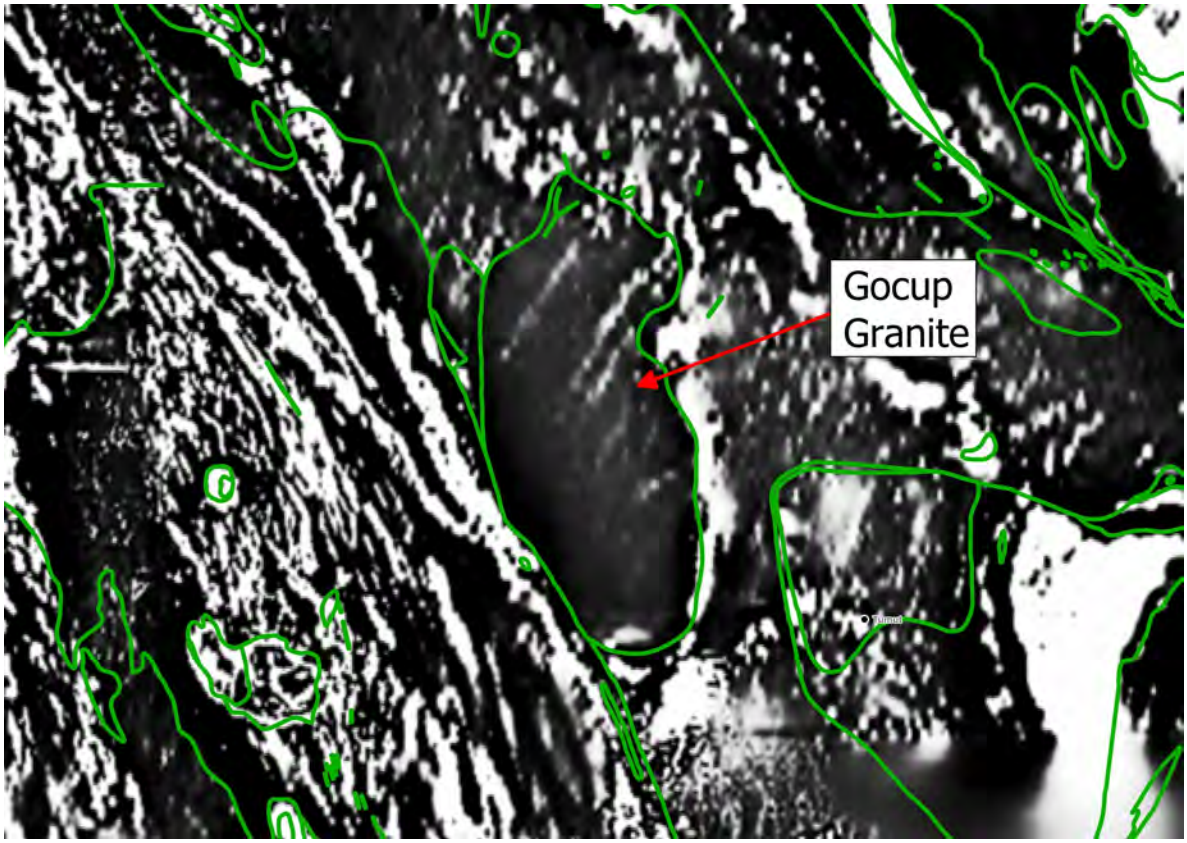

Figure 4.4: Total Magnetic Intensity (TMI) first vertical derivative of the Gocup Granite and surrounding units. Green lines are mapped unit boundaries. Modified from Geological Survey of New South Wales (2019) and Colquhoun et al. (2019).

The granites follow a succession from S-type magmatism to I-type magmatism to A-type magmatism which follows the typical succession an S to I to A-type progression (Downes et al., 2016; Collins et al., 2019). However, due to the rapid isotopic evolution of the granites, it may be a feature of the processes and architechure of the Tumut Trough rather than part of the widespread occurrences in the Lachlan Orogen (refer to Section 4.1.3).

4.1.3 Isotopic Evolution

The Wermatong Metabasalt records an ϵNd signature similar, albeit slightly less juvenile, to the basalts in the Macquarie Arc (Fig. 4.5). The Wermatong Metabasalt is very poorly constrained, only that it is older than the opening of the trough with no upper limit. The age is inferred here to be approximately 480 Ma, the same inferred age of the Bullawyarra Schist due to their shared deformation history. Interestingly, if it were to be given an age of 465 Ma, approximately the same age as the Brungle Creek Metabasalt (Bruce et al., 2021), it would form an isotopic trend with Phase 2 Macquarie Arc rocks. This may indicate the age of the Wermatong Metabasalt is younger than the inferred age of 480 Ma, but geochronological analysis of the Wermatong Metabasalt protolith is required to reliably correlated the ϵNd to the Macquarie Arc.

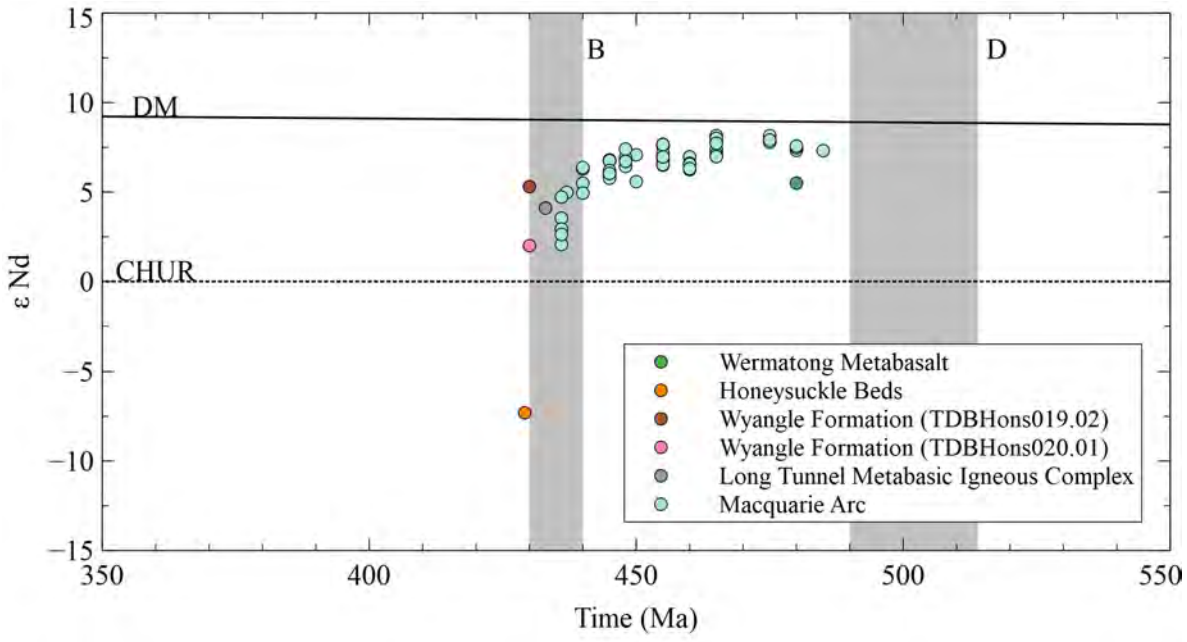

Figure 4.5: Sm-Nd isotope data from this study compared with those from the Macquarie Arc (Kemp et al., 2009). B - Benambran Orogeny, D - Delamerian Orogeny.

The differences in ϵNd values between Wyangle Formation samples may indicate that

the gabbro mapped as part of the Wyangle Formation is a young intrusive into the Wyangle Formation and not representative of the Wyangle Formation (also see Section 4.1.1). Geochronological analysis would need to be performed to confirm this interpretation.

The Long Tunnel Metabasic Igneous Complex records an ϵNd value similar to the Phase 4 Macquarie Arc (Fig. 4.5). It has similar geochemistry to the Wyangle Formation (Fig. 3.3). Both the Long Tunnel Metabasic Igneous Complex and Wyangle Formation have similar geochemistry to the Phase 4 Macquarie Arc North Parkes Intrusives, Wombin Volcanics and Goonumbla Volcanics (Hack et al., 2018). They may have been derived from a similar source to the Phase 4 Macquarie Arc. However, the Wyangle Formation is stratigraphically related to the Honeysuckle Beds as the Honeysuckle Beds intertongue (Basden, 1990) and overlie (Stuart-Smith et al., 1992) the Wyangle Formation. The Wyangle Formation is inferred to have an age of approximately 430 Ma and simply represent a mantle source with a minor crustal component.

The Sm-Nd and Lu-Hf data from samples of the Honeysuckle Beds are typically crustal (Figs. 4.5 and 4.6). Both Honeysuckle Beds samples (TDBHons017.01 and TDBHons018.01) are compositionally evolved (Fig. 3.1). As a follow up to this study, the mafic rocks in the Honeysuckle Beds could be analysed to better compare to other mafic rocks like those in the Long Tunnel Metabasic Igneous Complex and Wyangle Formation. The Honeysuckle Beds, along with the Blowering Formation, represents the crustal components of the Tumut Trough (Fig. 4.6). A potential source of these units may be the Adaminaby Group, which are Cambrian/Ordovician in age (Percival et al., 2011), based on the isotopes and age of the inherited grains in the Honeysuckle

Beds and Blowering Formation.

When compared to the typical isotopic evolution of the Lachlan Orogen (Fig. 4.6 a), the Tumut Trough shows a similar trend but in a much shorter period. The Lachlan Orogen isotopic signature is dominated by the mantle-like Macquarie Arc between 485 and 440 Ma, followed by S-type granites with low ϵHf values around 430 Ma (Kemp et al., 2009). I-type granites then form with ϵHf values of approximately -5 at 415 Ma which are followed by A-type granites with positive ϵHf values at around 390 and 375 Ma. Predictions from Collins (2002a,b) and subsequent evidence from Kemp et al. (2009) show that samples with a greater crustal contribution (towards negative ϵHf values) occur during early backarc closure, followed by the reworking of existing metasediments when subduction reinitiates (negative towards positive ϵHf values) and eventually returning to juvenile compositions (positive ϵHf values) as slab rollback occurs.

This is also seen in the granites of the Northern Lachlan Orogen and Southern Thomson Orogen (Fig. 4.6 b; Waltenberg et al., 2018) which is along strike of the Tumut Trough. The granites appear between 425 and 420 Ma with ϵHf values between -2 and 10, increasing in ϵHf as they become younger, with the youngest around 410 Ma.

These trends from crustal influenced magmatism to juvenile magmatism in the Tumut Trough and Northern Lachlan Orogen/Southern Thomson Orogen both occur between 430 and 410 Ma, a 20 million year time period. This is a much shorter period of time than the typical Lachlan Orogen trend that is reported to have taken twice as long (Kemp et al., 2009).

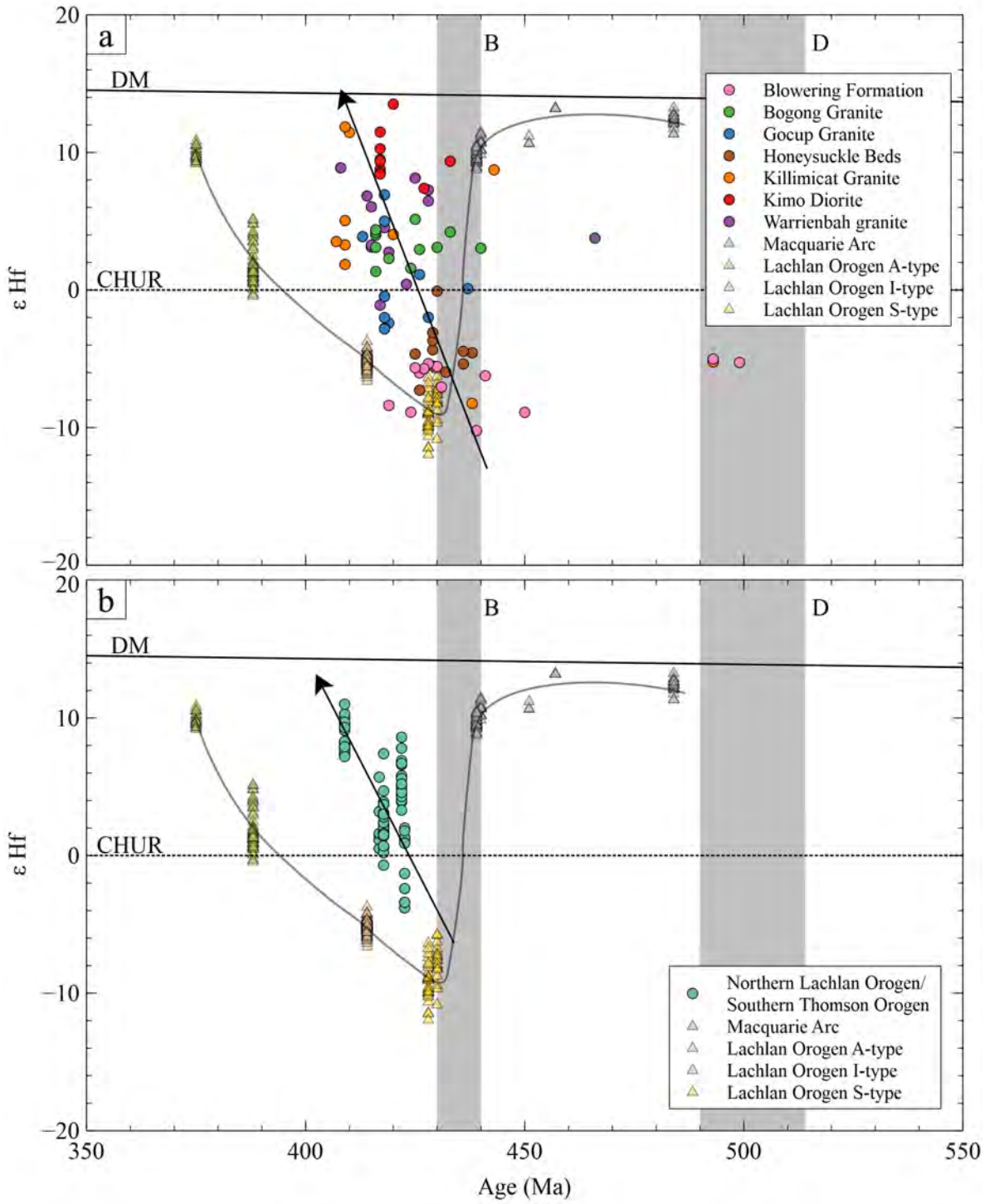

Figure 4.6: The isotopic evolution of the Macquarie Arc and Lachlan Orogen (Kemp et al., 2009) compared to a) this study and b) analyses from the Northern Lachlan Orogen/Southern Thomson Orogen (Waltenberg et al., 2018). Pathway for the Kemp et al. (2009) data is shown on both plots. Arrows indicate the trend of Tumut Trough data in a, and the Southern Thomson Orogen in b. B - Benambran Orogeny, D - Delamerian Orogeny.

The oldest A-type granite in the Tumut Trough is the Bogong Granite (416.8 ± 1.5 Ma) which is within error of the Kimo Diorite (417.4 ± 1.3 Ma) and not much younger than the Gocup Granite (418.5 ± 1.5 Ma). There are several possibilities, potentially in combination, for three types of granite appearing almost coevally, including the influence of the multiple sources, basement architecture, crustal thickness, relation to the rift axis or water flux melting (Jiang et al., 2011; Landenberger and Collins, 1996).

4.1.4 Tectonic Setting

Previous studies have considered the Tumut Trough to be a continental rift (Lightner, 1977), forearc basin (Crook, 1980), backarc basin (Ashley et al., 1979; Dadd, 1998) and transtensional pull apart basin (Powell, 1983; Stuart-Smith, 1990b). All of these are extensional environments. Therefore, it is generally agreed that the Tumut Trough is an extensional basin. The problem is where it sits in relation to the arc that was associated with a retreating, west dipping subduction zone (Glen, 2005; Rosenbaum, 2018).

Dadd (1998) suggested the magmatism that formed the Honeysuckle Beds occurred early in the backarc formation. When plotted on the Th/Yb v Nb/Yb diagram (Fig. 4.7), the majority of analyses of the magmatic rocks studied by Dadd (1998) plot in the overlap between oceanic and continental arc fields much like a majority of samples from this study (Fig. 3.4). Samples plotting away from the mantle array become more arc like, indicating they have been more strongly influenced by fluids migrating from the subducting slab. Dadd (1998) describes the magmatism that formed the Honeysuckle Beds as 'incipient'. This magmatism occurred early in the development

of the Tumut Trough, proximal to the arc, hence the significant subduction signature. Geochemical evidence from this study supports Dadd's suggestion of an incipient backarc setting for the Honeysuckle Beds; the wider Tumut Trough is also suggested to be an incipient backarc setting at this time.

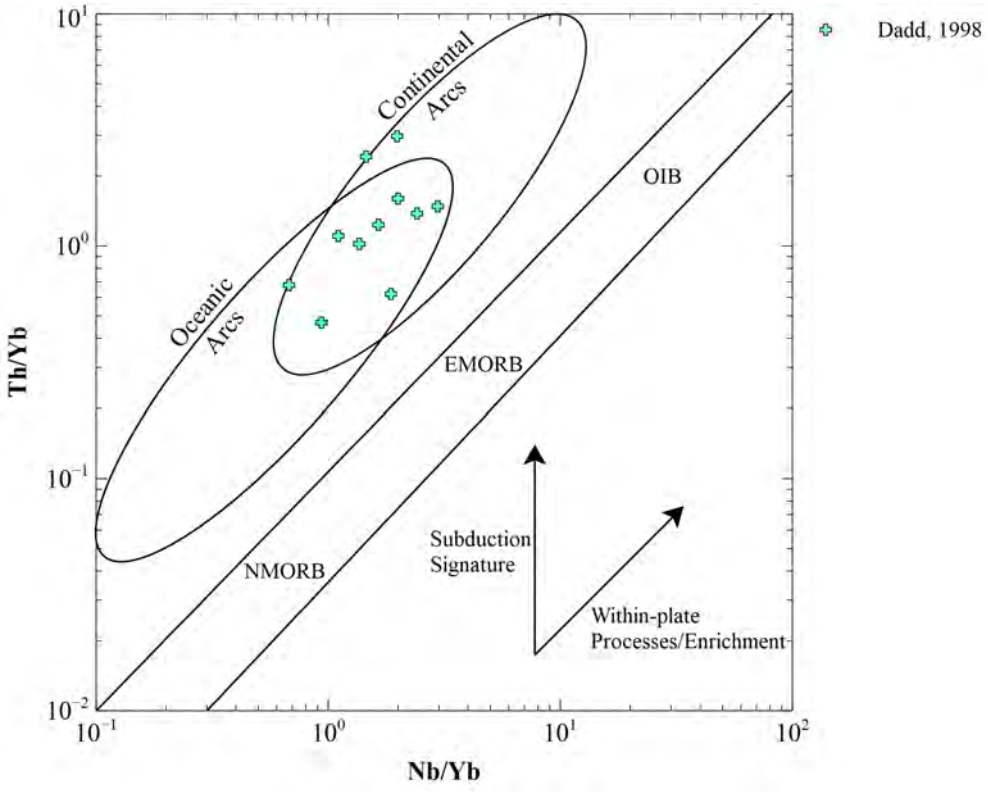

Figure 4.7: Th/Yb versus Nb/Yb (after Pearce, 2008, 2014) for the Honeysuckle Beds (Dadd, 1998) with the mantle array, oceanic arc and continental arc fields shown. Most analyses plot in the overlap between continental and oceanic arcs.

Most of the samples collected in this study were from the eastern side of the Tumut Trough. The sampling bias is due to many of the key mafic units outcropping on the eastern side of the trough, with no outcrop of any mafic units apart from the sampled Snowball and Long Tunnel Metabasic Igneous Complexes on the western side. Most of the analyses plot in areas with subduction influence (Fig. 3.4). The exception to this is the Wermatong Metabasalt (TDBHons008.01). The Wermatong Metabasalt is

thought to have been emplaced before the basin opening. It is multiply deformed like the Bullawyarra Schist, much more deformed than other rocks in the Tumut Trough indicating a shared deformation history. The Brungle Creek Metabasalt sample is a chert that has picked up traces of the arc volcanism, hence plotting with a subduction signature. It is also older than the basin opening, with Bruce et al. (2021) inferring an age between 465 - 468 Ma.

The Snowball Metabasic Igneous Complex sample (TDBHons013.01) is the only sample to plot exclusively in the oceanic arc field (Fig. 3.4), indicating that it is different to other units in the area. It also has flat N-MORB and chondrite spider diagrams (Ta/Yb = 1.28, La/Yb = 1.08, Figs. 3.3 and 3.2) unlike other samples. It may be part of bimodal volcanic sequence with the Frampton Volcanics as the Frampton Volcanics (428 $\pm$ 6 Ma) have a similar age to the Snowball Metabasic Igneous Complex titanite (427.8 $\pm$ 13.4 Ma), although the titanite age is a lower constrain as the titanites are metamorphic, and the Frampton Volcanics spatially lie along strike to the north and across strike to the east of the Snowball Metabasic Igneous Complex. Bimodal volcanics are typical rift related settings (Ishizuka et al., 2003; Yamasaki, 2018). The existing geochemistry available from the Frampton Volcanics is incomplete, which makes it difficult to conclude that it and the Snowball Metabasic Igneous Complex are related. If they are not related, it is plausible that the Snowball Metabasic Igneous Complex is structurally emplaced. Large boudins are found in the Snowball Metabasic Igneous Complex indicating high strain and deformation. The Snowball Metabasic Igneous Complex itself is contact metamorphosed, likely from granitic dykes that cut the foliation (W Collins 2020, pers. comm. 30 August).

A modern analogue to the Tumut Trough is the Okinawa Trough, an incipient backarc basin situated behind the Ryukyu arc south-west of Japan (Shinjo et al., 1999; Shinjo and Kato, 2000; Li et al., 2020). Samples from the Okinawa plot in the transition zone between oceanic and continental arcs, much like the Tumut Trough samples from this study (Fig. 4.8) and Dadd (1998). Some samples plot between the mantle array and arc fields indicating they are more distant from the arc and thus less affected by fluids fluxing from the subducting slab and therefore in a setting further from the arc.

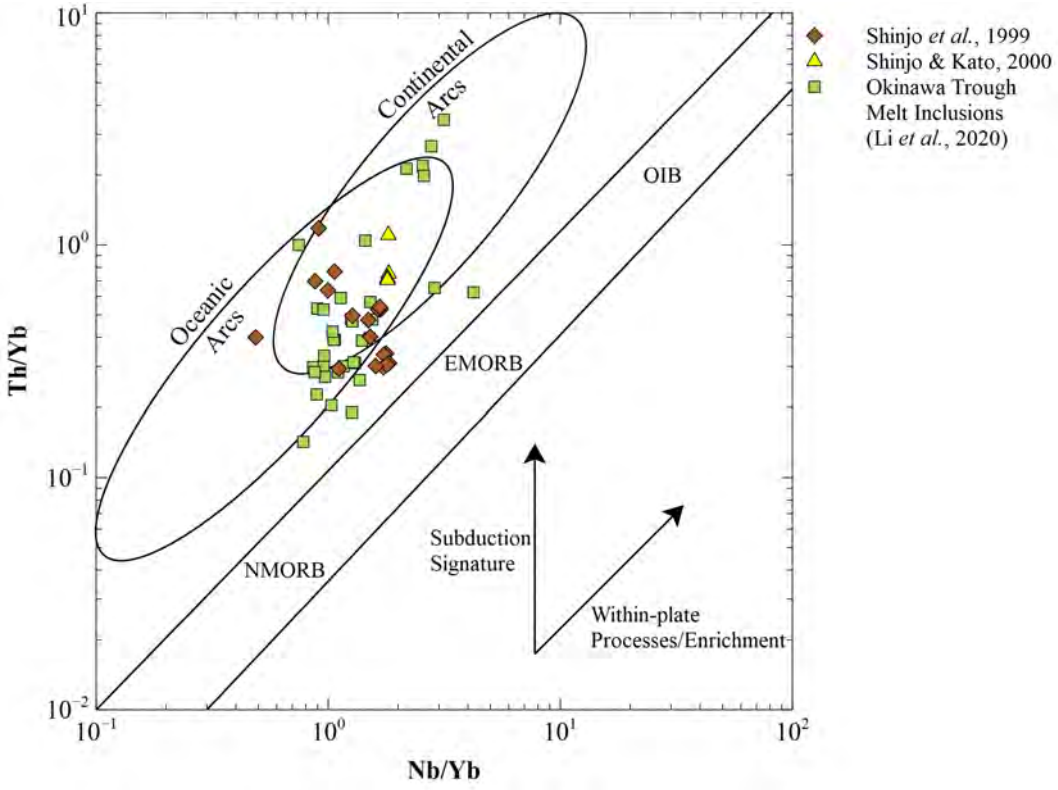

Figure 4.8: Th/Yb versus Nb/Yb (after Pearce, 2008, 2014) for the Okinawa Trough (Shinjo et al., 1999; Shinjo and Kato, 2000; Li et al., 2020) with the mantle array, oceanic arc and continental arc fields shown. Like Figure 3.4 and Figure 4.7, the majority of analyses plot in the overlap between ocanic and continental arcs.

The Okinawa Trough is a modern backarc basin that is still spreading (Shinjo and Kato, 2000) and the Honeysuckle Beds being incipient to the backarc (Dadd, 1998).

With the Okinawa Trough as an analogue and the suggestions from Dadd, there is a possibility that the wider Tumut Trough was also quite early in backarc basin formation, never fully extending to allow MORB-like magmas to be emplaced. Further sampling is required to confirm this.

The Tumut Trough also share similarities to the Gan-Hang rift in China. The Gan-Hang rift contains rift-related mafic rocks with variable chemistry including calc-alkaline trends with associated S and A-type magmatism occurring at roughly the same time (Jiang et al., 2011) like the Tumut Trough. The Tumut Trough can also be compared to the Warraweena Volcanics (Hack et al., 2018) in the Southern Thomson Orogen, along strike of the Tumut Trough, where there are also rift associated calc-alkaline rocks.

4.1.5 Potential Mineralisation

Pluton Mineralisation

Fractionation, oxidation state, degree of evolution and availability of fluids are all important factors in the mineralisation related to plutonic rocks (Blevin, 2004). Fractionation can be determined using compatible/incompatible element ratios (Plimer and Elliott, 1979), while degree of evolution can be determined using the K/Rb ratio (Blevin, 2004). Oxidation state can be found using the abundance of Fe^{2+} and Fe^{3+} in the pluton.

No mineralisation was directly observed in any of the plutonic rocks in hand specimen (see Appendix B). However, mineralisation may occur elsewhere in the pluton. Unfortunately, only Fe_2O_3 was analysed, with no FeO reported so the oxidation state

of the pluton (Blevin, 2004) cannot be used. Oxygen fugacity is related to the oxidation state of a pluton (Volovetskii et al., 2012) but could also not be determined as biotite grains were not individually analysed (Yavuz and Öztaş, 1997; Li et al., 2017). These parameters would have been useful in determining mineralisation potential, but this could be the basis for future study.

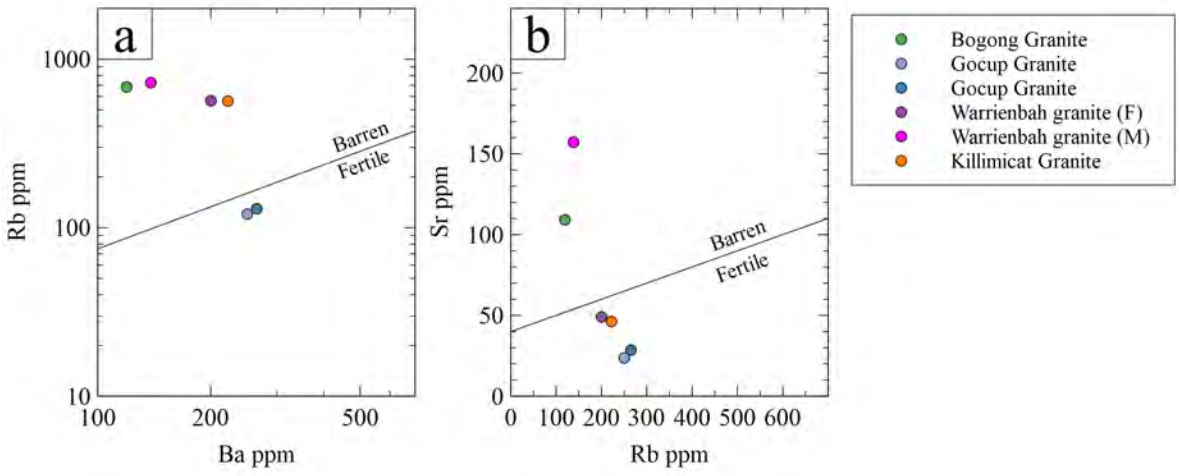

Figure 4.9: Pluton fertility diagrams using a) Rb and Ba, and b) Sr and Rb (after Ruiz et al., 2008).

In lieu of these indicators, Ruiz et al. (2008) uses Ba versus Rb and Sr versus Rb to distinguish between barren and fertile plutons. These plots were created for the granites in the Tumut Trough (Fig. 4.9 a, b). Figure 4.9 a shows the Gocup Granite is fertile while Figure 4.9 b shows the Killimicat Granite (which does contain an As-rich polymetallic deposit; Degeling, 1977) and Warrienbah granite also appear to be fertile. The Bogong Granite is barren in both plots. These trends are similar to the fractionation and degree of evolution trends (Fig. 3.10). By plotting as fertile and being the most fractionated and evolved pluton, the Gocup Granite has the greatest mineralisation potential. If mineralisation were to be found in the Gocup Granite, it would likely be Sn±W mineralisation (Blevin, 2004) due to being highly fractionated, provided there was enough Sn and W in the melt to begin with. This is not conclusive

unless mineralisation is observed (Blevin and Chappell, 1992, no mineralisation has yet been found in the Gocup Granite), but does give an indication of mineral potential.

Other Mineralisation

Although the Tumut Trough has a high potential for VAMS deposits (Fig. 1.6), no major VAMS deposits have been discovered (Downes, 2019). Only the Basin Creek No. 1 prospect, a minor VAMS deposit, is currently being explored (DevEx Resources, 2021a). It is being explored for gold and is associated with a felsic porphyry along the strike of the Tumut Trough. It lies within the Jackalass Slate on the western side of the exposed Tumut Trough.

Other mineralisation in the Tumut Trough appears to be mostly fault-bounded at contacts between serpentinites and other rock types with minor mineralisation within sheared and schistose rocks (refer to Section 1.1.5). These kinds of deposits typically occurred on the eastern side of the trough, with the exception of the Long Tunnel and Snowball Mines. Many of these deposits were mined before the 1940s, with some being further explored in the 1980s. If there was no further action after the exploration in the 1980s, the likelihood of discovering a large mineral deposit is small.

4.2 Refined Stratigraphy

The refined stratigraphy that has been produced using the results of this study are shown as a time-space plot (Fig. 4.10). There are still units whose age is unknown (see Table 1.1). These units have been constrained with field relationships where possible.

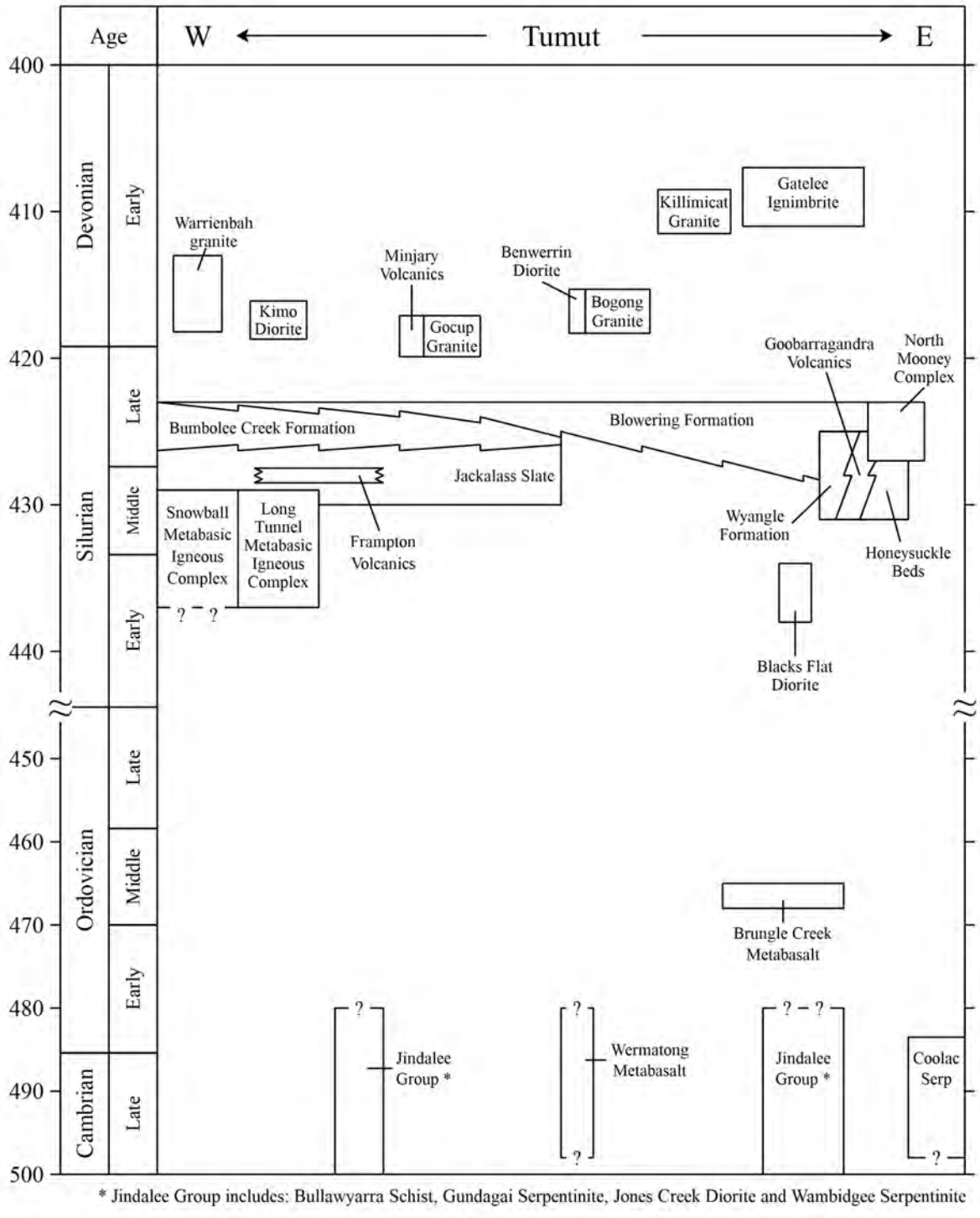

Figure 4.10: Time-space plot of the Tumut Trough with the westernmost units on the left and easternmost units on the right. ≈ indicates a change of scale.

The Jindalee Group is still considered to be the basement of the Tumut Trough (Fergusson, 2009). Around this time the Coolac Serpentinite would have been emplaced because, according to Bruce (2018), it cannot be younger than 483.5 ± 2.3 Ma. This is the age of a mantle-derived intrusion into the Coolac Serpentinite. There are currently no older ages to constrain its timing.

The Wermatong Metabasalt is a multiply deformed mafic schist (TDBHons008.01). No other rocks in this study showed the same level of deformation. However, the Bullawyarra Schist (part of the Jindalee Group) is described as a mafic schist (Basden, 1990; Stuart-Smith et al., 1992) which has been multiply deformed. Due to the similarity in deformation recorded in the Wermatong Metabasalt and the Bullawyarra Schist, and that no other rock units observed in the Tumut Trough have experienced the same deformation, the Wermatong Metabasalt has been interpreted to be approximately the same age as the Bullawyarra Schist at around 480 Ma. The upper and lower limits to its emplacement are unknown.

Bruce et al. (2021) suggested an age of 465 - 468 Ma based on the near-identical geochemistry between the chert in the Brungle Creek Metabasalt and chert blocks within the Jackalass Slate. The chert in the Jackalass Slate contains conodonts of Middle Ordovician age that Bruce et al. (2021) considers to be the age of the Brungle Creek Metabasalt. This implies the Brungle Creek Metabasalt formed approximately 30 million years before the opening of the Tumut Trough and is part of the basement to the trough.

The ages of 435.8 ± 2.1 Ma (Bodorkos et al., 2013) and 435.0 ± 6.4 Ma (Bell, 2019)

for the Blacks Flat Diorite is used for the time-space plot. These are U-Pb zircon ages and are both within error of each other, so they are considered to be reliable.

The Snowball Metabasic Igneous Complex and Long Tunnel Metabasic Igneous Complex lie on the western edge of the Tumut Trough (Fig. 1.3). Both of the complexes were subject to differing degrees of metamorphism. The Snowball Metabasic Igneous Complex was subject to amphibolite facies metamorphism, as it contains high-grade hornblende and plagioclase which is typical of amphibolite facies (see Appendix B). It is also contact metamorphosed from a granodiorite intrusion. The Long Tunnel Metabasic Igneous Complex was metamorphosed to greenschist facies (epidote and biotite altering to chlorite; see Appendix B). The granodiorite intrusion form veins within the Snowball Metabasic Igneous Complex which has a poorly defined boundary between itself and the surrounding rock. The secondary titanite in the Snowball Metabasic Igneous Complex would have formed during this event. However, it is not known how much older the emplacement of Snowball Metabasic Igneous Complex was. The Long Tunnel Metabasic Igneous Complex does not have a direct age, but is inferred to be Middle Silurian (Basden, 1990).

The titanite in the Snowball Metabasic Igneous Complex is metamorphic. The age of the titanite from the Snowball Metabasic Igneous Complex reflects the metamorphic event rather than emplacement, therefore giving a lower constraint. In thin section, the minerals do not have a preferred orientation and the surrounding country rock appears recrystallized. This is more likely to be a contact metamorphic event from the granitic dykes that cut foliation (W Collins 2020, pers. comm. 30 August) rather than a deformation event.

On the time-space plot, the Goobarragandra Volcanics, Wyangle Formation and Honeysuckle Beds are depicted as having similar ages. The U-Pb age obtained in this study for the Honeysuckle Beds is 429.1 ± 1.7 Ma. The Wyangle Formation is considered to be coeval with the Honeysuckle Beds by Basden (1990), while also stratigraphically underlying the Honeysuckle Beds. The age previously given for the Goobarragandra Volcanics (429 ± 16 Owen and Wyborn, 1979) which is the same as the Honeysuckle Beds. However, the boundary between the Goobarragandra Volcanics and Wyangle Formation is faulted (Basden, 1990), which may indicate a difference in age between them.

The ages for the North Mooney Complex (426.8 ± 2.2 Ma; Bodorkos et al., 2013) is used on the time-space plot. Refer to Section 4.1.1 for its relationship to the Honeysuckle Beds.

The Frampton Volcanics have isotopic ages of 428 ± 6 (Stuart-Smith et al., 1992) and 420.1 ± 1.7 Ma (Geoscience Australia, 2007). There is a large spacial difference between sampling locations, with the sample collected by Stuart-Smith et al. (1992) located closer to the study area than the one collected for Geoscience Australia. The sample for Geoscience Australia was collected at the northern extent of what is mapped as the Frampton Volcanics. The ages gathered from this location are close to the age of the Cowcumbala Rhyolite (415.9 ± 2.6 Ma; Geoscience Australia, 2007). For the purposes of the time-space plot, the age provided by Stuart-Smith et al. (1992) is used.

The Jackalass Slate has a maximum depositional age (MDA) of 430 ± 8 Ma (Bell, 2019). It stratigraphically occurs beneath the Bumbolee Creek Formation, which lies

beneath the Blowering Formation. Isotopic ages for the Blowering Formation of 432.1 ± 1.6 and 432.4 ± 4.3 Ma (Geoscience Australia, 2007; Ickert and Williams, 2011), are older (but within error of) the Jackalass Slate MDA. These ages come from samples located up to 30 km north of where the northernmost part of the Jackalass Slate is mapped.

The age obtained from this study (426.2 ± 1.3 Ma) for the Blowering Formation comes from a location within the study area. This age is slightly younger than Jackalass Slate MDA, and is adopted for the Blowering Formation within the Tumut Trough.

The Bumbolee Creek Formation MDA provided by Bell (2019) of 417.0 ± 2.3 Ma appears questionable. It is unlikely that the Blowering Formation was deposited over a prolonged period of 15 million years so that there can be ages around 430 Ma and it still overlying the Bumbolee Creek Formation. For this reason, the 417.0 ± 2.3 age was not used for the purposes of the time-space plot as it may not be representative of the Bumbolee Creek Formation, but may represent a younger, previously unknown unit. The Bumbolee Creek Formation was instead considered to lie between the Jackalass Slate and Blowering Formation in the Late Silurian.

The age for the Kimo Diorite obtained in this study is close to the age reported by Fraser et al. (2014), at 417.4 ± 1.3 Ma and 419.1 ± 2.7 Ma respectively. The Benwerrin Diorite is considered to be a mafic phase coeval with the Bogong Granite. The age on the Bogong Granite is 416.8 ± 1.5 Ma, which is close to the Kimo Diorite age. The Kimo Diorite and Benwerrin Diorite appear to have intruded in the same magmatic pulse (see Section 4.1.1).

The ages for the granites used in the time-space plot are all from this study (see Section 3.3.1). Previous ages on these granites were reported between the 1970s and 1990s and are mainly based on K-Ar and Rb-Sr determinations which are sensitive to changes in conditions. The Killimicat Granite and Warrienbah granite were previously inferred to be to be Early Devonian in age. This study puts discrete ages on the granites which are used in Fig. 4.10.

The Minjary Volcanics were considered to be coeval with the Gocup Granite. It was not investigated in this study, but Basden (1990) states that it has similar chemical and physical characteristics to the Gatelee Ignimbrite, that is dated at 409 $\pm$ 7.3 Ma (Bell, 2019), which is approximately 10 million younger than the Gocup Granite. With further study, the timing of the Minjary Volcanics may be moved from this position.

Chapter 5

Conclusion

The stratigraphy of the Tumut Trough has been refined based on U-Pb geochronology, whole-rock geochemistry, field relationships and isotopic evidence. Most notably, the model from (Dadd, 1998) was tested and provided evidence to support her suggestion that the Honeysuckle Beds were formed in an incipient backarc setting.

The Tumut Trough is interpreted to be a backarc basin that lies westward of the retreating, west dipping subduction zone. The data in this study resembles the Okinawa Trough, a modern backarc basin that sits behind the Ryukyu Arc near Japan.

All of the granites sampled were dated, with ages between 420 and 410 Ma, with the Blowering Formation and Honeysuckle Beds returning ages of 426.2 $\pm$ 1.3 and 429.1 $\pm$ 1.5 Ma respectively. Secondary titanite grains were recovered from the Snowball Metabasic Igneous Complex and returned a lower constraint of 427.8 $\pm$ 13.4 Ma. These discrete ages add to the literature, expanding the previously limited data. Not all units are dated, but further studies could be used to rectify this.

The granites of the Tumut Trough all seem to be tectonically related as can be seen in the isotope data. The magmatism that formed parts of the Blowering Formation and Honeysuckle Beds precede the granitic intrusions also appear tectonically related.

These units follow the same progression of the Lachlan Orogen but in a shorter period of time.

Other units were related where possible. It has been shown that the Honeysuckle Beds and North Mooney Complex may be cogenetic, and the Kimo Diorite and Benwerrin Diorite probably intruded in the same magmatic pulse.

Potential mineralisation is interpreted to be mainly fault bound with some possibility for VAMS deposits. VAMS deposits are likely as the Tumut Trough is an extensional setting, while the fault bound mineralisation is likely on the eastern side where faults are common.

5.1 Future Studies

There are a number of studies that could stem from this work that would help to further understand the Tumut Trough. A number of these would be to add to the still limited geochemistry and geochronological data, while others would be to determine more relationships between rock units as listed below.

Suggested studies are to:

- Compare the geochemistry and deformation of the Wermatong Metabasalt and Bullawyarra Schist to determine whether they could potentially be coeval. Also compare the Wermatong Metabasalt to the phase 2 Macquarie Arc rocks to see if there is a relationship between them like that seen isotopically.
- Attempt to determine an accurate emplacement age for the Snowball Metabasic Igneous Complex. Zircons can rarely be found in the Snowball Metabasic Igneous

Complex; 6 zircons were found in TDBHons002.05 (Drillhole DDH4 69.14 - 69.30 m).

- Analyse the Frampton Volcanics to determine if it forms bimodal sequence with the Snowball Metabasic Igneous Complex. Also date the Frampton Volcanics to confirm the age.

- Map and date the Jackalass Slate, Bumbolee Creek Formation and Blowering Formation throughout their extent. This should enable the accurate determination of their relationship to the rest of the Tumut Trough.

- Use oxygen fugacity and redox state of the granites to determine mineralisation potential.

- Date rock units like the Wyangle Formation, Benwerrin Diorite and Minjary Volcanics that currently have no associated absolute age.

- Date the Wyangle Formation to constrain its age.

- Analyse the isotopes (Sm-Nd or Lu-Hf if appropriate) of the mafic Honeysuckle Beds, Wyangle Formation, North Mooney Complex, Blacks Flat Diorite and Long Tunnel Metabasic Igneous Complex to track the evolution of the incipient backarc.

References

Akker, IV, Berger, A, Zwingmann, H, Todd, A, Schrank, CE, Jones, MW, Kewish, CM, Schmid, TC and Herwegh, M (2021), 'Structural and chemical resetting processes in white mica and their effect on K-Ar data during low temperature metamorphism', *Tectonophysics*, vol. 800, p. 228708, doi:10.1016/j.tecto.2020.228708

Ashley, PM, Brown, PF, Franklin, BJ, Ray, AS and Scheibner, E (1979), 'Field and geochemical characteristics of the Coolac Ophiolite suite and its possible origin in a marginal sea', *Journal of the Geological Society of Australia*, vol. 26, no. 1-2, pp. 45–60, doi:10.1080/00167617908729066

Basden, H (1986), 'Mineral Deposits in the Tumut 1:100,000 Sheet Area', Tech. Rep. GS1986/0106, Geological Survey of New South Wales, Sydney

Basden, H (1990), 'Geology of the Tumut 1:100,000 Sheet 8527', Tech. rep., Geological Survey of New South Wales, Sydney, 275 pp.

Bell, M (2019), 'The Geodynamic Significance of the Gilmore Fault Zone, Lachlan Orogen: Structural Characteristics, Kinematic History and Timing', Master's thesis, University of Newcastle

Belousova, E, Jiménez, J, Graham, I, Griffin, W, O'Reilly, S, Pearson, N, Martin, L, Craven, S and Talavera, C (2015), 'The enigma of crustal zircons in upper-mantle rocks: Clues from the Tumut ophiolite, Southeast Australia', *Geology*, vol. 43, no. 2, pp. 119–122, doi:10.1130/G36231.1

Berkman, DA and Nethery, J (1974), 'Drilling aid, Snowball Copper Mine', Tech. Rep. GS1974/061, Australian Oil & Gas Corporation Limited

Blevin, P and Chappell, B (1992), 'The role of magma sources, oxidation states and fractionation in determining the granite metallogeny of eastern australia', *Transactions of the Royal Society of Edinburgh: Earth Sciences*, vol. 83, doi: 10.1017/S0263593300007987

Blevin, PL (2004), 'Redox and Compositional Parameters for Interpreting the Granitoid Metallogeny of Eastern Australia: Implications for Gold-rich Ore Systems', *Resource Geology*, vol. 54, no. 3, pp. 241–252, doi:10.1111/j.1751-3928.2004.tb00205.x

Bodorkos, S, Blevin, PL, Simpson, CJ, Gilmore, PJ, Glen, RA, Greenfield, JE, Hegarty, R and Quinn, CD (2013), 'New SHRIMP U-Pb zircon ages from the Lachlan, Thomson and Delamerian orogens, New South Wales', Tech. Rep. GS2013/0427, Geological Survey of New South Wales, Maitland

Bouvier, A, Vervoort, JD and Patchett, PJ (2008), 'The Lu–Hf and Sm–Nd isotopic composition of CHUR: Constraints from unequilibrated chondrites and implications for the bulk composition of terrestrial planets', *Earth and Planetary Science Letters*, vol. 273, no. 1, pp. 48–57, doi:10.1016/j.epsl.2008.06.010

Bruce, MC (2018), 'Petrology, geochemistry and a probable late Cambrian age for harzburgites of the Coolac Serpentinite, New South Wales, Australia', *Australian Journal of Earth Sciences*, vol. 65, no. 3, pp. 335–355, doi:10.1080/08120099.2018.1433235

Bruce, MC, Percival, IG and Zhen, YY (2021), 'Unravelling the Tumut Trough: A Middle Ordovician age for the Brungle Creek Metabasalt, eastern Lachlan Orogen', in 'Australian Earth Sciences Convention',

Carne, JE (1908), 'The Copper-Mining Industry and the Distribution of Copper Ores in New South Wales', Tech. rep., Department of Mines Geological Survey, Sydney

Chu, NC, Taylor, RN, Chavagnac, V, Nesbitt, RW, Boella, RM, Milton, JA, German, CR, Bayon, G and Burton, K (2002), 'Hf isotope ratio analysis using multi-collector inductively coupled plasma mass spectrometry: an evaluation of isobaric interference corrections', *Journal of Analytical Atomic Spectrometry*, vol. 17, no. 12, pp. 1567–1574, doi:10.1039/B206707B

Collins, WJ (2002a), 'Hot orogens, tectonic switching, and creation of continental crust', *Geology*, vol. 30, pp. 535–538, doi:10.1130/0091-7613(2002)030⟨0535:HOTSAC⟩2.0.CO;2

Collins, WJ (2002b), 'Nature of extensional accretionary orogens', *Tectonics*, vol. 21, no. 4, pp. 6–1–6–12, doi:10.1029/2000TC001272

Collins, WJ, Huang, HQ, Bowden, P and Kemp, A (2019), 'Repeated S- I- A-type granite trilogy in the Lachlan Orogen, and geochemical contrasts with A-type granites in Nigeria: Implications for petrogenesis and tectonic discrimination', *Geological Society, London, Special Publications*, vol. 491, pp. SP491–2018, doi:10.1144/SP491-2018-159

Colquhoun, GP, Hughes, KS, Deyssing, L, Ballard, JC, G. Phillips, G, Troedson, AL, Folkes, CB and Fitzherbert, JA (2019), 'New South Wales Seamless Geology, version 1.1 [digital dataset]',
URL: *https://search.geoscience.nsw.gov.au/product/9232*

Corfu, F, Hanchar, JM, Hoskin, PW and Kinny, P (2003), 'Atlas of Zircon Textures', *Reviews in Mineralogy and Geochemistry*, vol. 53, no. 1, pp. 469–500, doi:10.2113/0530469

Crook, KAW (1980), 'Fore-arc evolution in the Tasman Geosyncline: The origin of the southeast Australian continental crust', *Journal of the Geological Society of Australia*, vol. 27, no. 1-2, pp. 215–232, doi:10.1080/00167618008729136

Dadd, K (1998), 'Incipient backarc magmatism in the Silurian Tumut Trough, New South Wales: An ancient analogue of the early Lau Basin', *Australian Journal of Earth Sciences*, vol. 45, pp. 109–121, doi:10.1080/08120099808728372

Dadd, K and Plioplis, A (2005), 'Facies Analysis, Geochemistry and Tectonic Setting of the Frampton Volcanics, southeastern New South Wales', in 'Specialist Group in Geochemistry, Mineralogy and Petrology', pp. 111–117

Degeling, PR (1977), 'Wagga Wagga 1:250 000 Metallogenic Map',
URL: *https://search.geoscience.nsw.gov.au/product/227*

DevEx Resources (2021a), 'Basin Creek Gold Project', Accessed on 03-02-2021
URL: *https://www.devexresources.com.au/basin-creek-project*

DevEx Resources (2021b), 'Bogong Project', Accessed on 03-02-2021
URL: *https://www.devexresources.com.au/bogong-project*

Donnellan, N, Camacho, A, Maas, R and Price, RC (2018), 'Mantle Upwelling or Plume Activity on the Periphery of the Warakurna LIP: Evidence from the Geochemistry and Petrogenesis of the Alcurra Dolerite in the Eastern Musgrave Province', *Journal of Petrology*, vol. 60, no. 2, pp. 301–327, doi:10.1093/petrology/egy113

Downes, P (2019), 'A mineral system model for volcanic-associated massive sulfide systems in the eastern Lachlan Orogen, New South Wales', Tech. Rep. GS2019/0560, Geological Survey of New South Wales

Downes, P, Blevin, P, Armstrong, R, Simpson, C, Sherwin, L, Tilley, D and Burton, G (2016), 'Outcomes of the Nymagee mineral system study — an improved understanding of the timing of events and prospectivity of the central Lachlan Orogen', *Quarterly Notes*, vol. 147

Downes, P, Pogson, D, Nix, L, Robson, D and Sherwin, L (2004), 'World-class mineral deposits of the Lachlan Orogen, New South Wales — Australia. ASEG2004 Excursion Guide', Tech. Rep. 2004/297, Geological Survey of New South Wales, doi:10.13140/RG.2.1.2892.9368

Fergusson, CL (2009), 'Tectonic evolution of the Ordovician Macquarie Arc, central New South Wales: arguments for subduction polarity and anticlockwise rotation', *Australian Journal of Earth Sciences*, vol. 56, no. 2, pp. 179–193, doi:10.1080/08120090802547017

Fisher, CM, Vervoort, JD and DuFrane, SA (2014), 'Accurate Hf isotope determinations of complex zircons using the "laser ablation split stream" method', *Geochemistry, Geophysics, Geosystems*, vol. 15, no. 1, pp. 121–139, doi:10.1002/2013GC004962

Ford, A, Peters, K, Downes, P, Blevin, P, Greenfield, J and Simpson, B (2019a), 'Mineral Potential Mapping As A Strategic Planning Tool In The Eastern Lachlan Orogen, NSW', in 'Discoveries in the Tasmanides', Wagga Wagga

Ford, A, Peters, K, Greenfield, J, Blevin, P, Downes, P, Fitzherbert, J and Simpson, B (2019b), 'Eastern Lachlan Orogen Mineral Potential Data Package',
URL: *https://search.geoscience.nsw.gov.au/product/9253*

Fraser, G, Gilmore, P, Fitzherbert, J, Trigg, S, Campbell, L, Deyssing, L, Thomas, O, Burton, G, Greenfield, J, Blevin, P and Simpson, C (2014), 'New SHRIMP U-Pb zircon ages from the Lachlan, southern Thomson and New England orogens, New South Wales', Tech. Rep. GS2014/0829, Geological Survey of New South Wales, Maitland

Funnell, FR (1990), 'PL 1089 - Long Tunnel Report on Activities for the two months to April 22nd, 1990', Tech. Rep. GS1989/157, CRA Exploration PTY Limited

Gain, SEM, Gréau, Y, Henry, H, Belousova, E, Dainis, I, Griffin, WL and O'Reilly, SY (2019), 'Mud Tank Zircon: Long-Term Evaluation of a Reference Material for U-Pb Dating, Hf-Isotope Analysis and Trace Element Analysis', *Geostandards and Geoanalytical Research*, vol. 43, no. 3, pp. 339–354, doi:10.1111/ggr.12265

Galley, AG, Hannington, MD and Jonasson, IR (2007), 'Volcanogenic Massive Sulphide Deposits', in Goodfellow, W (ed.), 'Mineral Deposits of Canada: A Synthesis of Major Deposit-Types, District Metallogeny, the Evolution of Geological Provinces, and Exploration Methods', 5, pp. 141–161, Geological Association of Canada, Mineral Deposits Division

Gemmell, J, Large, R and Zaw, K (1998), 'Palaeozoic volcanic-hosted massive sulphide deposits', *AGSO Journal of Australian Geology and Geophysics*, vol. 17, no. 4, pp. 129–137

Geological Survey of New South Wales (2019), 'MINVIEW',
URL: *https://minview.geoscience.nsw.gov.au/*

Geoscience Australia (2007), 'Geoscience Australia SHRIMP U-Pb geochronology interim data release July 2007',
URL: *http://pid.geoscience.gov.au/dataset/ga/65358*

Glen, RA (2005), 'The Tasmanides of eastern Australia', *Special Publication-Geological Society of London*, vol. 246, p. 23

Glen, RA and Walshe, JL (1999), 'Cross-structures in the Lachlan Orogen: The Lachlan Transverse Zone example', *Australian Journal of Earth Sciences*, vol. 46, no. 4, pp. 641–658, doi:10.1046/j.1440-0952.1999.00734.x

Glodny, J, Kühn, A and Austrheim, H (2008), 'Diffusion versus recrystallization processes in Rb–Sr geochronology: Isotopic relics in eclogite facies rocks, Western Gneiss Region, Norway', *Geochimica et Cosmochimica Acta*, vol. 72, no. 2, pp. 506–525, doi:10.1016/j.gca.2007.10.021

Gorton, M and Schandl, E (2000), 'From continents to island arcs: A geochemical index of tectonic setting for Arc-related and within-plate felsic to intermediate volcanic rocks', *Canadian Mineralogist - CAN MINERALOG*, vol. 38, pp. 1065–1073, doi:10.2113/gscanmin.38.5.1065

Graham, IT, Franklin, BJ, Marshall, B, Leitch, EC and Fanning, M (1996), 'Tectonic significance of 400 Ma zircon ages for ophiolitic rocks from the Lachlan Fold Belt, eastern Australia', *Geology*, vol. 24, no. 12, pp. 1111–1114, doi:10.1130/0091-7613(1996)024⟨1111:TSOMZA⟩2.3.CO;2

Gray, DR and Foster, DA (1997), 'Orogenic concepts; application and definition; Lachlan fold belt, eastern Australia', *American Journal of Science*, vol. 297, no. 9, pp. 859–891, doi:10.2475/ajs.297.9.859

Griffin, W, Pearson, N, Belousova, E and Saeed, A (2006), 'Comment: Hf-isotope heterogeneity in zircon 91500', *Chemical Geology*, vol. 233, no. 3, pp. 358–363, doi:10.1016/j.chemgeo.2006.03.007

Hack, AC, Dwyer, RC, Phillips, G, Whalan, S and Huang, HQ (2018), 'The age and tectonic significance of the Warraweena Volcanics and related rocks, southern Thomson Orogen', *Australian Journal of Earth Sciences*, vol. 65, no. 7-8, pp. 1071–1096, doi:10.1080/08120099.2018.1520147

Hollocher, K and Ruiz, J (1995), 'Major and trace element determinations on NIST glass standard reference materials 611, 612, 614 and 1834 by inductively coupled plasma-mass spectrometry', *Geostandards Newsletter*, vol. 19, pp. 27 – 34, doi:10.1111/j.1751-908X.1995.tb00149.x

Hoskin, PW (2005), 'Trace-element composition of hydrothermal zircon and the alteration of Hadean zircon from the Jack Hills, Australia', *Geochimica et Cosmochimica Acta*, vol. 69, no. 3, pp. 637–648, doi:10.1016/j.gca.2004.07.006

Hough, M, Bierlein, F and Wilde, A (2007), 'A review of the metallogeny and tectonics of the Lachlan Orogen', *Mineralium Deposita: International Journal of Geology, Mineralogy, and Geochemistry of Mineral Deposits*, vol. 42, no. 5, pp. 435–448, doi:10.1007/s00126-006-0073-7

Ickert, RB and Williams, IS (2011), 'U–Pb zircon geochronology of Silurian–Devonian granites in southeastern Australia: implications for the timing of the Benambran Orogeny and the I–S dichotomy', *Australian Journal of Earth Sciences*, vol. 58, no. 5, pp. 501–516, doi:10.1080/08120099.2011.562922

Ishizuka, O, Uto, K and Yuasa, M (2003), 'Volcanic history of the back-arc region of the Izu–Bonin (Ogasawara) arc', in 'Intra-Oceanic Subduction Systems: Tectonic and Magmatic Processes', Geological Society of London, doi:10.1144/GSL.SP.2003.219.01.09

Jackson, SE, Pearson, NJ, Griffin, WL and Belousova, EA (2004), 'The application of laser ablation-inductively coupled plasma-mass spectrometry to in situ U–Pb zircon geochronology', *Chemical Geology*, vol. 211, no. 1, pp. 47–69, doi:10.1016/j.chemgeo.2004.06.017

Jenkins, RB, Landenberger, B and Collins, WJ (2002), 'Late Palaeozoic retreating and advancing subduction boundary in the New England Fold Belt, New South Wales', *Australian Journal of Earth Sciences*, vol. 49, no. 3, pp. 467–489, doi:10.1046/j.1440-0952.2002.00932.x

Jiang, YH, Zhao, P, Zhou, Q, Liao, SY and Jin, GD (2011), 'Petrogenesis and tectonic implications of Early Cretaceous S- and A-type granites in the northwest of the Gan-Hang rift, SE China', *Lithos*, vol. 121, no. 1, pp. 55–73, doi:10.1016/j.lithos.2010.10.001

Jochum, KP, Nohl, U, Herwig, K, Lammel, E, Stoll, B and Hofmann, AW (2005), 'Georem: A new geochemical database for reference materials and isotopic standards', *Geostandards and Geoanalytical Research*, vol. 29, no. 3, pp. 333–338, doi:10.1111/j.1751-908X.2005.tb00904.x

Kemp, A, Hawkesworth, C, Collins, W, Gray, C and Blevin, P (2009), 'Isotopic evidence for rapid continental growth in an extensional accretionary orogen: The Tasmanides, eastern Australia', *Earth and Planetary Science Letters*, vol. 284, no. 3, pp. 455–466, doi:10.1016/j.epsl.2009.05.011

Kohn, MJ (2017), 'Titanite Petrochronology', *Reviews in Mineralogy and Geochemistry*, vol. 83, no. 1, pp. 419–441, doi:10.2138/rmg.2017.83.13

Landenberger, B and Collins, W (1996), 'Derivation of A-type Granites from a Dehydrated Charnockitic Lower Crust: Evidence from the Chaelundi Complex, Eastern Australia', *Journal of Petrology*, vol. 37, pp. 145–170, doi:10.1093/petrology/37.1.145

Li, X, Chi, G, Zhou, Y, Deng, T and Zhang, J (2017), 'Oxygen fugacity of Yanshanian granites in South China and implications for metallogeny', *Ore Geology Reviews*, vol. 88, pp. 690–701, doi:10.1016/j.oregeorev.2017.02.002

Li, X, Ren, Z, Zeng, Z, Yang, H, Zhang, L, Wang, X, Fang, B and Guo, K (2020), 'Petrogenesis of middle Okinawa Trough volcanic rocks: Constraints from lead isotopes in olivine-hosted melt inclusions', *Chemical Geology*, vol. 543, p. 119600, doi:10.1016/j.chemgeo.2020.119600

Lightner, J (1977), 'The stratigraphy, structure and depositional history of the Tumut region, NSW', Master's thesis, Australian National University

Long, X, Sun, M, Yuan, C, Kröner, A and Hu, A (2012), 'Zircon REE patterns and geochemical characteristics of Paleoproterozoic anatectic granite in the northern Tarim Craton, NW China: Implications for the reconstruction of the Columbia supercontinent', *Precambrian Research*, vol. 222-223, pp. 474–487, doi:10.1016/j.precamres.2011.09.009

Maas, R, Apukhtina, OB, Kamenetsky, VS, Ehrig, K, Sprung, P and Münker, C (2020), 'Carbonates at the supergiant Olympic Dam Cu-U-Au-Ag deposit, South Australia part 2: Sm-Nd, Lu-Hf and Sr-Pb isotope constraints on the chronology of carbonate deposition', *Ore Geology Reviews*, p. 103745, doi:10.1016/j.oregeorev.2020.103745

McDonough, W and Sun, SS (1995), 'The composition of the Earth', *Chem. Geol.*, vol. 67, pp. 1050–1056

Meffre, S and Glen, RA (2006), 'Low-Ti Silurian-Early Devonian continental rift tholeiites and plagiogranites in the Tumut area, NSW', *ASEG Extended Abstracts*, vol. 2006, no. 1, pp. 1–3, doi:10.1071/ASEG2006ab112

Morel, M, Nebel, O, Nebel-Jacobsen, Y, Miller, J and Vroon, P (2008), 'Hafnium isotope characterization of the GJ-1 zircon reference material by solution and laser-ablation MC-ICPMS', *Chemical Geology*, vol. 255, no. 1, pp. 231–235, doi:10.1016/j.chemgeo.2008.06.040

Nethery, J and Ramsden, A (1976), 'Geology and mineralisation in the southern Lachlan Fold Belt: Copper mineralisation at The Basin Creek No. 1 prospect, Tumut, New South Wales', *Bulletin of the Australian Society of Exploration Geophysicists*, vol. 7, no. 1, pp. 39–40

Nethery, JE (1975), 'Final report on exploration in the five year period to August 14', Tech. Rep. GS1975/123, A.O.G Minerals Pty. Limited

Owen, M and Wyborn, D (1979), 'Geology and geochemistry of the Tantangara and Brindabella 1:100 000 Sheet areas, New South Wales and Australian Capital Territory', Tech. Rep. Bulletin 204, Bureau of Mineral Resources, Canberra

Patchett, PJ and Tatsumoto, M (1981), 'A routine high-precision method for Lu-Hf isotope geochemistry and chronology', *Contributions to Mineralogy and Petrology*, vol. 75, no. 3, pp. 263–267

Paton, C, Hellstrom, J, Paul, B, Woodhead, J and Hergt, J (2011), 'Iolite: Freeware for the visualisation and processing of mass spectrometric data', *Journal of Analytical Atomic Spectrometry*, vol. 26, pp. 2508–2518, doi:10.1039/C1JA10172B

Pearce, J (2014), 'Immobile Element Fingerprinting of Ophiolites', *Elements*, vol. 10, pp. 101–108, doi:10.2113/gselements.10.2.101

Pearce, JA (2008), 'Geochemical fingerprinting of oceanic basalts with applications to ophiolite classification and the search for Archean oceanic crust', *Lithos*, vol. 100, no. 1, pp. 14–48, doi:10.1016/j.lithos.2007.06.016

Percival, I, Quinn, C and Glen, R (2011), 'A review of Cambrian and Ordovician stratigraphy in New South Wales', *Quarterly Notes*, vol. 137

Petrus, JA and Kamber, BS (2012), 'VizualAge: A Novel Approach to Laser Ablation ICP-MS U-Pb Geochronology Data Reduction', *Geostandards and Geoanalytical Research*, vol. 36, no. 3, pp. 247–270, doi:10.1111/j.1751-908X.2012.00158.x

Pin, C, Gannoun, A and Dupont, A (2014), 'Rapid, simultaneous separation of Sr, Pb, and Nd by extraction chromatography prior to isotope ratios determination by TIMS and MC-ICP-MS', *Journal of Analytical Atomic Spectrometry*, vol. 29, pp. 1858–1870, doi:10.1039/C4JA00169A

Plimer, I and Elliott, S (1979), 'The use of Rb/Sr ratios as a guide to mineralization', *Journal of Geochemical Exploration*, vol. 12, pp. 21–34, doi:10.1016/0375-6742(79)90060-8

Powell, CM (1983), 'Tectonic Relationship between the Late Ordovician and Late Silurian palaeogeographies of southeastern Australia', *Journal of the Geological Society of Australia*, vol. 30, no. 3-4, pp. 353–373, doi:10.1080/00167618308729262

Pupin, JP (1980), 'Zircon and granite petrology', *Contributions to Mineralogy and Petrology*, vol. 73, no. 3, pp. 207–220, doi:10.1007/BF00381441

Raczek, I, Jochum, KP and Hofmann, AW (2003), 'Neodymium and Strontium Isotope Data for USGS Reference Materials BCR-1, BCR-2, BHVO-1, BHVO-2, AGV-1, AGV-2, GSP-1, GSP-2 and Eight MPI-DING Reference Glasses', *Geostandards Newsletter*, vol. 27, no. 2, pp. 173–179, doi:10.1111/j.1751-908X.2003.tb00644.x

Raczek, I, Stoll, B, Hofmann, AW and Peter Jochum, K (2001), 'High-Precision Trace Element Data for the USGS Reference Materials BCR-1, BCR-2, BHVO-1, BHVO-2, AGV-1, AGV-2, DTS-1, DTS-2, GSP-1 and GSP-2 by ID-TIMS and MIC-SSMS', *Geostandards Newsletter*, vol. 25, no. 1, pp. 77–86, doi:10.1111/j.1751-908X.2001.tb00789.x

Raymond, OL, Totterdell, JM, Woods, MA and Stewart, AJ (2018), 'Australian Geological Provinces 2018.01 edition',
URL: *http://pid.geoscience.gov.au/dataset/ga/116823*

Richards, JR, Barkas, JP and Vallance, TG (1977), 'A lower Devonian point in the geological timescale', *Geochemical Journal*, vol. 11, no. 3, pp. 147–153, doi:10.2343/geochemj.11.147

Robinson, LJ (1995), 'Gundagai Gold Pty. Ltd. annual report on Exploration Licence 4142', Tech. Rep. GS1996/130, Gundagai Gold Pty. Ltd.

Rosenbaum, G (2018), 'The Tasmanides: Phanerozoic tectonic evolution of eastern Australia', *Annual Review of Earth and Planetary Sciences*, vol. 46, no. 1, pp. 291–325, doi:10.1146/annurev-earth-082517-010146

Ruiz, C, Fernández-Leyva, C and Locutura, J (2008), 'Geochemistry, geochronology and mineralisation potential of the granites in the Central Iberian Zone: The Jalama batholith', *Geochemistry*, vol. 68, no. 4, pp. 413–429, doi:10.1016/j.chemer.2006.11.001

Schaltegger, U and Davies, JH (2017), 'Petrochronology of Zircon and Baddeleyite in Igneous Rocks: Reconstructing Magmatic Processes at High Temporal Resolution', *Reviews in Mineralogy and Geochemistry*, vol. 83, no. 1, pp. 297–328, doi:10.2138/rmg.2017.83.10

Schmidt, BL, Pontifex, IR and Davis, LW (1975), 'Final report, completion of drill phase, EL 104', Tech. Rep. GS1971/730, Electrolytic Zinc Company of Australasia Limited

Schoene, B (2014), 'U–Th–Pb Geochronology', in Holland, HD and Turekian, KK (eds.), 'Treatise on Geochemistry', 2nd edn., pp. 341 – 378, Elsevier, Oxford, doi:10.1016/B978-0-08-095975-7.00310-7

Shand, S (1943), *Eruptive Rocks. Their Genesis, Composition, Classification, and Their Relation to Ore-Deposits with a Chapter on Meteorite*, John Wiley & Sons, New York

Shinjo, R, Chung, SL, Kato, Y and Kimura, M (1999), 'Geochemical and Sr-Nd isotopic characteristics of volcanic rocks from the Okinawa Trough and Ryukyu Arc: Implications for the evolution of a young, intracontinental back arc basin', *Journal of Geophysical Research*, vol. 1041, pp. 10591–10608, doi:10.1029/1999JB900040

Shinjo, R and Kato, Y (2000), 'Geochemical constraints on the origin of bimodal magmatism at the Okinawa Trough, an incipient back-arc basin', *Lithos*, vol. 54, pp. 117–137, doi:10.1016/S0024-4937(00)00034-7

Sinha, S (1983), *Systematics and the Properties of the Lanthanides*, D. Reidel Publishing Company, Dordrecht

Sláma, J, Košler, J, Condon, DJ, Crowley, JL, Gerdes, A, Hanchar, JM, Horstwood, MS, Morris, GA, Nasdala, L, Norberg, N, Schaltegger, U, Schoene, B, Tubrett, MN and Whitehouse, MJ (2008), 'Plešovice zircon — A new natural reference material for U–Pb and Hf isotopic microanalysis', *Chemical Geology*, vol. 249, no. 1, pp. 1–35, doi:10.1016/j.chemgeo.2007.11.005

Stuart-Smith, P (1990a), 'The emplacement and fault history of the Coolac Serpentinite, Lachlan Fold Belt, southeastern Australia', *Journal of Structural Geology*, vol. 12, no. 5, pp. 621–638, doi:10.1016/0191-8141(90)90078-D

Stuart-Smith, PG (1990b), 'Evidence for extensional tectonics in the Tumut Trough, Lachlan Fold Belt, NSW', *Australian Journal of Earth Sciences*, vol. 37, no. 2, pp. 147–167, doi:10.1080/08120099008727917

Stuart-Smith, PG, Hill, RI, Rickard, MJ and Etheridge, MA (1992), 'The stratigraphy and deformation history of the Tumut region: Implications for the development of the Lachlan Fold Belt', *Tectonophysics*, vol. 214, no. 1, pp. 211 – 237, doi:10.1016/0040-1951(92)90198-F

Sun, Ss and McDonough, WF (1989), 'Chemical and isotopic systematics of oceanic basalts: implications for mantle composition and processes', *Geological Society, London, Special Publications*, vol. 42, no. 1, pp. 313–345, doi:10.1144/GSL.SP.1989.042.01.19

Vance, D and Thirlwall, M (2002), 'An assessment of mass discrimination in MC-ICPMS using Nd isotopes', *Chemical Geology*, vol. 185, no. 3, pp. 227–240, doi:10.1016/S0009-2541(01)00402-8

Vermeesch, P (2018), 'IsoplotR: A free and open toolbox for geochronology', *Geoscience Frontiers*, vol. 9, no. 5, pp. 1479 – 1493, doi:10.1016/j.gsf.2018.04.001

Villaros, A, Stevens, G, Moyen, J and Buick, I (2009), 'The trace element compositions of S-type granites: evidence for disequilibrium melting and accessory phase entrainment in the source', *Contributions to Mineralogy and Petrology*, vol. 158, pp. 543–561

Volovetskii, MV, Lukanin, OA, Rusakov, VS and Kargal'tsev, AA (2012), 'Influence of oxygen fugacity and temperature on the redox state of iron in natural silicic aluminosilicate melts', *Geochemistry International*, vol. 50, pp. 330–343

Walker, S, Thirlwall, MF, Strachan, RA and Bird, AF (2016), 'Evidence from Rb–Sr mineral ages for multiple orogenic events in the Caledonides of Shetland, Scotland', *Journal of the Geological Society*, vol. 173, no. 3, pp. 489–503, doi:10.1144/jgs2015-034

Waltenberg, K, Bodorkos, S, Armstrong, R and Fu, B (2018), 'Mid- to lower-crustal architecture of the northern Lachlan and southern Thomson orogens: evidence from O–Hf isotopes', *Australian Journal of Earth Sciences*, vol. 65, no. 7-8, pp. 1009–1034, doi:10.1080/08120099.2018.1463928

Webb, AW (1980), 'K-Ar analyses (Tumut area)', Tech. Rep. GS1980/444, The Australian Mineral Development Laboratories, Frewville

Whalen, J and Chappell, B (1988), 'Opaque mineralogy and mafic mineral chemistry of I- and S-type granites of the Lachlan Fold Belt, southeast Australia', *American Mineralogist*, vol. 73, pp. 281–296

Whalen, J, Currie, K and Chappell, B (1987), 'A-type granites: geochemical characteristics, discrimination and petrogenesis', *Contributions to Mineralogy and Petrology*, vol. 95, pp. 407–419, doi:10.1007/BF00402202

Winchester, J and Floyd, P (1977), 'Geochemical discrimination of different magma series and their differentiation products using immobile elements', *Chemical Geology*, vol. 20, pp. 325–343, doi:10.1016/0009-2541(77)90057-2

Woodhead, J, Hergt, J, Shelley, M, Eggins, S and Kemp, R (2004), 'Zircon Hf-isotope analysis with an excimer laser, depth profiling, ablation of complex geometries, and concomitant age estimation', *Chemical Geology*, vol. 209, no. 1, pp. 121–135, doi: j.chemgeo.2004.04.026

Xia, L and Li, X (2019), 'Basalt geochemistry as a diagnostic indicator of tectonic setting', *Gondwana Research*, vol. 65, pp. 43–67, doi:10.1016/j.gr.2018.08.006

Yamasaki, T (2018), 'Mechanisms of bimodal volcanism and related hydrothermal mineralization in the middle Okinawa Trough, Japan', in 'AGU Fall Meeting Abstracts', vol. 2018

Yavuz, F and Öztaş, T (1997), 'BIOTERM—A program for evaluating and plotting microprobe analyses of biotite from barren and mineralized magmatic suites', *Computers and Geosciences*, vol. 23, no. 8, pp. 897–907, doi:10.1016/S0098-3004(97)00071-X

Zappettini, EO, Rubinstein, N, Crosta, S and Segal, SJ (2017), 'Intracontinental rift-related deposits: A review of key models', *Ore Geology Reviews*, vol. 89, pp. 594–608, doi:10.1016/j.oregeorev.2017.06.019

Appendix A - Samples

Samples gathered for this thesis appear in this appendix, with their sample numbers, location and what the sample was used for.

All coordinates are in GDA 94.

Table A1: A complete list of samples gathered for this thesis with their uses.

Sample Number	Rock Unit	Rock Type	Location	Uses
TDBHons001.01	Brungle Creek Metabasalt	Chert	-35.0877 148.7881	Petrography
TDBHons001.02	Brungle Creek Metabasalt	Crystal Tuff	-35.0877 148.7881	Petrography
TDBHons001.03	Brungle Creek Metabasalt	Brecciated Basalt	-35.0877 148.1881	Petrography
TDBHons001.04	Brungle Creek Metabasalt	Brecciated Basalt	-35.0877 148.1881	Petrography
TDBHons001.05	Brungle Creek Metabasalt	Brecciated Basalt	-35.0877 148.1881	Petrography
TDBHons001.06	Brungle Creek Metabasalt	Brecciated Basalt	-35.0877 148.1881	Petrography
TDBHons001.07	Brungle Creek Metabasalt	Brecciated Basalt	-35.0877 148.1881	Petrography
TDBHons002.01	Snowball Metabsaic Igneous Complex	Hornblende Diorite	-34.7662 148.2058	Petrography
TDBHons002.02	Snowball Metabsaic Igneous Complex	Agglomerate	-34.7662 148.2058	Petrography
TDBHons002.03	Snowball Metabsaic Igneous Complex	Hornblende Diorite	-34.7662 148.2058	Petrography
TDBHons002.04	Snowball Metabsaic Igneous Complex	Chloritic Rock	-34.7662 148.2058	Petrography
TDBHons002.05	Snowball Metabsaic Igneous Complex	Andesite	-34.7662 148.2058	Petrography
TDBHons003.01	Kimo Diorite	Diorite	-35.0347 148.0139	Petrography Geochemistry Geochronology Lu/Hf + REE

Sample Number	Rock Unit	Rock Type	Location	Uses
TDBHons003.02	Kimo Diorite	Diorite → Shear Contact	-35.0347 148.0139	Petrography
TDBHons003.03	Long Tunnel Metabsaic Igneous Complex	Basalt → Shear Contact	-35.0347 148.0139	Petrography
TDBHons003.04	Long Tunnel Metabsaic Igneous Complex	Basalt	-35.0347 148.0139	Petrography
TDBHons003.05	Long Tunnel Metabsaic Igneous Complex	Serpentinite	-35.0347 148.0139	Petrography
TDBHons003.06	Long Tunnel Metabsaic Igneous Complex	Talc-altered Serpentinite	-35.0347 148.0139	Petrography
TDBHons004.01	Honeysuckle Beds	Lithic Tuff	-34.7662 148.2058	Petrography
TDBHons004.02	Honeysuckle Beds	Schist	-34.7662 148.2058	Petrography
TDBHons004.03	Honeysuckle Beds	Dacite	-34.7662 148.2058	Petrography
TDBHons004.04	Honeysuckle Beds	Phyric Lava	-34.7662 148.2058	Petrography
TDBHons004.05	Honeysuckle Beds	Phyric Lava	-34.7662 148.2058	Petrography
TDBHons005.01	Honeysuckle Beds	Gabbro	-34.9133 148.2078	Petrography Geochemistry
TDBHons006.01	North Mooney Complex	Diorite	-34.9162 148.2111	Petrography Geochemistry
TDBHons007.01	Bogong Granite	Granite	-35.3717 148.3215	Petrography Geochemistry Geochronology Lu/Hf + REE
TDBHons008.01	Wermatong Metabasalt	Mafic Schist	-35.3728 148.3160	Petrography Geochemistry Sm/Nd
TDBHons009.01	Benwerrin Diorite	Gabbro	-35.3856 148.3320	Petrography Geochemistry
TDBHons010.01	Gocup Granite	Granite	-35.2536 148.1502	Petrography Geochemistry

Sample Number	Rock Unit	Rock Type	Location	Uses
TDBHons011.01	Gocup Granite	Granite	-35.2541 148.1532	Petrography Geochemistry Geochronology Lu/Hf + REE
TDBHons012.01	Warrienbah Granite	Granite	-35.1705 148.0553	Petrography Geochemistry Geochronology Lu/Hf + REE
TDBHons012.02	Warrienbah Granite	Granite	-35.1708 148.0550	Petrography Geochemistry
TDBHons013.01	Snowball Metabasic Igneous Complex	Diorite/ Granodiorite Hybrid	-35.1752 148.0551	Petrography Geochemistry Geochronology Lu/Hf + REE
TDBHons013.02	Snowball Metabasic Igneous Complex	Hornfels	-35.1752 148.0551	Petrography Geochemistry
TDBHons014.01	Wyangle Formation	Metabasalt	-35.1542 148.3125	Petrography Geochemistry
TDBHons015.01	Blowering Formation	Dacite	-35.1437 148.2816	Petrography Geochemistry Geochronology Lu/Hf + REE
TDBHons016.01[1]	Honeysuckle Beds	Rhyolite	-35.1438 148.2815	Petrography Geochemistry
TDBHons017.01	Honeysuckle Beds	Dacite	-35.1408 148.3124	Petrography Geochemistry Geochronology Lu/Hf + REE
TDBHons018.01	Honeysuckle Beds	Dacite	-35.1410 148.3119	Petrography Geochemistry Sm/Nd
TDBHons019.01	Wyangle Formation	Gabbro	-35.1436 148.3102	Petrography Geochemistry
TDBHons019.02	Wyangle Formation	Gabbro	-35.1436 148.3102	Petrography Geochemistry Sm/Nd
TDBHons019.03	Wyangle Formation	Gabbro	-35.1436 148.3102	Petrography Geochemistry
TDBHons020.01	Wyangle Formation	Metabasalt	-35.1439 148.3088	Petrography Geochemistry Sm/Nd

[1]Sample coordinates do not appear in the mapped area of the Honeysuckle Beds, unsure if this is the location of the sample or recording error.

Sample Number	Rock Unit	Rock Type	Location	Uses
TDBHons021.01	Brungle Creek Metabasalt	Chert	-35.1380 148.2464	Petrography Geochemistry
TDBHons022.01	Killimicat Granite	Granite	-35.1702 148.2307	Petrography Geochemistry Geochronology Lu/Hf + REE
TDBHons023.01	Frampton Volcanics	Metatuff	-35.1643 148.1656	Petrography Geochemistry
TDBHons024.01	Kimo Diorite	Diorite	-35.0342 148.0116	Petrography Geochemistry
TDBHons025.01	Long Tunnel Metabasic Igneous Complex	Basalt	-35.0383 148.0069	Petrography Geochemistry Sm/Nd
TDBHons026.01	Long Tunnel Metabasic Igneous Complex	Basalt	-35.0383 148.0069	Petrography Geochemistry

Table A2: Samples gathered from the drillcore housed at Londonderry Core Library.

Sample Number	Drillhole Name	Interval Start (m)	Interval End (m)	Interval Length (m)	Core Size (1/2, 1/4 etc.)
TDBHons001.01	IDY8	90.20	90.60	0.40	1/2
TDBHons001.02	IDY8	94.90	95.40	0.50	1/2
TDBHons001.03	IDY8	138.60	139.60	1.00	1/4
TDBHons001.04	IDY8	152.10	152.20	0.10	1/4
TDBHons001.05	IDY8	157.90	158.00	0.10	1/4
TDBHons001.06	IDY8	199.50	199.60	0.10	1/4
TDBHons001.07	IDY8	242.05	242.95	0.90	1/4
TDBHons002.01	DDH4	135.50	136.00	0.50	1/2
TDBHons002.02	DDH4	142.20	142.40	0.20	1/2
TDBHons002.03	DDH4	143.80	143.90	0.10	1/2
TDBHons002.04	DDH4	145.60	146.70	1.10	1/4
TDBHons002.05	DDH4	153.60	154.10	0.50	1/2
TDBHons003.01	DD90LT2	51.50	52.50	1.00	1/4
TDBHons003.02	DD90LT2	56.10	56.20	0.10	1/4
TDBHons003.03	DD90LT2	56.40	56.50	0.10	1/4
TDBHons003.04	DD90LT2	56.67	57.07	0.40	1/4
TDBHons003.05	DD90LT2	62.80	63.80	1.00	1/4
TDBHons003.06	DD90LT2	69.14	69.30	0.16	1/4
TDBHons004.01	R1	44.40	44.50	0.10	1/2
TDBHons004.02	R1	91.70	91.80	0.10	1/4
TDBHons004.03	R1	96.30	96.80	0.50	1/2
TDBHons004.04	R1	100.70	100.80	0.10	1/4
TDBHons004.05	R1	101.30	102.40	1.10	1/4

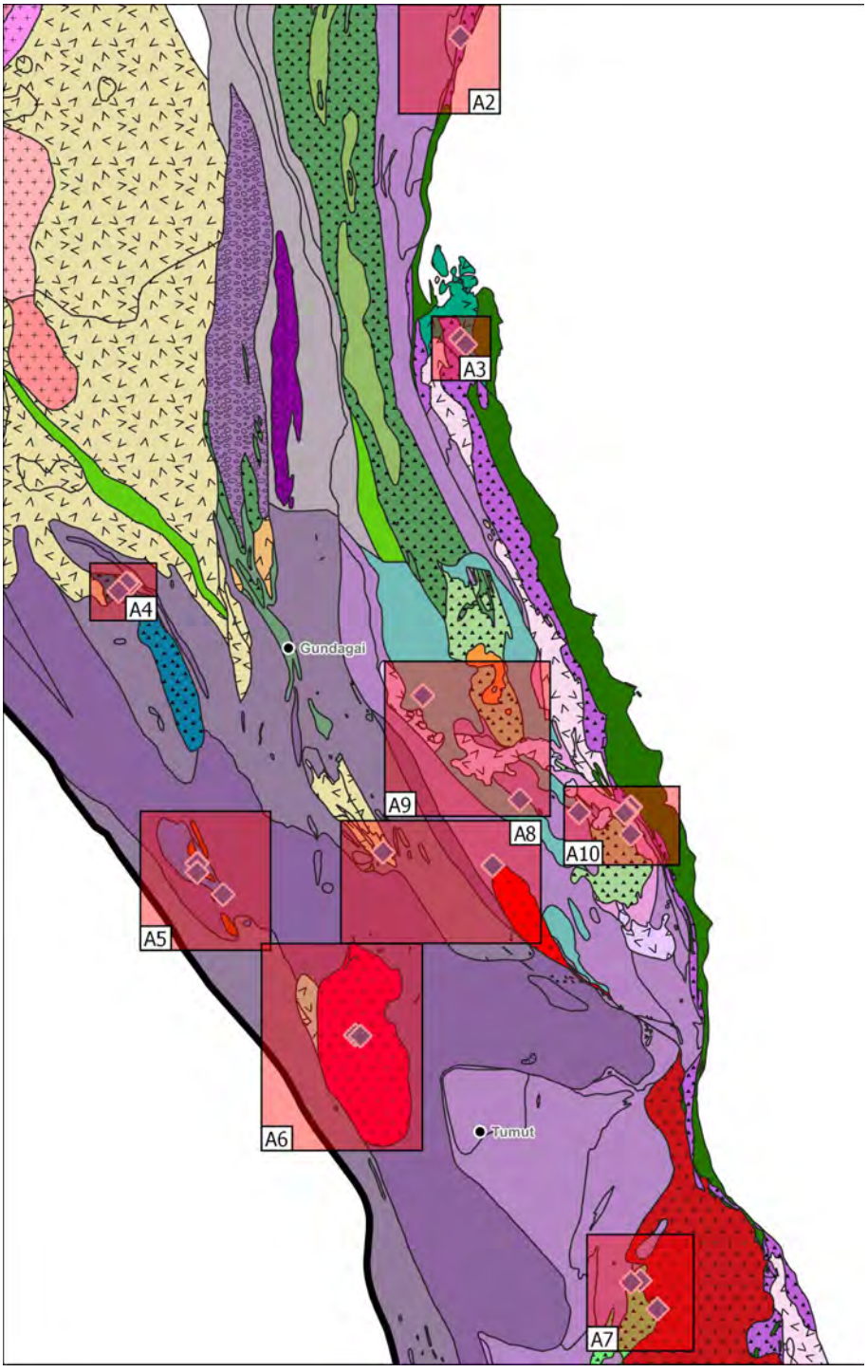

Figure A1: Map of the Tumut Trough sample locations for this study. It has been split into multiple maps as samples were collected close to unit boundaries where multiple samples could be collected of different units. They have been split into maps from figure A2 to A10, marked in the red boxes on this figure. Legend for this map is on the following page.

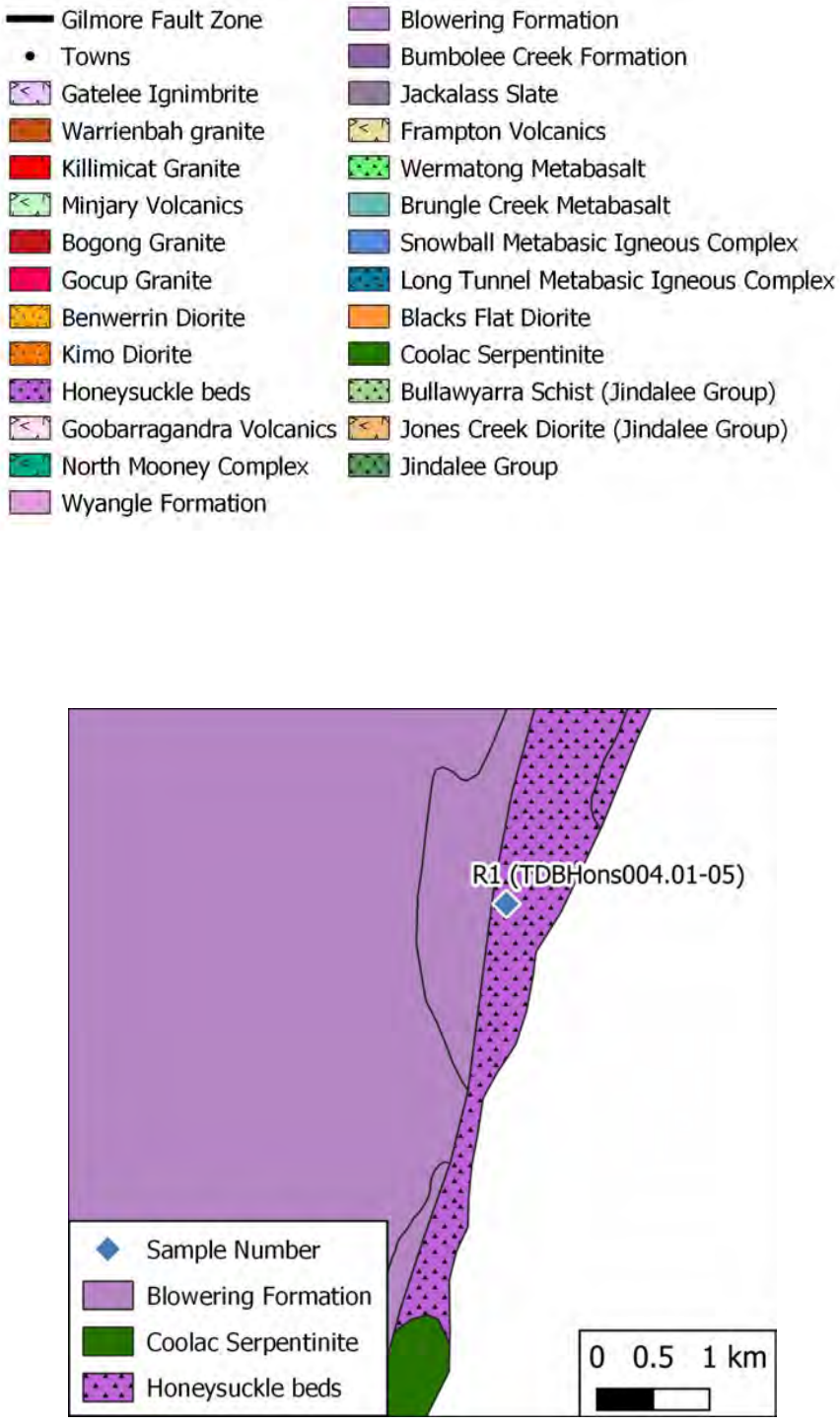

Figure A2: Location of drill hole R1 (TDBHons004.01-05)

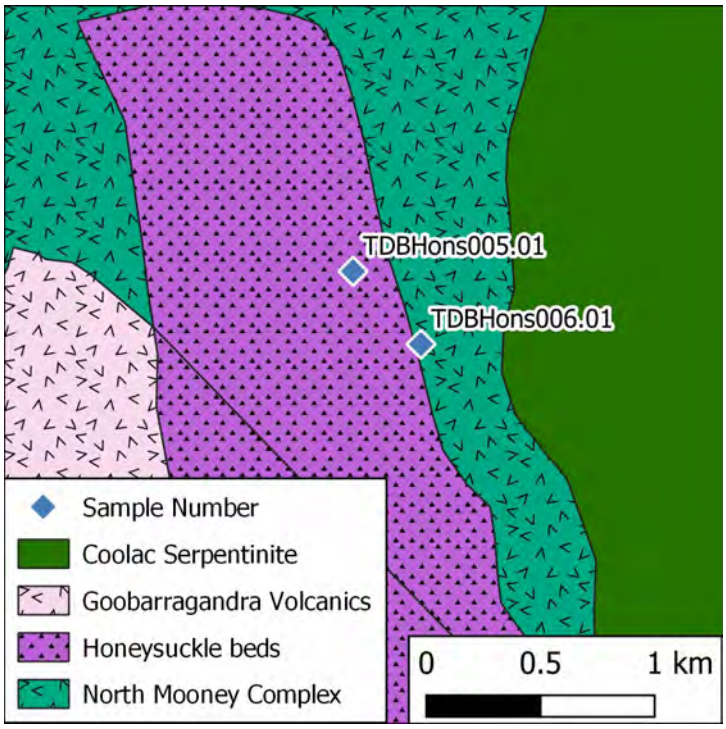

Figure A3: Location of samples TDBHons005.01 and TDBHons006.01

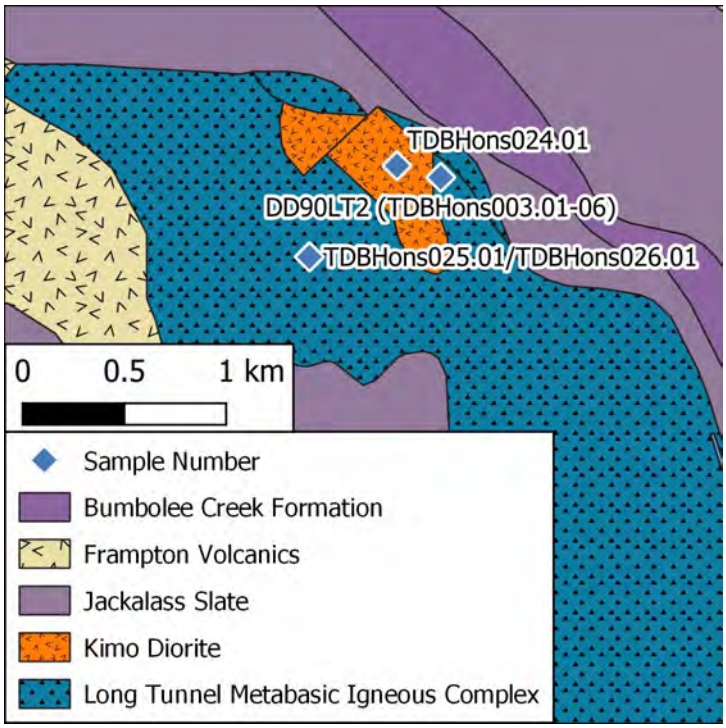

Figure A4: Location of samples TDBHons024.01, TDBHons025.01 and TDBHons006.01. Also located here is drill hole DD90LT2 (TDBHons003.01-06)

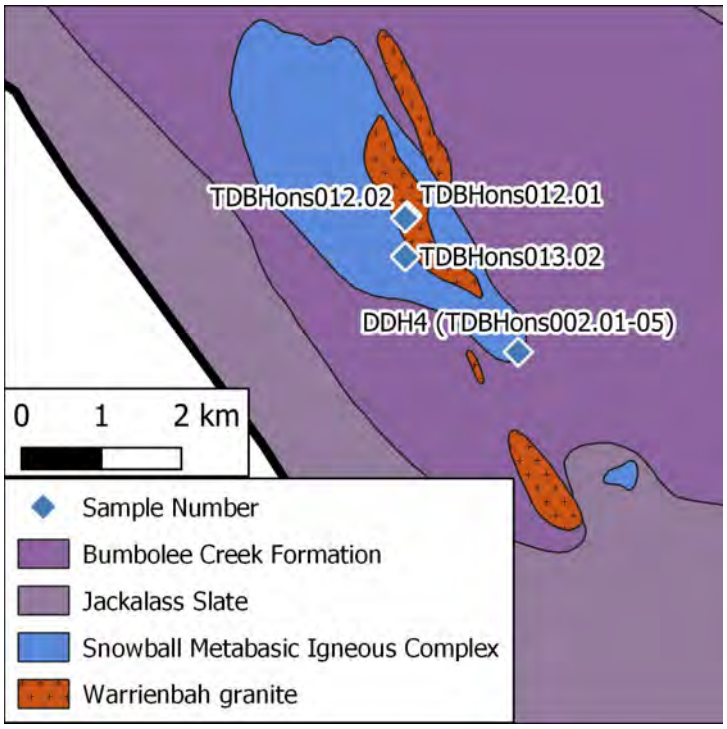

Figure A5: Location of samples TDBHons012.01-02 and TDBHons013.01-02. Also located here is drill hole DDH4 (TDBHons002.01-05)

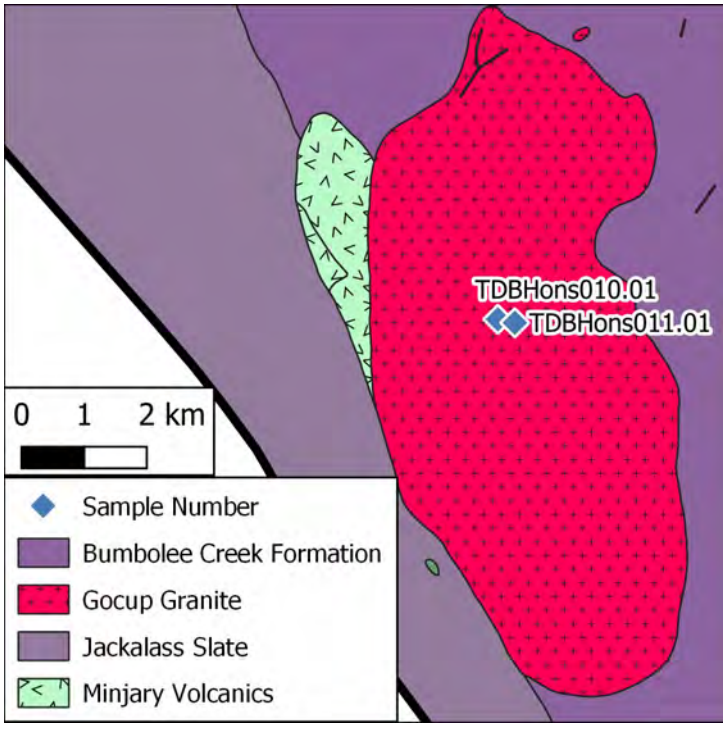

Figure A6: Location of samples TDBHons010.01 and TDBHons011.01

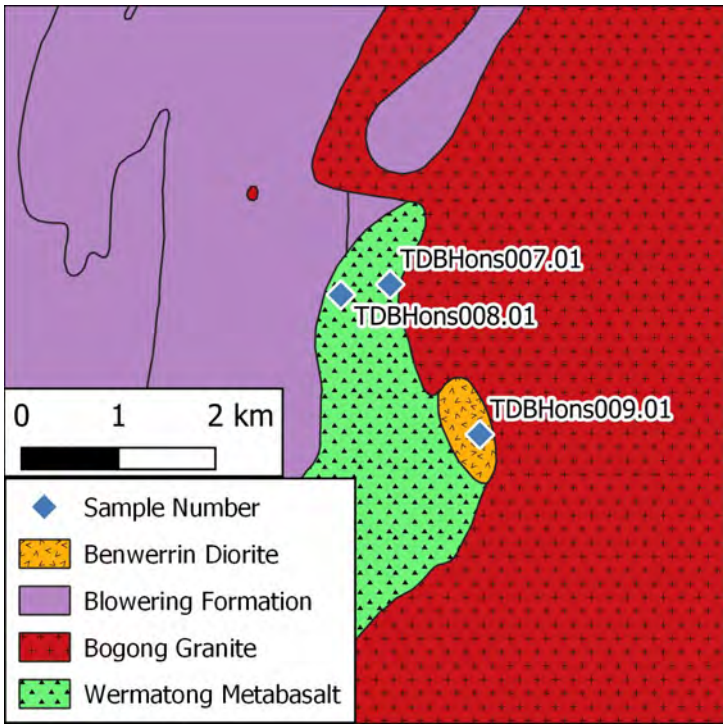

Figure A7: Location of samples TDBHons007.01, TDBHons008.01 and TDBHons009.01

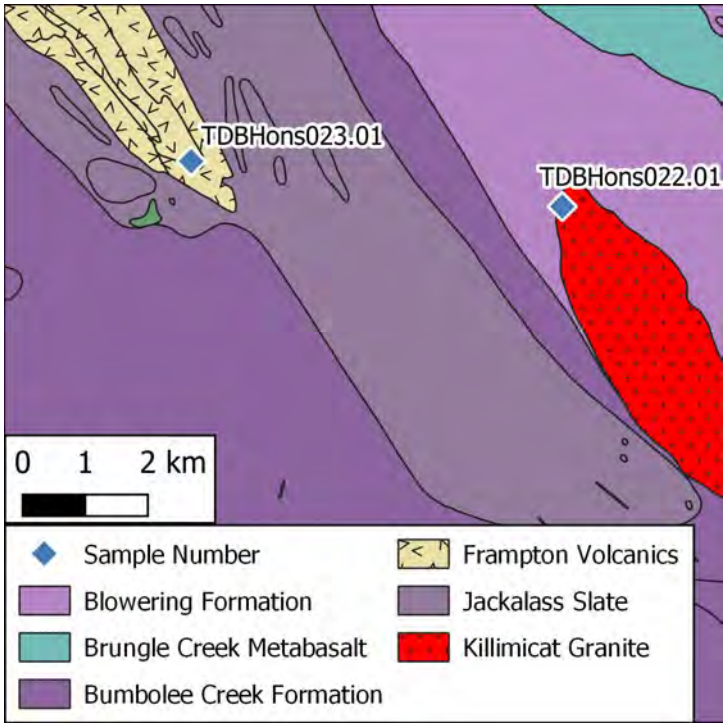

Figure A8: Location of samples TDBHons022.01 and TDBHons023.01

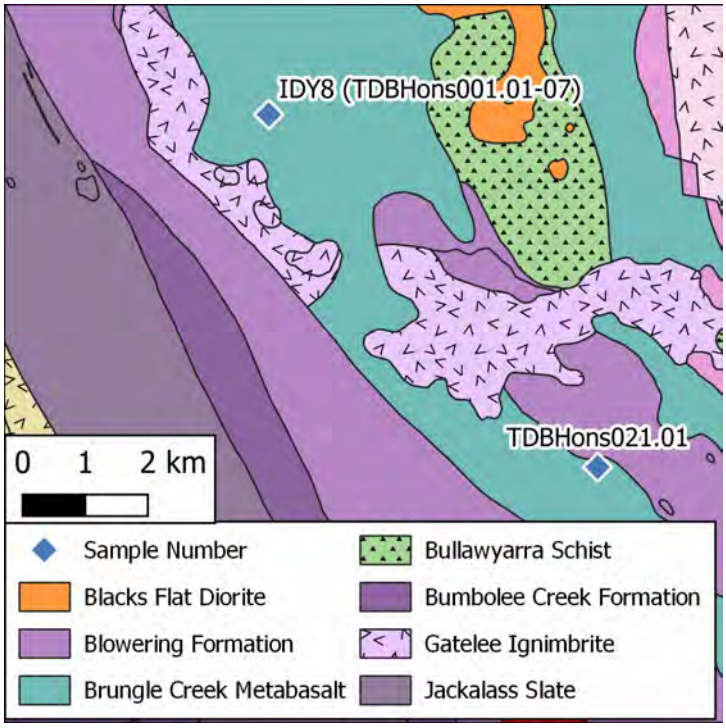

Figure A9: Location of sample TDBHons021.01. Also located here is drill hole IDY8 (TDBHons001.01-07)

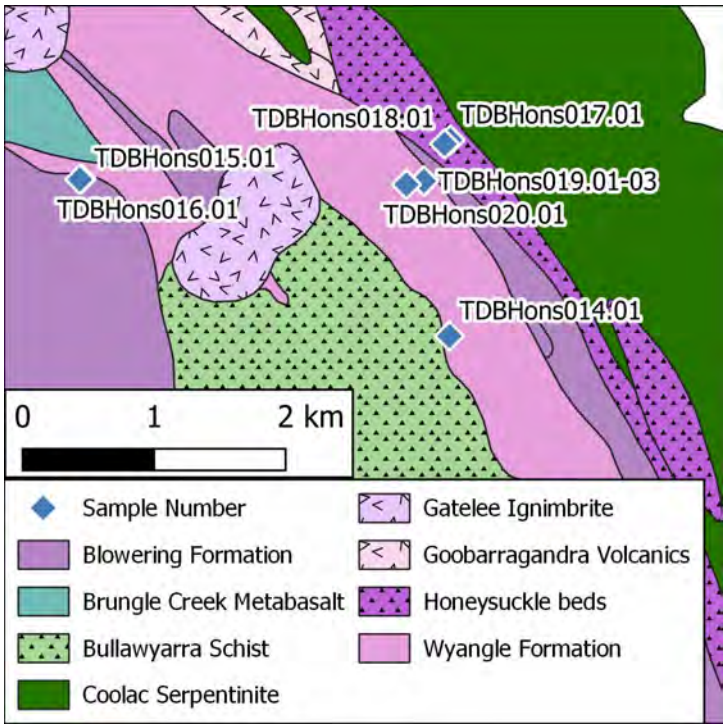

Figure A10: Location of samples TDBHons0014.01, TDBHons0015.01, TDBHons0016.01, TDBHons0017.01, TDBHons0018.01, TDBHons0019.01-03 and TDBHons020.01

Appendix B - Sample Descriptions

Sample descriptions of gathered samples appear in this appendix. Descriptions are ordered by rock unit in alphabetical order.

Benwerrin Diorite

Sample Number: TDBHons009.01

Medium grained, lineated gabbro (Fig. B1 a). Dominated by mafic minerals and plagioclase in hand specimen, both phases are strongly orientated and have an aspect ratio of 4:1. Individual grains are up to 8 mm long, but are normally approximately 4 mm in length. The plagioclase and mafic phases constitute approximately 50% of the rock each.

In thin section (Fig. B1 b), the rock is dominated by plagioclase, biotite (altering to chlorite; greenschist metamorphism) and hornblende. Minor amounts of quartz and epidote are present. Epidote is associated with clusters of biotite and hornblende.

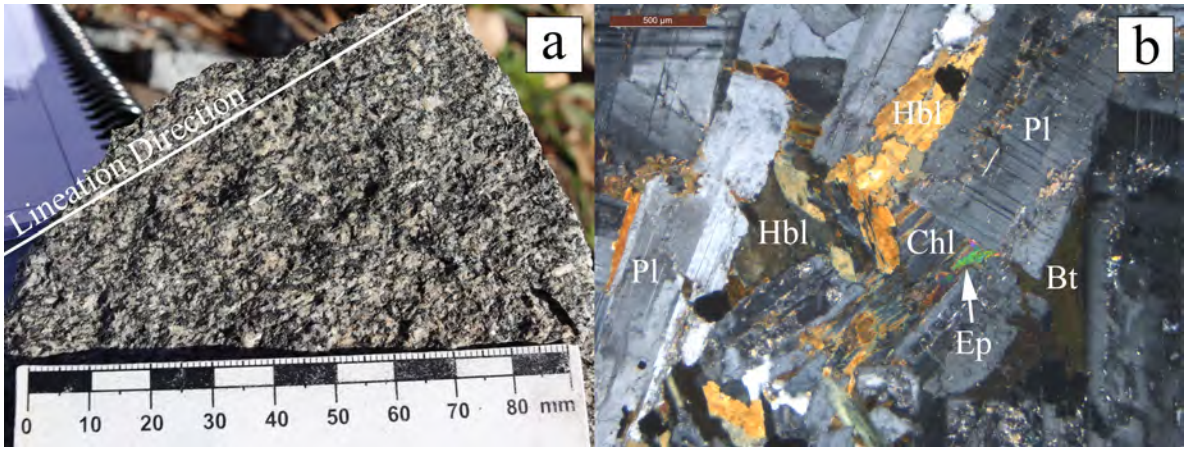

Figure B1: a) Photograph of the Benwerrin Diorite in the field, with flow lineations appearing parallel to the white line. b) Photomicrograph in cross-polarized light of a mafic cluster surrounded by plagioclase (Pl). Within this mafic cluster there is biotite (Bt) altering to chlorite (Chl), hornblende (Hbl) and epidote (Ep). Length of scale bar = 500 μm.

Blowering Formation

Sample Number: TDBHons015.01

Gray/green dacite (Fig. B2 a). Quartz and plagioclase occur as phenocrysts in a gray/green groundmass, minor biotite. Quartz and plagioclase occur up to 8 and 11 mm in length respectively.

In thin section, quartz and plagioclase phenocrysts (between 0.5 - 2 and 0.5 - 5 mm respectively) surrounded by a quartz matrix (Fig. B2 b). Biotite is partially altered to chlorite (up to 1.5 mm), with the cleavage within some biotite grains being notably dark and folded (Fig. B2 c). Zircons are small (100 μm), euhedral grains spread sparsely throughout the slide.

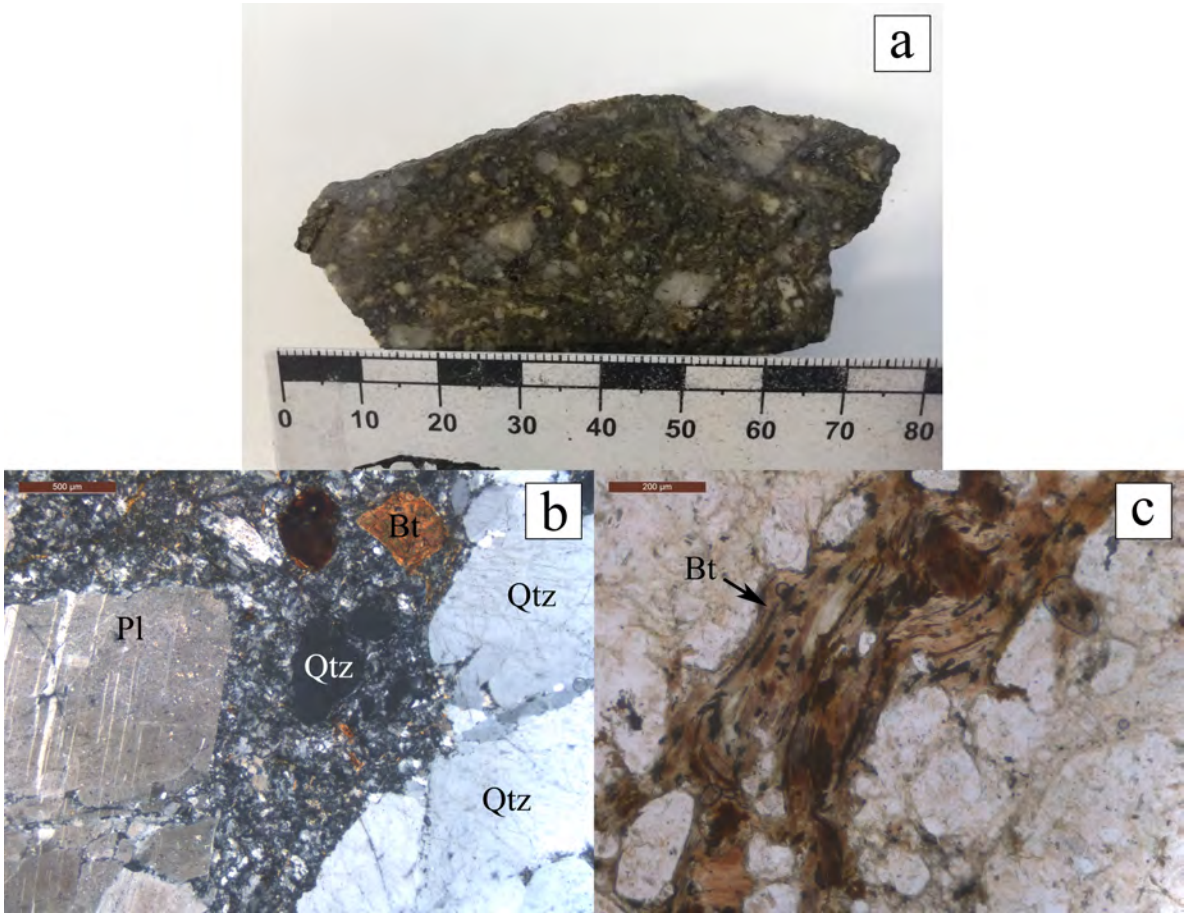

Figure B2: a) Photograph of the Blowering Formation field sample. b) Photomicrograph of the quartz (Qtz), plagioclase (Pl) and biotite (Bt) phenocrysts surrounded by fine-grained quartz aggregates. Length of scale bar = 500 μm. c) Biotite (Bt) deformed around phenocrysts. Length of scale bar = 200 μm.

Bogong Granite

Sample Number: TDBHons007.01

White/beige, medium grained granite with felsic vein (Fig. B3 a). K-felspar, plagioclase, quartz and mafic minerals are present in hand specimen. All minerals range from 1.5 - 3 mm in length. The felsic vein is 15 mm wide, with little to no mafic minerals. The grains are much smaller than the rest of the rock. Quartz is more abundant in the vein.

Majority quartz, plagioclase, perthitic orthoclase and interstitial hornblende. A felsic vein composed primarily of quartz with minor plagioclase, orthoclase as perthite and a few grains of zoned hornblende. The grains within the vein are generally smaller (0.2 - 2 mm) than that of the rest of the rock (0.5 - 3 mm). The vein has an overall width of 10 mm. Zircons appear subhedral, around 50 μm in diameter. Zircons are spread as isolated grains throughout the slide.

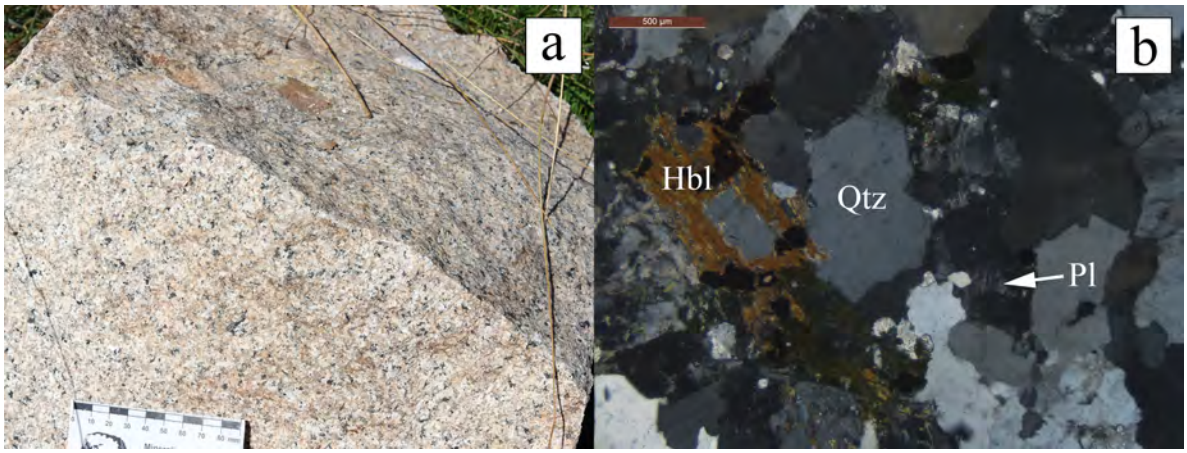

Figure B3: a) Photograph of the Bogong Granite in the field. b) Interstitial primary hornblende (Hbl) amongst quartz (Qtz) and minor plagioclase (Pl). Orthoclase not present in this field of view. Length of scale bar = 500 μm.

Brungle Creek Metabasalt

Sample Numbers: TDBHons001.01-07, TDBHons021.01

Massive gray chert occurs in the field (Fig. B4 a) and at shallow depths in drill core (TDBHons001.01 and TDBHons021.01). They are heavily veined and contains large quartz grains (up to 1 mm) in the groundmass. TDBHons001.01 also contains a calcite vein that is 5 mm wide. Further downhole is a massive gray rock (TDBHons001.02) referred to as a crystal tuff by Robinson (1995). At greater depths the rocks are chlorite-altered brecciated basalts (TDBHons001.03-07), evident from their green colour and extremely fine grainsize, while also appearing brecciated. Most of these deeper sections have calcite. TDBHons001.06 also has associated sulfides.

In drillcore, most samples are dominated by calcite and chlorite, especially in veins (Fig B4 b). The exception is the samples closest to the surface, with both the shallowest drillcore sample (TDBHons001.01) and the field sample (TDBHons021.01) being cherts. Both have a fine-grained quartz matrix with quartz veins throughout. Only the field sample (TDBHons021.01) has actinolite within the veins, while only the drillcore sample (TDBHons001.01) has calcite in the veins. Notably, TDBHons001.06 has large, fractured sulfide grains, with calcite filling the spaces.

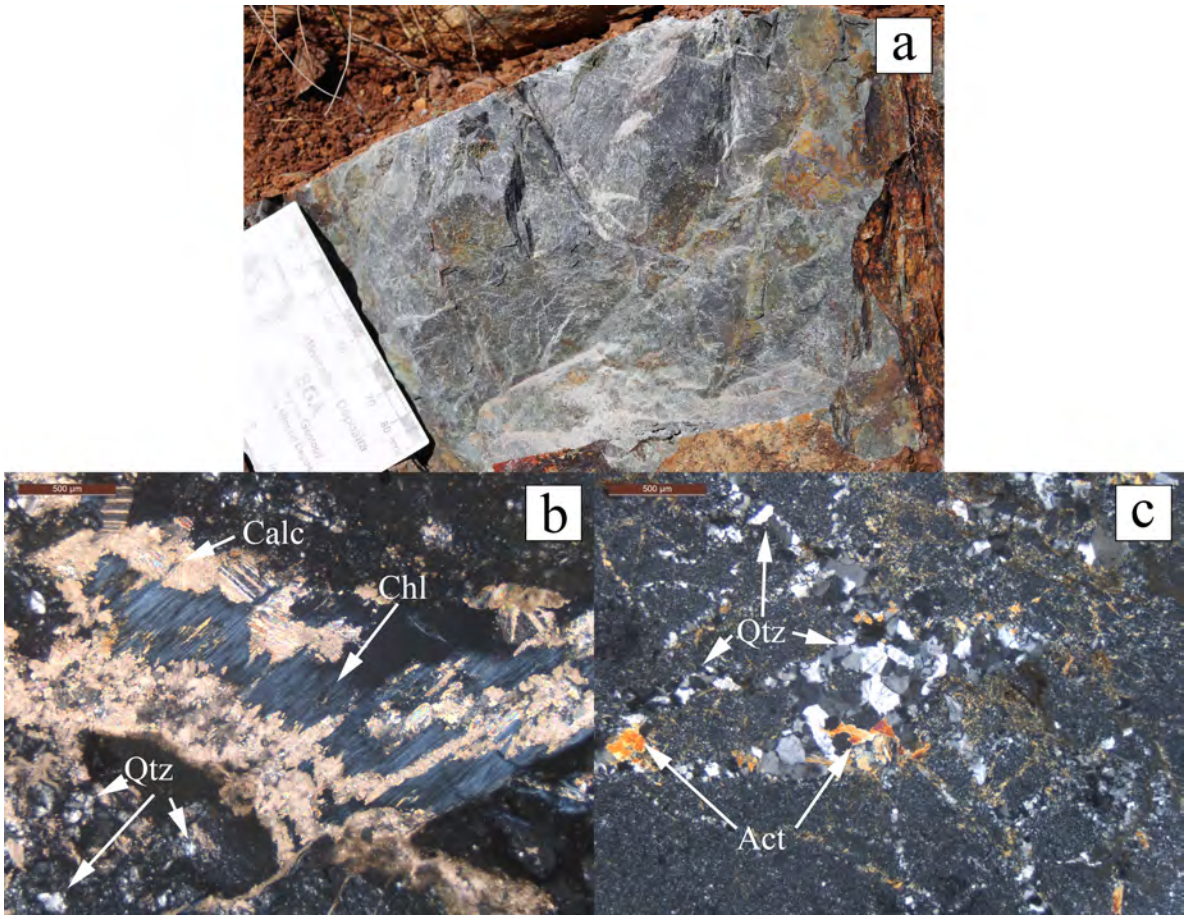

Figure B4: a) Photograph of the Brungle Creek Metabasalt in the field. Card length is approximately 80 mm. b) Chlorite (Chl) and calcite (Calc) vein in TDBHons001.06 with a quartz (Qtz) matrix. Length of scale bar = 500 μm. c) Veins of quartz (Qtz) and actinolite (Act) amongst a quartz matrix in TDBHons021.01. Length of scale bar = 500 μm.

Frampton Volcanics

Sample Number: TDBHons023.01

Green, fine-grained meta-tuff with quartz phenocrysts (Fig. B5 a). Minerals are lineated, generally only up to 1 mm long, with the exception of some quartz grains that can reach up to 7 mm.

In thin section, quartz occurs as polycrystalline aggregates, phenocrysts showing undulose extinction and fine-grained aggregates in the groundmass. Phenocrysts of plagioclase and orthoclase are present. The cleavage is defined by muscovite and calcite (Fig. B5 b). Composite grains of quartz and plagioclase occur as phenocrysts.

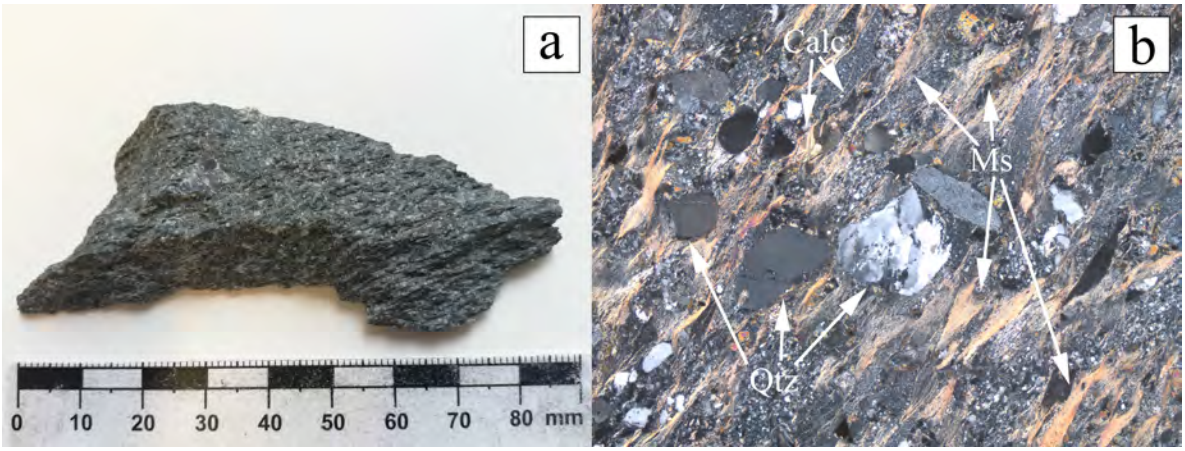

Figure B5: a) Photograph of the Frampton Volcanics hand specimen. b) Quartz (Qtz) phenocrysts upon a cleavage defined by Muscovite (Ms) and calcite (Calc). Field of view = 5.0 x 3.7 mm.

Gocup Granite

Sample Numbers: TDBHons010.01, TDBHons011.01

Partially weathered, beige/white, medium coarse-grained granite. Felspar and biotite all generally between 1 - 3 mm long, with the exception of quartz with appears as larger crystals up to 5 mm (TDBHons010.01). TDBHons011.01 is similar, except with large quartz and fine secondary mica as a light green mineral, being up to 15 mm and 7 mm respectively. It also contains muscovite replacing cordierite (B Landenberger, pers. comm. 2 March).

In thin section, the samples contains equigranular quartz, plagioclase and K-feldspar (all generally 2 mm across) with radial muscovite, green biotite (starting to alter) and fine secondary white mica (Fig. B6 b,c).

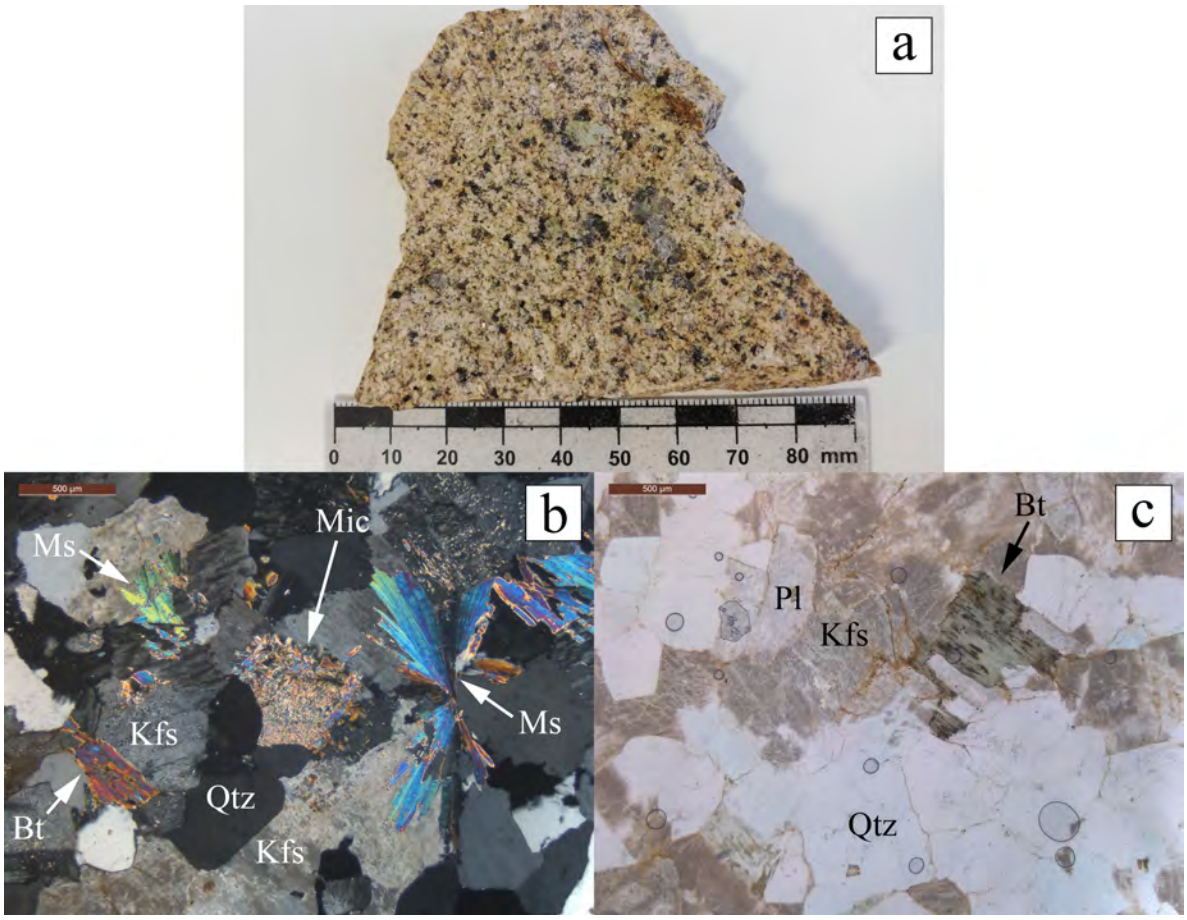

Figure B6: a) Photograph of the TDBHons011.01 hand specimen. b) Muscovite (Ms), biotite (Bt) and fine-grained secondary white mica (Mic) amongst coarse quartz (Qtz) and K-feldspar (Kfs) in TDBHons010.01. Length of scale bar = 500 μm. c) Plagioclase (Pl), K-feldspar (Kfs) and quartz (Qtz) with green biotite (Bt) in TDBHons011.01. Length of scale bar = 500 μm.

Honeysuckle Beds

Sample Numbers: TDBHons004.01-05, TDBHons005.01, TDBHons016.01, TDBHons017.01, TDBHons018.01

A variety of rock types exist in the Honeysuckle Beds. In drillcore, TDBHons004.01 and TDBHons004.03-05 are all massive grey rocks with green and white veins, while TDBHons004.02 is a light coloured, heavily foliated schist. In the field, TDBHons005.01 is a gabbro with fine-grained feldspar and mafic minerals, TDBHons016.01 is a light coloured rhyolite with mafic phenocrysts, TDBHons017.01 is a dacite with common quartz phenocrysts and less common mafic phenocrysts, and TDBHons018.01 is a dacite that is more green than TDBHons017.01, also containing quartz phenocrysts.

In thin section, the drillcore samples reveal their differences. TDBHons004.01 has multiple domains, a mafic rich groundmass, a large vein composed of fine-grained quartz and other large veins composed of calcite and polycrystalline quartz. The mafic rich portion is composed of plagioclase and quartz with large biotite clusters with minor alteration to chlorite. TDBHons004.02 has muscovite defining cleavage which folds around the more robust minerals. Quartz and calcite both occur as elongate aggregates parallel to foliation. Garnet is limited in this section to a handful of grains, the largest of which is 800 μm in diameter. Small zircons are also present. TDBHons004.03 appears to be a dacite with a fine groundmass, quartz and plagioclase veins, calcite veins and small biotite and chlorite grains. TDBHons004.04 and TDBHons004.05 are quartz and plagioclase phyric coherent lavas cut by veins containing calcite and chlorite.

The field samples are also quite different from sample to sample. TDBHons005.01 is composed of plagioclase and hornblende. A quartz vein is also present.

TDBHons016.01 contains altered plagioclase and clinopyroxene, with olivine phenocrysts and other phenocrysts replaced by chlorite. TDBHons017.01 contains common quartz (polycrystalline from plastic deformation and recrystallization) phenocrysts and rare plagioclase phenocrysts, biotite clusters, muscovite surrounded by fine mica and small quartz and epidote veins all within a quartz matrix. TDBHons018.01 has a fine quartz matrix with quartz, plagioclase and biotite phenocrysts.

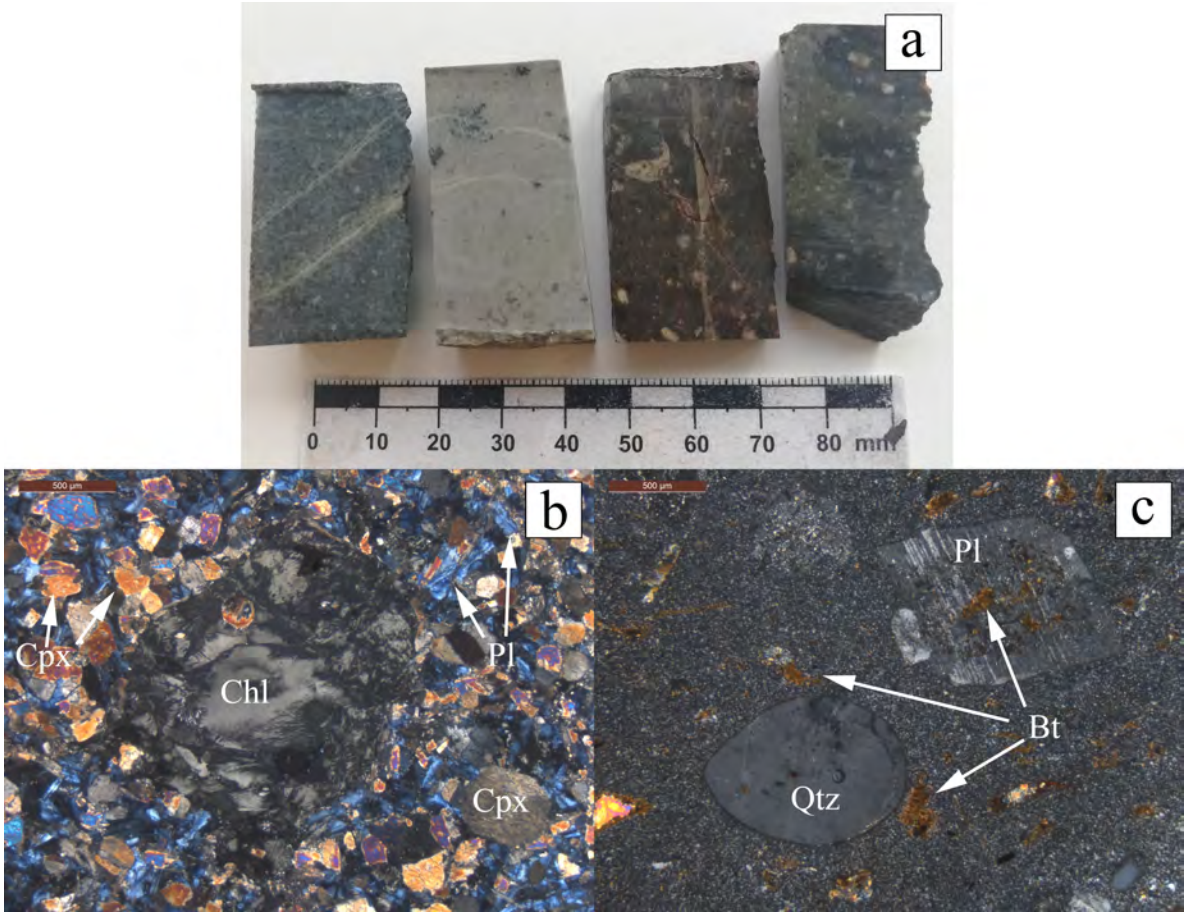

Figure B7: a) Blocks of (l-r) TDBHons005.01, TDBHons016.01, TDBHons017.01 and TDBHons018.01. b) Phenocryst replaced by chlorite (Chl) within a matrix of clinopyroxene (Cpx) and altered plagioclase (Pl) in TDBHons016.01. Length of scale bar = 500 μm. c) Quartz (Qtz) and plagioclase (Pl) phenocrysts within a fine quartz matrix in TDBHons017.01. Small biotite grains are present both within and outside the phenocrysts. Length of scale bar = 500 μm.

Killimicat Granite

Sample Number: TDBHons022.01

Pink, medium/coarse grained granite (Fig. B8 a). K-feldspar, plagioclase, quartz and biotite all occur in the rock, with the felsic minerals up to 6 mm long. The biotite is smaller and appears interstitial.

In thin section, quartz, plagioclase and perthitic orthoclase are dominant, all up to 5 mm across. Biotite is interstitial (Fig B8 b). Minor muscovite is present with some muscovite appearing with a strong preferred orientation within plagioclase grains.

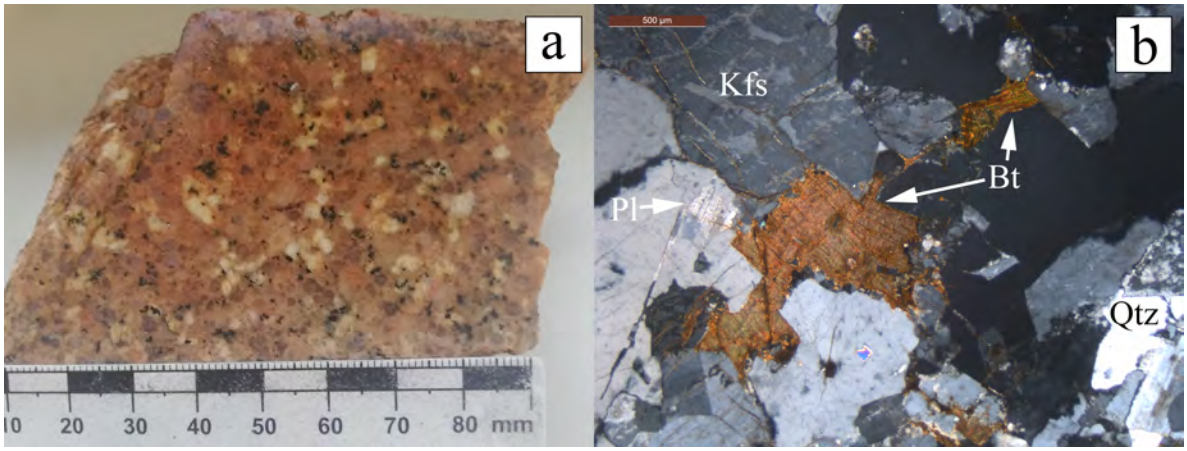

Figure B8: a) Photograph of the Killimicat Granite field sample. b) Interstitial biotite (Bt) amongst K-feldspar (Kfs), plagioclase (Pl) and quartz (Qtz). Length of scale bar = 500 μm.

Kimo Diorite

Sample Numbers: TDBHons003.01-02, TDBHons024.01

Pinkish grey, fine to medium grained diorite (Fig. B9 a). Biotite rich with feldspar and quartz. Grains are generally up to 1 mm in diameter, but some feldspars reach up to 3 mm long (TDBHons024.01). Drillcore has coarser grains, up to 5 mm. The lower contact of the Kimo Diorite appears to be sheared (TDBHons003.02). A section of TDBHons003.01 has sulfides incorporated into vein-like structures (Fig. B9 b).

In thin section, plagioclase is the dominant mineral, enclosing some smaller biotite grains. Plagioclase varies in size, ranging between 250 μm to 3 mm (Fig. B9 c,d). Quartz is uncommon, appearing as small (200 μm), rounded grains. Biotite (likely magmatic) ranges from brown to green in PPL, appearing in clusters. Calcite occurs as clusters, with individual grains ranging between 200 and 500 μm in length, and as large, isolated grains up to 2 mm. Epidote is found within and around the biotite clusters as rounded grains up to 200 μm in size, easily distinguishable due to its pale-yellow colour and high relief in PPL. Apatite appears as <0.1 mm grains which exist throughout the entire slide. Zircons are also <0.1 mm grains, but are less common than apatite.

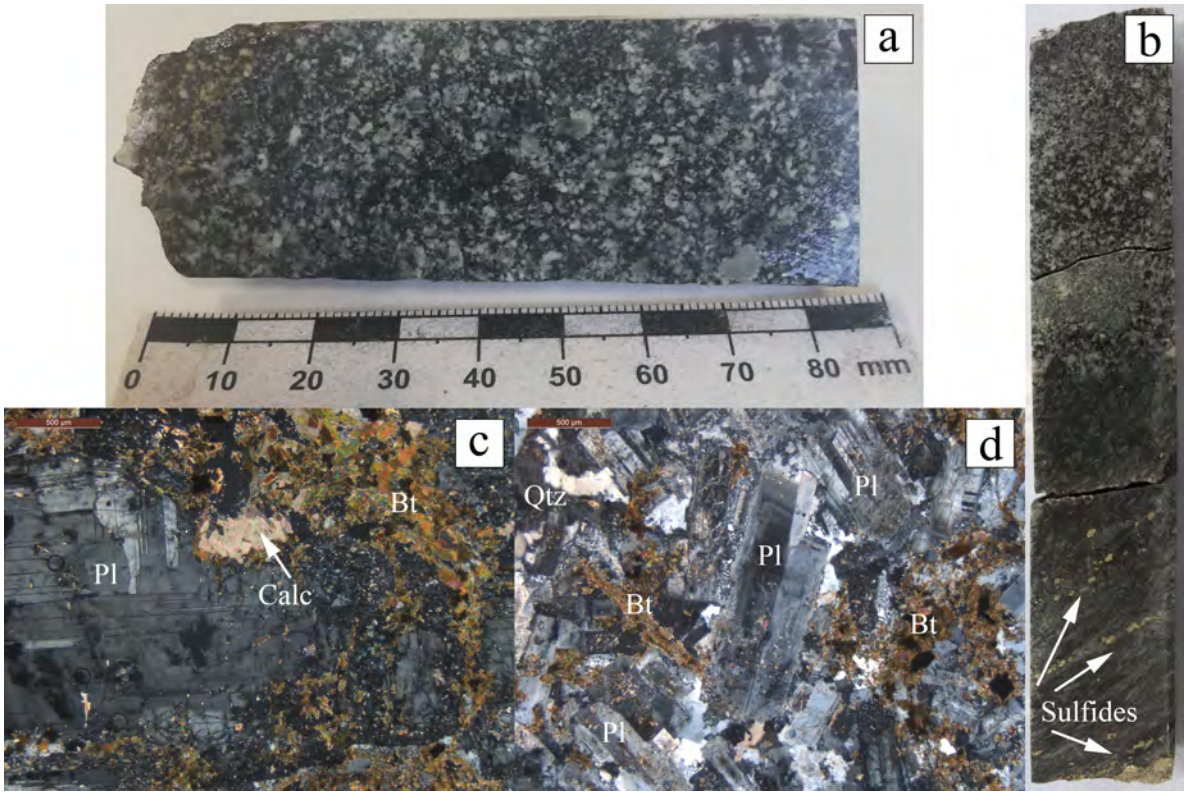

Figure B9: a) Section of the Kimo Diorite in drillcore. b) Section of drillcore that contains the contact between the Kimo Diorite and a finer grained material that hosts sulfide veins. Length of section = 15 cm. c) Large plagioclase (Pl) grain and smaller calcite (Calc) grain surrounded by biotite (Bt). Length of scale bar = 500 μm. d) Plagioclase (Pl) as the dominant mineral, with smaller amounts of biotite (Bt) and quartz (Qtz). Length of scale bar = 500 μm.

Long Tunnel Metabasic Igneous Complex

Sample Numbers: TDBHons003.03-06, TDBHons0025.01, TDBHons0026.01

Gray, fine-grained basalt (Fig. B10 a,b). Some samples are massive (TDBHons025.01) while others are porphyritic (TDBHons026.01). Coarser grained material in the porphyritic basalt is composed of feldspars. In drillcore it is also a massive basalt, but does have some sulfides and veins which are composed of quartz (TDBHons003.04). Top margin is sheared (TDBHons003.03). Beneath the Long Tunnel Metabasic Igneous Complex lies a massive serpentinite (TDBHons003.05) and talc-altered serpentinite (TDBHons003.06).

In thin section, plagioclase (up to 1 mm) and biotite (some altering to chlorite) are the major minerals (Fig. B10 c). There is minor quartz, some of which has been recrystallized (120° angles between grain boundaries) in TDBHons026.01. Epidote is found as rounded grains around 200 μm and calcite up to 500 μm.

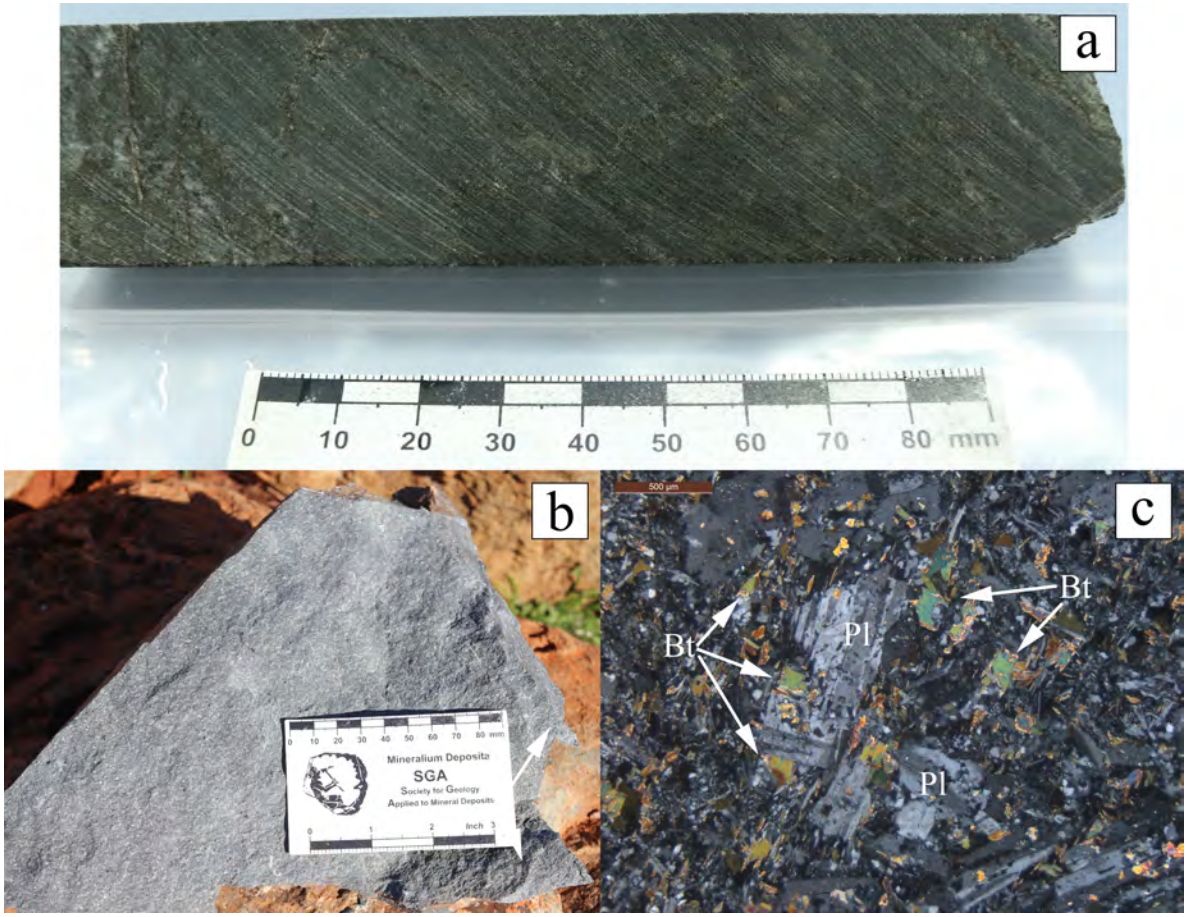

Figure B10: a) Photograph of the Long Tunnel Metabasic Igneous Complex in drillcore. b) Photograph of the Long Tunnel Metabasic Igneous Complex in the field. c) . Length of scale bar = 500 μm.

North Mooney Complex

Sample Number: TDBHons006.01

Green, fine-grained, porphyritic diorite (Fig. B11 a). Feldspar phenocrysts up to 2 mm. Thin veins appear throughout the rock.

In thin section, the feldspar phenocrysts are plagioclase, up to 2 mm. They appear amongst a groundmass of finer grained plagioclase and hornblende (Fig. B11 b), all up to 250 μm.

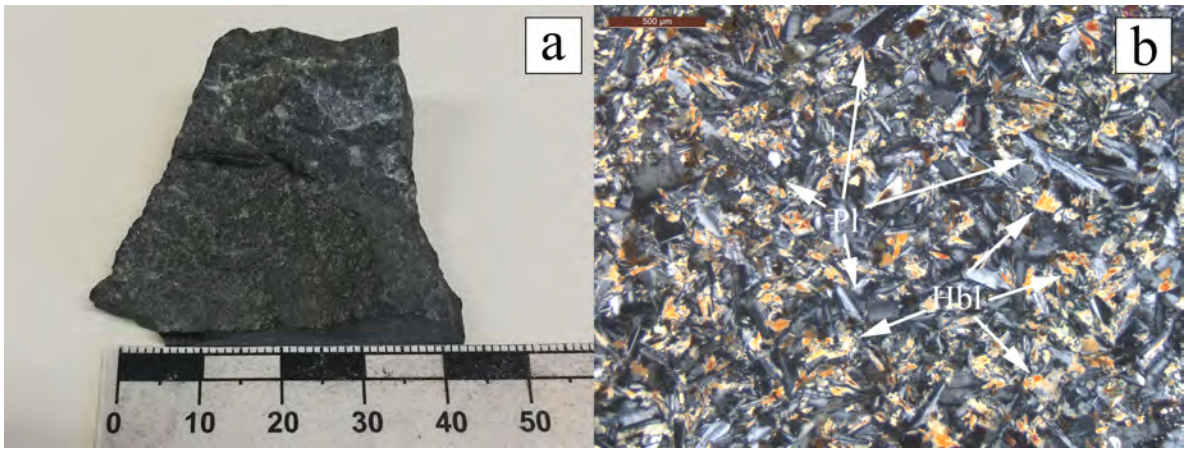

Figure B11: a) Photograph of the North Mooney Complex hand specimen. b) Fine-grained plagioclase (Pl) and hornblende (Hbl). Length of scale bar = 500 μm.

Snowball Metabasic Igneous Complex

Sample Numbers: TDBHons002.01-05, TDBHons013.01-02

The Snowball Metabasic Igneous Complex hosts a variety of rocks (Fig. B12 a) such as hornblende diorite (TDBHons002.01 and TDBHons002.03), agglomerate (TDBHons002.02), massive chloritic rock and andesite, both with sulfides (TDBHons002.04 and TDBHons002.05 respectively), diorite/granodiorite hybrid rock (TDBHons013.01, Fig B12 b) and hornfels (TDBHons013.02). The diorites are massive, gray/green rocks with medium/coarse mafic minerals and finer matrix. The agglomerate is dark gray, with separate domains between the darker 'bombs' and lighter matrix. Samples TDBHons002.04 and TDBHons002.05 are massive, fine-grained rocks with masses of sulfides. The diorite/granodiorite hybrid rock is a diorite that hosts granodiorite veins that have mixed with the original diorite to create three separate domains: the diorite, the granodiorite and the fine-grained buffer zone. The hornfels is the country rock to TDBHons013.02, appearing gray, massive and fine-grained.

In thin section, TDBHons002.01 quartz and calcite veins occur amongst hornblende. TDBHons002.02 is dominated by fine-grained actinolite. It has veins composed of fine quartz and coarse hornblende, up to 2 mm. TDBHons002.03 is hornblende-rich with fine-grained quartz and rare plagioclase. TDBHons002.04 is dominated by chlorite and opaque minerals (mainly sulfides). It contains common hornblende. TDBHons002.05 contains very common muscovite and less common hornblende. Veins are composed of quartz. TDBHons013.01 has been metamorphosed to at least amphibolite facies. The protolith was likely to be an intermediate magmatic rock, evident from rectangular plagioclase. It contains interlocking hornblende, quartz and plagioclase. Muscovite is present closer to the vein component. As it moves into the

vein component, titanite appears along with a heavily altered mineral assemblage (Fig. B12 c). TDBHons013.02 is composed of fine biotite, equigranular quartz and very fine muscovite (Fig. B12 d). The boundaries between three quartz grains create 120^o angles, indicating they have been recrystallised (Fig. B12 d inset).

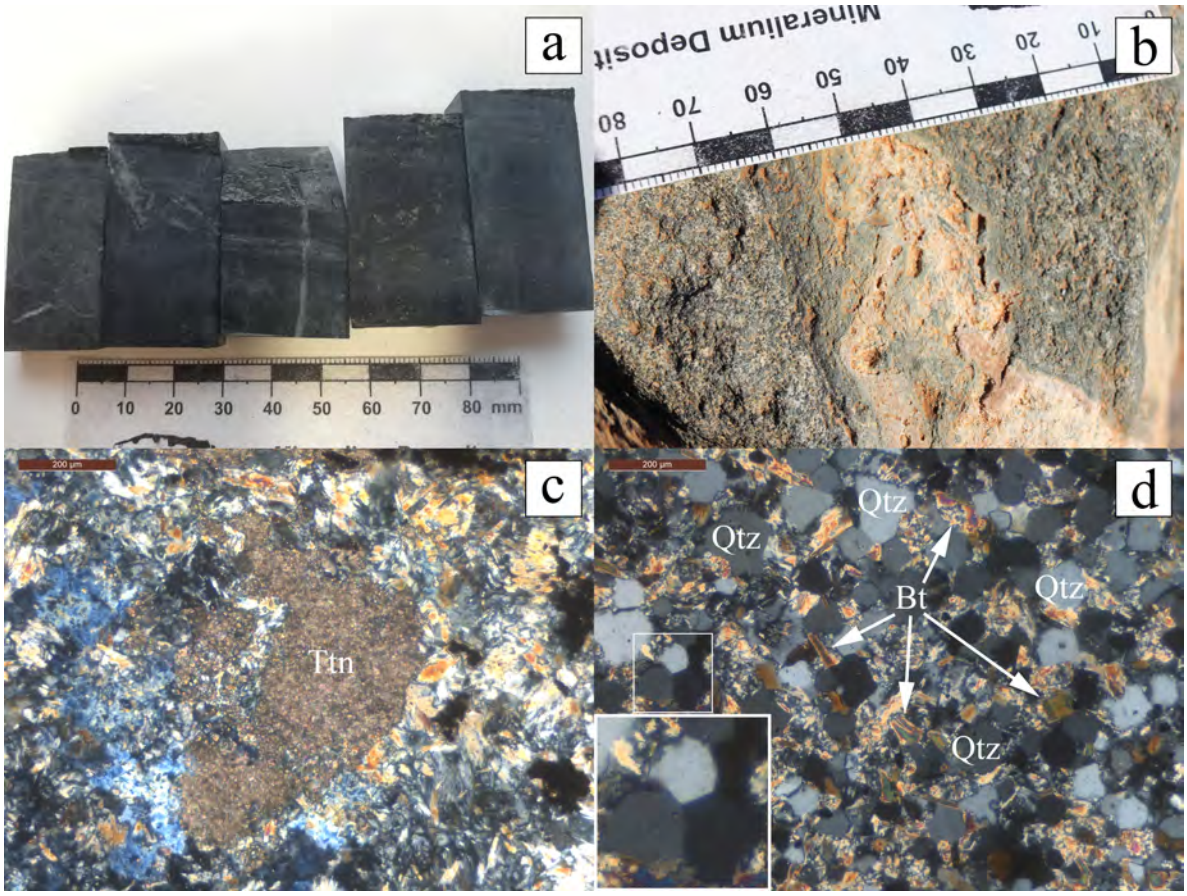

Figure B12: a) Drillcore samples (l-r) TDBHons002.01, TDBHons002.02, TDBHons002.03, TDBHons002.04, TDBHons002.05. b) Diorite/granodiorite hybrid rock. The three phases in the rock are the white granodiorite vein, gray/green host rock and fine-grained material between the vein and host rock. c) Polycrystalline secondary titanite (Ttn). Length of scale bar = 200 μm. d) Fine-grained quartz (Qtz) and biotite (Bt). The quartz has been recrystallized, evident from the boundaries between multiple quartz grains forming 120° angles (inset image). Length of scale bar = 200 μm.

Warrienbah granite (proposed name)

Sample Numbers: TDBHons012.01-02

The Warrienbah granite comes in two phases (Fig. B13 a); a felsic, beige, fine/medium grained granite (TDBHons012.01) and a mafic, gray, coarse grained granite (TDBHons012.02). The felsic phase contains beige feldspars, quartz and biotite, with grains approximately 2 mm long. The mafic phase is dominated by biotite, constituting up to approximately 40% of the rock. Also in the mafic phase are white/gray feldspars and quartz. Grains are 5 - 8 mm long.

Both phases contain quartz, plagioclase, orthoclase as perthite, microcline and interstitial biotite. The felsic phase contains more microcline and orthoclase than the mafic phase, with the mafic phase containing fine-grained secondary muscovite clusters, more biotite and more plagioclase (Fig. B13 b,c).

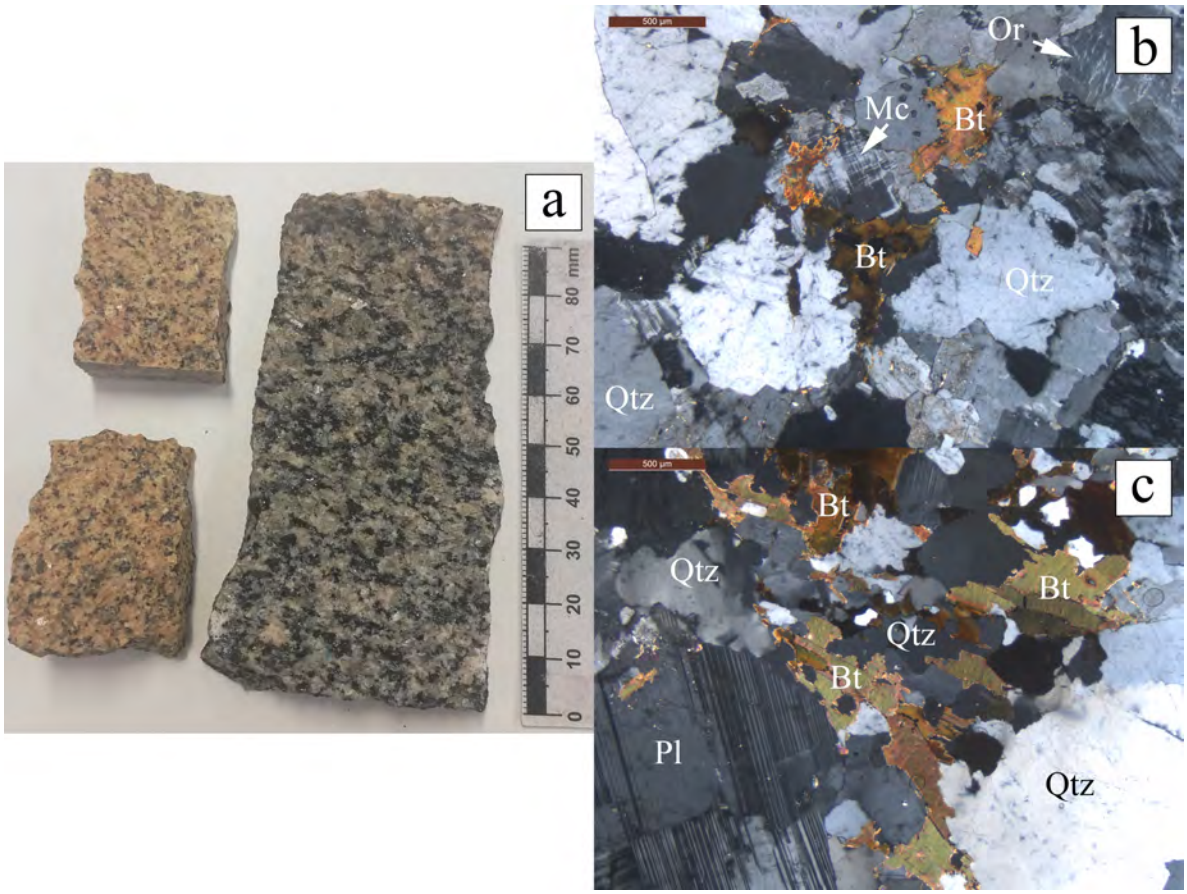

Figure B13: a) Comparison between the felsic (left) and mafic (right) phases of the Warrienbah granite. b) Felsic phase and c) mafic phase of the Warrienbah granite. The felsic phase has much less biotite (Bt) than the mafic phase, and contains more microcline (Mc) and orthoclase (Or) whereas the mafic phase contains more plagioclase (Pl). Both phases contain quartz (Qtz).

Wermatong Metabasalt

Sample Number: TDBHons008.01

Green mafic schist (Fig. B14 a). Grains are not visible. Multiply deformed with some folding, cleavage obvious.

In thin section it is dominated by actinolite with minor quartz. The actinolite was foliated before experiencing multiple folding events resulting in the multiply deformed schist (Fig. B14 b).

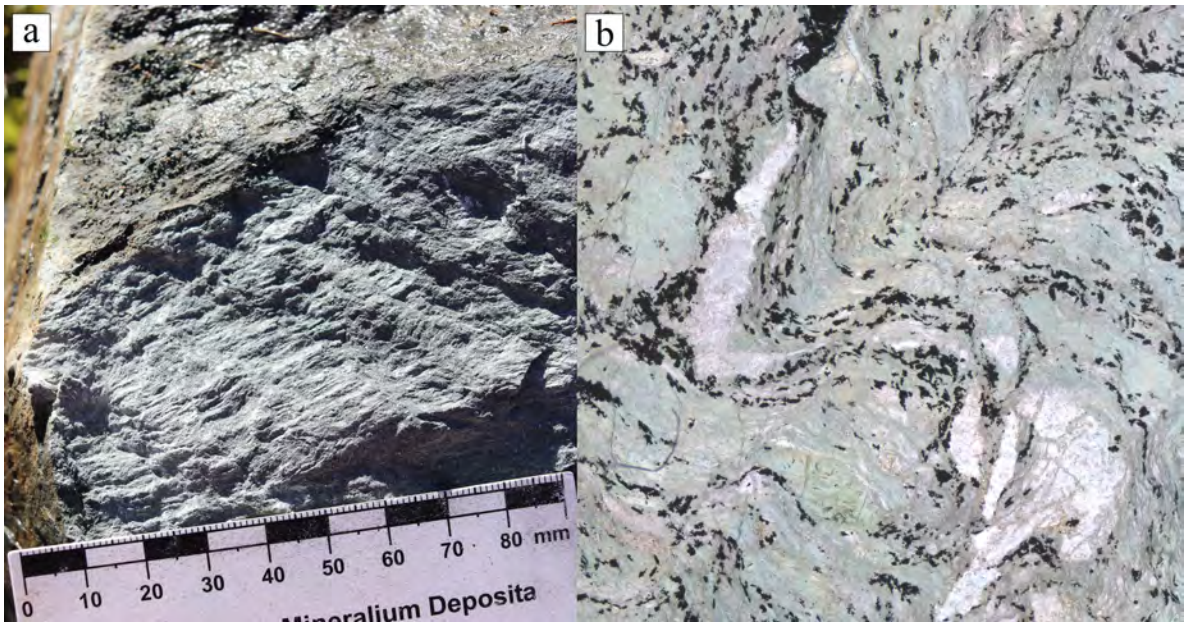

Figure B14: a) Sample TDBHons008.01 in the field. b) Mosaic of photomicrographs of the folding evident in thin section (TDBHons008.01). The white mineral is quartz while the green mineral is actinolite. The black grains are opaque minerals. Field of view = 5.5 x 5.5 mm.

Wyangle Formation

Sample Numbers: TDBHons014.01, TDBHons019.01-03, TDBHons020.01

A variety of rock types exist in the Wyangle Formation, from grey, massive metabasalts (TDBHons014.01 and TDBHons020.01), through medium grained gabbro (TDBHons019.02) to coarse grained gabbros (TDBHons019.01 and TDBHons019.03). The medium grained gabbro is composed of mafic minerals and feldspars of 1 mm diameter, while the coarse grained gabbro contains mafic minerals and feldspars with grains up to 5 mm long.

In thin section, the metabasalts contain fine-grained quartz (100 μm), with TDBHons014.01 containing calcite and chlorite and TDBHons020.01 having epidote as fine grains and veins 100 μm across. The medium grained gabbro contains plagioclase (altered), chlorite and clinopyroxene with the opaque minerals replaced by titanite. It has a low-grade metamorphic overprint. The coarse grained gabbros contain plagioclase with fine muscovite showing a strong preferred orientation, coarse clinopyoxene with a preferred orientation and minor quartz.

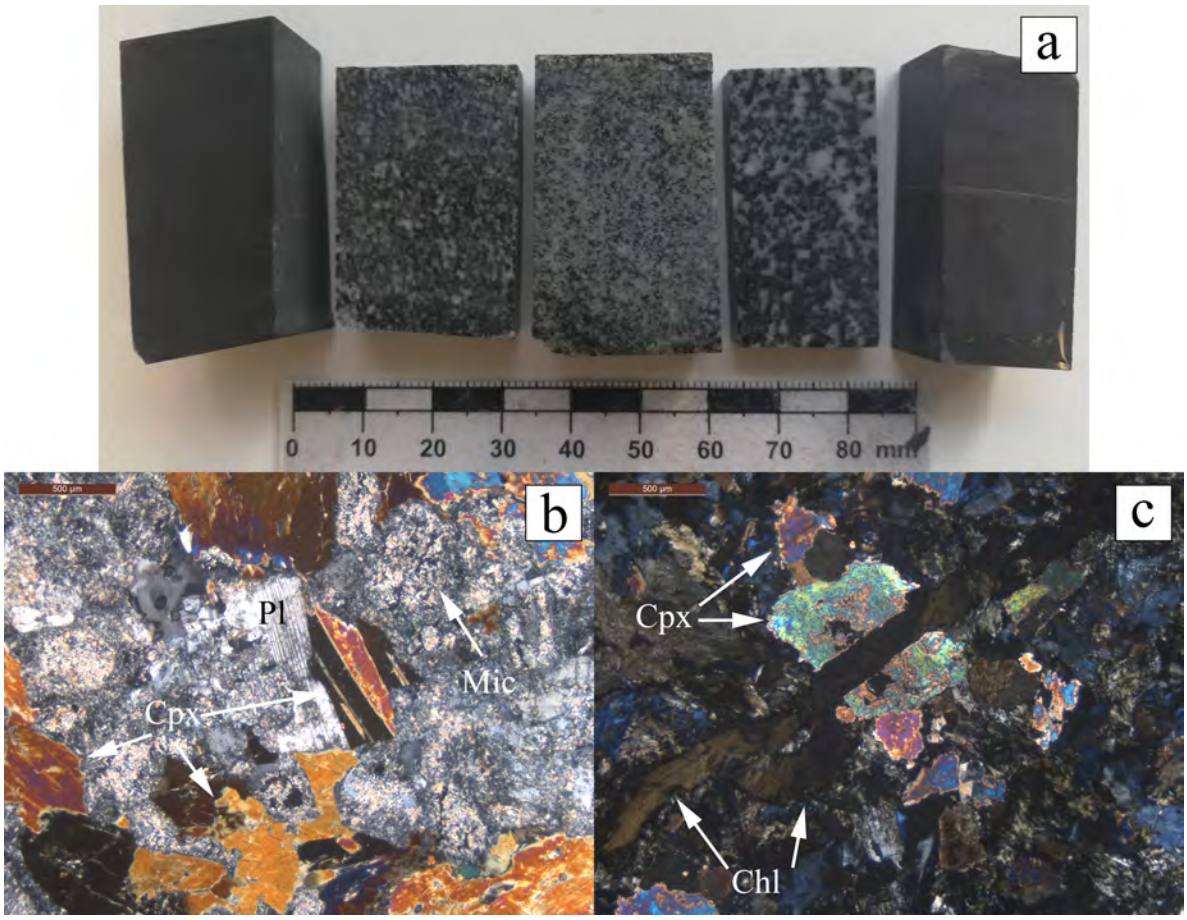

Figure B15: a) Blocks of (l-r) TDBHons014.01, TDBHons019.01, TDBHons019.02, TDBHons019.03 and TDBHons020.01. b) Plagioclase (Pl) and clinopyroxne (Cpx) within a fine-grained mica (Mic) matrix in TDBHons019.03. Length of scale bar = 500 μm. c) Chlorite (Chl) vein that has grown through a clinopyroxene (Cpx) grain in TDBHons019.02. Length of scale bar = 500 μm.

Appendix C - Geochemistry Data

Geochemical analysis of whole rock samples was performed at Intertek (Minerals) in Adelaide. The method of analysis, detection limits (Table C1) and raw geochemistry data (Table C2) are all reported in this appendix. Powders were milled in tungsten carbide ring mill and may conatain elevated tungsten concentrations. Where the element concentration is below detection limit, a dash (-) is present.

Table C1: Methods used for acquiring geochemistry data with their detection limits.

Element	Detection Limit	Units	Method	Element	Detection Limit	Units	Method
Al_2O_3	0.02	%	FB6/OE	Ni	1	ppm	4AB/OE
Ba	0.5	ppm	FB6/MS	P_2O_5	0.03	%	FB6/OE
CaO	0.02	%	FB6/OE	Pr	0.05	ppm	FB6/MS
Ce	0.5	ppm	FB6/MS	Rb	0.1	ppm	FB6/MS
Cr	20	ppm	FB6/OE	S	0.01	%	FB6/OE
Cs	0.05	ppm	FB6/MS	Sc	10	ppm	FB6/OE
Dy	0.05	ppm	FB6/MS	SiO_2	0.03	%	FB6/OE
Er	0.05	ppm	FB6/MS	Sm	0.05	ppm	FB6/MS
Eu	0.05	ppm	FB6/MS	Sn	1	ppm	FB6/MS
Fe_2O_3	0.02	%	FB6/OE	Sr	0.2	ppm	FB6/MS
Ga	0.1	ppm	FB6/MS	Ta	0.1	ppm	FB6/MS
Gd	0.05	ppm	FB6/MS	Tb	0.02	ppm	FB6/MS
Hf	0.1	ppm	FB6/MS	Th	0.05	ppm	FB6/MS
Ho	0.02	ppm	FB6/MS	TiO_2	0.02	%	FB6/OE
K_2O	0.02	%	FB6/OE	Tm	0.05	ppm	FB6/MS
La	0.2	ppm	FB6/MS	U	0.05	ppm	FB6/MS
Lu	0.02	ppm	FB6/MS	V	10	ppm	FB6/OE
MgO	0.02	%	FB6/OE	W	1	ppm	FB6/MS
MnO	0.02	%	FB6/OE	Y	0.5	ppm	FB6/MS
Na_2O	0.02	%	FB6/OE	Yb	0.05	ppm	FB6/MS
Nb	0.1	ppm	FB6/MS	Zr	1	ppm	FB6/MS
Nd	0.1	ppm	FB6/MS	LOI-1000	0.01	%	LOI/GR

FB6/OE	Lithium Borate Fusion ICP-OES
FB6/MS	Lithium Borate Fusion ICP-MS
4AB/OE	4 Acid Digest ICP-OES
LOI/GR	Lost on Ignition by Thermo Gravimetric Analysis

Table C2: Raw geochemistry data for samples analysed as part of this project.

Sample		TDBHons 003.01	TDBHons 005.01	TDBHons 006.01	TDBHons 007.01	TDBHons 008.01	TDBHons 009.01
Rock Unit		Kimo Diorite	Honeysuckle Beds	North Mooney Complex	Bogong Granite	Wermatong Metabasalt	Benwerrin Diorite
Lithology		Diorite	Gabbro	Diorite	Granite	Mafic Schist	Gabbro
SiO_2	%	59.2	52.67	51.53	69.03	48.34	51.82
TiO_2	%	1.02	0.62	0.66	0.26	2.26	2.66
Al_2O_3	%	16.08	15.11	17.24	13.55	11.41	15.65
Fe_2O_3	%	6.52	8.01	6.8	2.9	11.93	11.9
MnO	%	0.11	0.14	0.12	0.06	0.16	0.16
MgO	%	2.85	8.44	8.39	0.2	11.17	3.89
CaO	%	5.37	10.2	10.82	1.56	8.89	7.97
Na_2O	%	4.14	2.84	3.01	4.42	2.31	3.26
K_2O	%	2.01	0.21	0.19	3.46	0.1	1.05
P_2O_5	%	0.18	0.05	0.12	0.06	0.21	0.58
LOI	%	2.36	1.81	1.15	0.44	0.72	0.36
Total	%	99.88	100.13	100.05	95.94	97.56	99.31
S	%	0.04	0.03	0.02	-	0.06	0.01
Sc	ppm	16	42	34	-	31	30
V	ppm	117	204	175	-	234	325
Cr	ppm	32	380	346	-	612	-
Ni	ppm	21	131	148	1	397	2
Ga	ppm	18.6	14	13.8	19.7	16.9	20.9
Rb	ppm	50.8	7.9	5.7	119.4	2	51.8
Sr	ppm	332.7	196.5	221.4	109.2	271.7	319.4
Cs	ppm	1.73	0.18	0.11	2.9	0.2	4.41
Ba	ppm	641.5	75.3	52.8	684	27.9	249.2
W	ppm	301	102	80	706	50	91
Sn	ppm	2	-	1	3	1	3
Th	ppm	7.73	0.73	0.88	15.77	1.03	4.14
U	ppm	2.76	0.2	0.22	3.41	0.34	0.77
Nb	ppm	12.9	1.5	3.1	21.4	14.6	13.3
Ta	ppm	1.2	0.1	0.2	1.7	1	1.2
Zr	ppm	211	45	46	267	137	109
Hf	ppm	5.4	1.2	1.4	6.9	3.7	2.8
Y	ppm	28.6	18.6	17.7	49.6	24.2	24.9
La	ppm	29.9	4.8	7.1	69.4	12.3	22.6
Ce	ppm	56.1	9.9	14.1	138.7	27.4	46.3

Sample		TDBHons 003.01	TDBHons 005.01	TDBHons 006.01	TDBHons 007.01	TDBHons 008.01	TDBHons 009.01
Rock Unit		Kimo Diorite	Honeysuckle Beds	North Mooney Complex	Bogong Granite	Wermatong Metabasalt	Benwerrin Diorite
Lithology		Diorite	Gabbro	Diorite	Granite	Mafic Schist	Gabbro
Pr	ppm	6.42	1.51	1.89	13.58	3.84	5.59
Nd	ppm	24.4	7	8.5	49.3	18.5	24
Sm	ppm	5.37	2.3	2.18	9.85	5.34	5.42
Eu	ppm	1.42	0.83	0.73	1.58	1.6	1.9
Gd	ppm	5.02	2.47	2.75	8.63	5.2	5.5
Tb	ppm	0.76	0.43	0.46	1.36	0.81	0.75
Dy	ppm	4.77	2.96	2.8	8.99	4.77	4.56
Ho	ppm	0.95	0.67	0.61	1.77	0.88	0.91
Er	ppm	2.8	1.93	1.84	4.87	2.44	2.46
Tm	ppm	0.39	0.27	0.23	0.73	0.27	0.3
Yb	ppm	2.51	1.93	1.63	4.5	1.93	1.94
Lu	ppm	0.37	0.24	0.25	0.62	0.26	0.28

Data for more samples begin on the next page

Sample		TDBHons 010.01	TDBHons 011.01	TDBHons 012.01	TDBHons 012.02	TDBHons 013.01	TDBHons 013.02
Rock Unit		Gocup Granite	Gocup Granite	Warrienbah granite	Warrienbah granite	Snowball Metabasic Igneous Complex	Snowball Metabasic Igneous Complex
Lithology		Granite	Granite	Granite	Granite	Diorite Hybrid	Hornfels
SiO_2	%	74.99	73.54	73.13	68.76	48.66	67.91
TiO_2	%	0.09	0.1	0.19	0.69	1.38	0.62
Al_2O_3	%	12.91	12.64	12.15	14.03	15.36	15.84
Fe_2O_3	%	0.9	1.41	1.42	4.78	10.41	6.06
MnO	%	0.02	0.05	-	0.08	0.2	0.11
MgO	%	0.17	0.25	0.2	1.38	6.09	2.44
CaO	%	0.14	0.25	0.67	2.51	14.39	0.5
Na_2O	%	2.72	2.75	3.05	2.52	2.07	1.35
K_2O	%	5.23	5.14	4.87	4.2	0.25	3.77
P_2O_5	%	0.09	0.16	-	0.16	0.11	0.08
LOI	%	1.02	0.92	0.48	0.55	1.34	2.34
Total	%	98.28	97.21	96.16	99.67	100.29	101.02
S	%	-	-	-	0.01	0.03	-
Sc	ppm	-	-	-	13	43	15
V	ppm	-	11	-	80	267	108
Cr	ppm	-	-	-	24	106	81
Ni	ppm	-	1	1	11	48	38
Ga	ppm	16.8	17.2	16.7	18.8	23.5	21.3
Rb	ppm	250.3	265.1	200.2	138.5	7.5	146.3
Sr	ppm	23.6	28.6	49.1	157.2	120.9	58.5
Cs	ppm	7.85	10.61	6.61	4.43	0.36	9.03
Ba	ppm	120.5	129.5	566.7	725.2	136.5	460.2
W	ppm	489	353	393	263	163	138
Sn	ppm	4	8	5	4	1	5
Th	ppm	5.07	5.8	22.77	17.46	0.57	14.58
U	ppm	3.43	7.36	5.32	2.05	0.23	2.95
Nb	ppm	8.5	11.1	11.3	14.4	2.2	13.2
Ta	ppm	1.5	2.3	1.2	1.4	0.2	1.2
Zr	ppm	56	62	133	240	92	135
Hf	ppm	2	2.3	4.3	6.3	2.7	3.9
Y	ppm	21.4	24.8	40.7	38.5	37.6	30.8
La	ppm	8.7	10.5	34.9	46.6	5.7	38
Ce	ppm	17.9	21.5	71.9	89.3	12.9	73
Pr	ppm	2.18	2.61	7.71	10.06	2.24	8.45

Sample		TDBHons 010.01	TDBHons 011.01	TDBHons 012.01	TDBHons 012.02	TDBHons 013.01	TDBHons 013.02
Rock Unit		Gocup Granite	Gocup Granite	Warrienbah granite	Warrienbah granite	Snowball Metabasic Igneous Complex	Snowball Metabasic Igneous Complex
Lithology		Granite	Granite	Granite	Granite	Diorite Hybrid	Hornfels
Nd	ppm	8.1	10	27.5	37.7	11.3	31
Sm	ppm	2.41	2.85	5.79	7.9	3.79	6.42
Eu	ppm	0.15	0.33	0.73	1.59	1.36	1.15
Gd	ppm	2.38	3.05	5.47	6.69	5.06	5.6
Tb	ppm	0.52	0.6	0.97	1.08	0.9	0.79
Dy	ppm	3.48	4	6.38	6.56	6.12	5.08
Ho	ppm	0.67	0.77	1.38	1.35	1.39	1.11
Er	ppm	1.87	2.28	4.15	3.66	3.84	2.97
Tm	ppm	0.3	0.32	0.62	0.53	0.58	0.43
Yb	ppm	2	2	4	3.28	3.6	2.94
Lu	ppm	0.26	0.28	0.54	0.44	0.54	0.39

Data for more samples begin on the next page

Sample		TDBHons 014.01	TDBHons 015.01	TDBHons 016.01	TDBHons 017.01	TDBHons 018.01	TDBHons 019.01
Rock Unit		Wyangle Formation	Blowering Formation	Honeysuckle Beds	Honeysuckle Beds	Honeysuckle Beds	Wyangle Formation
Lithology		Meta-basalt	Dacite	Rhyolite	Dacite	Dacite	Gabbro
SiO_2	%	59.33	69.08	43.86	72.5	70.08	56.02
TiO_2	%	0.76	0.6	0.38	0.46	0.53	0.89
Al_2O_3	%	14.58	14.02	13.79	12.63	13.98	17.04
Fe_2O_3	%	6.76	4.35	8.01	3.33	4.14	7.97
MnO	%	0.18	0.05	0.14	0.06	0.06	0.17
MgO	%	3.38	1.97	9.84	1.3	1.5	4.76
CaO	%	3.17	0.79	21.24	1.68	2.04	6.12
Na_2O	%	5.73	2.93	0.04	2.51	3.54	5.05
K_2O	%	1.02	3.89	-	3.24	2.72	1.41
P_2O_5	%	0.27	0.18	-	0.04	0.09	0.1
LOI	%	4.4	2.15	2.53	1.73	1.39	1.17
Total	%	99.59	100.01	99.87	99.48	100.07	100.71
S	%	0.01	-	0.04	-	-	0.01
Sc	ppm	18	13	44	12	14	31
V	ppm	158	84	209	67	90	171
Cr	ppm	79	50	447	25	34	-
Ni	ppm	49	21	272	52	30	140
Ga	ppm	14.6	17.2	10.4	14.3	16.7	16.8
Rb	ppm	19.3	170.3	0.2	101.7	105.5	54
Sr	ppm	512.3	124.4	73.9	181.3	246	315.5
Cs	ppm	0.41	2.91	-	1.09	2.37	0.46
Ba	ppm	559.4	607.2	11.1	632.7	752.1	227.4
W	ppm	80	249	83	70	113	86
Sn	ppm	-	2	-	4	5	6
Th	ppm	5.55	16.11	0.81	12.14	13.55	4.76
U	ppm	1.77	2.94	0.32	2.47	3.01	0.55
Nb	ppm	11	11.7	1	8.1	9.3	4.6
Ta	ppm	0.7	1.1	-	0.9	1	0.4
Zr	ppm	108	173	25	142	157	101
Hf	ppm	2.9	4.6	0.9	3.8	4.3	3.2
Y	ppm	17.2	36.3	11.2	29.4	37.2	32.8
La	ppm	28.7	37	4.8	28.4	35.5	15.5
Ce	ppm	53.9	70.5	9.3	54.3	68.2	33.7
Pr	ppm	6.25	8.15	1.32	6.3	7.95	4.49
Nd	ppm	24.5	32.7	5.9	23.8	30	18.1

Sample		TDBHons 014.01	TDBHons 015.01	TDBHons 016.01	TDBHons 017.01	TDBHons 018.01	TDBHons 019.01
Rock Unit		Wyangle Formation	Blowering Formation	Honeysuckle Beds	Honeysuckle Beds	Honeysuckle Beds	Wyangle Formation
Lithology		Meta-basalt	Dacite	Rhyolite	Dacite	Andesite	Gabbro
Sm	ppm	5.15	6.95	1.49	4.6	6.45	4.73
Eu	ppm	1.35	1.16	0.48	0.87	1.1	1.3
Gd	ppm	3.8	6.23	1.58	4.55	6.1	5.19
Tb	ppm	0.55	0.96	0.3	0.76	0.97	0.9
Dy	ppm	3.13	5.68	1.8	4.86	6.16	5.45
Ho	ppm	0.64	1.17	0.38	1.07	1.38	1.15
Er	ppm	1.72	3.3	1.17	2.93	3.57	3.37
Tm	ppm	0.25	0.47	0.18	0.44	0.51	0.5
Yb	ppm	1.53	2.87	1.15	2.68	3.38	2.99
Lu	ppm	0.26	0.44	0.19	0.39	0.48	0.47

Data for more samples begin on the next page

Sample		TDBHons 019.02	TDBHons 019.03	TDBHons 020.01	TDBHons 021.01	TDBHons 022.01	TDBHons 023.01
Rock Unit		Wyangle Formation	Wyangle Formation	Wyangle Formation	Brungle Creek Metabasalt	Killimicat Granite	Frampton Volcanics
Lithology		Gabbro	Gabbro	Meta-basalt	Chert	Granite	Metatuff
SiO_2	%	36.22	52.12	67.51	82.04	75.76	69.48
TiO_2	%	0.56	0.64	0.56	0.26	0.17	0.62
Al_2O_3	%	19.53	18.36	13.35	5.61	12.34	13.51
Fe_2O_3	%	8.96	6.44	4.86	4.98	1.51	4.51
MnO	%	0.12	0.13	0.15	0.09	-	0.09
MgO	%	10.48	5.51	2.2	2.32	0.16	1.73
CaO	%	17.72	7.67	1.94	3.27	0.63	2.72
Na_2O	%	0.02	2.76	4.58	1.14	3.29	2.01
K_2O	%	-	3.52	1.58	1.43	4.69	2.76
P_2O_5	%	0.1	0.06	0.28	0.04	-	0.15
LOI	%	4.45	1.51	1.51	0.72	0.54	2.76
Total	%	98.18	98.74	98.52	101.91	99.09	100.34
S	%	0.02	0.02	-	0.01	-	-
Sc	ppm	48	29	15	10	-	15
V	ppm	263	170	109	57	13	68
Cr	ppm	419	-	47	39	-	26
Ni	ppm	216	38	24	33	1	24
Ga	ppm	12.4	14.8	13.1	5.8	18.8	15.6
Rb	ppm	0.4	131.6	32.7	16.9	222.1	108.8
Sr	ppm	402.6	382.1	782.8	90.4	46.2	385.1
Cs	ppm	0.11	0.7	0.5	0.23	7.79	3
Ba	ppm	18.9	505.3	822.3	286.2	563.9	833.3
W	ppm	33	111	100	300	376	150
Sn	ppm	-	6	1	-	4	3
Th	ppm	1.7	2.5	7.64	1.3	18.94	10.68
U	ppm	0.51	0.58	1.94	0.42	3.71	2.01
Nb	ppm	2.6	3.5	8.4	1.9	17.2	8.5
Ta	ppm	0.1	0.3	0.6	0.2	1.9	0.8
Zr	ppm	38	65	104	34	138	148
Hf	ppm	1.3	1.8	2.7	1	4.6	4.1
Y	ppm	17.6	23.7	17.7	8.5	52.6	36.9
La	ppm	11.4	11.2	36.2	3.7	47.7	30.2
Ce	ppm	21.6	23.3	62.2	9.9	93.8	57.6
Pr	ppm	2.75	2.99	6.82	1.36	10.9	6.81
Nd	ppm	10.9	12.4	26	5.9	41.1	26.6

Sample		TDBHons 019.02	TDBHons 019.03	TDBHons 020.01	TDBHons 021.01	TDBHons 022.01	TDBHons 023.01
Rock Unit		Wyangle Formation	Wyangle Formation	Wyangle Formation	Brungle Creek Metabasalt	Killimicat Granite	Frampton Volcanics
Lithology		Gabbro	Gabbro	Meta-basalt	Chert	Granite	Metatuff
Sm	ppm	2.66	3.17	4.79	1.52	8.78	5.47
Eu	ppm	1.11	0.9	1.23	0.35	1.02	1.36
Gd	ppm	2.91	3.29	3.93	1.53	8.41	5.17
Tb	ppm	0.46	0.6	0.52	0.26	1.31	0.78
Dy	ppm	2.83	3.88	3.1	1.56	8.36	4.69
Ho	ppm	0.7	0.86	0.64	0.36	1.79	1.05
Er	ppm	1.9	2.45	1.64	0.91	4.82	2.89
Tm	ppm	0.28	0.39	0.23	0.16	0.78	0.39
Yb	ppm	1.8	2.31	1.48	0.86	4.69	2.39
Lu	ppm	0.29	0.33	0.24	0.18	0.68	0.38

Data for more samples begin on the next page

Sample		TDBHons 024.01	TDBHons 025.01	TDBHons 026.01
Rock Unit		Kimo Diorite	Long Tunnel Metabasic Igneous Complex	Long Tunnel Metabasic Igneous Complex
Lithology		Diorite	Basalt	Basalt
SiO_2	%	61.39	48.82	61.49
TiO_2	%	0.95	0.87	0.65
Al_2O_3	%	16	19.91	16.36
Fe_2O_3	%	5.95	10.66	7.77
MnO	%	0.1	0.14	0.09
MgO	%	2.52	5.12	3.41
CaO	%	4.85	4.55	2.42
Na_2O	%	4.18	4.91	5.52
K_2O	%	2.06	1.01	0.89
P_2O_5	%	0.19	0.27	0.17
LOI	%	1.6	2.88	1.7
Total	%	99.8	99.17	100.51
S	%	0.01	0.03	0.04
Sc	ppm	14	31	23
V	ppm	107	239	193
Cr	ppm	30	-	-
Ni	ppm	19	14	11
Ga	ppm	17.3	18.4	12.5
Rb	ppm	58.8	20.8	20.7
Sr	ppm	309.8	625.5	292.5
Cs	ppm	1.33	0.35	0.43
Ba	ppm	591.9	717.4	510
W	ppm	107	34	129
Sn	ppm	2	1	-
Th	ppm	9.21	5.9	4.14
U	ppm	3.5	2.23	1.65
Nb	ppm	12.6	4.7	3.5
Ta	ppm	1.1	0.3	0.3
Zr	ppm	204	100	72
Hf	ppm	5.5	2.9	2.1
Y	ppm	26.5	24.2	18.2
La	ppm	31.1	28	20.4
Ce	ppm	58.3	54.7	40.1
Pr	ppm	6.49	6.68	4.93
Nd	ppm	24.8	27.4	20.1
Sm	ppm	5.17	6.24	4.24

Sample		TDBHons 024.01	TDBHons 025.01	TDBHons 026.01
Rock Unit		Kimo Diorite	Long Tunnel Metabasic Igneous Complex	Long Tunnel Metabasic Igneous Complex
Lithology		Diorite	Basalt	Basalt
Eu	ppm	1.36	1.5	1.19
Gd	ppm	4.7	5.02	3.58
Tb	ppm	0.73	0.72	0.52
Dy	ppm	4.46	4.4	3.09
Ho	ppm	1.01	0.91	0.67
Er	ppm	2.67	2.54	1.85
Tm	ppm	0.37	0.37	0.24
Yb	ppm	2.58	2.33	1.77
Lu	ppm	0.37	0.37	0.26

Appendix D - Geochronology Data

Geochronology data from the analysed zircons appear in this appendix. The following tables are in order of sample number (like in Sections 3.3). Within the tables, they are split into the 2 sessions and further divided by concordant and discordant data. Analysis spots are ordered by $^{206}Pb/^{238}U$ age.

Table D1: Geochronology data for the zircons from TDBHons003.01 (Kimo Diorite).

Spot Number	Mean U/Th	$^{207}Pb/^{235}U$	$\pm2\sigma$	$^{207}Pb/^{206}Pb$	$\pm2\sigma$	$^{206}Pb/^{238}U$	$\pm2\sigma$	Date (Ma)	$\pm2\sigma$ (Ma)	Conc (%)
Session 1										
Concordant Data (90 - 110 % Concordance)										
1-9	1.351	0.5075	0.0090	0.0556	0.0003	0.0661	0.0011	412.5	6.6	94.7
1-23	1.322	0.5098	0.0085	0.0559	0.0004	0.0661	0.0009	412.6	5.5	92.4
1-16	1.069	0.5079	0.0087	0.0558	0.0003	0.0661	0.0010	412.9	6.1	93.1
1-22	1.263	0.5084	0.0086	0.0556	0.0003	0.0663	0.0009	413.6	5.6	95.0
1-19	1.089	0.5092	0.0103	0.0557	0.0002	0.0664	0.0012	414.1	7.4	93.9
1-17	1.437	0.5142	0.0099	0.0559	0.0004	0.0667	0.0009	416.0	5.7	93.1
1-11	1.812	0.5116	0.0103	0.0558	0.0003	0.0667	0.0013	416.5	7.9	93.7
1-13	1.142	0.5113	0.0080	0.0554	0.0003	0.0669	0.0008	417.2	5.0	97.4
1-4	1.805	0.5128	0.0084	0.0558	0.0003	0.0669	0.0011	417.3	6.3	94.4
1-1	1.328	0.5111	0.0085	0.0554	0.0003	0.0669	0.0010	417.6	5.7	97.9
1-8b	0.782	0.5139	0.0089	0.0557	0.0003	0.0670	0.0009	417.9	5.5	95.0
1-5	1.184	0.5168	0.0080	0.0559	0.0003	0.0671	0.0008	418.4	5.1	93.6
1-21	1.125	0.5155	0.0086	0.0557	0.0003	0.0671	0.0008	418.4	5.1	95.0
1-12	2.117	0.5155	0.0084	0.0559	0.0003	0.0671	0.0009	418.7	5.5	94.1
1-7	1.858	0.5147	0.0081	0.0555	0.0003	0.0672	0.0008	419.0	5.0	97.4
1-10	1.578	0.5170	0.0082	0.0558	0.0003	0.0672	0.0009	419.4	5.2	94.5
1-2	1.559	0.5175	0.0083	0.0557	0.0003	0.0674	0.0009	420.7	5.1	95.8
1-14	1.661	0.5199	0.0084	0.0560	0.0004	0.0675	0.0009	420.8	5.3	93.3
1-6	1.119	0.5201	0.0081	0.0554	0.0002	0.0681	0.0008	424.5	5.1	99.0
1-20	1.047	0.5230	0.0080	0.0555	0.0002	0.0683	0.0008	426.0	5.1	98.9
1-8	0.782	0.5256	0.0084	0.0555	0.0003	0.0686	0.0009	427.6	5.5	99.2
1-12b	2.117	0.5294	0.0085	0.0557	0.0004	0.0689	0.0009	429.3	5.4	98.2
1-18	1.680	0.5306	0.0082	0.0557	0.0003	0.0690	0.0008	430.3	5.1	97.7
1-15	1.256	0.5435	0.0094	0.0566	0.0004	0.0700	0.0010	435.9	5.8	92.1
1-14b	1.661	0.5422	0.0096	0.0558	0.0004	0.0705	0.0010	439.4	6.1	99.6
Discordant Data (<90% and >110% Concordance)										
1-24	1.408	0.4485	0.0095	0.0585	0.0006	0.0555	0.0012	348.3	7.3	63.8
1-3	1.924	0.4798	0.0099	0.0576	0.0004	0.0606	0.0014	379.1	8.2	74.1
1-25	1.772	0.4802	0.0082	0.0570	0.0003	0.0610	0.0008	381.4	5.1	77.6

Spot Number	Mean U/Th	$^{207}Pb/^{235}U$	$\pm 2\sigma$	$^{207}Pb/^{206}Pb$	$\pm 2\sigma$	$^{206}Pb/^{238}U$	$\pm 2\sigma$	Date (Ma)	$\pm 2\sigma$ (Ma)	Conc (%)
Session 2										
Concordant Data (90 - 110 % Concordance)										
2-14	0.465	0.5094	0.0129	0.0540	0.0013	0.0674	0.0013	420.4	7.9	103.2
2-11	1.847	0.5007	0.0128	0.0553	0.0013	0.0675	0.0013	421.0	7.9	99.4
2-23	0.480	0.5162	0.0135	0.0548	0.0012	0.0693	0.0013	431.6	8.0	100.5
Discordant Data (<90% and >110% Concordance)										
2-22	0.772	0.3964	0.0163	0.0631	0.0024	0.0477	0.0010	300.4	6.1	42.3
2-12	0.428	0.6443	0.0851	0.0937	0.0096	0.0490	0.0014	308.0	8.8	23.7
2-15	0.761	0.4813	0.0316	0.0679	0.0039	0.0512	0.0013	321.6	8.0	35.1
2-9	0.880	0.4499	0.0219	0.0568	0.0024	0.0594	0.0015	372.1	9.4	64.6
2-6	0.776	0.4796	0.0210	0.0595	0.0024	0.0605	0.0016	380.1	9.5	61.1
2-8	0.841	0.4829	0.0295	0.0577	0.0028	0.0611	0.0013	382.5	8.1	58.6
2-20	0.835	0.4894	0.0222	0.0572	0.0019	0.0633	0.0013	395.7	7.8	71.0
2-21	0.881	0.8057	0.0411	0.0942	0.0051	0.0639	0.0018	398.9	11.1	27.7
2-4	0.828	0.5037	0.0217	0.0572	0.0020	0.0639	0.0013	399.3	7.6	67.0
2-17	0.935	0.5011	0.0253	0.0569	0.0022	0.0639	0.0014	399.3	8.6	69.8
2-24	0.809	0.5252	0.0232	0.0574	0.0024	0.0652	0.0014	407.0	8.3	69.5
2-3	1.066	0.4948	0.0220	0.0557	0.0022	0.0664	0.0013	414.5	8.0	80.1
2-5	0.693	0.5201	0.0212	0.0570	0.0017	0.0668	0.0013	416.7	8.0	79.8
2-2	0.724	0.5007	0.0176	0.0551	0.0016	0.0671	0.0013	418.4	8.0	89.7
2-1	1.260	0.5097	0.0201	0.0554	0.0017	0.0675	0.0013	421.9	7.7	82.9
2-10	0.632	0.5198	0.0166	0.0574	0.0016	0.0677	0.0013	422.3	7.8	80.0
2-13	1.274	0.5149	0.0247	0.0569	0.0022	0.0678	0.0014	422.6	8.7	74.1
2-19	0.824	0.5243	0.0183	0.0560	0.0018	0.0689	0.0013	429.3	8.0	83.4
2-18	0.434	0.5580	0.0173	0.0587	0.0016	0.0695	0.0014	433.1	8.2	75.6
2-16	0.933	0.5295	0.0202	0.0555	0.0019	0.0695	0.0014	433.2	8.5	85.0
2-7	0.865	0.5446	0.0384	0.0564	0.0031	0.0712	0.0017	443.5	10.3	64.5

Table D2: Geochronology data for the zircons from TDBHons007.01 (Bogong Granite).

Spot Number	Mean U/Th	$^{207}Pb/^{235}U$	$\pm2\sigma$	$^{207}Pb/^{206}Pb$	$\pm2\sigma$	$^{206}Pb/^{238}U$	$\pm2\sigma$	Date (Ma)	$\pm2\sigma$ (Ma)	Conc (%)
Session 1										
Concordant Data (90 - 110 % Concordance)										
1-10b	2.243	0.5078	0.0065	0.0556	0.0003	0.0663	0.0006	414.0	3.5	95.1
1-2	1.575	0.5070	0.0068	0.0552	0.0003	0.0666	0.0006	415.9	3.8	99.6
1-12	0.982	0.5158	0.0104	0.0563	0.0004	0.0667	0.0010	416.3	6.2	90.0
1-8b	1.295	0.5117	0.0101	0.0559	0.0004	0.0668	0.0010	416.7	5.9	93.6
1-14	1.423	0.5123	0.0066	0.0556	0.0003	0.0668	0.0006	417.0	3.5	96.2
1-10	2.243	0.5126	0.0070	0.0556	0.0004	0.0670	0.0006	417.8	3.9	96.4
1-5b	1.299	0.5147	0.0065	0.0556	0.0003	0.0671	0.0006	418.7	3.8	96.2
1-24b	2.570	0.5157	0.0066	0.0557	0.0004	0.0672	0.0006	419.2	3.5	95.1
1-8	1.295	0.5186	0.0065	0.0558	0.0004	0.0673	0.0006	419.9	3.5	94.9
1-1	1.417	0.5114	0.0064	0.0553	0.0003	0.0673	0.0006	420.0	3.6	99.3
1-24	2.570	0.5189	0.0067	0.0557	0.0004	0.0674	0.0006	420.8	3.4	95.5
1-18	1.467	0.5163	0.0061	0.0553	0.0003	0.0677	0.0006	422.5	3.4	100.2
1-5	1.299	0.5191	0.0066	0.0556	0.0003	0.0677	0.0006	422.6	3.4	97.4
1-14b	1.423	0.5205	0.0067	0.0558	0.0004	0.0678	0.0006	422.7	3.6	95.0
1-2b	1.575	0.5165	0.0063	0.0554	0.0003	0.0679	0.0006	423.2	3.5	99.5
1-7	1.864	0.5282	0.0120	0.0561	0.0003	0.0681	0.0016	424.8	9.4	92.6
1-1b	1.417	0.5195	0.0062	0.0553	0.0003	0.0682	0.0006	425.5	3.6	100.5
1-9	1.450	0.5191	0.0068	0.0553	0.0003	0.0683	0.0006	425.8	3.7	100.9
1-20	1.608	0.5246	0.0063	0.0557	0.0003	0.0683	0.0006	425.9	3.5	97.3
1-15	1.645	0.5290	0.0075	0.0555	0.0004	0.0693	0.0006	432.2	3.8	100.0
1-17	1.756	0.5441	0.0076	0.0565	0.0005	0.0698	0.0006	434.8	3.6	92.6
Discordant Data (<90% and >110% Concordance)										
1-11	0.985	0.5892	0.0076	0.0723	0.0006	0.0593	0.0005	371.1	3.1	37.4
1-22	2.990	0.5161	0.0081	0.0587	0.0006	0.0638	0.0006	398.9	3.4	72.3
1-13	1.943	0.5489	0.0078	0.0621	0.0006	0.0639	0.0008	399.5	5.0	59.3
1-6	1.542	0.5232	0.0066	0.0570	0.0004	0.0665	0.0006	415.0	3.4	84.5
1-16	1.379	0.5968	0.0076	0.0651	0.0005	0.0665	0.0006	415.3	3.4	53.7
1-3	1.760	0.7694	0.0440	0.0833	0.0043	0.0671	0.0008	418.6	5.0	33.6
1-23	1.391	0.6793	0.0319	0.0733	0.0034	0.0672	0.0006	419.4	3.5	42.1
1-4	1.388	0.8756	0.0445	0.0940	0.0040	0.0674	0.0007	420.8	4.4	28.3
1-19	1.529	0.5801	0.0089	0.0616	0.0006	0.0682	0.0006	425.1	3.5	64.5

Spot Number	Mean U/Th	$^{207}Pb/^{235}U$	$\pm 2\sigma$	$^{207}Pb/^{206}Pb$	$\pm 2\sigma$	$^{206}Pb/^{238}U$	$\pm 2\sigma$	Date (Ma)	$\pm 2\sigma$ (Ma)	Conc (%)
1-21	1.453	0.5740	0.0127	0.0598	0.0011	0.0696	0.0006	434.0	3.5	73.9
Session 2										
Concordant Data (90 - 110 % Concordance)										
2-15	1.134	0.4888	0.0155	0.0556	0.0014	0.0659	0.0012	411.2	7.4	91.4
2-19	1.150	0.5174	0.0101	0.0552	0.0010	0.0659	0.0013	411.7	8.0	94.8
2-5	0.788	0.5083	0.0149	0.0556	0.0014	0.0672	0.0012	419.4	7.5	93.1
Discordant Data (<90% and >110% Concordance)										
2-2	1.832	0.5873	0.0111	0.0720	0.0015	0.0572	0.0014	358.3	8.3	36.6
2-18	1.966	0.4827	0.0122	0.0571	0.0012	0.0606	0.0011	379.3	6.8	76.2
2-8	1.507	0.4957	0.0138	0.0592	0.0014	0.0611	0.0012	382.6	7.6	68.3
2-20	1.155	0.6594	0.0224	0.0795	0.0024	0.0616	0.0012	385.2	7.3	33.0
2-22	1.228	0.6080	0.0210	0.0727	0.0025	0.0619	0.0013	387.0	7.9	39.9
2-11	1.109	0.6309	0.0351	0.0740	0.0036	0.0622	0.0014	388.9	8.5	38.8
2-4	1.408	0.5027	0.0141	0.0579	0.0013	0.0632	0.0012	394.8	7.3	75.8
2-1	1.613	0.5343	0.0126	0.0604	0.0012	0.0634	0.0012	396.5	7.4	64.3
2-13	1.095	0.4793	0.0154	0.0560	0.0017	0.0641	0.0012	400.4	7.4	78.6
2-27	0.832	0.5151	0.0168	0.0585	0.0017	0.0643	0.0012	401.9	7.3	67.5
2-26	0.967	0.5213	0.0177	0.0577	0.0016	0.0656	0.0013	409.6	7.6	76.7
2-29	1.056	0.5959	0.0332	0.0665	0.0034	0.0662	0.0013	413.2	7.8	51.3
2-14	1.065	0.5305	0.0254	0.0592	0.0023	0.0664	0.0013	414.3	8.0	66.9
2-12	1.805	0.5367	0.0116	0.0580	0.0010	0.0670	0.0014	418.1	8.6	79.6
2-6	1.551	0.6035	0.0167	0.0664	0.0018	0.0677	0.0014	422.4	8.4	53.1
2-3	1.222	0.5301	0.0235	0.0564	0.0017	0.0681	0.0014	424.7	8.4	81.3
2-28	1.173	0.5397	0.0192	0.0579	0.0016	0.0684	0.0014	426.4	8.2	74.5
2-25	0.952	0.6017	0.0175	0.0647	0.0016	0.0684	0.0013	426.5	7.9	57.5
2-9	2.080	0.5369	0.0228	0.0579	0.0023	0.0685	0.0013	426.9	7.9	73.6
2-23	1.582	0.4994	0.0173	0.0555	0.0021	0.0687	0.0014	428.2	8.6	86.3
2-10	1.252	0.5873	0.0186	0.0623	0.0016	0.0691	0.0014	430.9	8.6	60.5
2-16	0.912	0.5346	0.0204	0.0574	0.0020	0.0692	0.0014	431.5	8.3	77.1
2-17	0.986	0.5587	0.0154	0.0590	0.0014	0.0696	0.0013	433.5	8.0	75.6
2-24	1.346	0.5225	0.0286	0.0550	0.0027	0.0698	0.0014	434.8	8.7	74.8
2-7	1.007	0.5321	0.0177	0.0566	0.0017	0.0698	0.0013	435.1	8.1	83.8
2-21	1.225	1.2856	0.0479	0.1314	0.0036	0.0724	0.0014	450.4	8.6	21.5

Table D3: Geochronology data for the zircons from TDBHons011.01 (Gocup Granite).

Spot Number	Mean U/Th	$^{207}Pb/^{235}U$	$\pm2\sigma$	$^{207}Pb/^{206}Pb$	$\pm2\sigma$	$^{206}Pb/^{238}U$	$\pm2\sigma$	Date (Ma)	$\pm2\sigma$ (Ma)	Conc (%)
Session 1										
Concordant Data (90 - 110 % Concordance)										
Main Population										
1-25	2.351	0.5129	0.0088	0.0560	0.0004	0.0665	0.0009	414.9	5.2	92.2
1-4	3.299	0.5116	0.0082	0.0557	0.0004	0.0666	0.0008	415.5	5.0	94.8
1-4b	3.299	0.5142	0.0088	0.0559	0.0005	0.0666	0.0009	415.8	5.2	93.1
1-20	7.738	0.5112	0.0077	0.0556	0.0003	0.0667	0.0008	416.4	4.9	96.0
1-21	2.396	0.5186	0.0094	0.0561	0.0005	0.0669	0.0008	417.3	5.1	92.0
1-26	3.223	0.5140	0.0083	0.0558	0.0003	0.0669	0.0008	417.6	5.0	94.0
1-24	1.372	0.5177	0.0084	0.0559	0.0003	0.0671	0.0009	418.4	5.2	93.9
1-16	2.496	0.5148	0.0081	0.0556	0.0003	0.0671	0.0008	418.9	4.9	96.5
1-2	1.977	0.5183	0.0087	0.0560	0.0004	0.0673	0.0009	420.1	5.5	92.9
1-7	5.935	0.5232	0.0083	0.0563	0.0004	0.0673	0.0008	420.1	5.0	90.4
1-15	5.693	0.5170	0.0080	0.0556	0.0003	0.0674	0.0008	420.4	5.0	96.8
1-9	3.579	0.5181	0.0082	0.0559	0.0003	0.0674	0.0008	420.5	5.0	94.3
1-13	2.170	0.5193	0.0085	0.0557	0.0003	0.0676	0.0009	421.8	5.3	96.0
1-19	5.108	0.5166	0.0080	0.0554	0.0003	0.0676	0.0008	421.8	5.0	98.9
1-18	1.636	0.5278	0.0083	0.0559	0.0003	0.0683	0.0008	425.9	5.0	95.1
Inherited Grains										
1-5	7.266	0.5335	0.0092	0.0557	0.0003	0.0698	0.0010	435.0	5.8	99.3
1-10	7.374	0.5461	0.0088	0.0560	0.0003	0.0708	0.0009	441.1	5.5	98.2
1-5b	7.266	0.5562	0.0085	0.0556	0.0003	0.0724	0.0009	450.8	5.3	103.2
1-2b	1.977	0.5630	0.0107	0.0560	0.0004	0.0728	0.0012	453.0	7.1	100.6
Discordant Data (<90% and >110% Concordance)										
1-3	4.678	1.8856	0.1545	0.3071	0.0357	0.0494	0.0024	310.3	14.8	9.5
1-11	2.680	1.4353	0.1374	0.1645	0.0115	0.0615	0.0018	384.9	10.7	15.9
1-6	2.349	0.9591	0.0827	0.1096	0.0085	0.0632	0.0011	395.1	6.9	23.2
1-12	3.385	0.5196	0.0089	0.0591	0.0004	0.0640	0.0009	399.6	5.4	70.3
1-22	4.005	0.5278	0.0081	0.0585	0.0004	0.0653	0.0008	407.5	4.9	74.4
1-23	2.591	1.5140	0.0592	0.1638	0.0051	0.0667	0.0009	416.1	5.2	16.8
1-8	3.840	0.5279	0.0083	0.0573	0.0003	0.0669	0.0008	417.3	4.9	83.1
1-17	1.815	0.8877	0.0347	0.0936	0.0030	0.0687	0.0009	428.4	5.3	28.8
1-14	5.580	0.8786	0.0170	0.0913	0.0021	0.0704	0.0015	438.3	9.2	30.4

Spot Number	Mean U/Th	$^{207}Pb/^{235}U$	$\pm 2\sigma$	$^{207}Pb/^{206}Pb$	$\pm 2\sigma$	$^{206}Pb/^{238}U$	$\pm 2\sigma$	Date (Ma)	$\pm 2\sigma$ (Ma)	Conc (%)
1-1	2.991	0.9811	0.0894	0.0986	0.0083	0.0712	0.0011	443.4	6.5	31.0
Session 2										
Concordant Data (90 - 110 % Concordance)										
2-32	4.794	0.5082	0.0250	0.0544	0.0020	0.0681	0.0015	424.5	9.0	92.2
2-13	5.536	0.5250	0.0199	0.0550	0.0017	0.0702	0.0015	437.1	9.1	93.3
Discordant Data (<90% and >110% Concordance)										
2-26	3.376	0.8179	0.0423	0.2628	0.0123	0.0236	0.0007	150.3	4.1	4.7
2-1	0.393	0.6728	0.0408	0.1547	0.0071	0.0328	0.0010	208.3	6.1	8.8
2-25	1.920	2.1331	0.0957	0.4336	0.0083	0.0363	0.0013	229.6	8.3	5.7
2-21	3.665	0.7918	0.0480	0.1151	0.0069	0.0516	0.0011	324.3	6.5	18.2
2-6	3.205	0.7902	0.0335	0.1087	0.0037	0.0541	0.0013	339.3	7.7	19.3
2-23	9.187	0.6395	0.0301	0.0791	0.0037	0.0593	0.0012	371.1	7.1	32.5
2-7	3.104	0.6407	0.0237	0.0758	0.0022	0.0626	0.0015	391.2	9.0	36.8
2-20	4.137	1.1446	0.0681	0.1308	0.0054	0.0641	0.0015	400.3	8.9	19.3
2-9	6.602	0.5663	0.0269	0.0630	0.0027	0.0648	0.0014	404.6	8.5	52.9
2-28	8.971	0.8237	0.0302	0.0940	0.0027	0.0649	0.0013	405.6	7.9	27.3
2-8	0.976	0.5000	0.0262	0.0557	0.0023	0.0650	0.0015	406.0	9.0	73.9
2-24	3.518	0.5243	0.0289	0.0572	0.0024	0.0655	0.0013	408.8	8.1	68.0
2-19	2.011	1.3173	0.0612	0.1486	0.0049	0.0659	0.0016	411.3	9.4	17.9
2-14	2.057	0.5202	0.0288	0.0570	0.0024	0.0660	0.0014	411.7	8.3	68.6
2-4	2.729	0.4873	0.0279	0.0545	0.0026	0.0660	0.0014	411.7	8.7	68.0
2-16	1.413	0.7834	0.0550	0.0872	0.0061	0.0660	0.0014	412.0	8.4	31.8
2-18	4.251	0.5044	0.0256	0.0567	0.0028	0.0660	0.0014	412.1	8.8	69.6
2-2	4.385	0.5255	0.0332	0.0562	0.0027	0.0661	0.0015	412.8	8.9	66.5
2-10	1.560	0.9703	0.0989	0.1077	0.0108	0.0664	0.0014	414.1	8.3	26.0
2-12	5.742	0.5096	0.0226	0.0559	0.0020	0.0664	0.0014	414.5	8.2	79.6
2-30	3.392	0.5499	0.0374	0.0600	0.0034	0.0666	0.0014	415.7	8.6	52.5
2-11	1.583	0.5132	0.0313	0.0554	0.0027	0.0672	0.0016	419.4	9.5	72.2
2-5	12.492	0.5195	0.0193	0.0563	0.0017	0.0673	0.0013	419.7	7.7	79.1
2-29	1.843	0.5551	0.0342	0.0576	0.0029	0.0674	0.0015	420.4	9.3	64.7
2-31	1.949	0.5310	0.0247	0.0573	0.0022	0.0677	0.0015	422.4	8.8	74.2
2-17	1.580	0.4975	0.0285	0.0552	0.0026	0.0678	0.0014	422.9	8.6	74.0
2-27	1.565	0.7088	0.0535	0.0730	0.0046	0.0682	0.0018	425.4	11.1	41.2
2-15	4.069	0.5407	0.0305	0.0565	0.0026	0.0684	0.0015	426.8	8.8	70.8
2-3	1.867	0.5538	0.0275	0.0588	0.0027	0.0686	0.0015	427.4	8.8	66.1

Spot Number	Mean U/Th	^{207}Pb $/^{235}U$	$\pm 2\sigma$	^{207}Pb $/^{206}Pb$	$\pm 2\sigma$	^{206}Pb $/^{238}U$	$\pm 2\sigma$	Date (Ma)	$\pm 2\sigma$ (Ma)	Conc (%)
2-22	2.756	0.5103	0.0239	0.0570	0.0025	0.0688	0.0014	429.0	8.5	75.6

Table D4: Geochronology data for the zircons from TDBHons012.01 (Warrienbah granite).

Spot Number	Mean U/Th	$^{207}Pb/^{235}U$	$\pm 2\sigma$	$^{207}Pb/^{206}Pb$	$\pm 2\sigma$	$^{206}Pb/^{238}U$	$\pm 2\sigma$	Date (Ma)	$\pm 2\sigma$ (Ma)	Conc (%)
Session 1										
Concordant Data (90 - 110 % Concordance)										
Main Population										
1-26b	1.152	0.5073	0.0082	0.0553	0.0003	0.0663	0.0008	413.9	5.1	98.0
1-23	3.809	0.5060	0.0081	0.0554	0.0002	0.0663	0.0008	414.1	5.1	97.1
1-26	1.152	0.5086	0.0081	0.0554	0.0003	0.0666	0.0008	415.5	5.1	97.0
1-23b	3.809	0.5126	0.0082	0.0555	0.0003	0.0668	0.0008	417.0	5.1	97.0
1-9	1.024	0.5125	0.0079	0.0554	0.0002	0.0671	0.0008	418.6	4.9	97.6
1-14	1.547	0.5177	0.0079	0.0551	0.0002	0.0681	0.0008	424.6	5.0	102.4
1-6	1.718	0.5290	0.0081	0.0557	0.0002	0.0687	0.0009	428.2	5.1	97.2
1-21	1.731	0.5285	0.0087	0.0556	0.0003	0.0688	0.0009	428.6	5.2	98.4
Inherited Grain										
1-5	0.651	0.5932	0.0185	0.0569	0.0005	0.0751	0.0015	466.7	9.1	96.3
Discordant Data (<90% and >110% Concordance)										
1-24	0.846	0.6100	0.0248	0.1074	0.0030	0.0410	0.0007	258.9	4.2	14.9
1-12	1.674	1.8502	0.0357	0.2850	0.0026	0.0477	0.0010	300.4	6.0	8.9
1-13	1.446	1.5451	0.0359	0.2172	0.0039	0.0520	0.0008	326.6	4.9	11.1
1-7	1.097	0.8703	0.0481	0.1179	0.0061	0.0539	0.0016	338.3	10.0	18.1
1-20	1.479	0.5798	0.0153	0.0670	0.0012	0.0627	0.0009	391.7	5.3	47.1
1-1	2.054	1.4516	0.0760	0.1675	0.0073	0.0632	0.0020	395.0	11.8	15.9
1-10	1.872	0.6880	0.0263	0.0766	0.0030	0.0655	0.0010	409.1	5.9	38.1
1-22	1.634	1.0598	0.0352	0.1184	0.0044	0.0657	0.0010	409.9	6.0	21.5
1-3	1.703	0.6410	0.0195	0.0704	0.0020	0.0664	0.0009	414.2	5.7	45.1
1-17	1.853	0.5366	0.0091	0.0577	0.0006	0.0676	0.0008	421.7	5.1	82.1
1-25	2.396	0.6525	0.0215	0.0695	0.0018	0.0680	0.0009	423.9	5.4	46.8
1-2	1.591	1.0554	0.1180	0.1099	0.0103	0.0681	0.0013	424.9	7.9	25.9
1-4	1.354	0.6070	0.0153	0.0636	0.0014	0.0692	0.0008	431.3	5.1	60.2
1-27	1.648	0.6084	0.0108	0.0638	0.0008	0.0693	0.0009	431.7	5.3	59.2
1-18	1.760	0.6596	0.0196	0.0690	0.0015	0.0693	0.0009	431.9	5.4	48.6
1-11	1.821	0.6000	0.0138	0.0625	0.0009	0.0696	0.0009	433.8	5.2	63.2
1-8	1.131	0.6303	0.1278	0.0659	0.0036	0.0723	0.0041	438.6	8.8	61.9
1-16	1.493	1.0782	0.0657	0.1099	0.0055	0.0705	0.0011	439.0	6.8	25.1

Spot Number	Mean U/Th	$^{207}Pb/^{235}U$	$\pm 2\sigma$	$^{207}Pb/^{206}Pb$	$\pm 2\sigma$	$^{206}Pb/^{238}U$	$\pm 2\sigma$	Date (Ma)	$\pm 2\sigma$ (Ma)	Conc (%)
1-15	1.304	0.6900	0.0234	0.0706	0.0025	0.0712	0.0011	443.4	6.4	48.1
1-19	1.701	1.3434	0.1947	0.1287	0.0159	0.0732	0.0016	455.5	9.5	24.6
Session 2										
Concordant Data (90 - 110 % Concordance)										
Main Population										
2-12	1.330	0.4827	0.0187	0.0540	0.0018	0.0660	0.0014	411.9	8.5	90.5
2-36	1.370	0.5129	0.0187	0.0549	0.0017	0.0672	0.0013	419.3	8.0	90.8
2-35	1.093	0.5125	0.0157	0.0548	0.0014	0.0681	0.0013	424.8	7.7	100.3
2-30	1.270	0.5147	0.0165	0.0545	0.0014	0.0683	0.0013	425.7	8.0	103.6
2-5	1.357	0.5317	0.0172	0.0562	0.0014	0.0694	0.0013	432.7	8.0	92.4
Inherited Grain										
2-1	1.085	0.5782	0.0129	0.0571	0.0010	0.0729	0.0016	453.7	9.3	92.9
Discordant Data (<90% and >110% Concordance)										
2-17	1.344	1.0937	0.0188	0.1901	0.0027	0.0389	0.0008	246.1	4.9	9.0
2-39	1.609	0.4460	0.0152	0.0645	0.0026	0.0497	0.0013	312.4	7.8	43.6
2-3	1.140	0.5264	0.0156	0.0769	0.0022	0.0509	0.0010	319.8	6.2	28.8
2-33	1.432	0.6394	0.0155	0.0866	0.0020	0.0523	0.0016	328.3	9.9	24.6
2-18	0.823	0.8477	0.0249	0.1079	0.0031	0.0537	0.0010	337.1	6.4	19.4
2-13	1.234	0.8567	0.0336	0.1181	0.0053	0.0539	0.0012	338.1	7.5	18.0
2-34	1.266	0.6016	0.0199	0.0798	0.0026	0.0548	0.0012	343.8	7.1	29.4
2-23	0.752	0.6344	0.0170	0.0804	0.0019	0.0549	0.0011	344.4	6.9	28.9
2-25	1.540	0.5241	0.0202	0.0673	0.0023	0.0559	0.0011	350.7	6.9	42.3
2-24	1.153	0.5223	0.0156	0.0658	0.0016	0.0568	0.0011	356.1	6.6	45.2
2-27	1.337	0.7024	0.0158	0.0815	0.0017	0.0615	0.0014	384.8	8.6	31.5
2-37	2.048	0.8357	0.1018	0.0963	0.0101	0.0618	0.0015	386.5	9.2	28.5
2-29	1.301	0.8755	0.0244	0.1019	0.0037	0.0619	0.0019	387.0	11.4	23.8
2-38	1.529	0.5133	0.0199	0.0595	0.0019	0.0625	0.0012	390.5	7.3	66.2
2-15	1.243	0.6624	0.0232	0.0742	0.0024	0.0650	0.0013	405.8	7.6	40.3
2-28	1.173	0.5785	0.0178	0.0647	0.0020	0.0650	0.0012	406.0	7.5	55.5
2-8	1.068	0.5133	0.0149	0.0568	0.0013	0.0656	0.0013	409.9	7.6	80.5
2-26	1.137	0.5449	0.0172	0.0596	0.0016	0.0657	0.0012	410.2	7.4	69.0
2-7	0.923	0.7374	0.0236	0.0813	0.0024	0.0659	0.0013	411.1	8.1	33.9
2-32	1.194	0.5243	0.0366	0.0545	0.0033	0.0668	0.0016	416.8	9.9	69.1
2-16	1.191	0.5771	0.0157	0.0630	0.0013	0.0668	0.0013	417.0	7.7	60.1
2-4	1.414	0.5599	0.0205	0.0599	0.0019	0.0673	0.0013	419.7	7.9	68.4

Spot Number	Mean U/Th	$^{207}Pb/^{235}U$	$\pm 2\sigma$	$^{207}Pb/^{206}Pb$	$\pm 2\sigma$	$^{206}Pb/^{238}U$	$\pm 2\sigma$	Date (Ma)	$\pm 2\sigma$ (Ma)	Conc (%)
2-10	1.186	0.6177	0.0166	0.0663	0.0015	0.0679	0.0013	423.2	8.0	53.1
2-2	1.017	0.5347	0.0229	0.0563	0.0018	0.0680	0.0013	423.9	8.1	82.8
2-6	1.192	0.5548	0.0164	0.0592	0.0015	0.0680	0.0014	423.9	8.2	75.8
2-19	1.429	0.7815	0.0273	0.0825	0.0027	0.0682	0.0013	425.1	8.0	34.7
2-21	0.827	0.5577	0.0188	0.0588	0.0015	0.0683	0.0013	425.8	8.1	75.3
2-31	1.219	0.5857	0.0141	0.0614	0.0013	0.0689	0.0014	429.7	8.4	66.8
2-22	1.059	0.5595	0.0229	0.0595	0.0020	0.0691	0.0014	430.8	8.6	69.2
2-14	1.311	0.5430	0.0149	0.0569	0.0014	0.0701	0.0013	436.5	7.9	87.7
2-11	1.000	0.6629	0.0212	0.0662	0.0019	0.0720	0.0015	448.1	8.7	56.5
2-9	1.648	0.5551	0.0257	0.0547	0.0021	0.0721	0.0017	448.6	10.0	89.3
2-20	0.926	7.5293	0.2266	0.4307	0.0070	0.1260	0.0029	764.6	16.4	19.0

Table D5: Geochronology data for the zircons from TDBHons015.01 (Blowering Formation).

Spot Number	Mean U/Th	$^{207}Pb/^{235}U$	$\pm 2\sigma$	$^{207}Pb/^{206}Pb$	$\pm 2\sigma$	$^{206}Pb/^{238}U$	$\pm 2\sigma$	Date (Ma)	$\pm 2\sigma$ (Ma)	Conc (%)
Session 1										
Concordant Data (90 - 110 % Concordance)										
Young Population										
1-26b	6.438	0.5192	0.0066	0.0558	0.0004	0.0674	0.0006	420.2	3.6	94.5
1-17b	6.339	0.5164	0.0063	0.0555	0.0003	0.0674	0.0006	420.6	3.3	97.1
Main Population										
1-21b	1.869	0.5229	0.0066	0.0559	0.0004	0.0678	0.0006	423.2	3.6	95.0
1-15b	4.655	0.5252	0.0065	0.0559	0.0004	0.0681	0.0006	424.4	3.5	94.5
1-20	3.002	0.5249	0.0067	0.0558	0.0003	0.0682	0.0006	425.2	3.7	95.8
1-25	3.469	0.5243	0.0064	0.0558	0.0003	0.0682	0.0006	425.2	3.4	95.9
1-26	6.438	0.5268	0.0070	0.0560	0.0004	0.0682	0.0006	425.2	3.8	94.1
1-19	4.911	0.5308	0.0069	0.0565	0.0004	0.0684	0.0006	426.5	3.6	90.9
1-23	7.445	0.5263	0.0064	0.0558	0.0003	0.0685	0.0006	427.3	3.4	96.6
1-21	1.869	0.5301	0.0069	0.0561	0.0004	0.0687	0.0007	428.1	4.0	94.0
1-18	1.870	0.5277	0.0066	0.0557	0.0003	0.0687	0.0006	428.2	3.6	97.7
1-17	6.339	0.5271	0.0068	0.0557	0.0003	0.0688	0.0006	428.9	3.6	97.9
1-15	4.655	0.5337	0.0071	0.0561	0.0004	0.0691	0.0006	430.5	3.7	94.5
1-13	2.050	0.5345	0.0068	0.0562	0.0004	0.0691	0.0006	430.6	3.6	93.8
1-8	6.804	0.5299	0.0064	0.0556	0.0003	0.0691	0.0006	430.9	3.5	99.0
1-11	3.409	0.5348	0.0076	0.0560	0.0004	0.0692	0.0008	431.4	4.8	95.7
1-18b	1.870	0.5313	0.0064	0.0557	0.0003	0.0693	0.0006	432.0	3.5	97.9
1-1	3.286	0.5414	0.0077	0.0565	0.0004	0.0693	0.0008	432.1	4.9	91.9
1-24	7.960	0.5337	0.0067	0.0559	0.0003	0.0694	0.0007	432.4	4.0	96.3
1-2b	4.086	0.5373	0.0068	0.0562	0.0003	0.0694	0.0006	432.4	3.6	94.2
1-5b	2.127	0.5360	0.0069	0.0561	0.0004	0.0694	0.0006	432.5	3.6	94.9
1-3	2.005	0.5359	0.0074	0.0558	0.0003	0.0696	0.0007	433.7	4.0	97.6
1-5	2.127	0.5400	0.0072	0.0558	0.0004	0.0700	0.0007	436.4	4.0	98.2
1-2	4.086	0.5419	0.0070	0.0558	0.0003	0.0703	0.0006	438.0	3.8	98.8
1-13b	2.050	0.5426	0.0074	0.0560	0.0005	0.0704	0.0006	438.6	3.8	97.7
1-7	3.566	0.5441	0.0066	0.0557	0.0003	0.0709	0.0006	441.4	3.6	100.1
1-20b	3.002	0.5460	0.0072	0.0560	0.0004	0.0709	0.0007	441.8	4.0	98.0
1-9	7.323	0.5569	0.0073	0.0559	0.0003	0.0724	0.0007	450.6	4.1	100.6

Spot Number	Mean U/Th	$^{207}Pb/^{235}U$	$\pm 2\sigma$	$^{207}Pb/^{206}Pb$	$\pm 2\sigma$	$^{206}Pb/^{238}U$	$\pm 2\sigma$	Date (Ma)	$\pm 2\sigma$ (Ma)	Conc (%)
Inherited Grain										
1-14	1.372	0.6400	0.0079	0.0577	0.0003	0.0805	0.0007	499.2	4.1	96.7
Discordant Data (<90% and >110% Concordance)										
1-4	4.466	0.5739	0.0113	0.0618	0.0009	0.0674	0.0006	420.2	3.6	63.4
1-22	1.995	0.5621	0.0085	0.0600	0.0006	0.0680	0.0006	424.3	3.5	70.8
1-16	3.340	0.7155	0.0204	0.0762	0.0021	0.0682	0.0006	425.3	3.4	39.2
1-6	8.090	0.5510	0.0067	0.0583	0.0003	0.0685	0.0006	427.3	3.4	79.1
1-12	4.316	0.7042	0.0110	0.0730	0.0008	0.0702	0.0006	437.3	3.5	43.3
1-10	2.716	0.6043	0.0083	0.0584	0.0004	0.0751	0.0007	466.6	4.0	85.8
Session 2										
Concordant Data (90 - 110 % Concordance; Inherited)										
2-6	2.230	0.6599	0.0270	0.0583	0.0018	0.0836	0.0016	517.7	9.8	95.2
Discordant Data (<90% and >110% Concordance)										
2-14	3.502	0.5256	0.0200	0.0604	0.0022	0.0647	0.0013	404.3	7.7	63.9
2-2	2.676	0.6094	0.0321	0.0649	0.0026	0.0664	0.0013	414.2	7.9	49.3
2-5	2.298	0.6350	0.0252	0.0695	0.0023	0.0668	0.0013	416.6	7.7	47.3
2-4	1.028	0.5689	0.0201	0.0620	0.0017	0.0677	0.0013	422.4	7.8	62.5
2-10	1.386	0.5117	0.0299	0.0541	0.0025	0.0679	0.0016	423.3	9.6	74.0
2-9	5.548	0.5413	0.0209	0.0580	0.0019	0.0686	0.0013	427.5	8.0	76.0
2-1	3.665	0.7550	0.0243	0.0814	0.0021	0.0689	0.0013	429.2	7.8	35.4
2-11	1.376	0.5218	0.0269	0.0559	0.0028	0.0696	0.0015	433.8	8.8	72.1
2-17	1.376	1.0179	0.0716	0.1051	0.0059	0.0705	0.0016	439.4	9.4	26.7
2-15	1.447	0.4948	0.0322	0.0513	0.0026	0.0708	0.0015	440.8	8.9	85.8
2-13	1.988	0.5565	0.0280	0.0564	0.0021	0.0710	0.0014	442.1	8.6	75.0
2-16	5.967	0.5499	0.0166	0.0565	0.0017	0.0722	0.0014	449.5	8.5	85.0
2-7	2.109	0.5810	0.0283	0.0590	0.0025	0.0724	0.0015	450.3	8.9	66.1
2-3	2.339	0.6098	0.0234	0.0582	0.0019	0.0760	0.0016	471.9	9.4	80.9
2-12	2.187	0.6163	0.0314	0.0584	0.0021	0.0763	0.0015	473.9	9.1	79.9
2-8	1.840	0.6990	0.0415	0.0623	0.0031	0.0799	0.0017	495.5	10.4	59.0

Table D6: Geochronology data for the zircons from TDBHons017.01 (Honeysuckle Beds).

Spot Number	Mean U/Th	$^{207}Pb/^{235}U$	$\pm2\sigma$	$^{207}Pb/^{206}Pb$	$\pm2\sigma$	$^{206}Pb/^{238}U$	$\pm2\sigma$	Date (Ma)	$\pm2\sigma$ (Ma)	Conc (%)
Session 1										
Concordant Data (90 - 110 % Concordance)										
Young Grain										
1-15	5.371	0.5211	0.0081	0.0559	0.0003	0.0677	0.0008	422.4	5.0	94.4
Main Population										
1-12	5.203	0.5240	0.0082	0.0560	0.0003	0.0681	0.0008	425.0	5.1	94.5
1-6	1.543	0.5271	0.0084	0.0559	0.0004	0.0683	0.0008	425.7	5.0	95.4
1-23	4.163	0.5253	0.0089	0.0560	0.0003	0.0683	0.0010	426.0	5.7	94.8
1-24	9.918	0.5251	0.0086	0.0557	0.0003	0.0685	0.0009	426.8	5.5	97.1
1-19b	4.167	0.5279	0.0082	0.0557	0.0003	0.0685	0.0008	427.3	5.1	96.9
1-7	6.267	0.5289	0.0080	0.0557	0.0002	0.0689	0.0008	429.3	5.0	97.7
1-26	3.050	0.5315	0.0081	0.0556	0.0002	0.0693	0.0009	431.7	5.1	99.0
1-10	4.498	0.5334	0.0081	0.0558	0.0002	0.0693	0.0008	432.1	5.1	97.9
1-14	5.739	0.5337	0.0081	0.0557	0.0002	0.0694	0.0008	432.7	5.1	98.4
1-20b	6.207	0.5316	0.0082	0.0554	0.0002	0.0695	0.0009	432.9	5.1	101.5
1-18	1.536	0.5381	0.0083	0.0560	0.0003	0.0698	0.0008	434.7	5.1	96.4
1-16	7.612	0.5331	0.0082	0.0555	0.0002	0.0698	0.0008	434.8	5.1	100.4
1-14b	5.739	0.5351	0.0083	0.0558	0.0003	0.0698	0.0009	435.1	5.3	98.0
1-27	6.036	0.5462	0.0082	0.0566	0.0002	0.0700	0.0008	435.9	5.1	92.1
1-17	6.955	0.5359	0.0081	0.0556	0.0002	0.0700	0.0008	436.1	5.1	100.4
1-20	6.207	0.5366	0.0081	0.0556	0.0002	0.0701	0.0008	436.8	5.1	100.4
1-19	4.167	0.5435	0.0083	0.0561	0.0003	0.0703	0.0009	438.0	5.2	95.9
1-16b	7.612	0.5395	0.0084	0.0555	0.0003	0.0705	0.0009	439.0	5.1	102.3
1-9	4.873	0.5415	0.0083	0.0558	0.0002	0.0705	0.0009	439.2	5.3	99.4
1-4b	5.376	0.5434	0.0089	0.0560	0.0003	0.0706	0.0009	439.6	5.4	97.1
1-22	5.964	0.5485	0.0087	0.0561	0.0003	0.0707	0.0009	440.6	5.2	96.8
1-11	4.026	0.5482	0.0085	0.0562	0.0003	0.0709	0.0009	441.7	5.2	96.5
1-8	4.936	0.5454	0.0085	0.0558	0.0002	0.0710	0.0009	442.4	5.2	99.8
1-25	2.658	0.5540	0.0093	0.0561	0.0004	0.0712	0.0009	443.6	5.5	97.9
1-4	5.376	0.5549	0.0085	0.0560	0.0003	0.0716	0.0009	446.0	5.2	98.4
Inherited Grain										
1-2	2.622	0.7116	0.0112	0.0585	0.0002	0.0881	0.0011	544.3	6.5	99.4

Spot Number	Mean U/Th	$^{207}Pb/^{235}U$	$\pm 2\sigma$	$^{207}Pb/^{206}Pb$	$\pm 2\sigma$	$^{206}Pb/^{238}U$	$\pm 2\sigma$	Date (Ma)	$\pm 2\sigma$ (Ma)	Conc (%)
Discordant Data (<90% and >110% Concordance)										
1-1	6.535	0.5352	0.0088	0.0596	0.0003	0.0651	0.0009	406.5	5.6	69.1
1-5	2.067	0.5667	0.0136	0.0607	0.0012	0.0677	0.0008	422.3	5.0	68.3
1-3	5.679	0.5320	0.0081	0.0568	0.0003	0.0679	0.0008	423.5	4.9	87.7
1-21	1.620	0.6010	0.0094	0.0633	0.0003	0.0689	0.0008	429.5	5.0	59.9
1-13	6.938	0.6476	0.0142	0.0613	0.0004	0.0766	0.0012	475.8	7.2	73.0
Session 2										
Concordant Data (90 - 110 % Concordance)										
Main Population										
2-9	5.197	0.5297	0.0167	0.0562	0.0016	0.0689	0.0013	429.6	7.8	91.6
2-4	2.760	0.5154	0.0286	0.0547	0.0026	0.0689	0.0017	429.7	10.5	91.6
2-1	4.796	0.5274	0.0193	0.0551	0.0020	0.0692	0.0014	431.4	8.2	90.5
2-2	6.367	0.5234	0.0154	0.0557	0.0015	0.0701	0.0013	436.8	7.9	92.6
Inherited Grain										
2-8	1.861	1.2399	0.0552	0.0681	0.0021	0.1276	0.0027	774.0	15.2	90.3
Discordant Data (<90% and >110% Concordance)										
2-16	2.274	0.5840	0.0290	0.0678	0.0027	0.0629	0.0013	393.1	7.8	45.5
2-18	1.454	0.5156	0.0176	0.0581	0.0016	0.0646	0.0013	403.4	7.9	72.0
2-7	4.060	0.5458	0.0192	0.0604	0.0018	0.0650	0.0013	405.9	7.7	64.5
2-5	3.360	0.5462	0.0244	0.0608	0.0021	0.0658	0.0013	410.7	8.1	61.8
2-15	4.270	0.5008	0.0148	0.0565	0.0013	0.0661	0.0012	412.5	7.4	85.3
2-20	2.939	0.5128	0.0221	0.0576	0.0022	0.0663	0.0013	413.6	7.8	73.9
2-6	4.775	0.5382	0.0204	0.0577	0.0018	0.0676	0.0013	421.8	7.7	74.7
2-13	4.846	0.5455	0.0202	0.0574	0.0018	0.0692	0.0014	431.6	8.4	79.5
2-19	4.351	0.5481	0.0212	0.0575	0.0020	0.0700	0.0014	436.3	8.2	76.3
2-10	4.021	0.5309	0.0149	0.0564	0.0014	0.0701	0.0013	436.5	7.7	86.1
2-11	3.139	0.5388	0.0272	0.0550	0.0023	0.0705	0.0014	438.9	8.3	86.5
2-17	3.195	0.5614	0.0224	0.0581	0.0020	0.0708	0.0014	440.7	8.6	77.0
2-3	1.026	0.5716	0.0355	0.0580	0.0029	0.0712	0.0016	443.1	9.5	62.2
2-12	8.357	0.6240	0.0184	0.0600	0.0016	0.0767	0.0015	476.5	8.8	80.3
2-14	6.563	1.2589	0.0449	0.0818	0.0016	0.1119	0.0026	683.7	15.3	55.7

Table D7: Geochronology data for the zircons from TDBHons022.01 (Killimicat Granite).

Spot Number	Mean U/Th	$^{207}Pb/^{235}U$	$\pm2\sigma$	$^{207}Pb/^{206}Pb$	$\pm2\sigma$	$^{206}Pb/^{238}U$	$\pm2\sigma$	Date (Ma)	$\pm2\sigma$ (Ma)	Conc (%)
Session 1										
Concordant Data (90 - 110 % Concordance)										
Main Population										
1-17	0.988	0.5014	0.0062	0.0557	0.0003	0.0654	0.0006	408.1	3.6	93.2
1-10	1.354	0.5043	0.0068	0.0561	0.0004	0.0654	0.0007	408.2	4.0	90.0
1-16	2.497	0.5056	0.0076	0.0559	0.0006	0.0655	0.0006	409.2	3.6	91.8
1-7	2.204	0.5000	0.0063	0.0552	0.0003	0.0656	0.0005	409.5	3.3	97.3
1-18	1.784	0.5036	0.0064	0.0555	0.0004	0.0656	0.0006	409.5	3.4	94.6
1-1	1.698	0.5018	0.0067	0.0555	0.0005	0.0656	0.0006	409.7	3.4	95.2
1-20	1.435	0.5066	0.0066	0.0556	0.0003	0.0660	0.0006	412.0	3.6	94.8
1-14b	2.077	0.5100	0.0073	0.0559	0.0006	0.0662	0.0006	413.2	3.5	92.3
1-18b	1.784	0.5132	0.0072	0.0559	0.0004	0.0667	0.0007	416.5	4.3	93.5
1-16b	2.497	0.5142	0.0071	0.0558	0.0004	0.0670	0.0007	417.8	4.1	94.5
1-11	2.325	0.5134	0.0062	0.0555	0.0003	0.0671	0.0006	418.8	3.4	96.8
1-6	1.568	0.5173	0.0064	0.0556	0.0003	0.0674	0.0006	420.5	3.4	96.8
1-22b	2.406	0.5188	0.0069	0.0559	0.0003	0.0674	0.0007	420.7	4.1	94.2
1-23	1.766	0.5184	0.0077	0.0558	0.0005	0.0675	0.0006	420.9	3.8	95.2
1-14	2.077	0.5212	0.0074	0.0556	0.0005	0.0679	0.0006	423.5	3.5	97.8
1-23b	1.766	0.5315	0.0085	0.0560	0.0006	0.0687	0.0007	428.2	4.2	94.7
Inherited Grains										
1-3	5.716	0.5395	0.0065	0.0558	0.0003	0.0703	0.0006	438.1	3.6	99.1
1-22	2.406	0.5605	0.0076	0.0557	0.0004	0.0729	0.0007	453.4	4.4	103.3
Discordant Data (<90% and >110% Concordance)										
1-15	5.086	0.4403	0.0071	0.0632	0.0006	0.0507	0.0006	318.8	3.8	44.7
1-13	2.736	0.4427	0.0087	0.0618	0.0008	0.0521	0.0013	327.2	7.9	49.4
1-12	1.517	0.5894	0.0325	0.0808	0.0030	0.0539	0.0016	338.6	10.1	28.5
1-8	2.368	0.5330	0.0083	0.0655	0.0019	0.0595	0.0013	372.6	7.8	48.2
1-19	1.104	0.5190	0.0081	0.0596	0.0005	0.0631	0.0007	394.3	4.0	67.1
1-2	2.328	0.6047	0.0246	0.0680	0.0041	0.0654	0.0013	408.6	7.7	50.4
1-21	1.153	0.5598	0.0146	0.0618	0.0012	0.0657	0.0006	409.9	3.9	61.6
1-9	6.891	0.5260	0.0085	0.0580	0.0004	0.0657	0.0007	410.1	4.0	78.0
1-5	1.199	0.5472	0.0143	0.0601	0.0014	0.0661	0.0005	412.4	3.3	69.3

Spot Number	Mean U/Th	$^{207}Pb/^{235}U$	$\pm 2\sigma$	$^{207}Pb/^{206}Pb$	$\pm 2\sigma$	$^{206}Pb/^{238}U$	$\pm 2\sigma$	Date (Ma)	$\pm 2\sigma$ (Ma)	Conc (%)
1-4	1.180	0.5499	0.0111	0.0592	0.0009	0.0674	0.0006	420.4	3.5	73.8
Session 2										
Concordant Data (90 - 110 % Concordance)										
Main Population										
2-17	2.159	0.4975	0.0172	0.0564	0.0017	0.0654	0.0014	408.3	8.2	90.9
2-24	1.035	0.4972	0.0158	0.0546	0.0014	0.0674	0.0013	420.2	7.9	92.0
2-18	1.027	0.5218	0.0263	0.0548	0.0022	0.0692	0.0015	431.4	8.8	91.1
Inherited Grains										
2-4	3.168	0.5365	0.0207	0.0559	0.0017	0.0707	0.0015	440.1	8.9	93.9
2-3	2.432	0.5585	0.0241	0.0552	0.0020	0.0731	0.0014	454.8	8.5	93.9
Discordant Data (<90% and >110% Concordance)										
2-10	2.937	0.6763	0.0193	0.0929	0.0039	0.0554	0.0020	347.4	12.1	24.1
2-31	1.967	0.6945	0.0231	0.0906	0.0033	0.0568	0.0014	356.3	8.4	25.5
2-9	1.406	0.4607	0.0123	0.0586	0.0015	0.0595	0.0011	372.6	7.0	68.5
2-8	1.710	0.4804	0.0199	0.0577	0.0023	0.0631	0.0013	394.4	7.7	63.9
2-7	1.178	0.4818	0.0228	0.0563	0.0022	0.0631	0.0013	394.7	7.9	69.9
2-20	1.710	0.5026	0.0160	0.0572	0.0015	0.0635	0.0012	397.0	7.3	78.0
2-22	1.145	0.5621	0.0313	0.0628	0.0030	0.0638	0.0014	398.9	8.5	52.8
2-25	0.911	0.5245	0.0169	0.0611	0.0017	0.0644	0.0013	402.3	8.0	62.4
2-21	1.393	0.4718	0.0269	0.0530	0.0026	0.0648	0.0015	404.6	9.2	75.3
2-29	0.785	0.5397	0.0236	0.0612	0.0024	0.0650	0.0013	405.8	8.0	59.6
2-12	0.974	0.4862	0.0220	0.0557	0.0023	0.0651	0.0014	406.2	8.6	69.4
2-11	0.620	0.7139	0.0245	0.0789	0.0023	0.0654	0.0013	408.5	7.6	35.7
2-33	0.784	0.4839	0.0224	0.0543	0.0023	0.0659	0.0013	411.1	8.1	77.4
2-14	3.517	0.4969	0.0209	0.0560	0.0020	0.0662	0.0013	413.0	7.9	79.8
2-30	1.170	0.5902	0.0287	0.0648	0.0026	0.0666	0.0014	415.8	8.6	54.1
2-23	0.789	0.7415	0.0324	0.0816	0.0035	0.0670	0.0015	417.9	9.1	35.4
2-15	1.022	0.5728	0.0308	0.0613	0.0028	0.0672	0.0014	419.0	8.3	56.0
2-13	4.761	0.5173	0.0200	0.0559	0.0018	0.0676	0.0013	421.9	7.9	81.0
2-27	1.262	0.5253	0.0279	0.0562	0.0025	0.0681	0.0015	424.4	9.1	70.8
2-28	1.063	0.5748	0.0253	0.0614	0.0023	0.0682	0.0014	425.5	8.5	65.0
2-26	0.674	0.5604	0.0263	0.0602	0.0020	0.0684	0.0014	426.7	8.4	68.8
2-1	0.772	0.5560	0.0443	0.0586	0.0036	0.0685	0.0018	426.9	10.7	57.2
2-2	0.952	0.6093	0.0380	0.0632	0.0034	0.0692	0.0015	431.1	9.0	50.0
2-6	0.829	0.8221	0.0498	0.0851	0.0041	0.0698	0.0016	434.9	9.6	34.5

Spot Number	Mean U/Th	$^{207}Pb/^{235}U$	$\pm 2\sigma$	$^{207}Pb/^{206}Pb$	$\pm 2\sigma$	$^{206}Pb/^{238}U$	$\pm 2\sigma$	Date (Ma)	$\pm 2\sigma$ (Ma)	Conc (%)
2-19	0.920	1.8697	0.1008	0.1937	0.0068	0.0704	0.0017	438.4	10.4	15.8
2-32	2.004	0.5556	0.0388	0.0573	0.0034	0.0714	0.0017	444.3	10.3	64.8
2-5	0.718	0.8916	0.0312	0.0912	0.0025	0.0717	0.0014	446.6	8.5	31.2
2-16	0.924	0.8952	0.0314	0.0827	0.0026	0.0815	0.0017	505.2	10.3	40.6

Table D8: Geochronology data for the titanites from TDBHons013.01 (Snowball Metabasic Igneous Complex)

Grain	Mean U/Th	$^{207}Pb/^{235}U$	$\pm 2\sigma$	$^{206}Pb/^{238}U$	$\pm 2\sigma$	Date (Ma)	$\pm 2\sigma$ (Ma)	Conc (%)
1	0.102	8.482	0.42	0.1405	0.01	437.2	35.4	-
27	0.113	7.071	0.38	0.1281	0.01	436.5	31.5	-
22	0.583	12.748	0.71	0.1768	0.01	425.6	49.9	-
14	0.705	5.616	0.28	0.1129	0.01	424.3	23.3	-
2	0.109	7.649	0.42	0.1308	0.01	418.9	31.8	-
26	0.900	6.969	0.34	0.1245	0.01	412.8	27.2	-
19	0.449	2.741	0.15	0.0860	0.00	411.2	21.5	-
24	0.324	7.024	0.36	0.1246	0.01	410.6	30.9	-
12	0.719	7.114	0.35	0.1235	0.01	406.8	26.2	-
28	0.583	10.189	0.49	0.1508	0.01	405.2	35.5	-
37	0.430	5.079	0.24	0.1054	0.00	404.5	23.4	-
29	0.750	43.018	2.83	0.4423	0.03	401.9	166.4	-
5	0.199	4.171	0.22	0.0977	0.00	400.8	22.9	-
31	0.759	8.058	0.43	0.1316	0.01	398.2	34.1	-
9	0.451	9.095	0.53	0.1398	0.01	397.0	34.4	-
34	0.529	2.976	0.17	0.0857	0.00	395.5	20.3	-
3	0.196	9.545	0.50	0.1459	0.01	392.3	37.1	-
20	0.056	6.438	0.35	0.1155	0.01	382.0	31.3	-
25	0.491	12.222	0.59	0.1651	0.01	380.5	38.5	-
15	0.171	4.937	0.26	0.1008	0.01	380.2	24.4	-
30	1.222	16.266	0.90	0.2025	0.01	367.8	64.4	-
33	0.706	12.418	0.67	0.1662	0.01	364.6	48.6	-
18	0.800	13.933	0.83	0.1775	0.01	360.0	54.0	-
23	0.526	26.357	1.37	0.2886	0.02	352.4	78.3	-
8	0.286	27.178	2.19	0.2901	0.02	347.6	94.6	-
21	0.815	9.921	0.53	0.1424	0.01	347.2	37.9	-
7	0.368	25.044	2.23	0.2708	0.02	346.3	104.4	-
13	0.737	13.097	0.71	0.1708	0.01	342.0	57.5	-
6	0.371	13.301	0.74	0.1717	0.01	334.6	60.8	-
10	1.000	18.295	0.93	0.2119	0.01	316.3	62.5	-
16	0.615	25.630	1.58	0.2797	0.02	314.1	102.7	-
36	0.533	22.843	1.33	0.2490	0.01	303.7	87.4	-
4	0.219	22.605	1.52	0.2453	0.02	302.3	100.8	-

Grain	Mean U/Th	$^{207}Pb/^{235}U$	$\pm 2\sigma$	$^{206}Pb/^{238}U$	$\pm 2\sigma$	Date (Ma)	$\pm 2\sigma$ (Ma)	Conc (%)
11	0.933	20.167	1.05	0.2214	0.01	290.4	65.3	-
17	1.091	32.171	1.80	0.3237	0.02	284.8	90.9	-
32	0.583	22.751	1.41	0.2443	0.02	228.6	99.7	-
38	1.000	48.457	2.62	0.4401	0.03	80.0	155.2	-
35	0.667	42.386	2.54	0.3984	0.03	21.1	172.4	-

Appendix E - Zircon Trace Elements

Zircon trace element data appears in this appendix. Tables are sorted by sample number and analyses sorted by spot number. The trace element data has been filtered and any results that were below the limit of quantification (3 $\times$ the limit of detection) are already excluded and replaced by a dash.

Table E1: Zircon trace element data for the Kimo Diorite zircons (TDBHons003.01).

Spot	Ti	Y	Zr	La	Ce	Pr	Nd	Sm	Eu	Gd	Tb	Dy	Ho	Er	Tm	Yb	Lu	Hf	Th	U
1	13.7	2590	424450	0.03	18.9	0.39	6.89	12.8	2.72	67.1	22.1	256	90.3	393	75.1	637	123	8379	248	329
2	20.0	1291	426558	0.01	11.5	0.15	2.42	4.96	1.13	27.4	9.33	115	43.8	201	39.8	352	72.0	8081	155	241
3	23.2	1029	432802	1.28	19.1	2.44	15.7	10.4	2.08	24.8	7.81	90.0	34.3	161	33.0	304	63.6	8467	108	208
4	15.7	997	424898	0.02	11.4	0.09	1.50	3.09	0.80	18.7	6.50	84.9	32.4	155	31.3	282	57.7	7946	108	196
5	26.4	1494	448505	5.94	48.4	5.49	34.2	21.3	5.08	48.4	13.8	148	51.1	222	43.4	379	73.9	8661	347	411
6	20.1	1701	434164	0.01	19.7	0.18	2.52	5.28	1.24	31.2	11.3	144	56.2	265	52.5	467	94.3	7928	414	463
7	16.8	1783	440610	0.01	17.0	0.17	2.36	4.77	1.23	29.9	10.9	143	58.0	282	57.8	521	109	7996	178	332
8	25.8	1843	425014	0.01	26.7	0.22	3.42	6.83	1.80	42.1	14.5	174	63.1	274	52.1	441	83.3	7718	440	344
9	77.3	1975	434459	0.42	20.5	0.91	8.29	10.3	2.25	49.4	15.8	187	68.1	304	58.7	502	99.2	8394	271	366
10	24.4	1612	435315	0.15	10.7	0.26	3.69	7.15	1.63	37.2	12.2	147	54.7	247	48.4	431	86.9	7847	125	198
11	18.8	1374	446651	0.00	13.6	0.09	1.86	4.02	0.90	23.2	8.54	110	45.5	219	45.3	409	84.6	8141	160	290
12	19.4	900	425944	0.33	9.63	0.17	1.82	2.56	0.75	15.9	5.82	74.2	29.8	144	30.1	271	57.2	7834	79	168
13	18.4	2525	433127	0.80	24.5	1.75	12.5	15.3	3.44	68.1	21.4	244	86.7	381	72.3	622	121	8012	365	417
14	16.0	1085	438948	2.93	19.7	1.12	6.68	4.66	0.91	22.2	7.46	92.8	36.0	172	34.5	309	64.2	8140	141	234
15	23.9	1156	421687	0.19	14.6	0.18	2.04	3.80	0.84	23.8	8.23	102	38.8	179	36.5	322	64.5	7776	223	280
16	137	1286	384645	5.43	27.2	1.04	5.39	5.56	1.25	27.5	9.36	115	44.2	199	38.7	340	66.9	7075	283	302
17	17.7	1796	430809	1.16	20.7	0.60	5.76	7.83	1.67	41.3	13.8	168	61.8	274	53.8	469	91.9	8341	211	303
18	17.4	967	428567	-	11.2	0.07	1.59	3.06	0.77	19.3	6.62	83.5	32.8	152	30.5	277	57.1	8076	139	233
19	18.7	3621	434985	0.50	34.6	1.44	13.8	17.2	3.86	89.6	29.9	355	126	550	105	892	169	8838	553	602
20	16.7	1749	427381	0.19	21.9	0.51	5.15	8.36	1.74	39.2	13.1	160	59.9	270	52.3	450	89.4	8066	404	423
21	12.4	1742	432186	0.07	15.7	0.32	4.02	6.81	1.77	40.1	13.8	164	60.3	275	52.8	465	91.0	8220	276	310
22	19.4	2294	428662	1.57	26.1	1.13	8.46	10.7	2.65	53.4	17.7	212	78.8	356	69.9	611	120	8196	321	406
23	28.8	1282	450245	12.1	61.9	8.51	50.5	25.6	4.36	49.0	12.5	129	44.0	190	37.9	336	65.9	8864	245	325
24	343	2855	444116	7.55	86.8	12.7	78.7	47.0	8.73	96.9	26.9	293	97.4	429	83.2	720	137	8684	394	555
25	138	1508	444319	1.86	30.2	3.10	19.6	11.6	2.89	33.1	10.8	129	49.8	237	49.0	450	88.1	8562	186	330

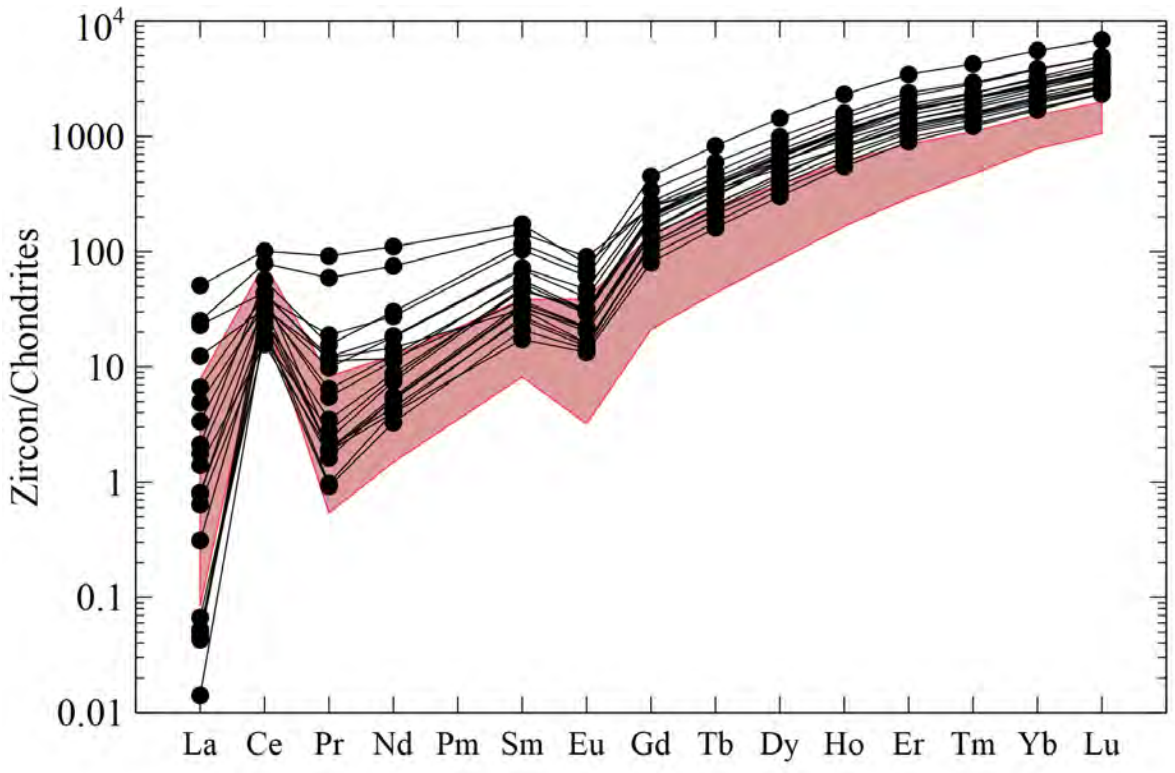

Figure E1: Zircon trace element patterns in the Kimo Diorite. Shaded red is the zircon trace element patterns from Long et al. (2012).

Table E2: Zircon trace element data for the Bogong Granite zircons (TDBHons007.01).

Spot	Ti	Y	Zr	La	Ce	Pr	Nd	Sm	Eu	Gd	Tb	Dy	Ho	Er	Tm	Yb	Lu	Hf	Th	U
1	7.38	1500	444256	6.67	31.8	2.67	13.8	7.07	0.99	34.8	11.7	141	52.9	237	45.3	396	76.1	8692	360	511
2	-	1247	430057	0.02	11.4	0.08	1.58	4.24	0.69	25.7	9.31	116	44.0	199	38.7	335	66.9	8450	262	412
3	118	2594	452349	6.55	35.2	3.17	16.3	12.3	1.19	57.9	20.5	251	94.6	420	78.7	659	126	10085	356	627
4	668	2157	431003	16.2	45.6	6.20	28.6	15.0	1.58	52.6	17.4	207	77.9	343	66.3	557	107	10342	763	1060
5	6.39	2782	435216	0.42	21.6	0.57	6.39	10.9	1.61	66.9	22.8	270	100	438	82.7	692	132	8825	526	683
6	7.85	1181	432856	7.32	33.6	3.37	18.3	8.49	0.87	30.2	9.68	114	41.9	183	35.4	308	58.8	8336	220	340
7	6.16	1963	427234	2.36	48.6	1.56	8.03	8.05	0.88	41.0	15.2	186	70.7	317	60.2	512	96.7	10411	474	883
8	-	2434	423152	3.65	41.6	1.65	11.5	11.0	1.53	61.6	20.5	242	87.3	382	69.4	582	110	8451	600	777
9	-	2394	424407	0.19	15.5	0.32	5.26	9.88	1.56	59.4	19.8	237	87.3	378	69.9	584	113	8122	333	483
10	-	992	430712	6.00	26.1	2.21	11.5	5.34	0.56	22.4	7.21	91.0	34.8	159	30.9	275	55.4	9243	138	311
11	18.3	1445	434721	5.44	25.3	2.98	15.8	12.0	1.93	43.8	13.4	146	51.0	223	41.8	350	69.6	8035	179	176
12	12.4	1545	434029	1.64	17.1	0.97	6.79	7.30	1.55	36.7	12.5	146	54.6	238	45.1	387	75.9	7217	538	528
13	11.6	3660	435915	31.3	109	13.3	62.6	31.2	4.05	106	33.3	378	134	575	108	879	166	9897	485	942
14	6.07	1435	435168	4.84	27.7	2.03	11.5	6.67	0.89	32.3	11.2	137	50.6	226	42.6	370	72.2	8376	286	407
15	9.08	1326	429604	6.02	25.7	2.69	12.3	7.12	0.88	31.0	10.5	127	47.6	218	41.7	357	70.2	8775	274	451
16	14.7	2786	425630	2.25	26.9	1.52	9.84	12.0	2.19	66.8	22.9	273	102	438	81.2	677	128	8981	499	688
17	-	1830	432883	0.19	20.9	0.19	2.52	5.59	0.80	36.0	13.6	172	65.0	293	55.5	475	91.4	9231	369	648
18	6.82	3862	429729	0.06	14.3	0.52	8.63	19.6	3.81	108	34.7	397	141	604	111	928	178	7957	424	623
19	-	904	418544	1.14	11.7	0.85	4.79	3.71	0.76	18.8	6.58	77.2	30.9	142	28.1	251	49.3	8472	248	378
20	-	2571	443973	9.21	33.4	3.24	18.2	15.3	2.10	70.9	23.1	259	93.4	400	73.4	610	116	8148	221	355
21	-	2000	423244	23.4	88.9	10.0	52.3	20.5	1.44	60.8	18.2	202	72.3	311	57.9	492	92.6	8515	444	646
22	11.1	906	445757	1.19	12.8	0.55	3.26	2.77	0.63	16.3	6.10	77.8	31.3	149	30.0	272	55.8	10311	118	352
23	45.0	1384	424847	1.59	20.2	0.82	5.44	5.71	0.88	31.0	10.6	129	48.9	220	42.1	366	72.5	8378	390	542
24	-	1249	432847	13.0	41.0	4.20	20.2	7.45	0.91	26.7	8.72	109	43.4	208	42.0	380	79.9	8314	128	329

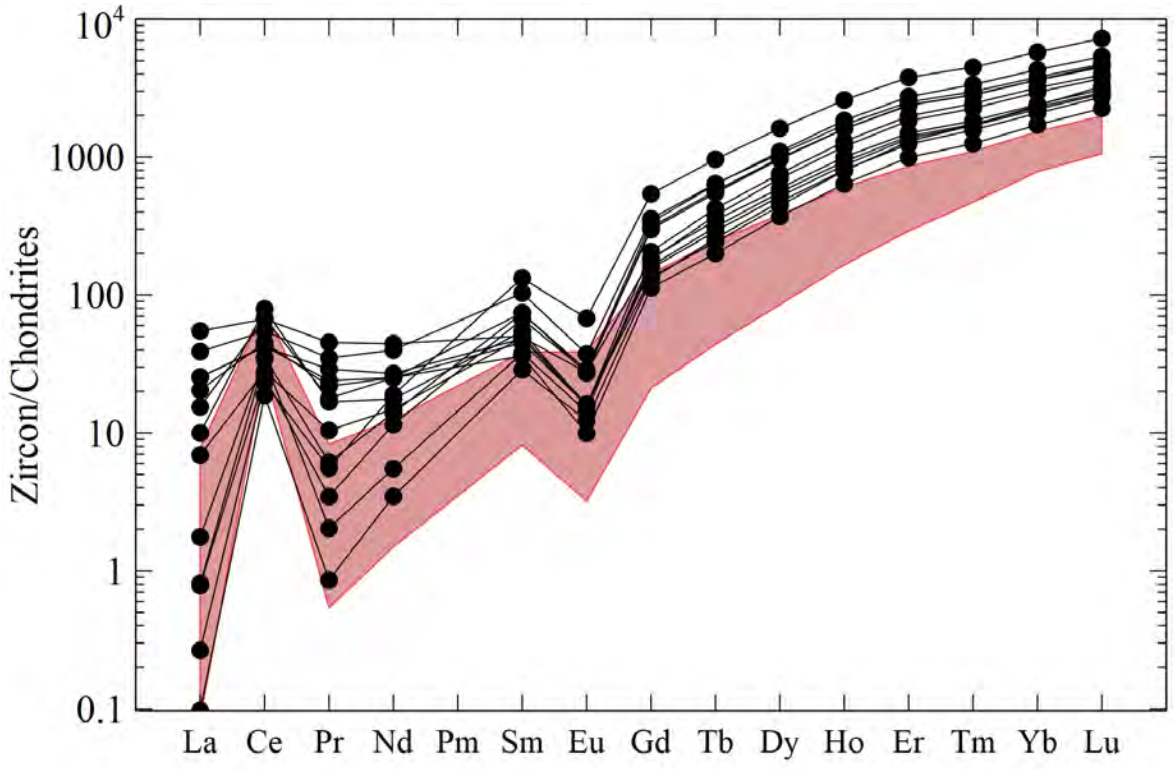

Figure E2: Zircon trace element patterns in the Bogong Granite. Shaded red is the zircon trace element patterns from Long et al. (2012).

Table E3: Zircon trace element data for the Gocup Granite zircons (TDBHons011.01).

Spot	Ti	Y	Zr	La	Ce	Pr	Nd	Sm	Eu	Gd	Tb	Dy	Ho	Er	Tm	Yb	Lu	Hf	Th	U
1	6.40	1736	447204	0.05	2.38	0.09	1.29	4.11	0.55	35.4	14.2	169	55.0	219	38.5	312	55.2	11330	62	186
2	13.7	3647	441320	-	5.28	0.20	4.46	10.1	1.35	65.0	24.7	330	124	561	107	878	160	10507	106	210
3	34.8	3924	451339	17.6	123	20.0	119	78.3	7.61	159	50.4	475	136	569	104	886	167	10920	116	541
4	5.56	1037	446898	0.01	3.18	0.04	1.21	3.42	0.42	25.6	9.64	107	32.8	128	21.9	175	30.7	11611	60	199
5	-	2374	445455	0.02	1.75	0.06	0.94	3.63	0.33	32.9	15.7	214	75.6	342	67.9	589	111	11511	47	341
6	8.22	2047	458799	0.52	5.65	0.80	5.66	7.75	0.85	44.2	17.2	194	65.5	273	48.9	401	73.6	11543	90	211
7	-	2004	455821	0.02	1.88	0.06	0.88	3.41	0.36	34.0	15.7	197	62.0	240	40.2	303	50.9	11847	52	311
8	7.43	1705	449933	0.00	2.58	0.05	1.24	4.60	0.55	34.8	14.2	165	53.6	225	39.8	329	59.3	11384	53	204
9	8.72	2320	453003	0.01	2.43	0.06	1.01	3.96	0.41	32.7	14.7	197	76.1	365	73.0	628	122	11382	58	207
10	5.73	1592	465426	-	1.89	0.04	0.68	2.83	0.34	26.5	12.0	153	49.4	201	35.1	281	50.2	11988	36	265
11	16.2	3972	462378	3.87	23.8	4.66	26.4	21.1	1.94	70.9	27.2	352	131	628	127	1115	215	11420	223	599
12	9.84	2682	443301	0.04	3.70	0.15	2.14	5.49	0.61	42.0	17.5	231	88.8	420	84.1	726	142	10819	65	221
13	10.6	2569	440388	0.01	4.08	0.08	2.11	5.80	0.62	45.0	17.4	226	86.4	406	79.7	692	135	10518	102	222
14	-	2642	427047	1.07	6.01	1.18	7.66	7.53	1.05	43.1	19.0	238	83.3	361	68.6	569	105	11156	56	313
15	-	2511	431167	0.15	2.44	0.10	0.90	3.67	0.44	32.0	15.8	217	79.7	350	66.7	561	104	11943	68	388
16	8.46	1463	424853	-	3.28	0.04	1.25	4.36	0.57	33.5	12.3	143	48.0	199	36.4	295	54.6	10968	63	157
17	8.72	2328	429837	0.14	6.72	0.23	3.09	6.23	0.76	43.9	17.4	214	77.6	343	65.2	547	103	11357	127	231
18	6.93	1147	414816	-	13.9	0.05	1.26	3.09	0.53	19.5	7.33	95.4	38.2	186	38.2	352	72.5	9668	132	216
19	7.24	1587	406592	-	1.88	0.04	0.95	4.10	0.46	32.6	13.6	158	50.1	193	33.0	256	45.5	11512	43	219
20	-	1527	415607	-	1.18	-	0.51	2.52	0.25	25.2	11.9	147	46.1	177	29.4	223	38.2	12031	32	246
21	6.08	2510	405002	0.02	4.32	0.12	2.52	6.88	0.82	50.1	20.1	244	81.6	339	61.3	491	88.5	11217	122	292
22	6.74	2284	411921	0.04	2.32	0.13	1.56	4.52	0.40	35.7	15.2	203	74.3	331	64.1	549	104	11194	51	204
23	16.4	1638	400037	0.56	5.12	0.79	5.22	5.63	0.62	33.0	13.8	162	52.5	207	35.6	278	49.4	11685	90	233
24	6.53	1645	402080	0.47	9.20	0.35	3.49	6.46	0.81	43.2	15.3	170	52.7	195	34.3	264	46.2	11553	160	220
25	8.44	1734	404109	0.01	3.35	0.06	1.46	4.92	0.52	35.4	13.6	161	56.4	242	44.9	373	70.3	11295	70	163
26	9.22	2831	396035	-	3.08	0.07	1.21	4.92	0.47	42.7	18.0	245	95.8	447	87.2	760	146	11017	73	235

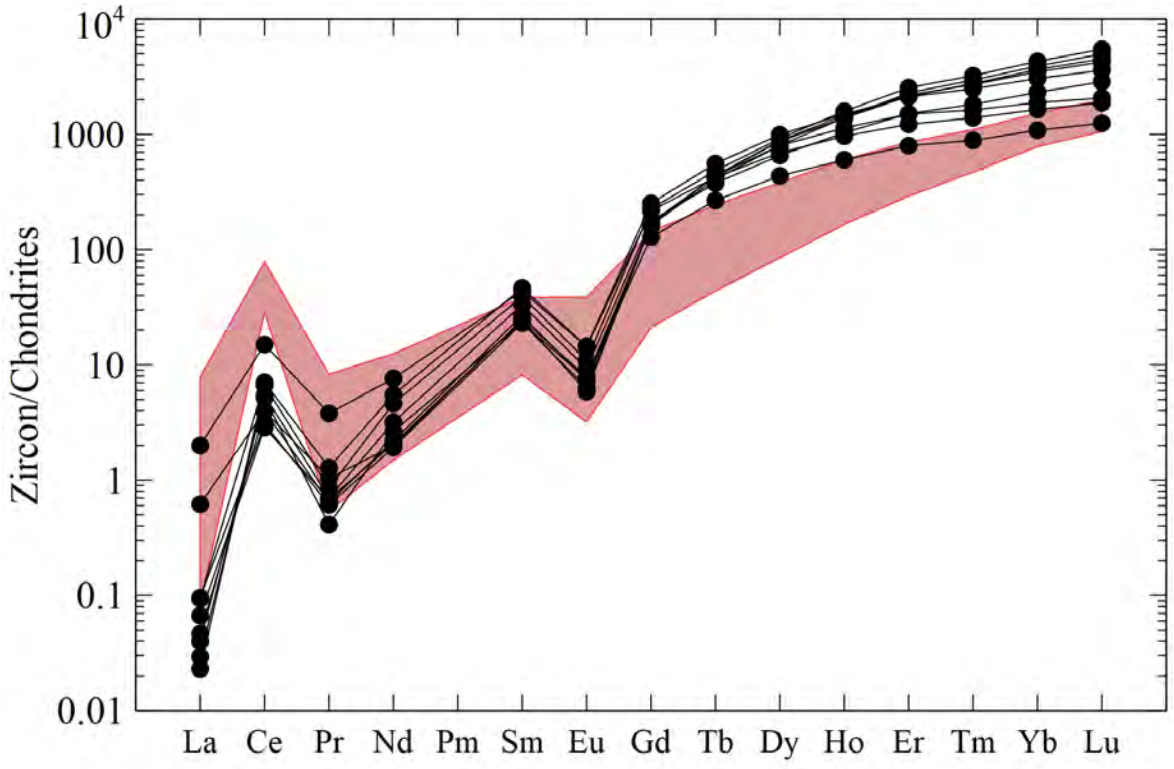

Figure E3: Zircon trace element patterns in the Gocup Granite. Shaded red is the zircon trace element patterns from Long et al. (2012).

Table E4: Zircon trace element data for the Warrienbah granite zircons (TDBHons012.01).

Spot	Ti	Y	Zr	La	Ce	Pr	Nd	Sm	Eu	Gd	Tb	Dy	Ho	Er	Tm	Yb	Lu	Hf	Th	U
1	129	6728	399733	94.6	295	37.3	171	106	11.1	237	78.7	796	229	855	154	1288	212	12037	443	910
2	42.8	4974	431330	44.7	149	18.5	91.7	46.4	3.81	133	46.4	506	169	728	141	1212	217	12467	712	1133
3	13.2	3647	430760	11.3	56.1	5.98	32.2	27.1	2.92	85.2	30.7	357	123	557	109	953	174	12327	530	903
4	7.91	1233	428550	2.49	21.2	1.46	8.01	6.48	1.10	22.6	7.89	95.0	37.3	195	45.2	486	109	9436	346	468
5	41.7	3983	432584	35.7	146	16.6	82.0	44.5	3.67	108	38.9	425	142	605	118	1011	177	12400	1644	1070
6	-	2129	439880	1.62	29.3	0.77	5.17	6.53	0.61	37.7	14.6	189	73.2	345	69.6	633	120	12346	498	856
7	96.4	7896	439953	71.6	264	30.7	154	105	11.6	258	89.1	923	261	1064	196	1605	259	11638	1019	1118
8	18.8	3646	438651	6.80	68.9	4.16	25.0	23.2	2.23	81.6	30.4	362	124	547	108	959	174	10675	1084	1226
9	13.6	2937	443290	0.07	14.9	0.44	7.58	14.3	2.70	78.1	25.2	299	107	457	85.4	752	137	9265	320	328
10	33.6	3846	448069	29.6	105	11.8	55.4	37.8	3.24	103	34.9	397	129	557	108	956	173	12334	499	935
11	16.1	2879	445584	20.0	89.7	9.81	51.4	22.5	1.40	65.3	21.6	266	98.1	460	92.9	857	158	12269	610	1111
12	163	12661	454211	183	659	83.6	378	218	24.0	479	146	1443	407	1529	277	2266	348	11986	611	1023
13	432	14245	465044	262	755	94.8	416	238	24.3	546	176	1729	463	1764	314	2539	394	12593	1293	1870
14	-	3232	450980	3.31	35.8	1.66	11.7	12.0	0.78	62.2	22.6	288	111	520	102	932	173	12176	579	896
15	9.64	2850	456191	4.27	33.4	2.14	15.3	14.1	2.02	67.3	22.9	288	102	457	89.8	780	143	10033	400	522
16	14.8	1955	461018	65.3	152	23.2	104	35.1	2.73	70.9	19.6	202	66.3	281	53.4	472	86.1	10408	276	412
17	-	2554	449479	2.15	31.0	1.02	5.69	7.89	0.64	44.8	17.7	226	87.4	409	82.3	760	142	12087	647	1199
18	7.59	2857	450353	34.8	131	15.7	81.9	29.5	1.50	70.9	22.3	269	99.1	452	90.7	838	155	11958	553	973
19	46.5	4399	461824	277	422	71.4	269	81.8	5.57	148	44.1	449	143	596	116	1011	177	12071	623	1059
20	20.9	4588	477142	16.4	83.2	8.67	43.6	36.2	3.10	112	41.4	473	157	685	134	1175	211	12558	774	1144
21	-	2188	463243	1.31	27.5	0.72	5.30	6.37	0.62	38.1	14.5	192	75.4	359	71.5	668	125	12441	578	1001
22	54.3	4810	461006	38.3	158	18.1	84.3	57.7	5.99	142	48.1	521	163	670	124	1077	188	11805	746	1218
23	-	1535	476836	0.01	4.96	0.13	2.29	8.26	1.02	53.6	18.0	177	48.2	172	29.3	247	44.2	12137	127	485
24	330	20011	457508	84.9	421	66.3	380	343	24.9	784	276	2806	736	2785	516	4285	638	11919	2666	2256
25	-	2688	489955	26.4	80.0	10.5	53.2	20.6	1.16	58.1	19.6	246	94.5	432	87.5	799	152	13118	341	817
26	6.00	3965	483742	0.02	12.7	0.34	6.78	15.4	2.54	90.7	30.5	383	148	678	130	1154	221	10709	457	526
27	9.49	2662	466810	10.6	58.0	4.33	21.5	15.2	1.44	56.2	20.3	248	91.9	417	82.8	747	139	12053	573	945

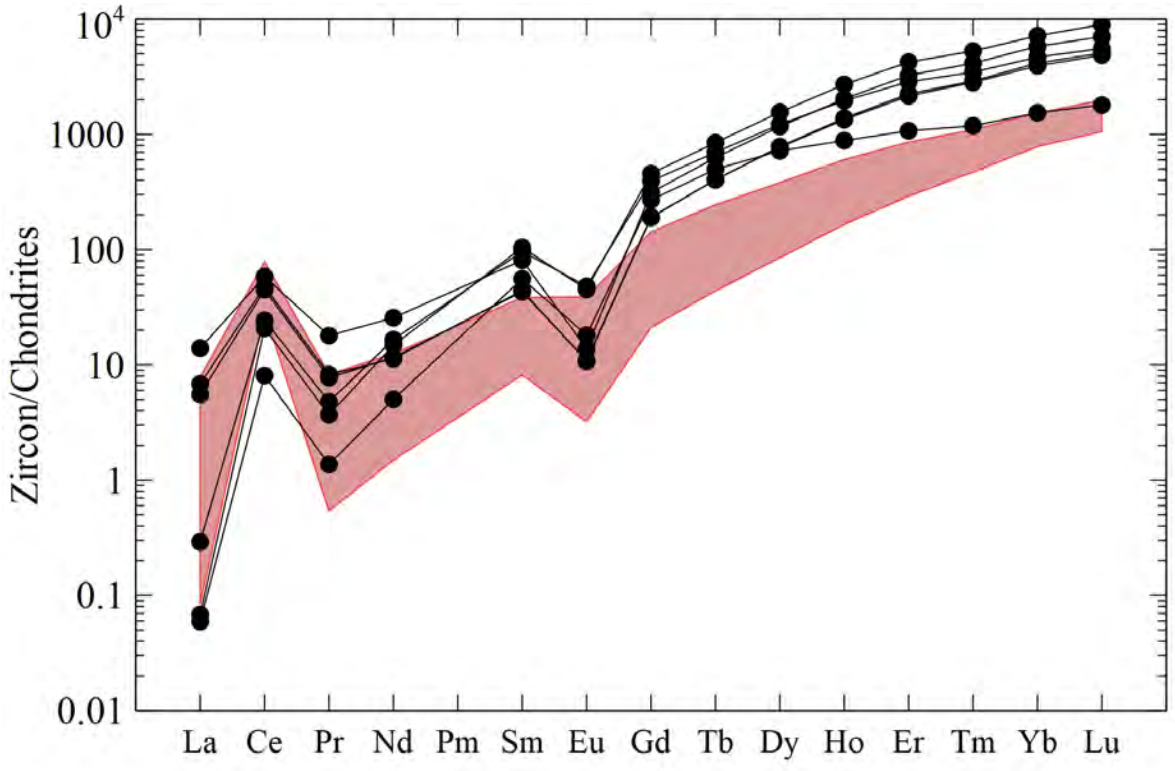

Figure E4: Zircon trace element patterns in the Warrienbah granite. Shaded red is the zircon trace element patterns from Long et al. (2012).

Table E5: Zircon trace element data for the Blowering Formation zircons (TDBHons015.01).

Spot	Ti	Y	Zr	La	Ce	Pr	Nd	Sm	Eu	Gd	Tb	Dy	Ho	Er	Tm	Yb	Lu	Hf	Th	U
1	8.73	2114	438300	0.02	4.87	0.09	1.66	4.39	0.46	31.3	13.1	176	71.8	352	72.6	665	135	11706	99	327
2	7.03	2084	441001	0.44	3.40	0.24	2.00	3.47	0.32	26.7	11.6	165	69.5	353	74.6	675	137	11303	77	314
3	15.7	1412	426380	0.02	6.57	0.08	1.34	3.99	0.41	26.9	9.92	122	48.0	223	43.8	389	78.2	9768	126	253
4	6.80	1857	443116	0.49	3.23	0.44	3.01	3.02	0.23	18.9	9.19	137	60.2	318	68.8	651	134	12568	73	326
5	-	851	426055	-	11.2	0.03	0.73	2.10	0.43	12.4	4.81	63.5	27.7	142	31.7	311	69.1	10321	115	245
6	10.7	2252	431054	0.19	1.62	0.16	1.07	2.06	0.18	21.0	10.8	168	74.9	392	86.4	808	164	12284	51	410
7	-	1808	441685	0.73	6.15	0.37	2.79	3.62	0.43	24.3	10.8	145	60.5	303	63.3	584	120	11729	84	299
8	-	3165	436693	-	1.41	0.03	0.77	3.16	0.24	31.1	15.6	235	105	554	119	1122	226	12019	70	477
9	-	1878	434894	-	1.46	0.01	0.38	1.94	0.14	18.9	9.49	143	61.8	320	69.7	649	133	12246	55	405
10	9.44	641	431145	0.08	11.0	0.07	0.91	2.13	0.43	11.7	4.36	54.1	21.0	102	20.9	195	41.2	10364	107	292
11	-	633	424334	0.13	5.67	0.05	0.48	1.16	0.14	8.24	3.65	48.4	20.8	101	21.3	204	41.6	11848	45	155
12	7.50	2467	421441	3.78	10.6	1.81	12.3	8.93	1.01	37.7	14.5	197	81.5	401	87.1	802	167	11463	84	362
13	6.58	1063	429142	1.00	12.9	0.40	2.25	2.69	0.35	16.7	6.45	85.5	35.2	174	36.3	331	69.0	10525	85	174
14	8.20	738	428253	-	20.3	0.03	0.42	1.49	0.21	10.7	4.43	58.1	23.7	118	24.9	233	48.6	11177	144	197
15	-	1565	440182	-	3.19	0.03	0.46	2.09	0.14	19.0	8.45	122	52.1	261	55.1	507	103	11661	58	268
16	-	2190	433903	4.71	12.2	2.56	16.6	9.48	1.23	36.4	13.2	172	70.9	345	71.3	649	131	11431	106	355
17	-	2430	441870	-	1.64	0.03	0.53	2.82	0.20	24.9	12.3	184	81.1	419	91.5	831	170	12125	74	471
18	-	1304	427399	-	9.54	0.05	1.10	3.07	0.43	22.5	8.62	112	44.9	215	43.4	392	78.5	11324	192	360
19	6.77	714	438097	0.01	1.65	0.05	0.69	1.81	0.21	12.3	4.67	59.7	23.2	108	22.0	200	40.3	11760	42	209
20	8.26	1227	429483	-	12.9	0.04	0.79	2.61	0.30	18.6	7.67	101	40.3	198	40.9	378	77.4	11160	123	370
21	-	673	441482	-	11.2	0.03	0.56	1.77	0.30	10.1	3.83	50.6	20.7	111	25.0	249	55.4	10862	142	266
22	-	945	430032	14.2	47.9	5.13	23.9	8.09	0.66	19.4	6.11	76.8	30.6	153	34.1	330	71.7	9888	121	241
23	-	3836	429573	-	1.30	0.03	0.86	3.76	0.19	37.2	19.3	291	127	663	143	1317	265	11692	70	524
24	-	3944	430792	0.56	3.24	0.48	3.49	4.82	0.31	38.5	19.5	296	130	679	149	1378	279	12228	78	619
25	9.87	1302	432379	-	2.25	0.03	0.59	2.19	0.07	18.3	7.90	107	43.5	208	42.8	386	77.8	11993	81	282
26	5.14	2408	427217	0.17	2.20	0.15	1.17	3.39	0.21	26.9	12.3	185	78.8	410	88.0	807	164	12037	70	454

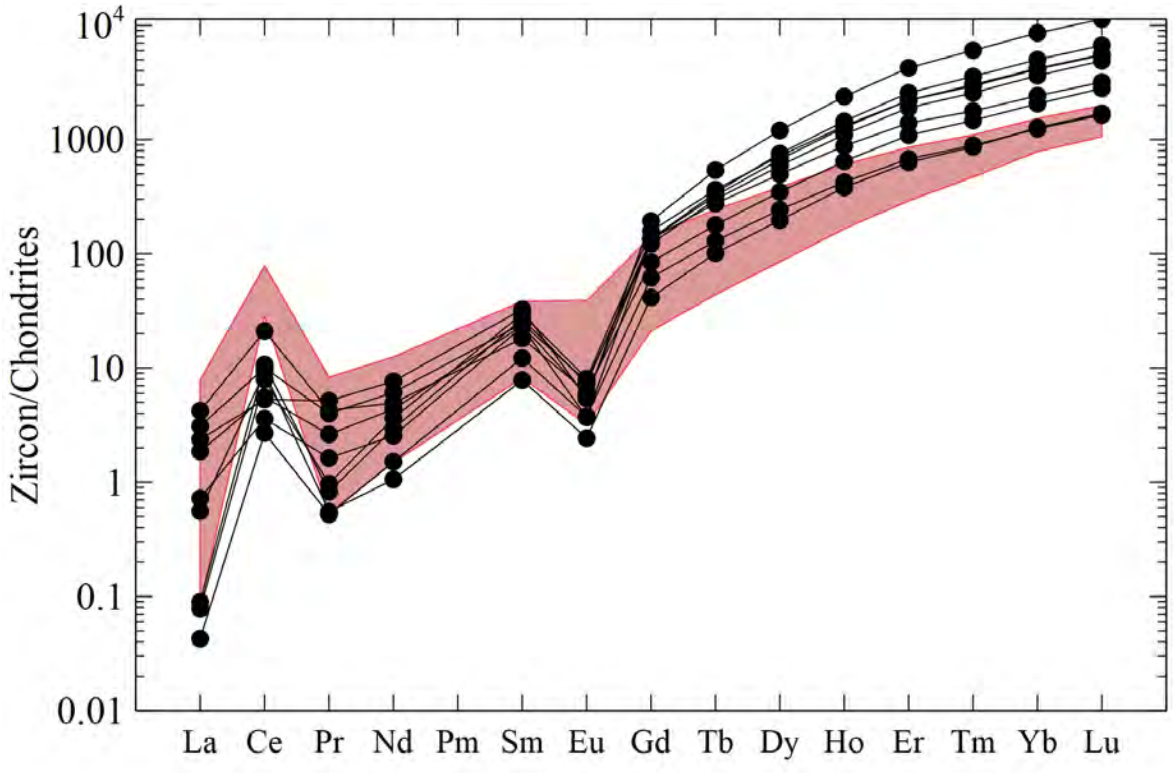

Figure E5: Zircon trace element patterns in the Blowering Formation. Shaded red is the zircon trace element patterns from Long et al. (2012).

Table E6: Zircon trace element data for the Honeysuckle Beds zircons (TDBHons017.01).

Spot	Ti	Y	Zr	La	Ce	Pr	Nd	Sm	Eu	Gd	Tb	Dy	Ho	Er	Tm	Yb	Lu	Hf	Th	U
1	34.6	2294	400786	1.28	7.18	0.95	5.44	4.20	0.52	24.6	11.7	175	73.8	380	82.1	774	159	12196	64	419
2	-	1104	393074	0.17	6.39	0.14	1.02	2.12	0.05	16.8	7.00	94.7	37.5	181	37.3	331	65.0	12266	277	726
3	7.16	3129	399531	0.76	4.62	0.42	2.98	4.32	0.34	31.6	15.5	241	105	542	116	1072	218	12426	90	509
4	-	1732	407120	0.01	2.39	0.03	0.60	1.90	0.15	17.7	8.57	131	56.7	299	66.0	624	129	12322	72	388
5	37.8	2917	408879	3.03	27.6	1.62	9.40	8.23	1.28	44.0	17.5	244	97.8	475	99.0	882	175	10807	247	510
6	9.38	1102	411472	-	6.07	0.05	0.85	3.08	0.30	20.1	7.47	98.9	37.8	178	34.9	307	63.3	11212	93	143
7	-	3038	404952	-	2.21	0.02	0.77	3.03	0.22	30.2	15.0	231	101	525	113	1043	208	12191	82	516
8	6.88	2987	408252	0.63	8.12	0.47	2.94	4.26	0.42	33.1	15.4	237	100	511	109	994	200	11930	114	561
9	-	2851	421568	-	2.74	-	0.82	3.40	0.25	29.8	14.4	217	94.9	494	106	981	195	12113	109	532
10	-	2713	420586	-	2.73	0.04	0.86	3.69	0.31	31.6	14.3	213	91.3	456	98.4	914	185	11603	87	390
11	-	2776	418313	0.18	4.62	0.16	1.60	3.59	0.34	28.9	14.1	213	91.3	473	102	948	189	11736	127	511
12	8.16	3113	442273	0.32	4.71	0.27	2.28	4.40	0.37	32.9	15.7	241	104	540	118	1107	223	12238	112	581
13	9.07	1578	440385	0.52	5.83	0.42	2.54	2.96	0.30	16.2	7.79	120	52.0	280	62.4	602	123	12579	48	333
14	5.46	2828	436306	-	2.04	0.04	0.81	3.47	0.20	31.2	14.7	223	94.5	482	104	948	188	12255	79	455
15	-	2260	436355	0.01	2.92	0.03	0.71	2.81	0.24	23.7	11.6	177	76.4	390	85.1	801	159	12094	79	422
16	-	3067	434892	-	1.44	0.02	0.65	3.01	0.17	28.1	14.8	232	100	517	113	1054	207	12399	69	523
17	-	2960	444321	-	1.74	0.03	0.55	2.93	0.24	28.1	14.2	227	98.7	512	113	1070	213	12448	75	522
18	8.64	552	441642	-	11.0	0.03	0.63	1.55	0.40	9.04	3.44	44.8	17.7	90.0	19.4	187	40.1	9735	104	159
19	7.39	3822	444301	1.67	9.15	1.03	6.19	6.91	0.48	47.5	20.9	313	130	640	135	1228	234	11442	122	507
20	-	3324	430831	0.01	2.09	0.04	0.69	3.41	0.25	33.2	16.5	256	112	582	126	1195	233	12153	101	629
21	11.4	874	449935	0.30	9.60	0.32	1.93	2.83	0.40	15.9	5.95	76.3	29.2	138	28.3	263	52.5	10558	101	163
22	-	2056	447063	0.05	3.17	0.06	0.82	2.30	0.21	20.7	10.0	155	67.5	352	77.3	756	152	12266	74	439
23	7.93	2760	432858	0.05	3.57	0.09	1.03	3.88	0.32	30.9	15.0	219	91.1	457	95.8	887	173	11419	97	405
24	-	2068	436443	0.00	1.21	0.02	0.29	1.68	0.12	18.0	9.77	158	68.9	371	87.2	889	180	13806	55	545
25	7.43	540	445855	-	4.58	0.01	0.34	1.15	0.12	7.99	3.12	41.8	17.4	87.2	19.5	191	40.4	11414	66	175
26	-	2827	429573	-	5.76	0.09	1.28	5.12	0.43	37.6	16.2	231	94.4	464	95.6	877	169	11087	177	540
27	5.22	3123	422333	0.18	2.98	0.16	1.64	3.32	0.34	32.1	15.9	245	106	542	117	1090	215	12082	89	535

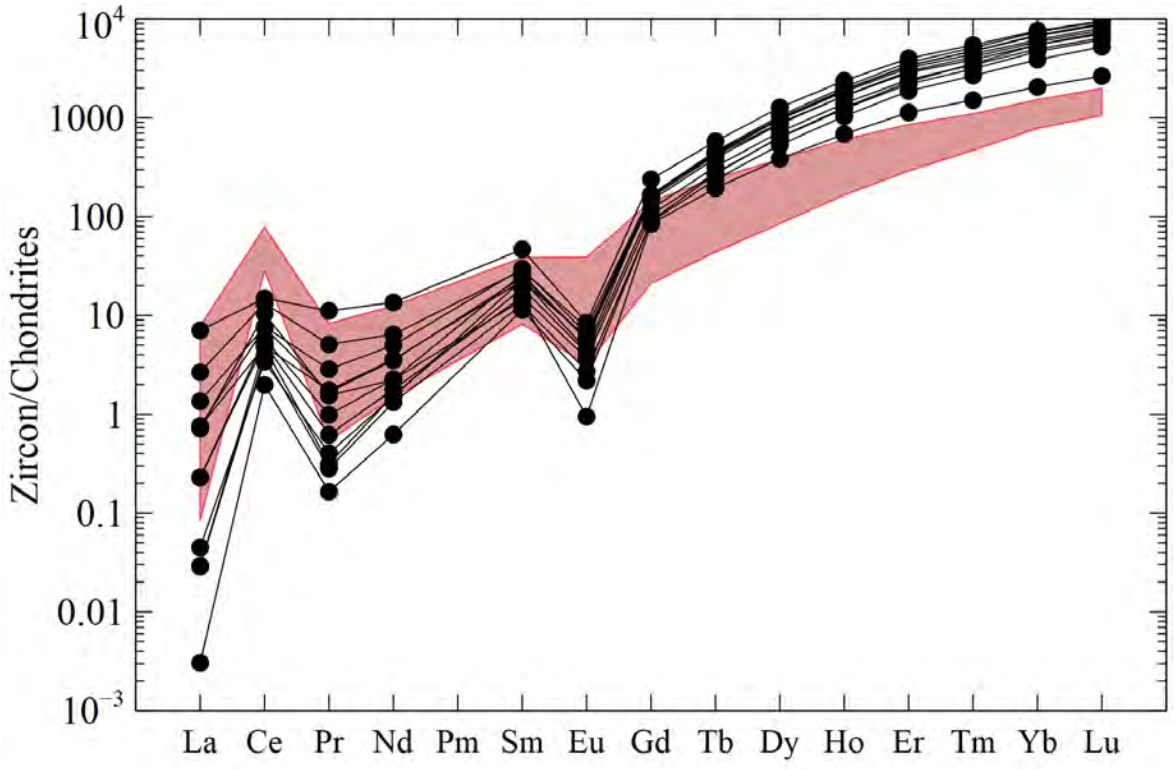

Figure E6: Zircon trace element patterns in the Honeysuckle Beds. Shaded red is the zircon trace element patterns from Long et al. (2012).

Table E7: Zircon trace element data for the Killimicat Granite zircons (TDBHons022.01).

Spot	Ti	Y	Zr	La	Ce	Pr	Nd	Sm	Eu	Gd	Tb	Dy	Ho	Er	Tm	Yb	Lu	Hf	Th	U
1	27.8	1411	436518	0.01	4.04	0.16	2.58	5.90	0.95	29.8	10.0	121	48.0	226	45.8	423	89.3	8424	69	118
2	8.75	2772	429269	7.35	60.1	4.07	19.9	19.4	3.13	73.2	23.6	281	93.3	409	80.9	706	134	11379	186	434
3	-	2651	437355	1.22	5.39	0.51	4.00	5.39	0.62	37.6	16.2	222	88.8	432	88.3	791	157	11714	96	548
4	10.3	2891	420525	1.66	15.9	0.82	7.56	13.3	1.21	73.8	23.7	280	105	455	87.9	751	148	10922	325	383
5	19.3	2406	434083	5.60	17.5	2.74	17.2	15.6	2.49	71.0	21.9	245	86.1	369	68.5	580	116	8345	147	177
6	-	1184	432088	0.01	11.5	0.05	1.30	3.51	0.46	24.7	8.55	109	42.4	196	38.8	343	68.6	11178	165	258
7	-	2624	429917	0.35	9.81	0.32	2.38	5.91	0.44	44.0	17.4	229	91.9	438	87.9	772	154	11859	215	473
8	9.96	2259	426859	1.40	17.8	0.95	7.20	9.20	1.09	47.5	17.3	210	79.1	361	70.2	616	122	10946	181	429
9	6.96	2593	450354	1.28	6.47	0.78	4.78	5.61	0.75	33.0	14.8	205	84.6	426	91.4	865	174	12950	69	478
10	-	1532	446677	0.01	11.7	0.12	1.86	4.93	0.70	31.4	11.4	140	54.1	248	49.2	434	85.9	10884	237	321
11	-	2350	434654	1.48	14.3	0.64	4.23	5.98	0.51	37.6	15.5	203	81.3	377	77.0	679	134	12450	407	947
12	34.5	3869	460085	6.34	32.7	4.58	25.4	26.4	3.10	99.7	35.2	404	140	607	120	1028	186	10382	268	406
13	7.64	2607	436942	5.69	35.5	3.30	19.4	15.6	2.15	59.2	20.6	244	90.9	394	79.7	711	138	13181	255	697
14	14.5	873	432014	-	3.68	0.06	1.25	2.69	0.69	15.9	5.65	71.5	29.3	145	29.7	277	59.6	8556	66	137
15	22.0	1999	455224	4.32	19.6	2.58	15.6	12.1	1.46	43.5	16.0	190	67.7	315	62.6	557	111	12438	107	545
16	7.30	2140	441694	0.08	4.23	0.14	2.01	5.31	0.56	37.4	14.2	183	72.5	346	70.8	642	128	10342	74	185
17	9.99	2064	427878	6.97	28.3	2.70	17.5	11.4	1.43	51.5	17.0	197	74.4	328	62.7	542	105	9551	319	315
18	8.89	2002	435031	-	6.69	0.10	1.93	5.29	0.57	37.8	14.1	177	68.4	320	63.9	567	112	10796	130	231
19	9.79	2476	438500	1.10	11.6	0.75	7.41	12.2	1.58	62.5	20.7	243	88.2	389	72.9	625	121	10270	254	280
20	10.7	2123	431498	0.02	6.40	0.27	3.91	9.05	1.34	50.7	16.7	203	74.7	334	63.6	558	110	9563	161	231
21	27.7	2155	415006	1.10	15.4	0.73	6.26	8.82	1.07	47.4	16.5	196	74.0	336	66.7	582	115	8983	262	302
22	11.5	2164	436395	0.03	3.16	0.09	2.19	5.81	0.52	39.2	14.8	191	74.5	349	70.1	626	124	10875	82	196
23	9.00	1008	443261	-	3.79	0.04	1.01	3.04	0.38	19.4	7.06	89.5	35.0	163	32.5	293	58.8	10625	65	115

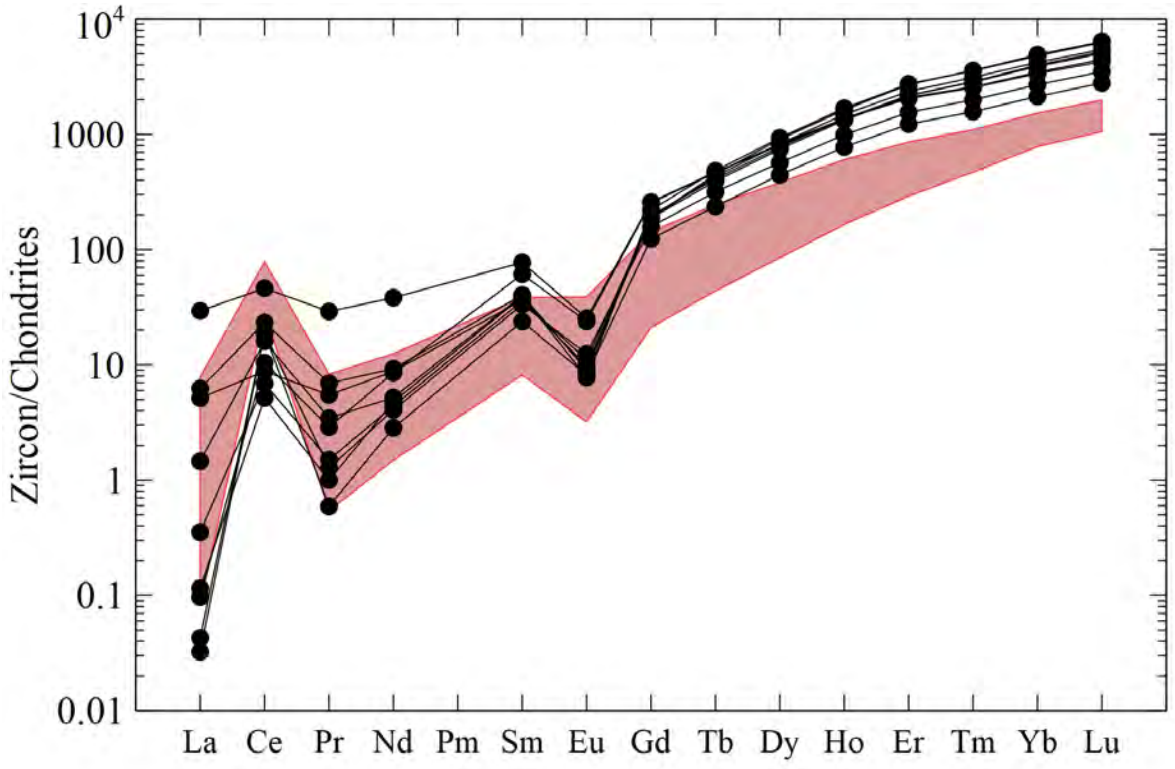

Figure E7: Zircon trace element patterns in the Killimicat Granite. Shaded red is the zircon trace element patterns from Long et al. (2012).

Appendix F - Sm-Nd Data

Sm-Nd data appears in this appendix. Analyses are sorted by sample number, with associated rock unit name and lithology.

Sample	Rock Unit	Lithology	Sm (ppm)	Nd (ppm)	$^{147}Sm/^{144}Nd$	$^{143}Nd/^{144}Nd$	Inferred Age	ϵNd
TDBHons 008.01	Wermatong Metabasalt	Mafic Schist	5.34	18.5	0.16131	0.51280	480.0	5.5
TDBHons 018.01	Honeysuckle Beds	Dacite	6.45	30.0	0.12627	0.51206	429.1[2]	-7.3
TDBHons 019.02	Wyangle Formation	Gabbro	2.66	10.9	0.13377	0.51273	430.0	5.3
TDBHons 020.01	Wyangle Formation	Metabasalt	4.79	26.0	0.11075	0.51249	430.0	2.0
TDBHons 025.01	Long Tunnel Metabasic Igneous Complex	Basalt	6.24	27.4	0.12136	0.51263	433.0	4.1

[2]Zircon age is used for the Honeysuckle Beds (refer to section 3.3.1) while an inferred age is used for the other units (refer to 4.2).

Appendix G - Lu-Hf Data

Lu-Hf data appears in this appendix. The following tables are in order of sample number and analyses sorted by spot number. There are some tables with rows highlighted in grey. These analyses have anomalous ϵHf results.

Table G1: Zircon Lu-Hf isotope data for the Kimo Diorite (TDBHons003.01)

Spot Number	$^{180}Hf/^{177}Hf$	$\pm 2\sigma$	$^{176}Yb/^{177}Hf$	$\pm 2\sigma$	$^{176}Lu/^{177}Hf$	$\pm 2\sigma$	$^{176}Hf/^{177}Hf$	$\pm 2\sigma$	Spot Age	ϵHf	$\pm 2\sigma$
1	1.88720	0.00014	0.11440	0.00750	0.003430	0.000240	0.282817	0.000039	417	9.48	0.39
2	1.88699	0.00016	0.08422	0.00053	0.002559	0.000011	0.282791	0.000035	417	8.80	0.35
4	1.88689	0.00015	0.04800	0.00160	0.001531	0.000030	0.282799	0.000035	417	9.37	0.35
5	1.88698	0.00015	0.04610	0.00130	0.001409	0.000032	0.282736	0.000042	427	7.39	0.42
6	1.88687	0.00015	0.13760	0.00200	0.004125	0.000075	0.282879	0.000031	417	11.48	0.31
7	1.88706	0.00014	0.17310	0.00570	0.005170	0.000110	0.282943	0.000042	420	13.51	0.42
9	1.88681	0.00012	0.05883	0.00077	0.001877	0.000022	0.282792	0.000032	433	9.36	0.32
10	1.88696	0.00012	0.04665	0.00082	0.001497	0.000032	0.282775	0.000034	417	8.53	0.34
11	1.88694	0.00012	0.06245	0.00024	0.001991	0.000026	0.282776	0.000033	417	8.43	0.33
12	1.88687	0.00013	0.04894	0.00070	0.001584	0.000047	0.282825	0.000039	417	10.27	0.39

Table G2: Zircon Lu-Hf isotope data for the Bogong Granite (TDBHons007.01)

Spot Number	$^{180}Hf/^{177}Hf$	$\pm 2\sigma$	$^{176}Yb/^{177}Hf$	$\pm 2\sigma$	$^{176}Lu/^{177}Hf$	$\pm 2\sigma$	$^{176}Hf/^{177}Hf$	$\pm 2\sigma$	Spot Age	ϵHf	$\pm 2\sigma$
1	1.88692	0.00013	0.05484	0.00066	0.001616	0.000016	0.282613	0.000034	426	2.95	0.34
2	1.88701	0.00014	0.07722	0.00059	0.002344	0.000010	0.282613	0.000029	440	3.04	0.29
3	1.88683	0.00013	0.03870	0.00250	0.001184	0.000061	0.282572	0.000040	424	1.58	0.40
4	1.88710	0.00014	0.05140	0.00240	0.001551	0.000064	0.282598	0.000038	419	2.29	0.38
5	1.88681	0.00011	0.04982	0.00092	0.001521	0.000019	0.282614	0.000029	430	3.10	0.29
6	1.88693	0.00011	0.09280	0.00100	0.002717	0.000029	0.282657	0.000033	416	3.99	0.33
7	1.88710	0.00014	0.03485	0.00056	0.001116	0.000028	0.282570	0.000034	416	1.35	0.34
8	1.88691	0.00013	0.05153	0.00046	0.001532	0.000020	0.282644	0.000029	433	4.22	0.29
9	1.88688	0.00014	0.03037	0.00023	0.000939	0.000001	0.282618	0.000031	416	3.10	0.31
10	1.88738	0.00016	0.03880	0.00290	0.001161	0.000085	0.282650	0.000034	416	4.17	0.34
11	1.88696	0.00014	0.04929	0.00054	0.001443	0.000008	0.282674	0.000035	425	5.14	0.35
12	1.88714	0.00016	0.08710	0.00700	0.002580	0.000190	0.282667	0.000036	416	4.38	0.36

Table G3: Zircon Lu-Hf isotope data for the Gocup Granite (TDBHons011.01)

Spot Number	$^{180}Hf/^{177}Hf$	$\pm 2\sigma$	$^{176}Yb/^{177}Hf$	$\pm 2\sigma$	$^{176}Lu/^{177}Hf$	$\pm 2\sigma$	$^{176}Hf/^{177}Hf$	$\pm 2\sigma$	Spot Age	ϵHf	$\pm 2\sigma$
1	1.88708	0.00010	0.05744	0.00051	0.001728	0.000026	0.282467	0.000033	419	-2.40	0.33
2	1.88703	0.00012	0.09750	0.00450	0.002950	0.000170	0.282572	0.000037	426	1.12	0.37
3	1.88713	0.00038	0.07200	0.01100	0.002180	0.000330	0.282680	0.000130	418	5.00	1.30
4	1.88695	0.00012	0.07550	0.00790	0.002240	0.000230	0.282531	0.000034	437	0.10	0.34
5	1.88705	0.00010	0.03694	0.00057	0.000977	0.000020	0.282451	0.000026	418	-2.78	0.26
6	1.88707	0.00011	0.08010	0.00200	0.002422	0.000069	0.282528	0.000027	418	-0.45	0.27
7	1.88719	0.00028	0.09600	0.01400	0.002920	0.000390	0.282740	0.000130	418	6.92	1.30
8	1.88701	0.00021	0.06178	0.00091	0.001862	0.000015	0.282649	0.000074	413	3.88	0.74
9	1.88699	0.00012	0.05005	0.00056	0.001476	0.000017	0.282471	0.000031	428	-1.99	0.31
10	1.88695	0.00013	0.03480	0.00120	0.001092	0.000031	0.282517	0.000026	418	-0.47	0.26
11	1.88694	0.00013	0.04076	0.00098	0.001237	0.000036	0.282475	0.000024	418	-2.00	0.24
12	1.88697	0.00010	0.01438	0.00051	0.000400	0.000017	0.282445	0.000031	418	-2.83	0.31

Table G4: Zircon Lu-Hf isotope data for the Warrienbah granite (TDBHons012.01)

Spot Number	$^{180}Hf/^{177}Hf$	$\pm 2\sigma$	$^{176}Yb/^{177}Hf$	$\pm 2\sigma$	$^{176}Lu/^{177}Hf$	$\pm 2\sigma$	$^{176}Hf/^{177}Hf$	$\pm 2\sigma$	Spot Age	ϵHf	$\pm 2\sigma$
1	1.88692	0.00015	0.04220	0.00160	0.001329	0.000039	0.282541	0.000029	423	0.42	0.29
2	1.88700	0.00011	0.09570	0.00640	0.002660	0.000180	0.282621	0.000032	466	3.77	0.32
3	1.88689	0.00014	0.04001	0.00080	0.001400	0.000030	0.282732	0.000032	428	7.27	0.32
4	1.88693	0.00017	0.09890	0.00410	0.002700	0.000130	0.282720	0.000043	428	6.47	0.43
5	1.88724	0.00013	0.11930	0.00630	0.003210	0.000180	0.282675	0.000035	418	4.53	0.35
6	1.88688	0.00012	0.06720	0.00460	0.001919	0.000085	0.282732	0.000029	414	6.83	0.29
7	1.88693	0.00013	0.05490	0.00280	0.001679	0.000058	0.282625	0.000032	415	3.12	0.32
8	1.88693	0.00010	0.08014	0.00065	0.002369	0.000010	0.282797	0.000032	408	8.88	0.32
9	1.88699	0.00011	0.07370	0.00120	0.002103	0.000025	0.282764	0.000033	425	8.14	0.33
10	1.88702	0.00012	0.03920	0.00066	0.001251	0.000016	0.282501	0.000029	417	-1.10	0.29
11	1.88699	0.00010	0.07104	0.00021	0.002096	0.000008	0.282711	0.000032	415	6.05	0.32
12	1.88697	0.00009	0.05382	0.00064	0.001672	0.000011	0.282612	0.000024	419	2.75	0.24
13	1.88690	0.00012	0.04527	0.00042	0.001398	0.000007	0.282627	0.000027	415	3.27	0.27

Table G5: Zircon Lu-Hf isotope data for the Blowering Formation (TDBHons015.01)

Spot Number	$^{180}Hf/^{177}Hf$	$\pm 2\sigma$	$^{176}Yb/^{177}Hf$	$\pm 2\sigma$	$^{176}Lu/^{177}Hf$	$\pm 2\sigma$	$^{176}Hf/^{177}Hf$	$\pm 2\sigma$	Spot Age	ϵHf	$\pm 2\sigma$
1	1.88696	0.00011	0.04458	0.00084	0.001383	0.000029	0.282295	0.000035	419	-8.39	0.35
2	1.88691	0.00011	0.02430	0.00110	0.000777	0.000030	0.282340	0.000032	493	-5.01	0.32
3	1.88689	0.00010	0.04105	0.00065	0.001300	0.000016	0.282342	0.000029	441	-6.23	0.29
4	1.88702	0.00011	0.03052	0.00059	0.000992	0.000011	0.282275	0.000033	424	-8.88	0.33
5	1.88696	0.00009	0.09761	0.00073	0.003101	0.000037	0.282382	0.000025	430	-5.56	0.25
6	1.88698	0.00010	0.02042	0.00008	0.000681	0.000004	0.282256	0.000031	450	-8.89	0.31
7	1.88698	0.00012	0.03710	0.00480	0.001180	0.000140	0.282324	0.000029	431	-7.05	0.29
8	1.88692	0.00013	0.02121	0.00023	0.000676	0.000003	0.282328	0.000030	499	-5.27	0.30
9	1.88699	0.00010	0.01270	0.00070	0.000450	0.000020	0.282368	0.000033	428	-5.35	0.33
10	1.88687	0.00014	0.02613	0.00054	0.000830	0.000012	0.282353	0.000028	426	-6.03	0.28
11	1.88687	0.00011	0.08280	0.00230	0.002571	0.000057	0.282375	0.000026	427	-5.72	0.26
12	1.88699	0.00013	0.02903	0.00038	0.000921	0.000016	0.282365	0.000030	425	-5.65	0.30
13	1.88703	0.00009	0.03241	0.00060	0.001004	0.000013	0.282228	0.000026	439	-10.22	0.26

Table G6: Zircon Lu-Hf isotope data for the Honeysuckle Beds (TDBHons017.01)

Spot Number	$^{180}Hf/^{177}Hf$	$\pm 2\sigma$	$^{176}Yb/^{177}Hf$	$\pm 2\sigma$	$^{176}Lu/^{177}Hf$	$\pm 2\sigma$	$^{176}Hf/^{177}Hf$	$\pm 2\sigma$	Spot Age	ϵHf	$\pm 2\sigma$
1	1.88699	0.00010	0.09930	0.00180	0.003205	0.000070	0.282385	0.000026	436	-5.37	0.26
2	1.88695	0.00012	0.06782	0.00040	0.002131	0.000021	0.282376	0.000028	429	-5.52	0.28
3	1.88692	0.00010	0.06940	0.00140	0.002195	0.000030	0.282362	0.000029	432	-5.97	0.29
4	1.88702	0.00010	0.08460	0.00130	0.002749	0.000029	0.282414	0.000023	429	-4.35	0.23
5	1.88696	0.00014	0.03812	0.00089	0.001302	0.000018	0.282248	0.000028	771	-2.43	0.28
6	1.88732	0.00037	0.06730	0.00180	0.002259	0.000032	0.282530	0.000190	430	-0.08	1.90
7	1.88711	0.00009	0.08990	0.00140	0.002771	0.000036	0.282403	0.000034	438	-4.56	0.34
8	1.88695	0.00011	0.09135	0.00066	0.002888	0.000038	0.282408	0.000027	436	-4.46	0.27
9	1.88687	0.00013	0.03081	0.00052	0.001002	0.000009	0.282319	0.000032	426	-7.28	0.32
10	1.88695	0.00010	0.07740	0.00200	0.002510	0.000100	0.282406	0.000030	425	-4.65	0.30
11	1.88705	0.00009	0.04440	0.00200	0.001456	0.000053	0.281702	0.000042	429	-29.18	0.42
12	1.88693	0.00012	0.08171	0.00082	0.002637	0.000008	0.282432	0.000035	429	-3.68	0.35
13	1.88702	0.00012	0.07392	0.00048	0.002423	0.000017	0.282447	0.000037	429	-3.09	0.37

Table G7: Zircon Lu-Hf isotope data for the Killimicat Granite (TDBHons022.01)

Spot Number	$^{180}Hf/^{177}Hf$	$\pm 2\sigma$	$^{176}Yb/^{177}Hf$	$\pm 2\sigma$	$^{176}Lu/^{177}Hf$	$\pm 2\sigma$	$^{176}Hf/^{177}Hf$	$\pm 2\sigma$	Spot Age	ϵHf	$\pm 2\sigma$
1	1.88702	0.00010	0.06440	0.00120	0.002041	0.000048	0.282293	0.000031	438	-8.24	0.31
2	1.88750	0.00076	0.03760	0.00260	0.001244	0.000058	0.282860	0.000260	410	11.45	2.60
3	1.88690	0.00013	0.05100	0.00130	0.001550	0.000034	0.282632	0.000041	409	3.28	0.41
4	1.88679	0.00011	0.02200	0.00170	0.000687	0.000044	0.280708	0.000029	409	-64.59	0.29
5	1.88690	0.00012	0.09310	0.00410	0.002860	0.000140	0.282353	0.000055	493	-5.23	0.55
6	1.88706	0.00012	0.04160	0.00250	0.001286	0.000066	0.282680	0.000028	409	5.05	0.28
7	1.88710	0.00025	0.06670	0.00110	0.002158	0.000037	0.282879	0.000099	409	11.86	0.99
8	1.88696	0.00013	0.06340	0.00420	0.001940	0.000120	0.282643	0.000031	407	3.52	0.31
9	1.88689	0.00013	0.05640	0.00047	0.001713	0.000024	0.282648	0.000034	420	4.04	0.34
10	1.88704	0.00012	0.06030	0.00180	0.001840	0.000046	0.282594	0.000032	409	1.86	0.32
11	1.88756	0.00015	0.06570	0.00200	0.002095	0.000081	0.282770	0.000058	443	8.73	0.58